SKOLKOVO INSTITUTE OF SCIENCE AND TECHNOLOGY

FAST INTEGRAL EQUATION METHODS AND PERFORMANCE BOUNDS OF MODERN MAGNETIC RESONANCE COILS

Doctoral Thesis

by

IOANNIS P. GEORGAKIS

DOCTORAL PROGRAM IN
COMPUTATIONAL AND DATA SCIENCE AND ENGINEERING

Supervisor
Professor Maxim Fedorov

Co-supervisor
Dr. Athanasios G. Polimeridis

Moscow - 2019

Abstract

The promise of improved signal-to-noise ratio (SNR), higher spatial/spectral resolution, and shorter imaging time continues to motivate the pursuit of high and ultra-high field magnetic resonance imaging. However, as field strength increases, the associated radiofrequency (RF) magnetic fields become inhomogeneous resulting in regions with SNR drops and loss of image quality, while local hot-spots, due to specific absorption rate (SAR) peaks, may occur. These challenges present the opportunity to design the next-generation, sophisticated RF coils which will yield higher SNR and faster image acquisition without compromising patient safety and image quality. Such design, however, requires long computational cycles, in order to explore the high-order parametric space and monitor the trade-offs between array degrees of freedom and various metrics, such as SNR, SAR, and transmit efficiency (TXE). During this process, electromagnetic (EM) modeling constitutes an essential tool.

This thesis employs analytical methods and develops novel numerical methods for modeling the interactions between EM waves and biological tissue and for computing theoretical RF coils performance bounds consistent with electrodynamic principles along with their corresponding optimal RF excitation patterns, which we term ideal current patterns (ICP). We employ analytical methods and introduce a new performance metric, the ultimate intrinsic TXE (UITXE), which is the theoretically largest TXE that can be achieved by any RF coil in uniform spherical objects and calculate its associated ICP on spherical surfaces. We further develop a novel volume integral equation solver for the accurate computation of EM fields distributions within highly inhomogeneous realistic human body models (RHBM). Our solver presents remarkably stable convergence properties and yields reliable EM fields for challenging modeling scenarios and coarse resolutions without necessarily refining the computational grid. Finally, we describe robust algorithms for generating a consistent numerical EM fields basis able to represent all EM fields distributions inside inhomogeneous, arbitrary objects and demonstrate how such basis can be used to derive UITXE inside RHBM and ICP on arbitrary excitation surfaces that yield optimal SNR within RHBM. UITXE can provide an absolute reference for coil benchmarking while ICP can inform the non-convex RF coil optimization problem by providing an intuitive initial guess. We believe that these tools can offer the framework for a truly robust optimization of next-generation RF coils.

List of Publications

Georgakis IP, Polimeridis AG. "Reduction of Volume-Volume Integrals Arising in Galerkin JM-VIE Formulations to Surface-Surface Integrals." *In 11th European Conference on Antennas and Propagation (EuCAP)*, 2017 Mar, Paris, France (pp. 324-326), IEEE.

Serralles JEC, Georgakis IP, Polimeridis AG, Daniel L, White JK, Sodickson DK, Lattanzi R. "Volumetric Reconstruction of Tissue Electrical Properties from B_1^+ and MR Signals Using Global Maxwell Tomography: Theory and Simulation Results." *In Proceedings of ISMRM 25th Annual Meeting Exhibition*, 2017 Apr, Honolulu, HI, USA (p. 3647), (Magna Cum Laude Merit Award and finalist for the Electromagnetic Tissue Properties study group poster prize competition).

Yucel AC, Bagci H, Georgakis IP, Polimeridis AG, White JK. "An FFT-accelerated Inductance Extractor for Voxelized Structures." *In 2018 International Applied Computational Electromagnetics Society Symposium (ACES)*, 2018 Mar, Denver, CO, USA (pp. 1-2).

Yucel AC, Georgakis IP, Polimeridis AG, Bagci H, White JK. "VoxHenry: FFT-accelerated Inductance Extraction for Voxelized Geometries." *IEEE Transactions on Microwave Theory and Techniques*. 2018 Apr;66(4):1723-35.

Georgakis IP, Polimeridis AG, Lattanzi R. "Ultimate Intrinsic Transmit Efficiency for RF Shimming." *In Proceedings of Joint Annual Meeting ISMRM-ESMRMB*, 2018 Jun, Paris, France (p. 0139).

Georgakis IP, Polimeridis AG, Lattanzi R. "Ideal Current Patterns for Optimal SNR in Realistic Heterogeneous Head Models." *In Proceedings of ISMRM 27th Annual Meeting and Exhibition*, 2019 May, Montreal, Canada (p. 1036).

Georgakis IP, Giannakopoulos II, Litsarev MS, Polimeridis AG. "A Fast Volume Integral Equation Solver with Linear Basis Functions for the Accurate Computation of Electromagnetic Fields in MRI." arXiv preprint arXiv:1902.02196, (under review).

Georgakis IP, Polimeridis AG, Lattanzi R. "Ultimate Intrinsic Transmit Efficiency for Radiofrequency Shimming." (under review).

Acknowledgments

In January 2015, I received an email saying that Dr. Athanasios Polimeridis would be giving an invited research talk on computational electromagnetics at Aristotle University of Thessaloniki (AUTh), where I had recently graduated from. Out of curiosity and thanks to the advice of my undergraduate thesis supervisor from AUTh, Prof. Nikolaos Kantartzis, I attended that lecture, which greatly impressed and inspired me. After much thinking and a long list of questions to Thanos, I decided to join, under his supervision, the PhD program at Skoltech, where I have been conducting my PhD since September 2015 at the Center for Computational and Data-Intensive Science and Engineering.

Ever since, Thanos has become my advisor to whom I am deeply grateful for many different reasons. For offering me the chance to work with him, for helping me develop an intuitive understanding of the fascinating world of electrodynamics and integral equations, and for sharing with me his substantial expertise in these fields. For believing in my abilities and nurturing me as a scientist with patience, support, numerous in-depth discussions, and through original ideas and valuable advice, that pointed into the right direction without revealing the exact answer, intending to help me research and deduce it on my own. For educating me not only as a scientist but as a person, too, and teaching me to be persistent and inquisitive. For all these reasons, Thanos, I owe you a big and honest thank you! Besides these, Thanos also provided me with the extraordinary opportunity to meet and collaborate with two remarkable people, Professor Jacob White and Associate Professor Riccardo Lattanzi, with each of them I had the real luck to work for a Term as exchange researcher at MIT Research Laboratory of Electronics and NYU Center for Advanced Imaging Innovation and Research, respectively.

Indeed, prior to joining Skoltech, I could have never imagined that I would have had the privilege to get one-to-one mentoring from one of the world's leading experts on integral equations and numerical sciences. In the beginning, after such meetings with Jacob, I felt overwhelmed by the sheer amount of information and ideas, reminding me of the phrase "education at MIT is like drinking from a fire hose." However, toward the end of my PhD, a five-minute talk with him would help me make progress on a project that had me stuck for months. More importantly, Jacob taught me by his example and his practical help, on many

different levels and in multiple occasions during my PhD, that genuinely caring people exist in the academic world. For this lesson and for sharing with me your profound knowledge in numerics, Jacob, I will always be grateful to you!

Still, my PhD would have been entirely different, had I not had the unique opportunity to work with Riccardo and the people at NYU. Riccardo offered me the chance to work on intriguing applications within the captivating MR field, where I could apply our computational tools adding extra value to them, shared with me his extensive expertise in ideal current patterns and ultimate metrics, and significantly assisted my transition into viewing research from the MR perspective. Together with these lessons, Riccardo taught me, by his example, that an academic can be modest and kind, while he was always on-a-different-level understanding, friendly, and approachable, yet thorough and analytical when it came to research, devoting to me plenty of his time and always willing to answer to my questions. For all these reasons, Riccardo, I feel the real need to express my deep gratitude to you by genuinely saying thank you!

I would also like to thank my formal supervisor, Professor Maxim Fedorov, Dr. Stamatis Lefkimmiatis, and Prof. Dmitry Dylov who all helped me in critical transitional periods of my PhD and made it possible to finish my graduate studies smoothly, as well as, Prof. Ivan Oseledets and Prof. Alexander Shapeev for providing their mathematical insight and for being in my Individual Doctoral Committee. A big thank you also to the members of our Skoltech group Mikhail Litsarev, Ilias Giannakopoulos, Georgy Guryev, Alexandra Tambova, and Efim Boeru. Our numerous discussions and exchange of ideas were an integral part of this PhD. I would also like to thank Prof. Luca Daniel and Prof. Elfar Adalsteinsson for what I learned from them during my MIT visit about numerics and MR image acquisition, as well as, Prof. Abdulkadir Yucel and Prof. Hakan Bagci for our joint collaboration. A special thank goes to Samuel Groth, José Serrallés, and Richard Zhang for sharing their mathematical rigor and providing feedback on my work. I would particularly like to thank Prof. Daniel Sodickson for holding sometimes more than twice-a-week research seminars at NYU and for asking inquisitive and many times philosophical questions to the speakers, all of which broadened my knowledge and understanding of the MR field. To that same direction contributed my colleague and friend Alessandro Palombit with his never-ending questions on the feasibility of an idea, his sometimes skeptical stance, and his application-oriented mindset to whom I would like to say a really big thank you. I would also like to thank Jing Li, Eros Montin, and Bei Zhang for our interactions during my NYU visit. Finally, I would like to thank many new people that I met in conferences. Especially, Prof. Vladimir Okhmatovski and Prof. Francesca Vipiana, for additionally agreeing to come to Moscow to be part of my jury, as well as, Prof. Martijn van Beurden, Prof. Michael Mattes, Prof. Nikolaos Tsitsas, Wyger Brink, Manushka Vaidya, Roeland Dilz, and Dimitrios Tzarouchis for our discussions and their advice.

For funding this work, I would like to thank the Skoltech-MIT Next Generation Program, without which none of this would have been possible.

I would also like to thank all the new people I met and friends I have made in Moscow, Boston, and New York, along the way. I will start with the people from my first year in Moscow and Skoltech: Prof. Panagiotis Karras, Konstantinos, Yaroslav, Ignasi, Keren, Hripsime, Tigran, Georgy, Andrew, Lee, Daria, Priyanko, Liu, Marina, thank you all. From Boston, I would like to especially thank Eleftheria for teaching me how important dedication is, as well as, Vangelis, Charis, Michalis, and Vasilis for introducing me to them. Back in Moscow and Skoltech, I would like to honestly thank Ilias, Filippos, and Alexandros for their friendship, for endless discussions and useful advice, as well as, Giorgos despite his short stay here. From New York, special thanks go to Alessandro and Jing for being amazing officemates, as well as, Antonis, Emmanouela, Teo, and Nikos for their friendship and help in need. During the last year of my stay in Moscow, I would like to especially thank Valeriya, for being the coolest officemate, my Greek and Cypriot friends: Evi, Marianna, Babis, Vana, Varvara, Adonis, Maria, Adam, Savvas, Vangelis, Alexandros, and Michalis, as well as, the international crew from Skoltech: Mauro, Vito, Strahinja, Kruna, Akshay, Dejan, Mohammad, Woong-Seon, Adriano, Julia, Harry, Vlad, Jean, and Saeed.

Of course, I would like to thank my closest friends from Greece, especially, Stratos, Nikos and Effimia, Giannis, and Giorgis for countless messages and calls, for always being willing to listen to my PhD life problems and for offering their advice and support, as well as, Thodoris, Lazaros, Arsenis, Dimitris, Nikos, Giorgos, Giannis, Nikos, Alexandros, Thanasis, Xenofon, and Christos. Last but not least, I would like to thank my family for their continued support and encouragement. My father, Panagiotis, for teaching me the value of discipline and hard work and my mother, Evangelia, for nurturing my love for physics ever since I was a little kid. My older brother, Michalis, for his sharp perspective and strong emotional and moral support during, not only this PhD, but all of my life, as well as, his wife Eleni for her warm encouragement, and my younger brother, Manolis, for his always positive attitude, even in the hardest of times, and for sharing with me the same passion for the sciences. I dedicate this thesis to all of you and to all my Teachers that have shaped my path until today!

Moscow, August 2019

Ioannis Georgakis

Contents

Abbreviations

1D	one-dimensional
2D	two-dimensional
3D	three-dimensional
4D	four-dimensional
6D	six-dimensional
ABC	absorbing boundary condition
CAD	computer-aided design
CFIE	combined field integral equation
CSF	cerebrospinal fluid
CT	computed tomography
DB-VIE	flux-based volume integral equation
DGF	dyadic Green's function
DoFs	Degrees of Freedom
DSVD	dipole singular value decomposition
EFIE	electric field integral equation
EH-VIE	field-based volume integral equation
EM	electromagnetic
EMF	electromotive force
FDA	Food and Drug Administration
FDTD	Finite Difference Time Domain
FEM	Finite Element Method
FFT	fast Fourier transform
GMRES	generalized minimum residual
GPU	graphical processing unit
ICP	ideal current patterns
IE	integral equation
JM-VIE	current-based volume integral equation
MARIE	Magnetic Resonance Integral Equation
MFIE	magnetic field integral equation

MoM	Method of Moments
MR	magnetic resonance
MRI	magnetic resonance imaging
NMR	nuclear magnetic resonance
PEC	perfect electric conductor
PMC	perfect magnetic conductor
PML	perfectly matched layer
ppm	parts per million
PWC	piece-wise constant
PWL	piece-wise linear
RF	radiofrequency
RMS	root mean square
RMSE	root mean square error
ROI	region of interest
RSVD	randomized singular value decomposition
RWG	Rao-Wilton-Glisson
SAR	specific absorption rate
SIE	surface integral equation
SNR	signal-to-noise ratio
SV	singular value
SSVD	surface singular value decomposition
SVD	singular value decomposition
TXE	transmit efficiency
UHF	ultra-high field
UISNR	ultimate intrinsic signal-to-noise ratio
UITXE	ultimate intrinsic transmit efficiency
VIE	volume integral equation
VSH	vector spherical harmonics

Notation and List of Symbols

Notation	Description
j	imaginary unit
a, A	scalar in $\mathbb{C}$
$\boldsymbol{a}, \boldsymbol{A}$	vector in $\mathbb{C}^3$, $\boldsymbol{a} = (a_x, a_y, a_z)$, $\boldsymbol{A} = (A_x, A_y, A_z)$
$\bar{\boldsymbol{A}}$	dyadic tensor, matrix in $\mathbb{C}^{3\times3}$
$\boldsymbol{\mathcal{A}}$	time-varying vector in $\mathbb{R}^3$, $\boldsymbol{\mathcal{A}} = (\mathcal{A}_x, \mathcal{A}_y, \mathcal{A}_z)$
$\mathbf{a}$	1D array, vector in $\mathbb{C}^N$
$\mathbf{A}$	2D array, matrix in $\mathbb{C}^{N_1\times N_2}$
$\underline{\mathbf{A}}$	mD array, tensor in $\mathbb{C}^{N_1\times N_2 \ldots \times N_m}$
$\mathcal{A}/\boldsymbol{\mathcal{A}}$	continuous operator acting in $\mathbb{C}^3/\mathbb{C}^6$
$.^H$	conjugate transpose superscript
$.^*$	complex conjugation superscript
$.^+$	superscript indicating spherical Hankel instead of Bessel function

Symbol	Unit	Description
a	m	spherical sample radius
$\mathbf{A}$	-	linear system matrix
A_l, B_l, C_l, D_l	-	Dirichlet boundary conditions coefficients
$A_n^{\pm}$	m^2	area of triangular element
b	m	spherical surface radius
$\mathbf{b}$	-	right-hand side vector
$\underline{\mathbf{b}}^{pl}$	-	right-hand side 3D tensor
$\boldsymbol{\mathcal{B}}, \boldsymbol{B}$	T	magnetic flux density
B_0	T	main static magnetic field
$\boldsymbol{B}_1$	T	RF magnetic field
B_1^+	T	RF transmit magnetic field, rotating with nuclear precession
B_1^-	T	RF receive magnetic field, rotating against nuclear precession
$\mathbf{B}_{1+}$	T	transmit sensitivity matrix
$\mathbf{B}_{1-}$	T	receive sensitivity matrix

$\mathbf{C}$	T	transmit sensitivity matrix
d	m	distance between the centers of a spherical sample and a loop coil
D	m	distance between spherical surface and spherical sample
$\boldsymbol{\mathcal{D}}, \boldsymbol{D}$	$\mathrm{Cb/m^2}$	electric flux density
$\mathbf{e}_{\mathrm{inc}}$	$\mathrm{V \cdot m^2}$	"tested" incident electric field vector
$\underline{\mathbf{e}}_{\mathrm{inc}}^{pl}$	$\mathrm{V \cdot m^2}$	"tested" incident electric field 3D tensor
$\boldsymbol{\mathcal{E}}, \boldsymbol{E}$	$\mathrm{V/m}$	electric field intensity
$\mathbf{E}_{\mathrm{tot}}$	$\mathrm{V \cdot m^2}$	total electric field basis
f_0	Hz	Larmor frequency
$\boldsymbol{f_n}$	-	basis/expansion function
$\boldsymbol{f_m}$	-	testing/weight function
g	-	scalar wave Green's function
$\mathbf{G}$	-	Gram matrix
$\underline{\mathbf{G}}^{pl}$	-	Gram 3D tensor
$\bar{\boldsymbol{G}}$	-	electric field DGF
$\bar{\boldsymbol{G}}_{s,1}$	-	scattering component of electric field DGF inside dielectric sphere
$\bar{\boldsymbol{G}}_{s,2}$	-	scattering component of electric field DGF outside dielectric sphere
G_x	$\mathrm{T/m}$	gradient magnetic field in x-direction
h	m	resolution
$\hbar$	$\mathrm{J \cdot s/rad}$	reduced Planck constant
$h_l^{(1)}$	-	spherical Hankel function of the first kind and l
$\mathbf{h}_{\mathrm{inc}}$	$\mathrm{A \cdot m^2}$	"tested" incident magnetic field vector
$\boldsymbol{\mathcal{H}}, \boldsymbol{H}$	$\mathrm{A/m}$	magnetic field intensity
$\mathbf{H}_{\mathrm{tot}}$	$\mathrm{A \cdot m^2}$	total magnetic field basis
$\mathcal{I}$	-	identity operator
$\bar{\boldsymbol{I}}$	-	identity dyadic operator
j_l	-	spherical Bessel function of the first kind and order l
$\boldsymbol{\mathcal{J}}_b$	$\mathrm{A/m^2}$	bound electric current density
$\boldsymbol{\mathcal{J}}_c, \boldsymbol{J}_c$	$\mathrm{A/m^2}$	conduction electric current density
$\boldsymbol{\mathcal{J}}_d$	$\mathrm{A/m^2}$	displacement electric current density
$\boldsymbol{J}_{\mathrm{eq}}$	$\mathrm{A/m}$	equivalent electric surface current density
$\boldsymbol{J}_{\mathrm{eq}}$	$\mathrm{A/m^2}$	equivalent volumetric polarization current density
$\boldsymbol{\mathcal{J}}_i, \boldsymbol{J}_i$	$\mathrm{A/m^2}$	impressed electric current density
$\boldsymbol{J}_s, \boldsymbol{K}$	$\mathrm{A/m}$	electric surface current density
k	$\mathrm{rad/m}$	complex wavenumber inside medium
k_0	$\mathrm{rad/m}$	free-space wavenumber
k_{in}	$\mathrm{rad/m}$	complex wavenumber inside medium
$\mathcal{K}$	-	continuous integro-differential operator
$\mathbf{K}$	-	Galerkin MoM matrix for $\mathcal{K}$ operator

l, m	-	order of multipole expansion
l_n	m	length of common triangle edge
$l_{\max}$	-	finite order of multipole expansion
$\mathcal{L}$	-	continuous integro-differential operator
L_x, L_y, L_z	m	dimensions of rectangular domain
$\boldsymbol{m}$	$\mathrm{A} \cdot \mathrm{m}^2$	nuclear magnetic moment
$\boldsymbol{m}$	-	compound index showing observation voxel center
$\boldsymbol{\mathcal{M}}, \boldsymbol{M}$	$\mathrm{A/m}$	nuclear magnetization (magnetic polarization)
M_0	$\mathrm{A/m}$	equilibrium nuclear magnetization
$\boldsymbol{\mathcal{M}}_c, \boldsymbol{M}_c$	$\mathrm{V/m}^2$	conduction magnetic current density
$\boldsymbol{\mathcal{M}}_d$	$\mathrm{V/m}^2$	displacement magnetic current density
$\boldsymbol{M}_{\mathrm{eq}}$	$\mathrm{V/m}$	equivalent magnetic surface current density
$\boldsymbol{M}_{\mathrm{eq}}$	$\mathrm{V/m}^2$	equivalent volumetric magnetization current density
$\boldsymbol{\mathcal{M}}_i, \boldsymbol{M}_i$	$\mathrm{V/m}^2$	impressed magnetic current density
$\boldsymbol{M}_{l,m}$	-	vector spherical harmonic function
$\boldsymbol{M}_s$	$\mathrm{V/m}$	magnetic surface current density
$\mathcal{M}_\phi$	-	multiplication operator with function ϕ
$\mathbf{M}_\phi$	-	diagonal matrix with function's ϕ values
$\underline{\mathbf{M}}_\phi$	-	3D tensor with function's ϕ values
$\boldsymbol{n}$	-	compound index showing source voxel center
$\hat{\boldsymbol{n}}$	-	normal vector to a surface
$\mathcal{N}$	-	continuous integro-differential operator
$\mathbf{N}$	-	Galerkin MoM matrix for $\mathcal{N}$ operator
$\underline{\mathbf{N}}^{pl,ql'}$	-	Toeplitz defining 3D tensor for $\mathcal{N}$ operator
$\boldsymbol{N}_{l,m}$	-	vector spherical harmonic function
$\boldsymbol{N}_{\boldsymbol{n}}^l$	-	PWL basis functions
N_V	-	number of voxels
N_x, N_y, N_z	-	number of voxels along x, y, z axis
p	-	degree of highest complete polynomial
$\boldsymbol{p}_e$	$\mathrm{C} \cdot \mathrm{m}$	electric dipole moment
$\boldsymbol{p}_m$	$\mathrm{Wb} \cdot \mathrm{m}$	magnetic dipole moment
$\boldsymbol{\mathcal{P}}$	$\mathrm{Cb/m}^2$	electric polarization
$\mathbf{P}$	-	preconditioner
p_{abs}	$\mathrm{W/m}^3$	absorbed power density
P_{abs}	W	absorbed power
P_l^m	-	associated Legendre function of order (l, m)
$P_{\boldsymbol{n}}$	-	volumetric pulse
$\boldsymbol{r}, \boldsymbol{r}_{\boldsymbol{m}}$	m	observation point
$\boldsymbol{r}', \boldsymbol{r}_{\boldsymbol{n}}$	m	source point

r_{2D}	m	radius of circular disk 2D ROI across spherical sample's central plane
r_{3D}	m	radius of spherical 3D ROI concentric to spherical sample
r_{vox}	m	voxel position across spherical sample's diameter
$\hat{\boldsymbol{r}}, \hat{\boldsymbol{\theta}}, \hat{\boldsymbol{\phi}}$	-	unit vectors of spherical coordinates system (radial, polar, azimuthal)
R	m	radius of loop coil
$\mathbf{R}_L$	W	basis fields noise covariance matrix
R_c	Ω	resistance of receive coil
R_s	Ω	resistance of imaging sample
t	s	time
T	K	temperature
$\mathbf{T}$	-	boundary conditions transformation matrix
T_1	s	spin-lattice relaxation time constant
T_2	s	spin-spin relaxation time constant
$T_n^{\pm}$	-	triangular element
SAR	$\mathrm{W/kg}$	specific absorption rate
$\mathbf{U}$	-	unitary matrix with the left-singular vectors as columns
$\mathbf{U}_e$	$\mathrm{V} \cdot \mathrm{m}^2$	incident electric fields basis
$\mathbf{U}_m$	$\mathrm{A} \cdot \mathrm{m}^2$	incident magnetic fields basis
$\mathbf{V}$	-	unitary matrix with the right-singular vectors as columns
$V_{l,m}^M$	-	weighting coefficients of magnetic-type surface currents
$V_{l,m}^N$	-	weighting coefficients of electric-type surface currents
$\mathbf{w}$	-	weighting coefficients complex vector
$W_{l,m}^E$	-	expansion coefficients of electric-type surface currents
$W_{l,m}^M$	-	expansion coefficients of magnetic-type surface currents
$\mathbf{x}$	-	unknowns vector
$\underline{\mathbf{x}}^{pl}$	-	unknowns 3D tensor
$\hat{\boldsymbol{x}}, \hat{\boldsymbol{y}}, \hat{\boldsymbol{z}}$	-	unit vectors of a Cartesian coordinates system
$\mathbf{X}_e$	$\mathrm{A/m}^2$	equivalent polarization currents basis
$\mathbf{X}_m$	$\mathrm{V/m}^2$	equivalent magnetization currents basis
$\boldsymbol{X}_{l,m}$	-	vector spherical harmonic function
$Y_{l,m}$	-	Laplace spherical harmonic function
α	rad	azimuthal angular position of loop coil center
β	rad	polar angular position of loop coil center
γ	$\mathrm{rad} \cdot \mathrm{Hz/T}$	gyromagnetic ratio
δ	-	Dirac delta function
$\boldsymbol{\Gamma}$	T^2	average transmit sensitivity covariance matrix
Δf	Hz	bandwidth of receive filters
ΔV	m^3	voxel volume
$\Delta x, \Delta y, \Delta z$	m	voxel side lengths

ϵ_0	$\mathrm{F/m}$	free-space permittivity
ϵ_r	-	relative permittivity constant
$\dot{\epsilon}_r$	-	relative complex permittivity
η	$\mathrm{T^2/W}$	transmit efficiency
κ	$\mathrm{J/K}$	Boltzmann constant
λ	m	effective wavelength
λ_0	m	free-space wavelength
μ_0	$\mathrm{H/m}$	free-space permeability
μ_r	-	relative permeability constant
$\dot{\mu}_r$	-	relative complex permeability
ρ	$\mathrm{kg/m^3}$	tissue density
ρ_0	-	number of nuclei per unit volume
ρ_b	$\mathrm{Cb/m^3}$	bound electric charge density
ρ_e	$\mathrm{Cb/m^3}$	electric charge density
$\rho_{e,i}$	$\mathrm{Cb/m^3}$	impressed electric charge density
$\rho_{e,s}$	$\mathrm{Cb/m^2}$	electric surface charge density
ρ_m	$\mathrm{Wb/m^3}$	magnetic charge density
$\rho_{m,i}$	$\mathrm{Wb/m^3}$	impressed magnetic charge density
$\rho_{m,s}$	$\mathrm{Wb/m^2}$	magnetic surface charge density
$\boldsymbol{\rho}_n^{\pm}$	m	position vector with respect to free vertex of triangle
σ	$\mathrm{S/m}$	electric current conductivity
σ_m	Ω/m	magnetic current conductivity
$\mathbf{\Sigma}$	-	diagonal matrix with the singular values
$\mathbf{\Phi}$	W	RF power covariance matrix
χ_e	-	electric susceptibility constant
χ_m	-	magnetic susceptibility constant
$\psi_{l,m}$	-	scalar wave eigenfunction
$\mathbf{\Psi}$	W	sample noise covariance matrix
ω_0	$\mathrm{rad/s}$	angular Larmor frequency
Ω_0	sr	solid angle

List of Figures

List of Tables

1 Introduction

1.1 Problem Statement and Literature Review

The design of next-generation magnetic resonance (MR) scanners is inextricably linked to the design of sophisticated radiofrequency (RF) coil arrays. Unfortunately, a direct application of existing full-wave electromagnetic (EM) tools cannot fully explore the high-order parametric space and monitor the trade-offs between the array design degrees of freedom and the various metrics such as intrinsic signal-to-noise ratio (SNR), specific absorption rate (SAR), and transmit efficiency (TXE). Such metrics can characterize the RF array of an MR scanner and are shortly explained here. Specifically, the basic determinants of SNR in magnetic resonance imaging (MRI) are the signal voltage amplitude and the root mean square (RMS) noise voltage at the output of the detector, and it is mainly used for image evaluation and measurement of contrast enhancement. SNR is also used for quality assurance, pulse sequence comparison, and RF coil comparison. Additionally, SAR is a measure of the rate at which energy is absorbed by the human body when exposed to an RF EM field and it is defined as the power absorbed per mass of tissue measured in watts per kilogram. Finally, an approach for evaluating the efficiency of a conventional transmit coil is to measure the amplitude of the created B_1^+ field, or spin flip angle, given a certain input power, which can be compactly represented by TXE.

Recent technological advances and trends increasingly lead to high and ultra-high field (UHF) strength MRI promising improved SNR and higher spatial/spectral resolution. However, as we move to higher static magnetic field strengths, the operating Larmor frequency of the RF coils increases, too. Higher frequencies entail smaller wavelengths that become comparable to the effective dimension of the human body and interact more strongly with the biological tissue. Consequently, SAR, which depends on the conductivity and the density of the human tissue, and more importantly on the electric field spatial distribution, can become large posing the risk of damaging the human tissue due to excessive heat deposition over it. Furthermore, the magnetic field becomes inhomogeneous, which translates to regions with SNR drops and loss of image quality. Taking into account all these factors, one naturally realizes the need for highly sophisticated, tunable RF coil arrays which, however, require

long design cycles. The general objective of the thesis is to address these challenges, by reliably and accurately modeling the interactions between EM waves and biological tissue and by deriving performance bounds for RF transmit coils for the above-mentioned TXE metric along with surface current distributions that yield the optimal EM fields that maximize SNR. These tools aim to give physical insight into the development of task-optimal RF coil arrays that could possibly approach the ultimate performance.

Over the last years, the scientific community has been making use of both analytical and numerical techniques for computing the EM fields distributions and the associated performance metrics. Each approach has its own distinct advantages and usability. Analytical electrodynamic simulations are valuable since they provide rapid and rigorous results that yield insight into fundamental dependencies for different metrics using comparatively simple geometrical models. Furthermore, in contrast with numerical methods, they are not time-consuming, and their computational complexity does not grow as the number of modeled coils increases, facilitating the simulation of different coil-sample configurations and the exploration of various parameters, adding generality to the results and observed trends. However, for heterogeneous body models, full-wave numerical computation is currently the only practical way to obtain realistic spatial distributions of the EM fields and the associated absorbed/deposited power, described by SAR. Below, we review part of the wide variety of analytical and numerical methods used to calculate RF EM fields in MRI, as well as, theoretical bounds of performance for SNR and SAR metrics.

Analytical solutions to Maxwell equations can only be derived for simplified sample geometries [6–9] including spheres, multi-layered spheroids, infinitely long cylinders, cones, and slabs. Theoretical limits of performance for the MR-related metrics of SNR and SAR in such samples have also been introduced and extensively studied in the literature [10–19] yielding great insight into expected and observed trends in MRI signal, noise, and safety. Among these different approaches, limits on performance were calculated by utilizing complete analytical EM fields bases of vector spherical or cylindrical harmonic wave functions, where the surface currents modes were constrained onto spherical or cylindrical shells, respectively [15]. This generalized framework has allowed for the calculation of the associated current distributions that yield the best possible values of SNR or SAR consistent with electrodynamic principles. Over the last years, these so-called ideal current patterns (ICP) have provided new physical insight into the design of optimal coil arrays that approach the ultimate performance [20–29].

However, to analyze more realistic and complex scenarios, numerical methods have to be employed in order to solve Maxwell equations, in particular, if highly inhomogeneous objects are to be modeled, e.g., anatomical realistic body models. The most broadly used numerical methods to calculate EM fields distributions in MRI are the Finite Difference

Time Domain (FDTD) Method [30] and the Finite Element Method (FEM) [31, 32]. However, with regard to the numerical techniques for computing the EM fields in inhomogeneous dielectrics, such as the human body, there is also a vast amount of literature and a rich investigative activity that focuses on integral equation (IE) methods [33–57]. Over the last years, the MRI community has utilized a standard volume integral equation (VIE) solver based on electric flux densities to calculate the EM scattering from realistic human body models, which, however has recently proven to have unstable convergence properties [58, 59]. This finding motivated researchers to develop a new stable current-based VIE solver with piece-wise constant (PWC) approximations [60] for MR modeling which can be combined in a straightforward manner with surface integral equation (SIE) methods to model the homogeneous conductors of the RF coil arrays [61–63]. This generalized framework [60,64–66] has offered great flexibility in exploiting certain problem properties by customization of the method and has further allowed for the calculation of performance bounds for SNR [67–70] and SAR amplification factor for RF hyperthermia [71] in heterogeneous head models within reasonable time and manageable computational resources. More recently, the ICP that yield optimal SNR have also been described for the case of cylindrical and open spherical surfaces [68, 72], by cleverly combining the vector wave eigenfunction expansion of the spherical and cylindrical Helmholtz operator with the above-mentioned ultra-fast VIE solver [64] and, lately, another promising approach which allows to predict, rapidly and intuitively, the form of ICP on any arbitrary surface surrounding any arbitrary body has been introduced [73].

1.2 Thesis Structure and Contributions

The focal point of this dissertation revolves around modeling the interactions between EM waves and biological tissue, employing analytical and developing numerical methods for the calculation of theoretical performance bounds consistent with electrodynamics and independent of any particular coil design, as well as, the computation of ideal RF excitation patterns. The structure and the contributions of the thesis are explained in detail below.

The *first* chapter is an introductory chapter and starts with the problem that the thesis aims to tackle along with the literature review that summarizes the investigative activity that has been ongoing in the direction of analytical and numerical EM fields computation methods for MR modeling, both for the case of the RF coils and the human body. Furthermore, it reviews the scientific contributions with respect to the calculation of ultimate SNR, SAR, and their associated current distributions and points to important studies that demonstrate how they are a great source of physical insight into the design of optimal RF coil arrays. Then, the thesis structure and contributions are described.

The *second* chapter starts with the description of the physical principles that govern the

nuclear magnetic resonance (NMR) phenomenon and the MRI system components that are required to appropriately manipulate the magnetic fields in order to generate the MR image. The associated metrics of SNR and SAR are introduced along with the safety regulations and image quality considerations that have to be taken into account when operating and designing an MRI system. It continues with a comprehensive report of the opportunities and challenges that arise at UHF MRI along with the description of Maxwell and constitutive equations. Such challenges necessitate the fast and accurate EM modeling of the associated RF coils but at the same time they present an opportunity to design the next-generation tunable coils that can yield higher SNR and faster image acquisition without compromising patient safety and image quality. Finally, a detailed review of the existing analytical and numerical methods for EM fields computations is presented including FDTD, FEM, and IE methods. Their distinct characteristics and applicability within the MR modeling field are described, and their advantages and disadvantages are compared with each other.

The *third* chapter is devoted to the description and formulation of analytical electrodynamic techniques for EM fields and performance bounds calculations, specifically for the case of RF transmit coils. It starts by reviewing existing metrics that measure the efficiency of RF shimming methods and transmit coils and then it describes the TXE metric of choice and how its largest possible value can be computed in uniform head-mimicking spherical samples by expanding the dyadic Green's function in a basis of vector spherical harmonic (VSH) functions. It also explains how the corresponding ICP that yield the ultimate intrinsic transmit efficiency (UITXE) can be calculated followed by a detailed investigation of the ICP and UITXE behavior for different B_0 field strengths, spherical sample sizes, and target excitation regions of interest. Finally, finite RF coil arrays are assessed with respect to the ultimate performance.

The contributions of this chapter are briefly summarized as follows. First, we introduce a novel performance metric, namely, the UITXE [74, 75] which is the theoretically largest TXE that can be achieved by any coil using RF shimming for a given imaging sample and target excitation region. Second, we employ a complete basis of surface current modes, constrained on a spherical shell, as transmit elements of a hypothetical infinite array and compute UITXE for head-mimicking uniform spherical samples by maximizing the square of the net B_1^+ per unit RF power deposition. Then, the corresponding RF shimming weights are used to appropriately combine the current modes into ICP. Finally, we investigate the behavior of UITXE and ICP for different magnetic field strengths, excitation regions, and sample sizes and evaluate the performance of finite arrays with respect to the UITXE. Analytical EM simulation techniques are rapid, rigorous, and provide great physical insight into observed patterns and trends of MR-related metrics and EM fields distributions behavior. However, in order to more closely account for what happens in reality, numerical methods have to be employed, which should take into account the high inhomogeneity and geomet-

rical complexity of the human body.

The *fourth* chapter deals exactly with that problem and it is devoted to the development of a novel numerical solver [76, 77] that accurately models the EM scattering from extremely inhomogeneous objects and/or objects with high contrast, which is the case of the human body. This numerical solver can be employed for the precise computation of the EM fields distributions over the body and their associated figure of merits, such as B_1 fields, local SAR, SNR, and TXE. First, SIE methods, that can be used for the RF coil modeling, are described and then the focus shifts on VIE methods and their different formulations for EM scattering computation from inhomogeneous media. Specifically, we introduce and develop a fast and accurate, current-based VIE solver with piece-wise linear (PWL) basis functions that yields reliable EM fields, without the need of refining the computational grid.

The novel contribution of this chapter is the development of a stable volume integral equation solver based on polarization/magnetization currents, for the accurate and efficient computation of the EM scattering from highly inhomogeneous and high contrast objects [76,77]. For this purpose, we employ the Galerkin Method of Moments to discretize the formulation with discontinuous PWL basis functions on uniform voxelized grids, allowing for the acceleration of the associated matrix-vector products in an iterative solver, with the help of fast Fourier transform (FFT). Through numerical experiments, we illustrate that the resulting discretized formulation is well-conditioned and has superior convergence properties than the discretized version with PWC approximations and than a more standard VIE formulation based on electric flux densities [57]. Specifically, the number of iterations of the iterative solver remains practically the same as with the case of PWC basis functions and is much smaller than that of the flux-based solver, for highly inhomogeneous scatterers. Another favorable feature of the proposed scheme is its superior accuracy. To demonstrate that, we present a comparative analysis between the PWC and the PWL basis solver for a homogeneous sphere, comparing both solvers with analytical results obtained with Mie series [78], and for realistic head models. We further show that even when numerically treating the case of dielectric shimming [79], where high-permittivity dielectric pads are placed in the vicinity of a realistic head model, the suggested solver performs effectively.

Having developed a numerical solver that generates reliable EM fields, the next focal point is the description of robust algorithms to generate a numerical EM fields basis inside an inhomogeneous, arbitrary scatterer that is consistent with electrodynamics [80], to which task is devoted the *fifth* chapter of this dissertation. In particular, this chapter starts with the description of the steps that are required for the EM fields basis generation in realistic human body models. This step can be considered as an extension of the Mie theory [78] to arbitrarily complex geometries. In order to generate the basis, first, we excite the scatterer with a large number of electric and/or magnetic dipoles, placed over a closed surface that surrounds

the scatterer at a predefined distance. Then, we calculate the incident electric and magnetic fields within the scatterer and apply randomized singular value decomposition (RSVD) [81] to the matrix that maps the dipole currents to the incident fields. By using random, distributed in voxels electric and/or magnetic dipoles, RSVD computation can be accelerated via the FFT-based matrix-vector product. However, to model arbitrary surfaces sometimes it is more suitable to place the equivalent currents sources on a triangulated grid [75] or even use ideal Hertzian dipoles tangential to the surface of interest [82]. This may hinder the fast application of RSVD, since the grid is no longer uniform, but still the subspace of the sources-to-object coupling matrix can be calculated fast by adaptive cross approximation of the matrix [83–86] or even by directly applying singular value decomposition (SVD) when memory and computation time restrictions permit. Throughout this chapter, we make use of all three approaches depending on the application at hand. Having constructed a basis of incident EM fields, we then proceed to the evaluation of the total fields with our in-house VIE solvers [60,77]. In this chapter, we present the key points for the basis generation, study the impact that electrical distance has on the singular value (SV) drop, demonstrate its ability to reconstruct different EM fields, and compare its numerical accuracy and convergence properties [80] against a complete analytical basis derived in a spherical coordinate system for the TXE and SNR metrics. Then, we compute the UITXE [75] for realistic head models, similarly to the ultimate intrinsic SNR (UISNR) [67] case, against which ultimate metrics we compare existing coil designs and thus assess the room for improvement of specific arrays. Together with these performance bounds, we also compute the associated current distributions on a given arbitrary surface that yield the corresponding optimal SNR distribution [82]. These numerical ICP can inform the non-convex coil optimization problem with an intuitive initial guess and could lead to truly task-optimal coil designs.

The novel contributions of this chapter can be summarized as follows. First, we introduce a general numerical framework for the generation of a basis for the EM fields that any coil design can induce in inhomogeneous human body models with realistic tissue characteristics [80]. The generation of such basis involves the combination of the IE formulation of the Maxwell equations and the development of a fast VIE solver. It borrows the concept of the Huygens's surface equivalence principle and makes use of fast approaches to rapidly explore the full space of incident fields that can be induced in the human body model. In addition to the generation of the EM fields basis, we study its convergence properties for different incident and total EM fields reconstruction and its numerical accuracy for different MR metrics. We further show how to use such basis to obtain useful information, such as the UITXE [75], that serves as a performance upper-bound for assessing RF transmit arrays and, finally, how to obtain RF current excitation patterns in arbitrary surfaces outside the body [82] that generate an optimal field distribution in terms of SNR. We believe that these newly developed tools can offer the framework for truly robust optimization of next-

generation RF coils.

In the final *sixth* chapter of the thesis, conclusions are presented along with a summary of the contributions of the thesis. Potential future work is suggested and research extensions and perspectives are described. Finally, three appendices are presented for the in-depth understanding of critical aspects and mathematical derivations that have been omitted from the main matter of the thesis for clarity and brevity.

2 Electromagnetic Fields Considerations in MRI

MRI is a non-invasive and powerful imaging technique that has played and continues to play a significant role in the medical community. MRI generates three-dimensional (3D), cross-sectional tomographic images similar to those of x-ray computed tomography (CT) [3]. Recently, an impressive 100 micron resolution 7T MRI scan of an *ex vivo* human brain has been presented highlighting the immense imaging capability of MRI [87]. In clinical application, it enhances the diagnostic accuracy of medical doctors and assists them in the planning of a surgical operation, thus limiting the risk for a patient during an operative and invasive procedure, since it allows the visualization of the structure and pathologies of the human body. It also helps laboratory researchers, e.g., neurologists and biologists, to drive the discovery of novel anatomical structures and develop an intuitive understanding of physiological working principles. Its main advantage is that, contrary to other imaging techniques, such as x-ray CT, MRI does not expose the patient to harmful ionizing radiation thus, it can be considered safer. Also, thanks to the dependence of the MR signal to various tissue parameters, MRI can provide more information than other imaging alternatives. MRI is based on the interactions between EM RF fields and certain atomic nuclei in the body, in the presence of a strong static magnetic field, making it a system whose design strongly depends on a fundamental understanding of the underlying EM principles and working mechanisms. Understanding such interactions between biological tissues and EM fields, especially at high and ultra-high field strengths, becomes crucial for the safe and effective RF coil design as well as for gaining useful insight into limits of performance [12, 15, 67].

In this chapter, we describe the basic principles and give an overview of the components of an MRI system, namely, the main magnet, the RF transmit and receive coils, and the gradient coils. Then, we describe the opportunities and challenges that are associated with UHF MRI and finally we review the analytical and numerical methods and tools for the calculation of EM RF fields in MRI.

2.1 Principles and Components of an MRI System

MRI belongs to a larger group of techniques that are based on the NMR phenomenon which describes the interactions of nuclei and magnetic fields and its basic principles were first discovered in bulk materials independently by Bloch [88] and Purcell [89] in 1946. However, for many years NMR was primarily applied in spectroscopy until 1973 when Lauterbur proposed using it for imaging purposes [90]. In principle, NMR occurs for various atoms (^{1}H, ^{31}P, ^{23}Na, etc.), however, the human body is abundant with hydrogen in the form of water, so ^{1}H-based imaging is most broadly used. From now on, the nuclei type is assumed to be hydrogen unless mentioned otherwise.

Magnetic Fields in MRI

MRI relies on the manipulation of bulk nuclear magnetic moments (magnetization), inside the biological tissue, by three kinds of carefully engineered magnetic fields. The *first* is a static magnetic field $\boldsymbol{B}_0 = B_0\hat{\boldsymbol{z}}$ (main magnetic field, typically along z-direction), parallel to which the nuclear magnetic moments tend to align and at the same time precess around. The angular frequency of the precession (Larmor frequency) varies linearly with B_0 field strength:

$$\omega_0 = \gamma B_0, \tag{2.1}$$

where γ is the gyromagnetic ratio and depends on the nuclear species. For protons it is given as $\gamma/2\pi = 42.58\mathrm{MHz/T}$. For typical MRI purposes, ω_0 is the angular frequency of the EM RF fields (on the order of 10-500MHz). The magnetization vector $\boldsymbol{M}$, is defined as the elementary nuclear magnetic moment per unit volume,

$$\boldsymbol{M} = \frac{d\boldsymbol{m}}{dV}, \tag{2.2}$$

where such volume should be sufficiently small and localized considering that in the imaging of the human body there are countless ($\sim 10^{19}$) hydrogen nuclei in any cubic millimeter of tissue [1], and at thermal equilibrium takes the form:

$$\boldsymbol{M}_0 = \frac{\rho_0\gamma^2\hbar^2}{4\kappa T}\boldsymbol{B}_0, \tag{2.3}$$

where ρ_0 is the number of nuclei per unit volume, $\hbar$ is the reduced Planck constant, κ is the Boltzmann constant, and T is the temperature in Kelvin. At equilibrium, without the presence of an external RF $\boldsymbol{B}_1$ field, $\boldsymbol{M}$ is aligned with $\boldsymbol{B}_0$ and there are no transverse (x or y) components or net precession, and subsequently, no RF signal to be detected [91] (Figure 2.1).

The *second* kind of magnetic fields, namely, the RF magnetic field $\boldsymbol{B}_1$ is responsible for

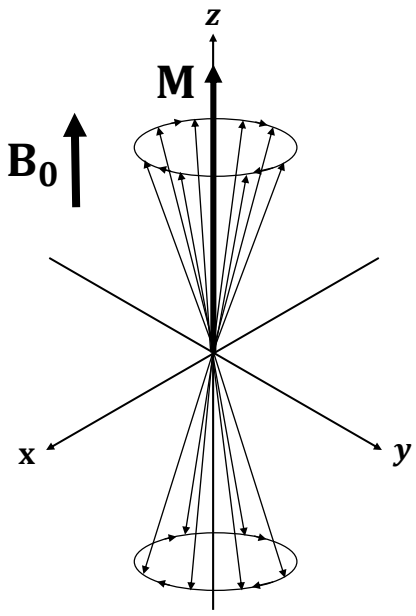

Figure 2.1: An ensemble of ^{1}H nuclei precessing at equilibrium around a static magnetic field $\boldsymbol{B}_0$ oriented in the longitudinal direction (z-axis) producing a static net magnetization $\boldsymbol{M}$ oriented in the longitudinal direction, too, but no net magnetization in the transverse (x–y) plane, thus no detectable RF signal [1].

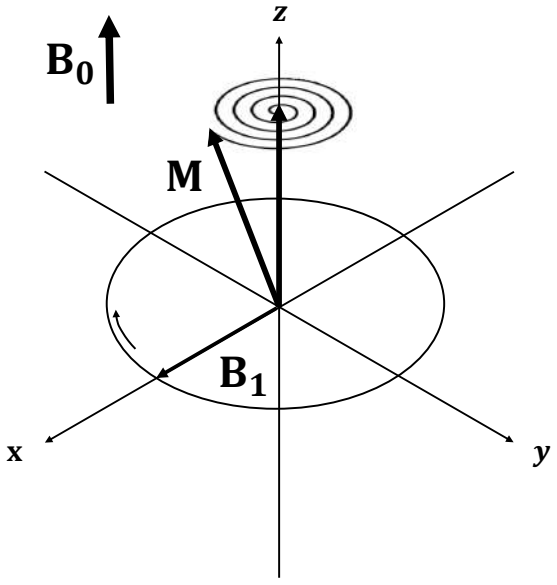

Figure 2.2: $\boldsymbol{B}_1$ RF field tuned to the Larmor frequency and applied in the transverse plane induces nutation of the magnetization vector as it tips it away from z-axis (laboratory frame of reference) [2].

the generation of detectable MR signals. To achieve that, $\boldsymbol{B}_1$ is applied perpendicular to $\boldsymbol{B}_0$ and tuned to the Larmor frequency and typically has the form of a circularly polarized

field, $\boldsymbol{B}_1 = B_1(t)(\cos(\omega_0 t)\hat{\boldsymbol{x}} - \sin(\omega_0 t)\hat{\boldsymbol{y}})$. Such field tips the magnetization $\boldsymbol{M}$ away from its alignment with $\boldsymbol{B}_0$, and subsequently the magnetization vector precesses around $\boldsymbol{B}_0$ and relaxes to its equilibrium according to Bloch equation [2]:

$$\frac{d\boldsymbol{M}(t)}{dt} = \gamma \boldsymbol{M}(t) \times \boldsymbol{B}(t) - \frac{M_x(t)\hat{\boldsymbol{x}} + M_y(t)\hat{\boldsymbol{y}}}{T_2} - \frac{(M_z(t) - M_0)\hat{\boldsymbol{z}}}{T_1}, \tag{2.4}$$

where $\boldsymbol{B}(t) = B_0\hat{\boldsymbol{z}} + B_1(t)(\cos(\omega_0 t)\hat{\boldsymbol{x}} - \sin(\omega_0 t)\hat{\boldsymbol{y}})$, T_1 is the tissue-dependent spin-lattice relaxation time constant and describes the mechanism by which the longitudinal-z magnetization component reaches its equilibrium and T_2 is the tissue-dependent spin-spin relaxation time constant and describes the mechanism by which the transverse-xy magnetization exponentially decades to its equilibrium. Specifically, right after a 90° RF excitation pulse the behavior of the transverse component is described as [2]:

$$M_{xy}(t) = M_0 e^{-t/T_2}, \tag{2.5}$$

and the behavior of the longitudinal component as:

$$M_z(t) = M_0(1 - e^{-t/T_1}), \tag{2.6}$$

since instantly after the 90° RF pulse $M_z(0) = 0$ and $M_{xy}(0) = M_0$. A schematic representation of this phenomenon is displayed in Figure 2.2.

Since the net magnetic field has now a transverse component, such precession produces a time-varying magnetic flux which induces a voltage or an or electromotive force (EMF) in the signal detector (receive RF coil). The induced voltage or EMF is given, according to Faraday's law of induction, as [91–94]:

$$\text{EMF} = -\frac{d}{dt}\int_V \boldsymbol{M}(\boldsymbol{r}, t) \cdot \boldsymbol{B}_{\text{r}}(\boldsymbol{r}) dV, \tag{2.7}$$

where the integral is calculated over the whole imaging volume, and $\boldsymbol{B}_{\text{r}}(\boldsymbol{r})$ measures the sensitivity defined by a hypothetical magnetic field that is generated by the unit current carrying receive coil, according to the principle of reciprocity [92]. It should be noted that the EMF computed by the above equation is proportional to the strength of the MR signal.

The *third* set of magnetic fields that are required in order for an MR image to be generated are the gradient fields, and they are responsible for the main spatial encoding mechanism. The three gradient fields are applied along the same direction with $\boldsymbol{B}_0$ and their amplitude varies linearly with position (Figure 2.3). For example, if we apply a gradient field G_x in x-direction, then the magnetic field will take the form $B_0 + G_x x$ and the Larmor frequency

will become a function of the spins locations as follows:

$$\omega(x) = \gamma(B_0 + G_x x) = \omega_0 + \gamma G_x x. \tag{2.8}$$

By applying specifically designed gradient encoding fields in all three directions, both before and during signal acquisition, a multidimensional signal is produced that includes the phase and frequency encoding information in each spatial location. The MR image, in the form of a spatial signal amplitude map, can then be retrieved by multidimensional Fourier transform.

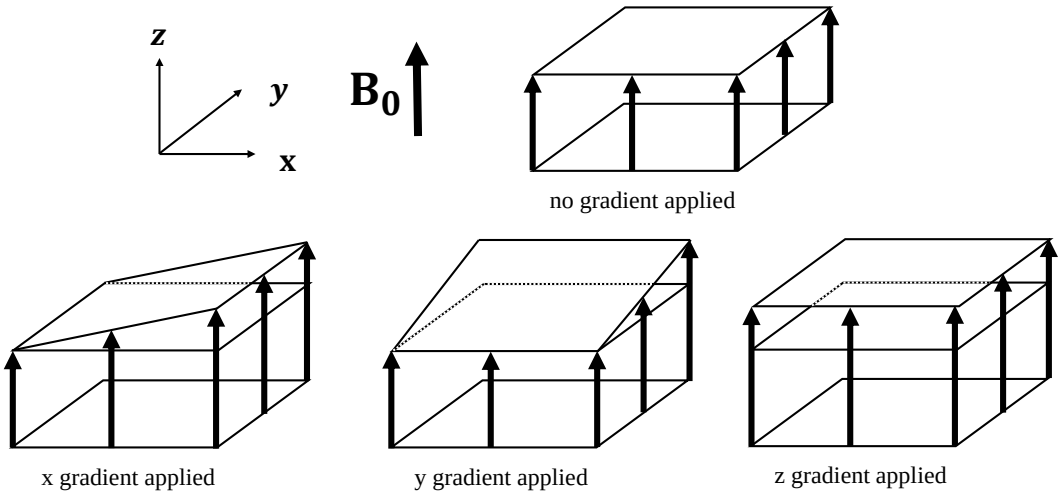

Figure 2.3: Gradient fields along x, y, and z direction aligned with $\boldsymbol{B}_0$. The z gradient is commonly used for slice selection.

SNR is a representative metric for overall image quality, where for the single receive coil case the induced signal is given by the EMF, as in Eq. 2.7, and the corresponding noise is given by:

$$\text{noise} = \sqrt{4\kappa T(R_c + R_s)\Delta f}. \tag{2.9}$$

Here, κ is Boltzmann constant, T is temperature in Kelvin, Δf is the bandwidth of the receive filters, R_c is the resistance of the receive coil and R_s the resistance of the imaging sample. R_c is determined by the conductors configuration/design, the electronics, and the material of the receive coil and R_s is determined by the deposited/absorbed RF power in the imaging sample. In many practical applications, MR scanners use arrays of receive coils where the noise correlation or covariance between the distinct elements/coils must also be taken into account.

The magnetic fields of an MRI system must follow specific regulations and guidelines. Usually, the maximally allowed inhomogeneity of B_0 is 5 parts per million (ppm) within the imaging domain. Furthermore, B_0 is required to have high temporal stability, typically $\ll$0.1 ppm/hr [91]. Similarly, gradient fields have to be sufficiently linear within the imaging domain in order for the spatial encoding to properly map each corresponding position.

A final requirement, which is many times mentioned and considered throughout this thesis, is the homogeneity of the RF $\boldsymbol{B}_1$ field over the imaging subject, which becomes quite challenging in UHF but at the same time presents an opportunity for developing a new form of electrical properties-based quantitative imaging by exploiting the MR signal, as recent studies have shown [95–99].

Such magnetic fields interact in a complex way with biological tissue and might affect image quality and patient safety unless carefully designed. Specifically, the susceptibility contrast between different tissues or between tissue and air can perturb the B_0 field (on the order of ppm), leading to strong artifacts for certain imaging applications [100]. Furthermore, the fast on and off switching of gradient fields can induce electric fields that might cause peripheral nerve stimulation which should be restricted to a stimulation that is barely perceived by a patient [101]. Finally, RF fields interact strongly with the highly inhomogeneous biological tissue, especially when their effective wavelength is comparable with the human body dimension. $\boldsymbol{B}_1$ field can become inhomogeneous resulting in images with regions with SNR drops and the $\boldsymbol{E}$ field can generate local SAR hot-spots with corresponding excessive tissue heating.

MRI System Components

As it is discussed above, modern MRI systems consist of the main magnet, the RF coils that could be either a single transceiver or two separate transmit and receive coils, the gradient coils, typically one for each direction, and a computer system to coordinate the above components [3, 102] (Figure 2.4). The main magnet's purpose is the generation of a homogeneous static magnetic field B_0 over the imaging domain. For clinical MRI, 1.5T and 3T are most common, while more recently U.S. Food and Drug Administration (FDA) has cleared the first 7T MRI device [103]. Typically, super-conductive magnets are used to produce the required high-strength solenoid static field. As mentioned before, B_0 is required to be uniform within the imaging subject, thus shim coils are usually employed to smooth possible inhomogeneities [104, 105]. The RF coil's role is to generate a homogeneous $\boldsymbol{B}_1$ field to tip the magnetic moments and receive the spatially encoded EMF. An MRI system can either have a single transceiver coil or two separate coils since they have distinct roles. Specifically, the RF transmit coil is designed to generate a uniform RF field throughout the imaging region of interest (ROI) whereas the receive coil has to have higher sensitivity to obtain a high-quality MR image, while uniformity is not strictly imposed. Furthermore, the received signal passes through filters and amplifiers before the final image reconstruction. The gradient coils are designed to produce uniform gradient fields, along x, y, and z directions and are required to quickly switch on and off to reduce image distortion. Finally, a computer system is responsible for setting the desired pulse sequences, coordinating the coils' excitations, and reconstructing the MR image.

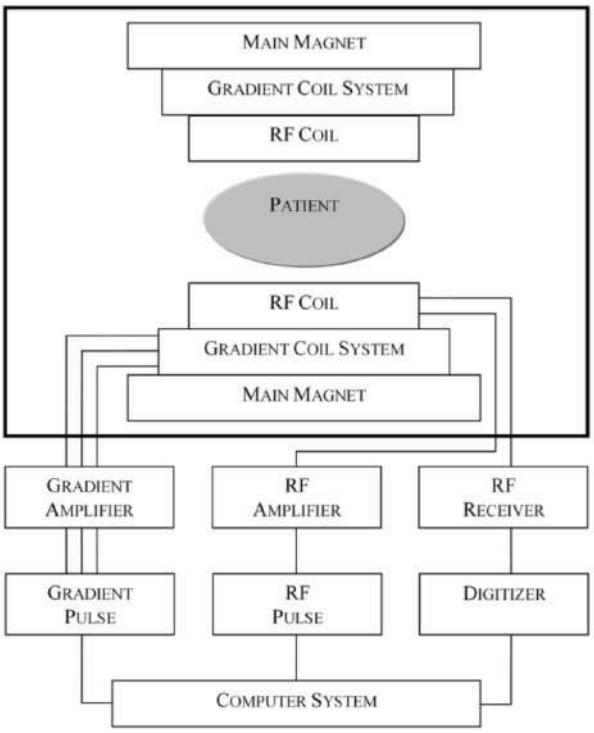

Figure 2.4: MRI system's components [3].

The aim of this dissertation revolves around theoretical performance bounds of the RF coils of a modern MR scanner, so it is worth mentioning a more detailed description of those. As we have briefly mentioned before, the role of the RF coils is twofold: first, in the transmit case, they generate the RF $\boldsymbol{B}_1$ field that tips the magnetization vector away from $\boldsymbol{B}_0$ alignment and second, in the receive case, they pick up on the voltage that is induced on their conductors according to the EMF as the magnetization vector precesses and relaxes up until it reaches its equilibrium. Although, the receive and transmit coils can be incorporated in a single transceiver coil, it is more common for a clinical MR scanner to be composed by a large built-in volume transmit coil and several receive coils with various designs to fit the shape and properties of each anatomical part of the body [91]. The homogeneity of the $\boldsymbol{B}_1$ transmit field is important in order for the magnetization vector to be uniformly tipped at each spatial location, however, the inhomogeneous biological tissue perturbs the $\boldsymbol{B}_1$ field distribution, especially for higher field strengths where the effective wavelength of the corresponding operating frequency becomes short and comparable with the human body dimension. Furthermore, optimizing the design of RF coils poses a challenging task, which, despite decades of collective experience, has remained a largely empirical process [73]. The main constraints that have to be respected when designing an RF coil are the associated safety considerations, where the RF deposited power has to be monitored and controlled to avoid potential tissue heating, and image quality concerns, where the aim is to generate a

homogeneous field despite the body geometrical complexity and tissue inhomogeneity. To address such challenges, EM modeling is a necessary tool either through analytical or numerical approaches, depending on the application at hand. Specifically, analytical computations are useful for designing the main magnet and the gradient coils, however, numerical tools are more commonly used for RF coil modeling and for EM field distributions computations within inhomogeneous human body models, where the full-wave solution of Maxwell equations is required.

2.2 Opportunities and Challenges in Ultra-High Field MRI

The above-mentioned safety considerations and design requirements for an MRI system, make EM modeling an essential tool for optimizing most aspects of MRI design and clinical application, especially at UHF strengths. An opportunity that emerges at UHF is that SNR increases super-linearly with the main magnet's strength B_0 [20, 106] which fact strongly motivates the pursuit of MRI at higher magnetic fields. However, at high frequencies the interactions of the EM fields with biological tissue result in perturbations of EM field distributions that depend on the particular tissue requiring accurate modeling of EM effects and novel coil designs to enhance image quality and to prevent adverse effects in patients. In detail, at UHF the following challenges have to be confronted [107]: i) high B_0 field strength entails an increase in the operating RF frequency and in the absorbed power as described by SAR, ii) the effective wavelength becomes comparable to the human body dimension and the $\boldsymbol{B}_1$ field is no longer uniform, iii) the electrical permittivity and conductivity of biological tissue are inhomogeneous and depend on the operating frequency, i.e., they are dispersive, and iv) local hot-spots due to SAR peaks may occur. In the next paragraphs, we will describe these challenges in detail.

Maxwell and Constitutive Equations

The spatial and temporal distribution of RF EM fields required for the tipping of the magnetization vector and for receiving the EMF follow Maxwell equations. Maxwell equations give the relationship between EM fields, electric/magnetic currents, and electric/magnetic charges for a given medium and source distribution as well as for given boundary conditions. Below, we present the macroscopic Maxwell equations that can provide useful physical intuition on how the relevant RF fields in MR behave. In differential time domain form and by introducing for symmetry the magnetic current density and the magnetic charge density,

they can be written as [108, 109]:

$$\nabla \times \boldsymbol{\mathcal{E}} = -\boldsymbol{\mathcal{M}}_i - \boldsymbol{\mathcal{M}}_c - \frac{\partial \boldsymbol{\mathcal{B}}}{\partial t}, \tag{2.10a}$$

$$\nabla \times \boldsymbol{\mathcal{H}} = \boldsymbol{\mathcal{J}}_i + \boldsymbol{\mathcal{J}}_c + \frac{\partial \boldsymbol{\mathcal{D}}}{\partial t}, \tag{2.10b}$$

$$\nabla \cdot \boldsymbol{\mathcal{D}} = \rho_e, \tag{2.10c}$$

$$\nabla \cdot \boldsymbol{\mathcal{B}} = \rho_m, \tag{2.10d}$$

where

$$\boldsymbol{\mathcal{J}}_{ic} = \boldsymbol{\mathcal{J}}_i + \boldsymbol{\mathcal{J}}_c, \tag{2.11a}$$

$$\boldsymbol{\mathcal{J}}_d = \frac{\partial \boldsymbol{\mathcal{D}}}{\partial t}, \tag{2.11b}$$

$$\boldsymbol{\mathcal{M}}_{ic} = \boldsymbol{\mathcal{M}}_i + \boldsymbol{\mathcal{M}}_c, \tag{2.11c}$$

$$\boldsymbol{\mathcal{M}}_d = \frac{\partial \boldsymbol{\mathcal{B}}}{\partial t}. \tag{2.11d}$$

All these field quantities ($\boldsymbol{\mathcal{E}}, \boldsymbol{\mathcal{H}}, \boldsymbol{\mathcal{D}}, \boldsymbol{\mathcal{B}}, ...$) are assumed time-varying and they are functions of the position vector $\boldsymbol{r}$ and time t as $\boldsymbol{\mathcal{E}} = \boldsymbol{\mathcal{E}}(\boldsymbol{r}, t)$ and their definitions and units are given below:

- $\boldsymbol{\mathcal{E}}$: electric field intensity ($\mathrm{V/m}$),
- $\boldsymbol{\mathcal{H}}$: magnetic field intensity ($\mathrm{A/m}$),
- $\boldsymbol{\mathcal{D}}$: electric flux density ($\mathrm{Cb/m^2}$),
- $\boldsymbol{\mathcal{B}}$: magnetic flux density (T, $\mathrm{Wb/m^2}$),
- $\boldsymbol{\mathcal{J}}_i$: impressed (sources/excitations) electric current density ($\mathrm{A/m^2}$),
- $\boldsymbol{\mathcal{J}}_c$: conduction electric current density ($\mathrm{A/m^2}$),
- $\boldsymbol{\mathcal{J}}_d$: displacement electric current density ($\mathrm{A/m^2}$),
- $\boldsymbol{\mathcal{M}}_i$: impressed (sources/excitations) magnetic current density ($\mathrm{V/m^2}$),
- $\boldsymbol{\mathcal{M}}_c$: conduction magnetic current density ($\mathrm{V/m^2}$),
- $\boldsymbol{\mathcal{M}}_d$: displacement magnetic current density ($\mathrm{V/m^2}$),
- ρ_e: electric charge density ($\mathrm{Cb/m^3}$),
- ρ_m: magnetic charge density ($\mathrm{Wb/m^3}$).

It should be highlighted that the magnetic current densities ($\boldsymbol{\mathcal{M}}_i$ and $\boldsymbol{\mathcal{M}}_c$) and the magnetic charge density (ρ_m) are fictitious/logistic quantities that have been introduced for symmetry

and can be employed in computational electromagnetism algorithms (equivalent fictitious sources) [109], as we show in Chapter 4. However, to the date, there is no evidence that they correspond to a physical quantity or phenomenon. Also, it should be noted that, both here and in Eq. 2.4, the fields are time-varying although in the previous section the notation is different in order to follow the one commonly used in MR-related literature. Finally, the fictitious magnetic currents mentioned above should not be confused with the nuclear magnetization (magnetic polarization) vector that is defined as $\boldsymbol{M}$ in the previous section and corresponds to existing bound current densities [110] due to the net magnetic moments contributions per unit volume, as we will shortly describe in the next paragraphs. Finally, from Eq. 2.10, the continuity equations can be derived as:

$$\nabla \cdot \boldsymbol{\mathcal{J}}_{ic} + \frac{\partial \rho_e}{\partial t} = 0, \tag{2.12a}$$

$$\nabla \cdot \boldsymbol{\mathcal{M}}_{ic} + \frac{\partial \rho_m}{\partial t} = 0. \tag{2.12b}$$

In order for a unique solution to exist, macroscopic Maxwell equations should be accompanied by the constitutive equations which describe the interactions of EM fields with the medium (dielectric, magnetic, and/or conductive) and are given as [108]:

$$\boldsymbol{\mathcal{D}} = \epsilon \boldsymbol{\mathcal{E}} = \epsilon_0 \epsilon_r \boldsymbol{\mathcal{E}}, \tag{2.13a}$$

$$\boldsymbol{\mathcal{B}} = \mu \boldsymbol{\mathcal{H}} = \mu_0 \mu_r \boldsymbol{\mathcal{H}}, \tag{2.13b}$$

$$\boldsymbol{\mathcal{J}}_c = \sigma \boldsymbol{\mathcal{E}}, \tag{2.13c}$$

$$\boldsymbol{\mathcal{M}}_c = \sigma_m \boldsymbol{\mathcal{H}}, \tag{2.13d}$$

where the constant terms that characterize the medium can be summarized as follows:

- ϵ_0: free-space permittivity ($8.854 \cdot 10^{-12}\mathrm{F/m}$),
- μ_0: free-space permeability ($4\pi \cdot 10^{-7}\mathrm{H/m}$),
- ϵ_r: relative permittivity constant of the medium,
- μ_r: relative permeability constant of the medium,
- σ: electric current conductivity ($\mathrm{S/m}$),
- σ_m: magnetic current conductivity (Ω/m).

In their general form, the electrical properties, also referred as constitutive parameters, can be: i) independent of the field intensities and then the medium is characterized as linear, ii) uniform without spatial dependence and then the medium is characterized as homogeneous, iii) dependent of the operating frequency and then the medium is characterized as dispersive, and iv) independent of the field polarity and then the medium is characterized as isotropic.

Studies [5, 111–113] on the electrical properties of the human body have shown that it is inhomogeneous, dispersive, and anisotropic and we will discuss such properties in detail in the next paragraphs of this section.

Furthermore, when a dielectric/magnetic material is subject to an external electric/magnetic field, the randomly oriented electric/magnetic dipoles align with that field, or in other words they become polarized, and bound, real-world volumetric currents and charges arise [108, 110, 114] which take the form:

$$\boldsymbol{\mathcal{J}}_b = \frac{\partial \boldsymbol{\mathcal{P}}}{\partial t} + \nabla \times \boldsymbol{\mathcal{M}}, \tag{2.14a}$$

$$\rho_b = -\nabla \cdot \boldsymbol{\mathcal{P}}, \tag{2.14b}$$

where the contributions of the auxiliary electric polarization density ($\boldsymbol{\mathcal{P}}$) with units Cb/m^2 and magnetic polarization (nuclear magnetization) density ($\boldsymbol{\mathcal{M}}$) with units A/m are added to the electric/magnetic flux densities as [110, 114]:

$$\boldsymbol{\mathcal{D}} \triangleq \epsilon_0 \boldsymbol{\mathcal{E}} + \boldsymbol{\mathcal{P}}, \tag{2.15a}$$

$$\boldsymbol{\mathcal{B}} \triangleq \mu_0 (\boldsymbol{\mathcal{H}} + \boldsymbol{\mathcal{M}}). \tag{2.15b}$$

The bound currents ($\boldsymbol{\mathcal{J}}_b$) have units of A/m^2 and the bound charges (ρ_b) Cb/m^3 and their contributions are incorporated into Maxwell equations in Eq. 2.10 through the electric and magnetic flux density vectors. By substituting the definitions in Eq. 2.15 into the macroscopic Maxwell equations 2.10 it is instructive to rewrite 2.10b and 2.10c into their microscopic equivalent form as:

$$\nabla \times \left(\frac{\boldsymbol{\mathcal{B}}}{\mu_0} \right) = \boldsymbol{\mathcal{J}}_i + \boldsymbol{\mathcal{J}}_c + \underbrace{\nabla \times \boldsymbol{\mathcal{M}} + \frac{\partial \boldsymbol{\mathcal{P}}}{\partial t}}_{\boldsymbol{\mathcal{J}}_b} + \frac{\partial (\epsilon_0 \boldsymbol{\mathcal{E}})}{\partial t}, \tag{2.16a}$$

$$\nabla \cdot (\epsilon_0 \boldsymbol{\mathcal{E}}) = \rho_e \underbrace{-\nabla \cdot (\boldsymbol{\mathcal{P}})}_{\rho_b}. \tag{2.16b}$$

Then, the total electric current density due to the medium properties is $\boldsymbol{\mathcal{J}}_t = \boldsymbol{\mathcal{J}}_c + \boldsymbol{\mathcal{J}}_b$ and the total electric charge density is $\rho_t = \rho_e + \rho_b$, taking into account the free (conductive) and the bound currents/charges. Similar definitions for the fictitious magnetic charges and magnetic currents can be found in the literature [110, 115], where an interested reader can refer to, however, they are outside the scope of this dissertation and we omit them for brevity and clarity. Finally, it is useful to rewrite Eq. 2.15 as follows:

$$\boldsymbol{\mathcal{P}} = \epsilon_0 (\epsilon_r - 1) \boldsymbol{\mathcal{E}}, \tag{2.17a}$$

$$\boldsymbol{\mathcal{M}} = (\mu_r - 1) \boldsymbol{\mathcal{H}}, \tag{2.17b}$$

since, a similar definition is exploited by the volume equivalence principle [109], where equivalent volumetric magnetization and polarization currents are introduced for EM scattering computations from inhomogeneous media and we use such principle in Chapter 4 to derive our current-based VIE solver. Finally, we mention once again that the magnetic polarization in Eq. 2.15 is the same with the nuclear magnetization $\boldsymbol{M}$ in the previous section, despite the slight inconsistency in the notation, and such definition of the magnetization allows for an elegant derivation of the SNR in NMR [94].

For the case of time-harmonic sources, represented as $e^{j\omega t}$, Maxwell equations can be rewritten in terms of complex spatial vectors, $\boldsymbol{E}(\boldsymbol{r})$, with $\boldsymbol{\mathcal{E}}(\boldsymbol{r},t) = \mathrm{Re}\{\boldsymbol{E}(\boldsymbol{r})e^{j\omega t}\}$. With this transformation, their macroscopic form along with the continuity equations are given as:

$$\nabla \times \boldsymbol{E} = -\boldsymbol{M}_i - \boldsymbol{M}_c - j\omega\boldsymbol{B}, \tag{2.18a}$$
$$\nabla \times \boldsymbol{H} = \boldsymbol{J}_i + \boldsymbol{J}_c + j\omega\boldsymbol{D}, \tag{2.18b}$$
$$\nabla \cdot \boldsymbol{D} = \rho_e, \tag{2.18c}$$
$$\nabla \cdot \boldsymbol{B} = \rho_m, \tag{2.18d}$$
$$\nabla \cdot \boldsymbol{J}_{ic} + j\omega\rho_e = 0, \tag{2.18e}$$
$$\nabla \cdot \boldsymbol{M}_{ic} + j\omega\rho_m = 0. \tag{2.18f}$$

Similarly, in their phasor form, the constitutive equations are written a:

$$\boldsymbol{D} = \epsilon\boldsymbol{E}, \tag{2.19a}$$
$$\boldsymbol{B} = \mu\boldsymbol{H}, \tag{2.19b}$$
$$\boldsymbol{J}_c = \sigma\boldsymbol{E}, \tag{2.19c}$$
$$\boldsymbol{M}_c = \sigma_m\boldsymbol{H}. \tag{2.19d}$$

Such form allows writing Maxwell equations in a more compact way:

$$\nabla \times \boldsymbol{E} = -\boldsymbol{M}_i - j\omega\dot{\mu}\boldsymbol{H}, \tag{2.20a}$$
$$\nabla \times \boldsymbol{H} = \boldsymbol{J}_i + j\omega\dot{\epsilon}\boldsymbol{E}, \tag{2.20b}$$
$$\nabla \cdot (\dot{\epsilon}\boldsymbol{E}) = -\left(\nabla \cdot \boldsymbol{J}_i\right)/j\omega, \tag{2.20c}$$
$$\nabla \cdot (\dot{\mu}\boldsymbol{H}) = -\left(\nabla \cdot \boldsymbol{M}_i\right)/j\omega, \tag{2.20d}$$

where $\dot{\epsilon} = \epsilon_0\dot{\epsilon}_r$, $\dot{\mu} = \mu_0\dot{\mu}_r$, and we have introduced the relative complex permittivity $\dot{\epsilon}_r$ and the relative complex permeability $\dot{\mu}_r$ to include all material losses as:

$$\dot{\epsilon}_r = \epsilon_r - j\frac{\sigma}{\omega\epsilon_0} = \epsilon_r' - j\epsilon_r'', \tag{2.21a}$$

$$\dot{\mu}_r = \mu_r - j\frac{\sigma_m}{\omega\mu_0} = \mu_r' - j\mu_r''. \tag{2.21b}$$

Eqs. 2.18 and 2.19 along with Sommerfeld-Müller radiation condition can uniquely describe EM fields problems with uniform and bounded currents/charges sources distributions. However, when the electrical properties of the medium exhibit discontinuities or when across such boundaries there exist currents/charges sources distributions, then the EM fields vectors also exhibit discontinuity and their behavior across such boundaries is described by the following boundary conditions [108, 109]:

$$\hat{\boldsymbol{n}} \times (\boldsymbol{E}_2 - \boldsymbol{E}_1) = -\boldsymbol{M}_s, \tag{2.22a}$$

$$\hat{\boldsymbol{n}} \times (\boldsymbol{H}_2 - \boldsymbol{H}_1) = \boldsymbol{J}_s, \tag{2.22b}$$

$$\hat{\boldsymbol{n}} \cdot (\boldsymbol{D}_2 - \boldsymbol{D}_1) = \rho_{e,s}, \tag{2.22c}$$

$$\hat{\boldsymbol{n}} \cdot (\boldsymbol{B}_2 - \boldsymbol{B}_1) = \rho_{m,s}, \tag{2.22d}$$

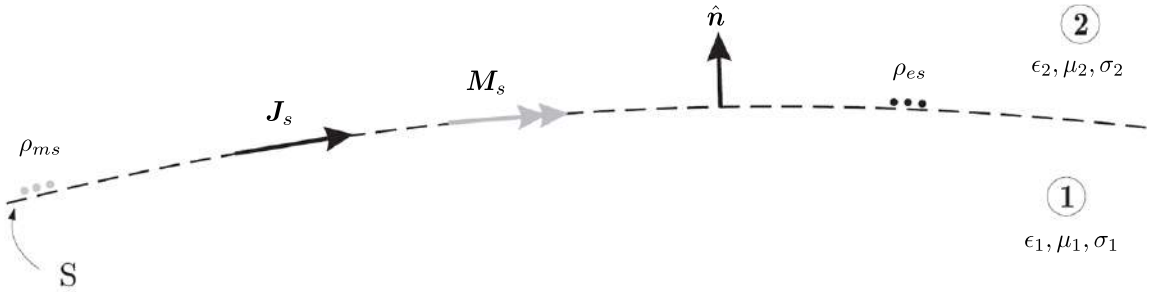

Figure 2.5: Interface between two media with different electrical properties and relevant magnetic and electric surface current and surface charge densities [4].

where subscript s indicates currents/charges tangential to the surface/interface between the two media and $\hat{\boldsymbol{n}}$ is the unit normal vector of the interface pointing from medium 1 to medium 2 (Figure 2.5). $\boldsymbol{M}_s$ and $\boldsymbol{J}_s$ are the magnetic and electric surface current densities with units $\mathrm{V/m}$ and $\mathrm{A/m}$, respectively, and $\rho_{m,s}$ and $\rho_{e,s}$ are the magnetic and electric surface charge densities with units $\mathrm{Wb/m^2}$ and $\mathrm{Cb/m^2}$, respectively. These current densities are particularly useful for the derivation of the surface (or Huygens's) equivalence principle [109] which provides the theoretical background for the formulation of SIE methods. Such SIE methods can be readily used for modeling the RF coils of an MR scanner and will be further discussed both in the next section and in Chapter 4. Finally, the surface equivalence principle can be applied by constraining all possible currents sources onto a hypothetical surface and computing their corresponding EM fields inside the devoid-of-sources

volume that this surface encapsulates [108, 109, 116]. In this way, a basis set of EM fields can be generated within the source-free volume and such EM fields basis generation along with its application within the MR field will be discussed in Chapter 5.

Electrical Properties of Biological Tissue

Having described Maxwell and constitutive equations, we now continue with a detailed report of the electrical properties behavior of biological tissue. As we briefly mentioned before, the biological tissue electrical properties are dispersive due to relaxation mechanisms. Specifically, up to 100MHz their frequency response is mainly characterized by passive cell membrane capacitance, Maxwell-Wagner polarization, intracellular organelle membranes, and protein molecule response [107]. For frequencies higher than 100MHz dipolar mechanisms in polar media (water, salts, proteins) dictate the tissue frequency response when an external field is applied [111, 112]. Furthermore, during the relaxation process, EM energy is dissipated and converted into heat and such phenomenon is represented by the tissue electrical conductivity. Throughout this dissertation we have used a parametric model of the biological tissue dispersive (Figure 2.6) and inhomogeneous (Figure 2.7) behavior [113]. Furthermore, all numerical experiments for EM scattering and performances bounds computations have been conducted for realistic, voxelized human body models from Virtual Family Population [5] with inhomogeneous frequency-dependent electrical properties.

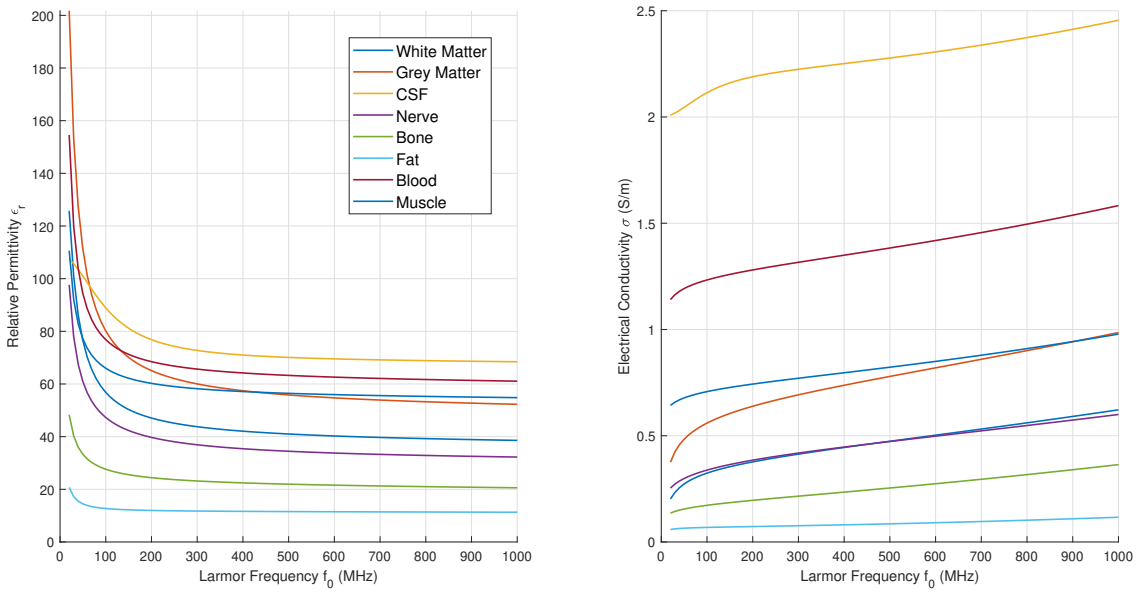

Figure 2.6: Frequency response of relative permittivity (ϵ_r) and electrical conductivity (σ) for MR-related frequencies from 20MHz up to 1000MHz corresponding to 0.47T up to 23.48T B_0 field strengths, for different tissues according to data from Virtual Family Population [5]. At low frequencies, tissues present high relative permittivity due to relaxation mechanisms. The relative permittivity shows a decreasing trend with increasing frequency while the electrical conductivity increases.

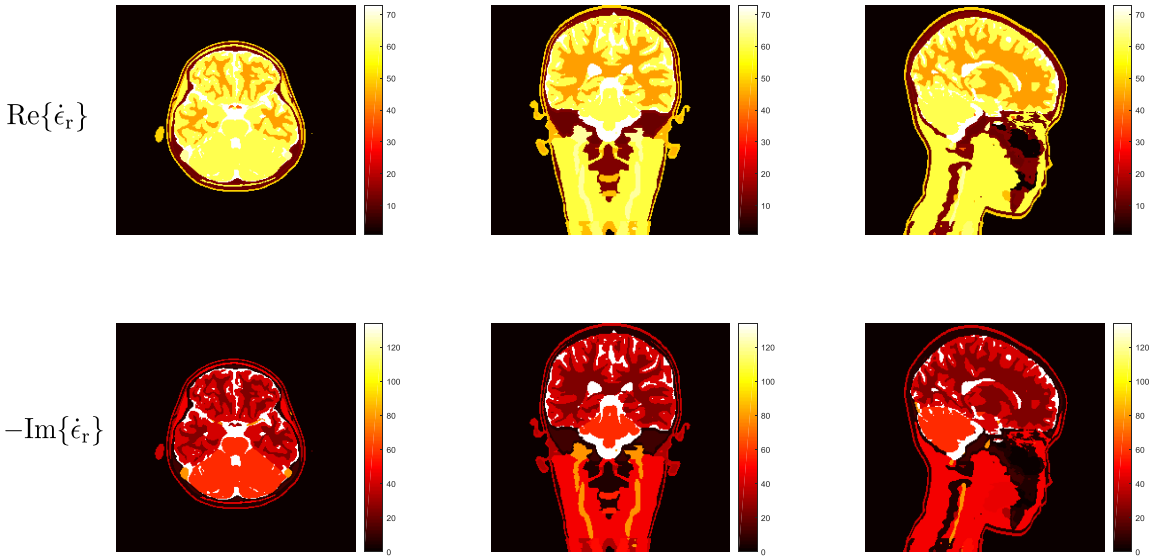

Figure 2.7: Real and imaginary part of relative complex permittivity ($\dot{\epsilon}_r$) distribution for "Billie" realistic head model at 7T according to data from Virtual Family Population [5]. The tissue presents high heterogeneity and contrast.

Except for the inhomogeneity and dispersion that the biological tissue possesses, specific body tissues, such as fibers and nerve bundles, are anisotropic with respect to their electrical conductivity [107]. However, such tissue characteristic is not usually taken into account, considering instead an isotropic model, due to lack of consistent knowledge of how such nerve bundles and fibers are oriented in 3D space [112]. Finally, body tissues present magnetic properties, where the magnetic susceptibility ($\chi_m = \mu_r - 1$) magnitude and its variations are in the order of magnitude of 10^{-6} [117]. Even such small variations of the magnetic susceptibility can distort the MR signal due to the high B_0 field strength. However, the magnetic susceptibility effect to the RF EM fields, usually, is not considered since its contribution is order of magnitudes less significant than the one from the dielectric properties [107]. So, in practice and in our RF EM fields numerical computations we have considered purely dielectric biological tissue and assumed vacuum permeability ($\mu = \mu_0$).

RF Safety and Image Quality Considerations in MRI

The electric field that is induced inside the lossy (electrically conductive) human body tissue deposits RF energy which is converted into heat. Such absorbed/deposited RF EM power may have detrimental effects to a patient due to excessive tissue heating. Therefore, there exist standards that regulate the exposure to RF EM fields [118, 119] and more specific ones associated with MR equipment safety [120]. In particular, the latter introduce SAR which measures the RF-induced tissue-deposited heat which can be coupled with bio-heat transfer

equations [107]. Local SAR is determined by the dissipated or absorbed RF power divided by the mass of an arbitrarily small volume (ΔV) with tissue as:

$$\mathrm{SAR}(\boldsymbol{r}) = \frac{\sigma(\boldsymbol{r})|\boldsymbol{E}(\boldsymbol{r})|^2}{2\rho(\boldsymbol{r})\Delta V}, \tag{2.23}$$

where $\sigma(\boldsymbol{r})$ is the inhomogeneous electrical conductivity, $|\boldsymbol{E}(\boldsymbol{r})|$ is the magnitude of the electric field, and $\rho(\boldsymbol{r})$ is the density of the specific tissue and it is measured in watts per kilogram ($\mathrm{W/kg}$). From the above equation, it is straightforward to derive the global SAR as the average value of the local SAR over the volume of interest, e.g., the human head or the corresponding body region, as:

$$\mathrm{SAR} = \frac{1}{V}\int\limits_{V} \frac{\sigma(\boldsymbol{r})|\boldsymbol{E}(\boldsymbol{r})|^2}{2\rho(\boldsymbol{r})} dV. \tag{2.24}$$

The absorbed RF energy due to magnetic losses can be neglected compared against the one due to dielectric losses.

According to Eq. 2.23, SAR depends on the electric field, electrical conductivity, and tissue density spatial distributions, whose characteristics are highly inhomogeneous, resulting in a non-uniform SAR, too. Furthermore, SAR can be averaged over smaller or larger volumes (e.g., 10g or whole-body averaged SAR) depending on the heating sensitivity of each body region according to specific safety regulations [120]. Global SAR is typically averaged over larger volumes such as the human head or the whole body while local SAR is averaged over 10g or even 1g tissue mass [107]. Naturally, that leads to local SAR aspects being stricter regulations to satisfy but when satisfied they are considered a much safer path to avoid excessive localized heat deposition that can potentially burn the human tissue.

SAR aspects introduce heating-related threshold values that are independent of the RF operating frequency, however, SAR distribution itself strongly depends on the RF frequency since the electrical conductivity is dispersive and the electric field distribution changes, depending on the effective wavelength. The effective wavelength is given as $\lambda = \frac{\lambda_0}{\sqrt{\epsilon_r}}$ and for higher field strengths it becomes comparable with the geometrical size of the human body (Figure 2.8) giving rise to local SAR hot-spots and B_1^+ inhomogeneities, demanding the full-wave Maxwell equations solution for problems with large electrical size. Over the past years, there have been investigations on the frequency dependence of the power deposition in uniform spherical samples [121, 122] for which there exists an analytical solution and for more realistic scenarios with anatomical head models [107], which can be investigated by the use of full-wave RF simulations, both demonstrating the SAR dependence on frequency. As a further demonstration of such effect, we present in Figure 2.9 the dissipated/absorbed power density [108] with units of $\mathrm{W/m^3}$ (which is analogous to local SAR without being

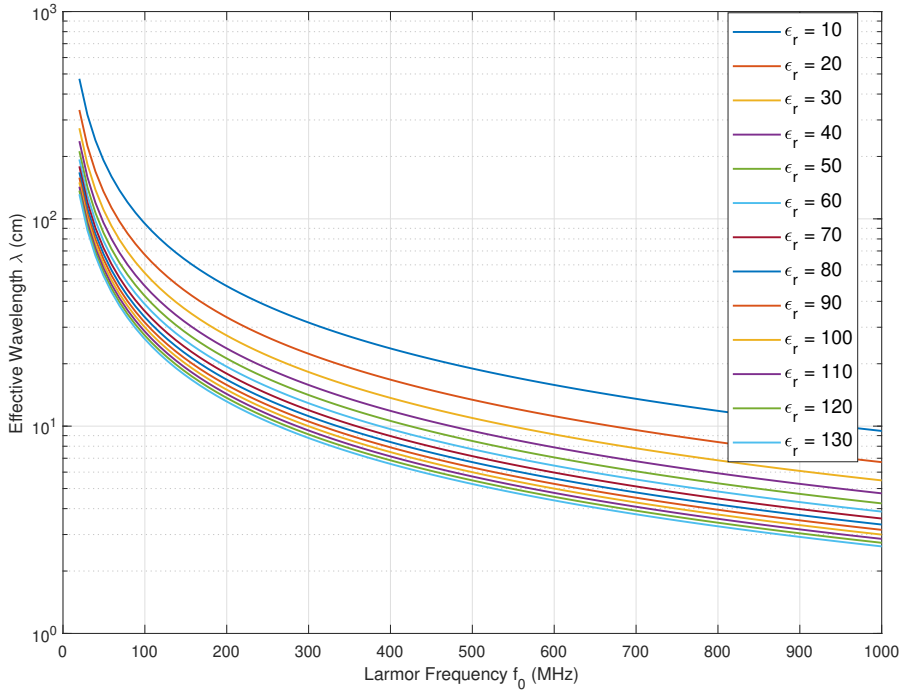

Figure 2.8: Effective wavelength, $\lambda = \frac{\lambda_0}{\sqrt{\epsilon_r}}$, for MR-related frequencies from 20MHz up to 1000MHz corresponding to 0.47T up to 23.48T B_0 field strengths and different relative permittivity values. At 7T cerebrospinal fluid (CSF), in Figure 2.6, has relative permittivity $\epsilon_r = 72$ corresponding to an effective wavelength of 12cm.

scaled with the tissue mass since $p_{\text{abs}}(\boldsymbol{r}) = \frac{1}{2}\sigma(\boldsymbol{r})|\boldsymbol{E}(\boldsymbol{r})|^2$), the magnitude, and the phase of $B_1^+ = \mu_0(H_x + jH_y)/2$ [93, 123] for "Duke" realistic head model at 1.5T, 7T, and 10.5T, excited by an 8-rung birdcage coil where each rung is driven with a unit-magnitude sinusoidal current and the neighboring elements have a $360°/8 = 45°$ phase shift. Here, we can indeed notice the challenges that arise at UHF, as described at the beginning of this section. Specifically, the absorbed power density (local SAR) increases significantly and so does the corresponding dissipated power (global SAR over the volume of the head) with units of W, $P_{\text{abs}} = \int_V p_{\text{abs}}(\boldsymbol{r})dV$, which at 1.5T, 7T, and 10.5T is 3.5W, 93.7W, and 146.5W, respectively. Furthermore, local SAR peaks can be observed, especially at 10.5T. Finally, except for safety concerns, transition to UHF might also entail image quality implications since both the magnitude and the phase of B_1^+ becomes increasingly inhomogeneous as field strength grows. The EM fields computations were performed with our current-based VIE solver [77] that will be extensively described in Chapter 4.

Our results above are in agreement with studies in the literature where it has been shown that greater RF power is required to generate the same flip angle as field strength increases [124]. Furthermore, another study demonstrated that both local and global absorbed/deposited power within a realistic head model excited by an 8-channel array with RF shimming [122, 125] targeting B_1^+ field homogeneity increased less than quadratically with increas-

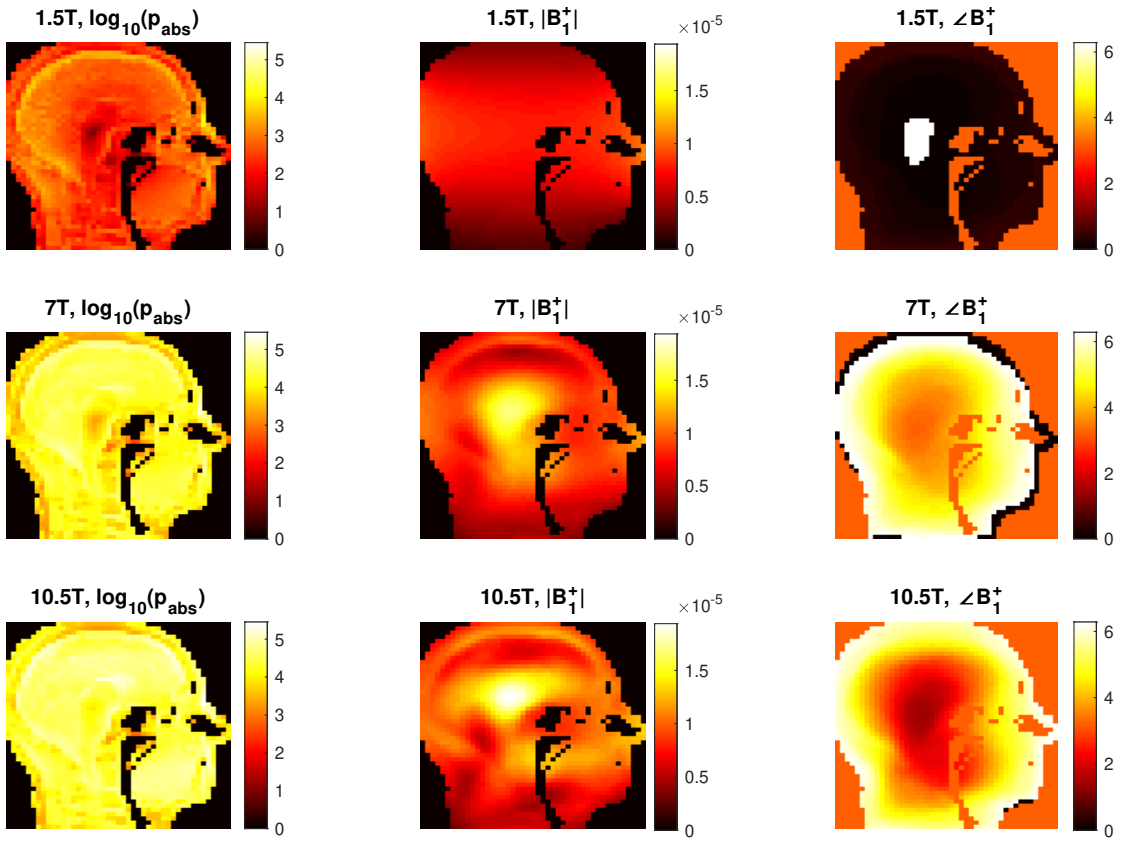

Figure 2.9: Absorbed power density p_{abs} in $\mathrm{W/m^3}$ in logarithmic scale, B_1^+ magnitude in T, and B_1^+ phase in rad within "Duke" realistic head model with 5mm resolution and heterogeneous and dispersive electrical properties at 1.5T, 7T, and 10.5T. The challenges regarding an increased SAR and an inhomogeneous B_1^+ associated with UHF strength are observed.

ing B_0 field strength [106] .

As we mentioned above, with respect to RF safety in MRI, there exist local and global SAR aspects that have to be monitored and not exceeded during an MR scan. Peaks in local SAR, especially at UHF strength, lead to the conclusion that local SAR aspects provide a stricter and more crucial assessment criterion than global SAR aspects, e.g., whole body or head averaged. However, their real-time monitoring is more challenging especially for time-varying RF pulses and parallel transmission [107] and in many cases global SAR aspect is assumed as the most critical which can reduce significantly the validity of safety assessment during an MR scan. In particular, there exist several studies that have demonstrated that local SAR thresholds can be exceeded, earlier than global SAR ones, even at conventional field strengths [126–128]. Finally, for clinical MR scanners with volume transit coils, only global SAR is monitored, however, for head coils above 7T, local SAR aspects are also taken into account. With these in mind, we can conclude that local effects are typically underestimated by global SAR aspects making local SAR a stricter metric to satisfy, especially at high-field

strengths.

Until today, the absence of an integrated body coil/resonator hinders the application of UHF MRI systems since transmit coils that are typically placed in the vicinity of the patient/sample [107] result in increases of local SAR at superficial tissues, while receive coils in the vicinity of the patient/sample could improve image quality and SNR. In particular, close-to-subject transmit coils generate electric fields with high and localized dissipated power, even when global SAR has reasonable values. Specifically, local SAR increases exponentially in head-mimicking uniform phantoms as transmit coils approach the subject [27], however, as their distance to the subject increases, local SAR decreases but global SAR gets higher in order to generate the same homogeneous B_1^+ profile.

Finally, with regard to the magnetic fields, their adverse effects are primarily associated with the static and the gradient magnetic fields which take values of T and mT, respectively, while RF fields take values of μT. Specifically, the spatial gradient of the static field can exert a force on an object [129] and the fast on and off switching of the gradient coils can induce electric fields that might cause peripheral nerve stimulation [101]. Regarding the RF fields, the peak magnitude of the RF electric field depends on both the peak magnitude of RF magnetic field and the operating frequency, and electric currents are generated due to magnetic induction. Due to these currents, the problem of heating can be acute particularly when metallic implants are present [129]. However, it is important to note that such heating problem does not directly originate from the RF magnetic field rather from its associated electric field, as we have described above. Finally, an interesting study demonstrates that man-made polarized EM fields are more biologically active leading to increased interference effects than natural EM fields that are typically not polarized [130] and such study could possibly be taken into account when formulating MR safety guidelines.

2.3 Electromagnetic Fields Computations in MRI

From the above, it should be clear that the design of highly sophisticated, tunable RF coils is critical for the development and deployment of an MRI system, both for the case of transmit coils that should not exceed SAR limits and should generate a homogeneous $\boldsymbol{B}_1$ field and for receive coils in order to optimize their design with respect to SNR, especially for high-field systems ($\geq$3T). Hence, sophisticated RF simulations tools have to be employed for safety/performance assessment and design optimization of both receive and transmit coils, especially when the full-wave EM solution is required. Then, by computing the 3D EM fields distribution and post-processing such fields, various metrics can be computed that are either impractical or inaccurate to calculate with *in vivo* measurements or in phantoms. In particular, numerical computations in realistic inhomogeneous head/body models are, to date, the only practical way to compute the 3D local SAR distribution which should

respect local SAR aspects to avoid excessive and localized heating [107]. However, the computational time and complexity of numerical methods grows rapidly, when there is a necessity to model a great number of RF coils restricting the number of configurations of different RF coils-samples that can be explored within reasonable time and computational resources and limiting the generality of the observed trends. Therefore, electrodynamic simulations have a valuable role since they provide rapid and rigorous results for different metrics and parameters (such as shape and dimensions of the object and the conductors, electrical properties of the tissues, or field strength) yielding useful insight into underlying working mechanisms and physical principles by using relatively simple geometrical models such as uniform spheres and cylinders [14]. Below, we review part of the broad variety of analytical and numerical methods used to compute RF EM fields in MRI as well as theoretical bounds of performance for the SNR and SAR metrics.

2.3.1 Analytical Methods

Analytical solutions to Maxwell equations can only be derived for simplified sample geometries [7–9] including spheres, multi-layered spheroids, infinitely long cylinders, cones, and slabs. Theoretical limits of performance for the MR-related metrics of SNR and SAR in such samples have been introduced and extensively studied in the literature [10–19] yielding great insight into expected and observed trends in MRI signal, noise, and safety. Among these different approaches, limits on performance are calculated by utilizing complete analytical EM fields bases of vector spherical or cylindrical harmonic wave functions, where the surface currents distributions are constrained onto spherical or cylindrical shells, respectively [15]. This generalized framework, based on dyadic Green's functions (DGF) expansion, enables to characterize the EM fields in tissue-mimicking dielectric spheres and cylinders and allows for the calculation of the associated current distributions that yield the best possible values of SNR or SAR consistent with electrodynamic principles. Over the last years, these ICP distributions have provided new physical insight into the design of optimal coil arrays that approach the ultimate performance [20–29]. In Chapter 3, we use this generalized framework and introduce the UITXE in head-mimicking uniform spherical samples as the largest possible TXE that can be achieved according to electrodynamics. Finally, we study the behavior of ICP for various parameters and assess how different arrays can approach the optimal performance [74, 75].

2.3.2 Numerical Methods

Analytical techniques yield great insight into expected and observed trends in MR signal, noise, and safety. However, in order to analyze more realistic and complex scenarios, numerical methods have to be employed in order to solve Maxwell equations, in particular, if highly inhomogeneous materials are to be modeled, e.g., anatomical realistic body mod-

els. Numerical simulations within the MR field typically share the following characteristics [107]: first, they involve large computational domains or volumes that should cover the cross-section of the human body/head and, depending on the application, a significant z-directed part along the MR bore, second, the RF coils should be sufficiently fine to consider complex geometries and designs, and third, anatomical realistic body models with inhomogeneous and dispersive electrical properties and resolution in the range of mm should be utilized. Furthermore, at UHF MRI, multiple channel RF arrays are employed and usually the EM fields distribution for each element of the array is required. Taken into consideration all these factors, one can realize the large computational cost and complexity for the implementation of accurate numerical methods and the need for their acceleration. The most broadly used numerical method to calculate EM fields distributions in MRI is the FDTD and the FEM. However, there have also been recent contributions for EM fields computations in MRI based on the combination of VIE and SIE methods [60, 64–66] which offer great flexibility in exploiting certain problem properties by customization of the method and have allowed for the calculation of performance bounds for SNR [67, 68] and SAR amplification factor for RF hyperthermia [71] in heterogeneous head models within reasonable time and manageable computational resources.

Finite Difference Time Domain

The numerical solution of Maxwell equations for an arbitrary 3D geometry requires an appropriate discretization of the solution domain. Within the MR field, FDTD [30] is one of the most commonly used methods, where the domain is typically discretized with rectangular hexahedral elements that divide the medium electrical properties in volumetric elements (voxels). For the case of a simple implementation, a single medium property is assigned at each voxel and the medium is considered as piece-wise homogeneous. For volumes that have boundaries with high curvature, such approximation leads to the so-called staircase approximation error and the numerical solution of the EM fields presents numerical error which, however, can be significantly reduced by refining the computational domain or by subpixel smoothing [131]. Naturally, by increasing the spatial resolution, the number of the unknowns or the degrees of freedom, the memory, and the computational time requirements increase. To mitigate such memory requirements, there exist FDTD implementations that utilize non-uniform grids or conformal meshes [132, 133] that locally refine the domain where structures with fine details are present and preserve the shape of the object's boundary, thus improving the accuracy of the numerical solution and, at the same time, reducing the number of voxels required to properly represent the geometry, in a discrete way.

The resolution is typically chosen based on the fine or coarse geometrical details of the structure to be modeled in order to achieve sufficient numerical accuracy. Furthermore, it also correlates with the operating frequency and usually it is recommended the maximum voxel

edge length to be at least smaller than the smallest wavelength divided by twenty. FDTD uses the well-known discretization scheme called Yee cell [134], where the electric field components are discretized across the edges of the voxel and the magnetic field components normal to the voxel faces. This scheme ensures the continuity of the EM fields components across physical boundaries between materials and it is an elegant arrangement to approximate curl equations. Yee cell further allows for using central differences in both space and time to approximate the partial differential form of Maxwell equations and, usually, the time step follows the leap-frog algorithm where the EM fields are computed at time instants with half time step difference between the electric and magnetic field. Such time step is inversely related to the diagonal of smallest discretization element in order for the computations to be stable and converge leading to an increased computational time when fine discretization schemes are employed.

Since FDTD is a time domain method, it allows to obtain a broadband frequency response by using a single time-domain excitation with the required bandwidth and central frequency (e.g., a Gaussian pulse) and then by applying discrete Fourier transform to the time-domain solution. This is can be useful for computing the scattering parameters and for the tuning and matching of the RF coils. Finally, by combining EM and circuit network simulations, the tuning, matching, and decoupling of multiple channel RF coils can be optimized [135]. A further advantage of FDTD is that its memory complexity scales linearly with the number of discretization elements and, thus, it is feasible to solve problems of large scale with reasonable memory demands. However, when a fine discretization is required (for modeling geometrical details) or when resonant structures are modeled, long computation times are required. Finally, for the case of multiple channel RF arrays, a distinct FDTD simulation is required for each excitation port multiplying the needed computation time. However, such time demands can be accelerated by the use of the highly parallel structure of graphical processing units (GPUs) since FDTD is parallelizable in a straightforward manner [136–138].

FDTD requires the truncation of the computational grid, where special conditions for the EM fields have to be enforced in order to model free-space and/or absorb the traveling EM waves, otherwise spurious reflections arise. Such grid truncation techniques include the Mur absorbing boundary condition (ABC) [139], the Liao ABC [140], and the perfectly matched layer (PML) [141]. Necessarily, there has to exist a minimum distance between the modeled structure and the ABC, in order for the ABC to be placed farther than the reactive near-field zone, otherwise numerical instabilities are very probable to arise. Both the enforced ABCs and their distance to the geometry, depend on the specific problem and have to be chosen in a way that the EM fields distribution within the geometry are not distorted or altered by the possibly insufficiently absorbed EM fields and remain the same with EM fields if a larger computational domain was considered [142].

To sum up, FDTD provides intuitive and broadband 3D EM field distributions, is a general and versatile tool, and is directly compatible with human anatomical voxelized models [5]. However, FDTD typically requires very large computational domains, small time steps, fine spatial discretization, and the introduction of ABCs that sometimes lead to prohibitively long simulation times which can be accelerated, up to a certain extent, with the use of GPUs.

Finite Element Method

Similarly to FDTD, FEM is a partial differential equations method but, in contrast with FDTD, it is applied in the frequency domain [31, 32]. FEM typically employs an unstructured tetrahedral discretization scheme which is helpful for modeling geometries with curvature and gives flexibility to model both small and large geometrical scales, however, it is not so straightforward for modeling the human anatomy since surface body models are hard to generate [143] and typically contain fewer number of tissues and anatomical details [107]. The entire space along with the appropriate ABCs should still be discretized, but usually FEM entails a smaller number of tetrahedra than FDTD leading to not such excessively long computational times [144]. Since FEM is a frequency domain method, it is useful for modeling resonant structures and RF systems which makes it suitable for the MR modeling case, which is a single frequency analysis, where the RF coils are tuned to the Larmor frequency and multiple channel arrays can be modeled simultaneously. However, FEM has higher memory demands than FDTD and results to a large but sparse linear system of equations, which, depending on the memory requirements of the application, can be solved with either direct or iterative methods.

Integral Equation Methods

Both FDTD and FEM are partial differential equations methods which are relatively straightforward to implement, are general and versatile tools, and give rise to sparse matrices. However, they typically entail a large number of unknowns and long computational times and demand the application of ABCs that further expand the domain. To the remedy of the above-mentioned limitations, come IE methods that automatically satisfy radiation conditions, thus there is no need for ABCs, are a highly customizable tool, allow for higher-order approximations and dimensionality reduction of the problem, and they are frequency domain methods, similarly to FEM, with its associated narrow-band characteristics and benefits.

Specifically, SIE methods are typically used to compute the surface current distributions on the conductors of the RF coil or its shield as well as its scattering parameters and are usually discretized on a triangular grid where there is no need to discretize the surrounding air, since the EM fields can be computed by applying the free-space DGF on the conductors' currents. VIE methods are used to model the human body model and compute the EM fields distributions within it and the associated metrics of interest such SNR, SAR, and TXE among

others, and similarly to FDTD, they are discretized with voxels ensuring their compatibility with the voxelized, anatomical models [5]. Furthermore, VIE and SIE methods can be combined in a straightforward, analytical way, by applying the free-space DGF, which eliminates the need to discretize the space between the body model and the RF coil, leading to a great reduction of the required voxels/triangles and computational time.

SIE and VIE methods are usually discretized with the Method of Moments (MoM) [61] approach in order to form a linear system of equations. In contrast to partial differential equation methods, IE methods give rise to dense matrices. Such matrices, however, have special properties, e.g., when discretized on a uniform grid they are Toeplitz, for the one-dimensional (1D) case, or multilevel block Toeplitz with multilevel Toeplitz blocks for higher dimensions due to the translation invariance of the Green's function kernels. Furthermore, independently of the discretization scheme, they are block low-rank due to the smoothing property of the Green's function kernels for remote elements interactions [66,145]. Both these properties, the Toeplitz structure and the block low-rank nature, are exploited in Chapter 4 and 5, respectively, and will be further discussed there. Finally, VIE and SIE give rise to complicated singular integrals that should be computed as accurately as possible, to which direction there is a big body of literature and investigative activity [146–158] and readily available sophisticated packages that can handle the singularities [159, 160].

Over the last years, the MRI community has utilized a standard VIE solver based on electric flux densities [43] to calculate the EM scattering from inhomogeneous anatomical body models, which, however has recently proven to have unstable convergence properties [58, 59]. This finding motivated researchers to develop a new stable current-based VIE solver with PWC approximations [60] for MR modeling which can be combined in a straightforward manner with SIE methods to model the conductors of the coil arrays [61–63]. This generalized framework [60, 64, 66] has yielded results comparable with FDTD, despite the intrinsically different modeling of the setup, and offered great flexibility in exploiting certain problem properties by customization of the method. Specifically, among others, it allowed for the calculation of performance bounds for SNR [67–70] and SAR amplification factor for RF hyperthermia [71] in heterogeneous head models within reasonable time and manageable computational resources, providing an absolute reference against which RF coil performance can be assessed [25] and introduced the notion of MR-specific Green's function [161] for the ultra-fast RF coil design [65].

Summary

Choosing the appropriate numerical method, depends on the electrical properties and shape of the geometry, the bandwidth over which the solution is required, and the available computational resources that will yield reasonable solution times and sufficient accuracy. Despite their inherent differences in discretizing Maxwell equations, FDTD, FEM, and IE are

expected to give comparable results, as we illustrate in Chapter 4, for the same scatterer-excitation setup. Except for the numerical solvers themselves, simulation suites should also come with a user-friendly graphical users interface and visualization tools, computer-aided design (CAD) models for the RF coils and human body models, co-simulation tools for optimizing the RF networks, hardware-based acceleration on GPUs or heterogeneous computing platforms, and a post-processing capability for running user-defined scripts to extract useful pieces of information and relevant metrics within the MR field (e.g., SAR, SNR, TXE). A Matlab-based suite that integrates part of the above characteristics is the Magnetic Resonance Integral Equation (MARIE) [64] suite, an updated version of which, MARIE 2.0, is soon to be released which will introduce the following additional characteristics: lumped elements in the RF coil model through the delta-gap method [162], superior numerical accuracy of the computed EM fields through a higher-order VIE solver with PWL basis functions [77], GPU-based acceleration and memory footprint reduction with Tucker decomposition [163], a fast coupled surface-volume IE solver by applying precorrected FFT on the triangular grid of the RF coil [164], simple optimization of lumped elements (tuning and matching), and optimized code in C++ for the most time consuming parts of the solvers. Furthermore, thermal solvers could provide the RF-induced temperature distribution and monitor its potential increase and Bloch simulation suites [165, 166] can provide numerical results that consider the contributions of all static, RF, and gradient magnetic fields. Finally, several commercial software exist such as Sim4Life (ZMT, Zurich, Switzerland) and XFdtd (REMCOM, State College, PA, USA) which are based on the FDTD method, CST Studio Suite (CST AG, Darmstadt, Germany) that employs the finite integration technique, and HFSS (ANSYS Inc., Canonsburg, PA, USA), COMSOL Multiphysics® (COMSOL AB, Stockholm, Sweden), and FEKO (Altair HyperWorks, Troy, MI, USA) that are based on the FEM [107].

3 Analytical Electrodynamic Techniques and Performance Bounds of MR Transmit Coils

Analytical solutions to Maxwell equations can only be derived for simplified sample geometries [7–9] including spheres, multi-layered spheroids, infinitely long cylinders, cones, and slabs. Theoretical limits of performance for the MR-related metrics of SNR and SAR in such samples have been introduced and extensively studied in the literature [10–19, 167] yielding great insight into expected and observed trends in MRI signal, noise, and safety. Additionally, it has been shown that such theoretical performance limits can be used as absolute references against which to evaluate RF coil performance and to derive guidelines for optimal coil design [20–29]. For example, the UISNR can be used to assess receive arrays [21, 25, 26, 168], while the associated ICP could be employed to guide coil design [15, 22, 23, 169]. Ultimate performance bounds were also used to investigate transmit array performance, in terms of SAR and excitation homogeneity, as a function of the number of coil elements in RF shimming and parallel transmission [14, 170]. However, they have not been used yet to obtain physical insight on optimal transmit array design. The aim of this chapter is to introduce a novel performance metric, the UITXE [74, 75] which is the largest possible TXE over a target excitation region that can be achieved for a specific sample and field strength, consistent with electrodynamic constraints. UITXE provides the largest theoretical TXE independent of any particular coil design since it is computed by a complete basis of EM fields where orthogonal EM basis fields are added and every EM basis field can be associated with a hypothetical coil which guarantees that UITXE is an upper-bound of transmit performance. Additionally, UITXE considers only sample losses, while in an experimental setup there are power losses due to radiation, losses in dielectric materials other than the sample, losses in lumped elements and losses due to reflected power [171] which all ensure that the TXE of an array in an experimental setup will be smaller than that in a simulation setup and further guarantee that the measured TXE will be smaller than the UITXE. Therefore, the goal of UITXE is to provide an absolute reference to assess coil performance, independent of any particular design, and derive new physical insights into the design of optimal transmit coils.

3.1 Transmit Efficiency Assessment and Radiofrequency Shimming Approaches

In order to assess the efficiency of an RF transmit coil, a common approach is to measure the amplitude of the RF transmit magnetic field (B_1^+) over a specific ROI, with respect to the RF power deposited in the body. Such assessment, can be captured by TXE metric, which becomes even more relevant at high and UHF MRI ($\geq$7T), where the arising inhomogeneities of the B_1^+ field can deteriorate image quality and electric field interference effects might violate the constraints for SAR [14]. For the case of multiple channel transmission, TXE can be evaluated experimentally by combining a rapid calibration scheme for measuring the power correlation matrix [172–174] and a B_1^+ mapping technique [175]. However, as the sheer number of possible weighting configurations, for driving distinct transmit channels or ports for RF shimming [122, 125] or parallel excitation [176, 177] increases, there arises the question of how to calculate the shim or parallel excitation weights that can optimally lead to reductions in B_1^+ field inhomogeneities and efficient SAR management.

Towards that direction, different RF shimming methods have been proposed in the literature [178], including local phase RF shimming [179] that aims at B_1^+ phase coherence at small ROIs. Additionally, depending on the nature of the application at hand, other methods focus on B_1^+ magnitude and phase homogeneity [122], B_1^+ magnitude homogeneity excluding the homogeneity of its phase [180], balancing B_1^+ homogeneity and SAR minimization [14, 181, 182], B_1^+ homogeneity by applying sequentially two distinct RF shim weights [183], and accommodating the adiabatic condition of RF pulses [184, 185]. In this chapter, we use a unifying TXE metric introduced by Zhu et al. [186] which is defined as B_1^+ magnitude squared per unit dissipated power. The feasibility of this RF shimming method has been further demonstrated in a practical application reported by Deniz et al. [171] concerning the imaging study of hip articular cartilage. This particular definition for RF shimming provides a valid solution when compared against other conventional approaches. Specifically, some RF shimming methods [179, 185] are only based on B_1^+ constructive interference neglecting the power deposition effects of the electric field, while others do not account for field interactions between individual transmit elements [187, 188], which have proven to be not a good approach for parallel transmission systems [174, 182]. On the contrary, the utilized RF shimming method is regularized by the power correlation matrix and enables the calculation of a global optimum for the shim weights without the need of computationally expensive nonlinear search algorithms [184, 189].

As it has been demonstrated in [171], the maximum TXE and its corresponding RF shimming coefficients can be readily calculated for a multiple channel array. However, there is an intrinsic limitation in that approach, namely, the maximum TXE metric is a relative perfor-

mance metric that characterizes a coil but cannot describe how much room for improvement there is. Furthermore, the TXE metric does not provide any insight into the optimal coil design for a given imaging task and solely describes the performance a particular RF array can achieve.

Lately, several theoretical performance bounds have been proposed to evaluate and optimize RF coils and MR techniques associated with the highest possible SNR, the lowest possible RF power deposition or the ultimate SAR amplification factor both for simplified sample geometries (head-mimicking uniform spheres or cylinders) and for heterogeneous head models [5, 10–12, 14, 67, 71, 167]. In this chapter, we introduce a novel performance metric, the UITXE [74,75], which is the largest possible TXE that can be achieved for a specific object and field strength consistent with electrodynamic constraints. UITXE represents a theoretical performance upper-bound and provides an absolute performance reference independent of any particular coil design. In this way, it can be used to assess the absolute performance of actual finite transmit arrays and evaluate RF shimming algorithms, both in simulations and experiments. Our technique also allows calculating the associated ideal current distributions that yields UITXE, as it has been demonstrated for SNR and SAR [15,68], which could provide new physical insight into the design of optimal coils that approach the ultimate performance [20–29].

RF shimming [122, 125] was initially proposed to mitigate B_1^+ inhomogeneities by adequately adjusting the relative amplitudes and phases of multiple transmit elements driven with the same RF waveform. By controlling the relative amplitude and phase of the individual transmit elements of a multiple channel array, TXE can be maximized as demonstrated by Deniz et al. [171]. Here, we use a TXE metric defined as B_1^+ magnitude squared in the excitation ROI per unit dissipated power over the entire volume of the sample [171, 186]:

$$\eta = \frac{\text{average}|B_1^+(\boldsymbol{r})|^2}{\frac{1}{2}\int_{V'}\sigma(\boldsymbol{r}')|\boldsymbol{E}(\boldsymbol{r}')|^2 dV'}. \tag{3.1}$$

The rationale of this definition lies within a linear system's superposition principle which implies that the net B_1^+ and electric field at each spatial location $\boldsymbol{r}$ of a multiple channel transmit array can be expressed as:

$$\begin{aligned} B_1^+(\boldsymbol{r}) &= \sum_{n=1}^{N} w_n b_n^+(\boldsymbol{r}), \\ \boldsymbol{E}(\boldsymbol{r}) &= \sum_{n=1}^{N} w_n \boldsymbol{e}_n(\boldsymbol{r}), \end{aligned} \tag{3.2}$$

where N is the number of the transmit elements, w_n are the complex-valued RF shimming coefficients that correspond to the driving amplitude and phase modulation of the nth chan-

nel of a transmit array and $b_n^+(\boldsymbol{r})$ and $\boldsymbol{e}_n(\boldsymbol{r})$ represent, respectively, the B_1^+ and electric fields corresponding to unit weighting on the nth channel and zero weights on the others. This definition further allows for TXE metric to be expressed as a ratio of quadratic forms. Specifically, by choosing a target excitation ROI with Q spatial locations or voxels, the net B_1^+ can be combined in matrix form as $\mathbf{b}_1^+ = \mathbf{C}\mathbf{w}$ where $\mathbf{C}$ is a $Q \times N$ matrix with $\mathbf{C}_{qn} = b_n^+(\boldsymbol{r}_q)$. Consequently, the average transmit field squared in the ROI reads:

$$\text{average}|B_1^+(\boldsymbol{r})|^2 = \mathbf{w}^H \boldsymbol{\Gamma} \mathbf{w}, \tag{3.3}$$

where $\boldsymbol{\Gamma} = \mathbf{C}^{\mathbf{H}}\mathbf{C}/Q$ is an $N \times N$ positive-definite complex Hermitian matrix and it represents the B_1^+ correlation matrix with ^{H} superscript denoting the conjugate transpose operation. Similarly, by exploiting the linear superposition of the net electric field, the deposited or absorbed RF power from a multiple channel array into the object is expressed as:

$$P_{\text{abs}} = \frac{1}{2} \int_V \sigma(\boldsymbol{r}) |\boldsymbol{E}(\boldsymbol{r})|^2 dV = \mathbf{w}^H \boldsymbol{\Phi} \mathbf{w}, \tag{3.4}$$

where $\sigma(\boldsymbol{r})$ represents the electrical conductivity and Φ is an $N \times N$ positive-definite complex Hermitian power correlation matrix whose elements are given as:

$$\boldsymbol{\Phi}_{ij} = \frac{1}{2} \int_V \sigma(\boldsymbol{r}) \boldsymbol{e}_i^*(\boldsymbol{r}) \cdot \boldsymbol{e}_j(\boldsymbol{r}) dV, \tag{3.5}$$

with $i, j \in \{1, .., N\}$ and * superscript denoting the complex conjugation. Substituting the above expressions for the RF transmit field squared and deposited power, Eq. 3.1 can be rewritten in a more treatable form, as a ratio of quadratic forms:

$$\eta = \frac{\mathbf{w}^H \boldsymbol{\Gamma} \mathbf{w}}{\mathbf{w}^H \boldsymbol{\Phi} \mathbf{w}}, \tag{3.6}$$

where a suitable unit for TXE metric is $(\mu\text{T})^2/\text{W}$ and $\mathbf{w}$ are the complex-valued RF shimming weights. The problem of finding the maximum TXE can be treated as a generalized eigenvalue problem ($\boldsymbol{\Gamma}\mathbf{w} = \lambda\boldsymbol{\Phi}\mathbf{w}$) which has a closed solution and guarantees the calculation of the global optimum [171,186,190]. Specifically, the largest eigenvalue, which can be computed numerically (e.g., with the Matlab function `eigs`$(\boldsymbol{\Gamma}, \boldsymbol{\Phi}, 1)$), corresponds to the maximum TXE ($\eta_{\max}$) and the associated eigenvector gives the corresponding RF shimming weights ($\mathbf{w}_{\max}$) that yield maximum TXE, when used as driving amplitudes and phases in a given RF array.

3.2 Basis of Electromagnetic Fields and Bounds of Transmit Performance

In order to find the theoretical largest TXE, which we call UITXE, and use it as an absolute performance reference for the evaluation of RF transmit arrays, it is necessary that UITXE is independent of any particular array design. Therefore, instead of EM fields from actual, physically realizable coils, we use a complete basis of orthogonal EM modes [10–12, 14, 15, 67, 71, 74], that are consistent with electrodynamic principles, and treat them as the elements of a hypothetical infinite array. In direct analogy to the case of finite transmit arrays, the net electric and B_1^+ fields are expressed as a linear combination of the contributions of the complete set of basis fields:

$$\begin{aligned} B_1^+(\boldsymbol{r}) &= \sum_{n=1}^{\infty} w_{n,b} b_{n,b}^+(\boldsymbol{r}), \\ \boldsymbol{E}(\boldsymbol{r}) &= \sum_{n=1}^{\infty} w_{n,b} \boldsymbol{e}_{n,b}(\boldsymbol{r}), \end{aligned} \tag{3.7}$$

where $b_{n,b}^+(\boldsymbol{r})$ and $\boldsymbol{e}_{n,b}(\boldsymbol{r})$ are the B_1^+ and electric field modes of the complete basis.

To generate a complete EM basis, the object should be fully encapsulated by a closed surface and according to the surface equivalence or Huygens's principle, any EM field distribution, inside the devoid-of-sources volume surrounded by the surface, can be generated by a current distribution flowing on the surface [108, 109, 116]. Thus, all possible EM fields generated inside the object by any external RF array can be reproduced by some current density flowing on the surrounding Huygens's surface. Since the operator that maps electric currents on the surface to incident EM fields over the object is compact [66], UITXE converges to its optimal value as the number of basis elements increases. This property allows to use a finite number of basis functions (let N now be the number of modes where convergence to a maximum is observed) enabling the computation of UITXE, since in practice it is not feasible to use infinite number of modes. Therefore, the converged maximum eigenvalue of the generalized eigenvalue problem $\boldsymbol{\Gamma}_b \mathbf{w}_b = \lambda \boldsymbol{\Phi}_b \mathbf{w}_b$ for N number of modes is the ultimate: $\tilde{\eta} = \lambda_{\max,N}$.

Apart from the performance bounds themselves, ICP were also proposed as the surface current distributions that result in the highest possible SNR or the lowest possible RF power deposition consistent with electrodynamic principles [15, 68]. ICP can be a source of physical intuition about the determinants of coil performance and could lead to task-optimal RF arrays designs. Specifically, there are several studies with the aim to approach the performance bounds with novel coil designs inspired by ICP and assess their overall performance [20–29]. Additionally, ICP can provide a framework to separate the curl-free and divergence-free current components and study their contributions to the ultimate perfor-

mance at different magnetic field strengths [19, 68, 73]. ICP can be derived for the case of UITXE, too, since the eigenvector ($\tilde{\mathbf{w}}_b$) associated with the largest eigenvalue ($\tilde{\eta}$) provides the shimming weights, which can be used to optimally combine the current basis modes $\boldsymbol{j}_{n,b}(\boldsymbol{r})$. Following the same notation as before, ICP are given as the linear combination of the N current modes that are sufficient for UITXE to converge:

$$\tilde{\boldsymbol{J}}(\boldsymbol{r}) = \sum_{n=1}^{N} \tilde{w}_{n,b} \boldsymbol{j}_{n,b}(\boldsymbol{r}). \tag{3.8}$$

3.2.1 Ultimate Intrinsic Transmit Efficiency in Spherical Samples

UITXE is the largest possible TXE, for a specific object and magnetic field strength, allowed by electrodynamics and does not depend on a particular coil geometry. In order to calculate the UITXE we use a framework [15] based on the eigenfunction expansion of the DGF [191], which enables the rapid calculation of TXE in a homogeneous spherical sample for finite arrays of loop coils and for the ultimate case. It further allows to calculate the surface current distribution that yields UITXE as a weighted combination of surface current modes.

Specifically, we consider a uniform, head-mimicking spherical sample with radius a surrounded by a concentric spherical surface with radius b, onto which we constrain the current to flow [15, 191]:

$$\boldsymbol{J}(r, \theta, \phi) = \boldsymbol{K}(\theta, \phi) \frac{\delta(r - b)}{b^2 \sin\theta}, \tag{3.9}$$

where r (radial), θ (polar), and ϕ (azimuthal) are spherical coordinates and $\boldsymbol{K}$ is the surface current density, which can be expressed as a weighted sum of basis current modes [15, 192]:

$$\boldsymbol{K}(\theta, \phi) = \sum_{l=0}^{\infty} \sum_{m=-l}^{l} -j\sqrt{l(l+1)} \left[W_{l,m}^{M} \boldsymbol{X}_{l,m}(\theta, \phi) + W_{l,m}^{E} \hat{\boldsymbol{r}} \times \boldsymbol{X}_{l,m}(\theta, \phi) \right]. \tag{3.10}$$

Here, l and m are mode indices, $j = \sqrt{-1}$ is the imaginary unit, $W_{l,m}^{M}$ and $W_{l,m}^{E}$ are the series expansion coefficients representing magnetic-type (divergence-free) and electric-type (curl-free) surface current contributions, respectively, $\hat{\boldsymbol{r}}$ is the unit vector in the radial direction, and $\boldsymbol{X}_{l,m}$ is a VSH (see Appendix A). According to the surface equivalence principle [108, 109, 116], the basis in Eq. 3.10 can represent all possible EM fields distributions within the sample, even when it consists only of one kind of current sources [193] (in this chapter we consider only electric current sources). The net EM fields generated by the current modes inside the sphere can be calculated using the appropriate DGF branch (see Appendix A) and

they read:

$$\begin{aligned}\boldsymbol{E}(\boldsymbol{r}) &= -\omega\mu_0 k_0 \sum_{l=0}^{\infty}\sum_{m=-l}^{l}\left[V_{l,m}^{M}\boldsymbol{M}_{l,m}(k_{\text{in}},\boldsymbol{r}) + V_{l,m}^{N}\boldsymbol{N}_{l,m}(k_{\text{in}},\boldsymbol{r})\right], \\ \boldsymbol{B}(\boldsymbol{r}) &= -j\mu_0 k_0 k_{\text{in}} \sum_{l=0}^{\infty}\sum_{m=-l}^{l}\left[V_{l,m}^{M}\boldsymbol{N}_{l,m}(k_{\text{in}},\boldsymbol{r}) + V_{l,m}^{N}\boldsymbol{M}_{l,m}(k_{\text{in}},\boldsymbol{r})\right].\end{aligned} \tag{3.11}$$

Here, ω is the angular frequency, μ_0 is the free-space permeability, $k_0 = \omega\sqrt{\mu_0\epsilon_0}$ is the free-space wavenumber and ϵ_0 is the free-space permittivity. Also, $k_{\text{in}} = k_0\sqrt{\epsilon_r - j\frac{\sigma}{\omega\epsilon_0}}$ is the complex wavenumber inside the lossy, dielectric sphere with relative permittivity ϵ_r and electric conductivity σ. $\boldsymbol{M}_{l,m}$ and $\boldsymbol{N}_{l,m}$ are spherical vector wave functions used to construct the DGF since they are solutions of the vector wave equation, whereas $V_{l,m}^{M}$ and $V_{l,m}^{N}$ are weighting coefficients derived by multiplying the current series expansion coefficients by a transformation matrix $\mathbf{T}$, which accounts for boundary conditions at the surface of both the spherical sample and the current-bearing spherical surface. All the relevant functions are defined in the Appendix A. Also, it should be noted that we use $e^{j\omega t}$ harmonic time variation for all fields and currents, which is omitted for brevity.

If we use the current modes as hypothetical elements of an infinite coil array, we can construct the transmit sensitivity matrix $\mathbf{C}_{\text{mode}}$, containing the associated B_1^+ transmit fields for each mode at the target excitation ROI with Q voxels, and accordingly calculate the B_1^+ correlation matrix $\mathbf{\Gamma}_{\text{mode}}$.We also construct the power correlation matrix $\mathbf{\Phi}_{\text{mode}}$ accounting for the interactions between the electric field modes (see Appendix A). It should be noted that we use a finite $l_{\max}$ resulting in $N = (l_{\max}+1)^2$ number of modes, where we consider each mode as the sum of the electric-type and magnetic-type contributions. Finally, we solve the generalized eigenvalue problem $\mathbf{\Gamma}_{\text{mode}}\mathbf{w} = \lambda\mathbf{\Phi}_{\text{mode}}\mathbf{w}$, as it is demonstrated in the literature [171, 186, 190], and derive the UITXE for a spherical sample and the corresponding weighting coefficients that yield UITXE which can be substituted in Eq. 3.10 to calculate the ICP in the surrounding spherical surface.

Table 3.1: Electrical Properties of Average Brain Tissue.

Field strength B_0 (T)	0.5	1.5	3	7	10.5	14	21
Larmor frequency f_0 (MHz)	21.3	63.9	127.7	298.0	447.0	596.1	894.1
Relative permittivity ϵ_r	157.5	82.7	63.1	51.9	49.1	47.6	45.9
Electric conductivity σ (S/m)	0.30	0.40	0.46	0.55	0.61	0.66	0.76

UITXE calculations are performed for a head-mimicking spherical sample with uniform, frequency-dependent electrical properties, chosen as the average of brain grey and white

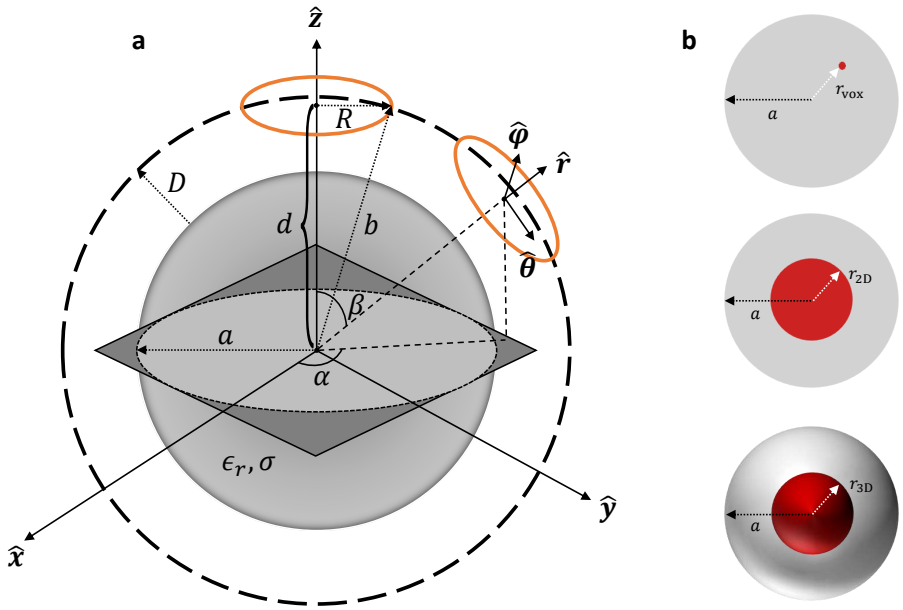

Figure 3.1: Schematic representations of the spherical geometry and relevant simulation settings. (**a**) Schematic representation of the homogeneous spherical sample with frequency dependent electrical properties ϵ_r, σ and radius a surrounded by a current-bearing 2D spherical surface with radius b. Circular loop coils (orange) with radius R are arranged on the spherical surface and can be appropriately rotated by azimuthal (α) and polar (β) angles to compose different finite arrays designs. (**b**) Schematic representation of the ROIs. TXE calculations, for both the ultimate and the case of finite arrays, are performed for single voxels across the diameter of the sample, 2D circular disk ROIs on a transverse plane through the center of the object, and 3D spherical ROIs concentric with the spherical sample.

matter [5] for various magnetic field strengths ($B_0 = 0.5, 1.5, 3, 7, 10.5, 14, 21\mathrm{T}$) as shown in Table 3.1. We consider spherical samples with different radii $a = 7.5, 10, 15\mathrm{cm}$ and the radius of the two-dimensional (2D) spherical surface with the current basis modes is $b = D + a$, placed at distance $D = 1.5\mathrm{cm}$ from the sample (Figure 3.1a). We calculate UITXE for single voxels, 2D and 3D ROIs (Figure 3.1b). Specifically, we compute UITXE across the diameter of each spherical sample, in 2D ROIs that have the shape of a circular disk located around the center of the spherical sample in the axial plane for increasing size of the inner disk radius (r_{2D}) and in 3D spherical ROIs concentric with the spherical sample for increasing size of the inner sphere radius (r_{3D}) (Figures 3.2, 3.4, and 3.6). We use expansion order $l_{\max} = 45$ for which all calculations converge and the convergence results are summarized in Figures B.1, B.2, and B.3 for single voxels at $r_{\mathrm{vox}} = 0, 0.5a, 0.95a$, 2D ROIs with size $r_{2D} = 0.3a, 0.6a, 0.9a$, and 3D ROIs with size $r_{3D} = 0.3a, 0.6a, 0.9a$, respectively. For the spherical sample with $a = 10\mathrm{cm}$ and selected single voxels ($r_{\mathrm{vox}} = 0, 0.4a, 0.7a$), 2D ROIs ($r_{2D} = 0.3a, 0.6a, 0.9a$), and 3D ROIs ($r_{3D} = 0.3a, 0.6a, 0.9a$), we compute the associated ICP for magnetic field strengths $B_0 = 1.5, 7, 10.5, 21\mathrm{T}$ at $t = 0$ (Figures 3.3, 3.5, and 3.7).

The TXE of particular, finite RF arrays can be calculated within the same DGF framework by applying appropriate weighting coefficients to the B_1^+ and electric field modes. Specifically, if the net current is constrained to flow on the conductors of circular loop coils, then, only the magnetic-type contributions survive and the weights can be derived analytically [15]:

$$W_{lm}^{\text{loop},M} = -\frac{2\pi R}{l+1}\sqrt{\frac{4\pi}{2l+1}}Y_{l,m}^{*}(\beta,\alpha)\left[\cot\theta Y_{l,0}(\theta,\phi) - \sqrt{\frac{2l+1}{2l-1}}\csc\theta Y_{l-1,0}(\theta,\phi)\right]\Bigg|_{\theta=\arccos\frac{d}{\sqrt{d^2+R^2}}},$$
$$W_{l,m}^{\text{loop},E} = 0, \tag{3.12}$$

where α and β define the angular position of the center of the loop coil on the sphere, d is the distance from the center of the spherical sample to the center of the loop coil and R is the radius of the loop coil (Figure 3.1a). Then, it is straightforward to calculate the coil transmit sensitivity and power correlation matrix by substituting Eq. 3.12 into Eqs. [A.10] and [A.12], respectively.

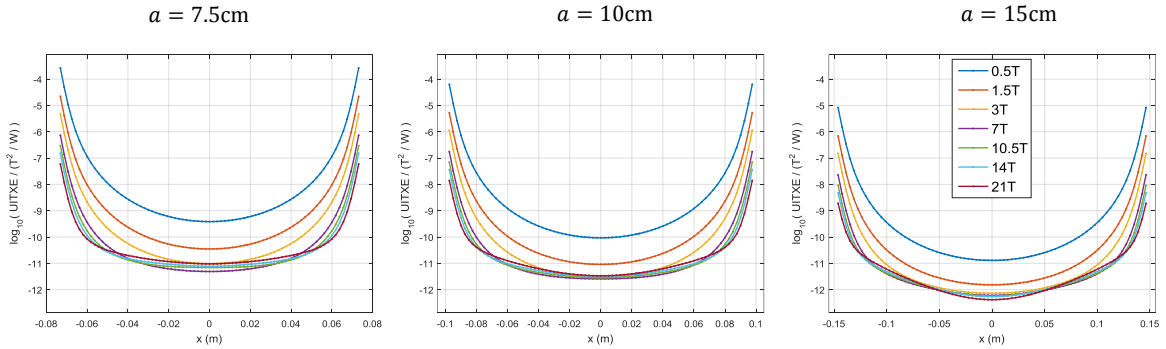

Figure 3.2: Ultimate intrinsic transmit efficiency as a function of voxel position across the diameter of the sphere, for different object size and magnetic field strengths. UITXE is presented in logarithmic scale for spherical samples with radii $a = 7.5, 10, 15\text{cm}$ and brain-mimicking electrical properties at the corresponding magnetic field strengths $B_0 = 0.5, 1.5, 3, 7, 10.5, 14, 21\text{T}$ across the diameter of the sample. It is observed that UITXE decreases as the size of the object increases and as the magnetic field strength increases up to 7T. However, for ultra-high field strengths and voxels closer to the center, it increases again. Closer to the edge of the spherical sample, UITXE is order of magnitudes higher than in the center, for all object sizes and field strengths.

In this chapter, we consider different arrays designs composed of loop coils. First, we simulate fully encircling arrays with 8, 16, 24 and 32 number of channels/loops and calculate their TXE at each voxel at the central axial plane of the spherical sample with $a = 10\text{cm}$ and for magnetic field strengths $B_0 = 3, 7, 10.5\text{T}$. Then, we compare their TXE with respect to the UITXE, by introducing a coil performance metric defined as the percentage of the ultimate that the arrays reach: $100\%\text{TXE}_{\text{array}}/\text{UITXE}$ (Figure 3.8). Next, we simulate

belt-shaped arrays placed around the central axial plane of the spherical sample with 8, 16, 24 and 32 number of channels/loops, calculate their TXE at 2D circular disk ROIs at the central axial plane with increasing disk radius for magnetic field strengths $B_0 = 3, 7, 10.5\mathrm{T}$ and assess their performance (Figure 3.9).

3.2.2 Behavior of Ultimate Intrinsic Transmit Efficiency

In this section, we investigate the behavior of UITXE by studying different target excitation ROIs, namely, single voxels, 2D, and 3D, and by calculating convergence with increasing number of basis modes along with the associated ICP that yield the UITXE.

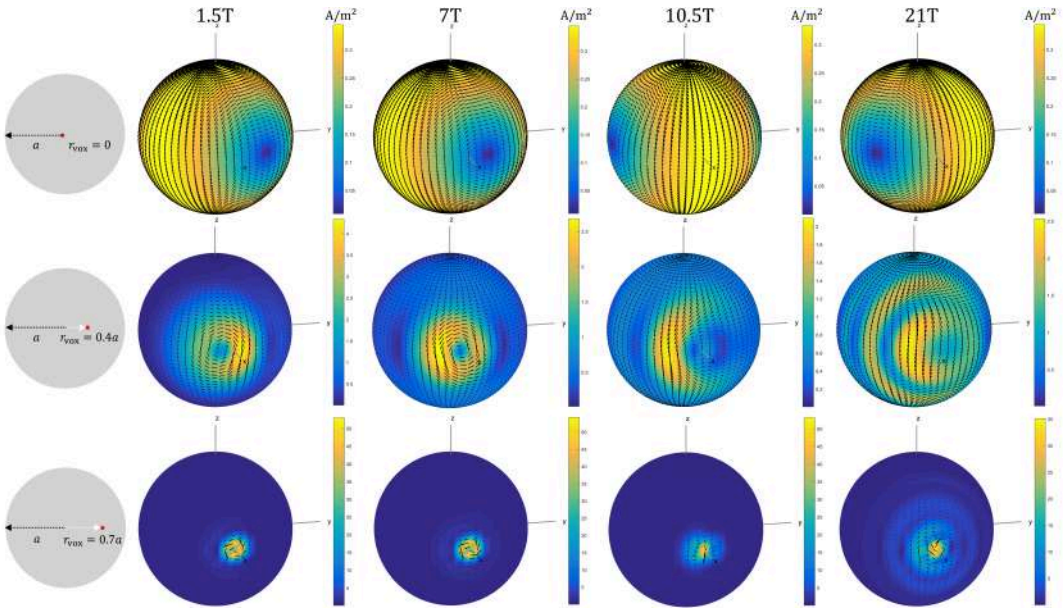

Figure 3.3: Snapshots at time zero of ideal current patterns yielding the ultimate transmit efficiency as a function of voxel position, for various main magnetic field strengths. The magnitude of ideal current patterns at $\omega t = 0$ is shown for a spherical sample with radius $a = 10\mathrm{cm}$, for voxels at the center ($r_{\mathrm{vox}} = 0$), at an intermediate position ($r_{\mathrm{vox}} = 0.4a$), and near the surface ($r_{\mathrm{vox}} = 0.7a$). The corresponding voxel positions can be seen at a schematic at the first column. The other columns show ideal current patterns for increasing field strength $B_0 = 1.5, 7, 10.5, 21\mathrm{T}$. The shape and magnitude of the ideal current patterns vary significantly within different voxel positions. Specifically, at the center, they resemble two large distributed loops on opposite sides of the sphere precessing at Larmor frequency for all field strengths. At the intermediate and near-the-surface position, they become increasingly localized around the target voxel. As the magnetic field increases, their shape also changes and becomes more complex, especially for the case of the intermediate voxel position.

UITXE in Single Voxels

For the case of single voxels, UITXE presents a similar trend with that of UISNR [12, 67], where it increases as the target voxel approaches the surface of the sphere (Figure 3.2).

However, unlike the case of UISNR, UITXE decreases as the main magnetic field increases, up to 7T, and then gradually increases again. This holds particularly for spherical samples with smaller sizes and for interior regions of the sample. Specifically, at the center of the spherical sample with $a = 7.5, 10\text{cm}$, at 7T UITXE is $4.9(\mu\text{T})^2/\text{W}$ and $2.57(\mu\text{T})^2/\text{W}$, respectively, while at 21T it is $9.55(\mu\text{T})^2/\text{W}$ and $3.39(\mu\text{T})^2/\text{W}$ corresponding to a 94.9% and 31.91% increase. Figure B.1 summarizes how rapidly UITXE approaches a limiting value as the order of the multipole expansion $l_{\max}$, and, therefore, the number of spherical harmonics in the basis set, increases for all studied fields and object sizes, especially for the center and intermediate voxel locations. It is interesting to note that for large object sizes ($a = 15\text{cm}$) and for intermediate voxel optimization, UITXE converges more slowly for increasing field strength. Specifically, at 0.5T, 7T, 21T the required number of basis modes for convergence is 49, 96, 155, respectively. This effect can be observed for smaller object sizes, however, it is less dominant and the difference between the demanded modes for convergence for distinct field strengths is not so great. Figure 3.3 shows the magnitude of the associated ICP that yield UITXE in the corresponding single voxels and different field strengths at $\omega t = 0$ and as they evolve in time, respectively. The shape of ICP, associated with UITXE in single voxels, bares close resemblance to the corresponding shape of ICP yielding UISNR [15]. In detail, they both take the form of large distributed loops precessing at Larmor frequency for central voxels and at every field strength and alternate between distributed single-loop and distributed figure-eight for intermediate voxels, becoming increasingly complex for higher fields.

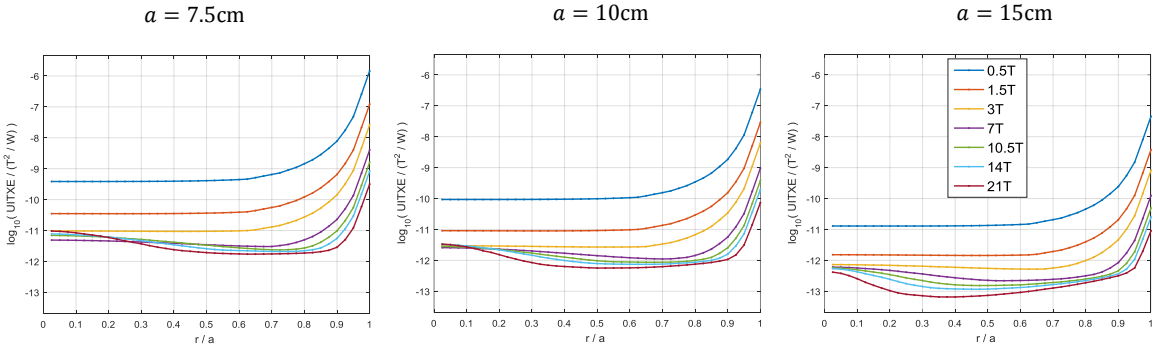

Figure 3.4: Ultimate intrinsic transmit efficiency as a function of the size of the two-dimensional excitation region of interest, for different object size and magnetic field strengths. UITXE is presented in logarithmic scale for spherical samples with radii $a = 7.5, 10, 15\text{cm}$ and brain-mimicking electrical properties at the corresponding magnetic field strengths $B_0 = 0.5, 1.5, 3, 7, 10.5, 14, 21\text{T}$ for increasing radius of the 2D circular disk ROI. It can be seen that UITXE is higher for smaller object sizes and lower field strengths, except for the case of small ROI and object size, where it is higher for ultra-high field strengths. UITXE in 2D ROIs remains constant until the ROI size is almost as large as the sphere section, where it increases sharply since the contributions of the edge voxels dictate the value of UITXE in the whole ROI when averaged.

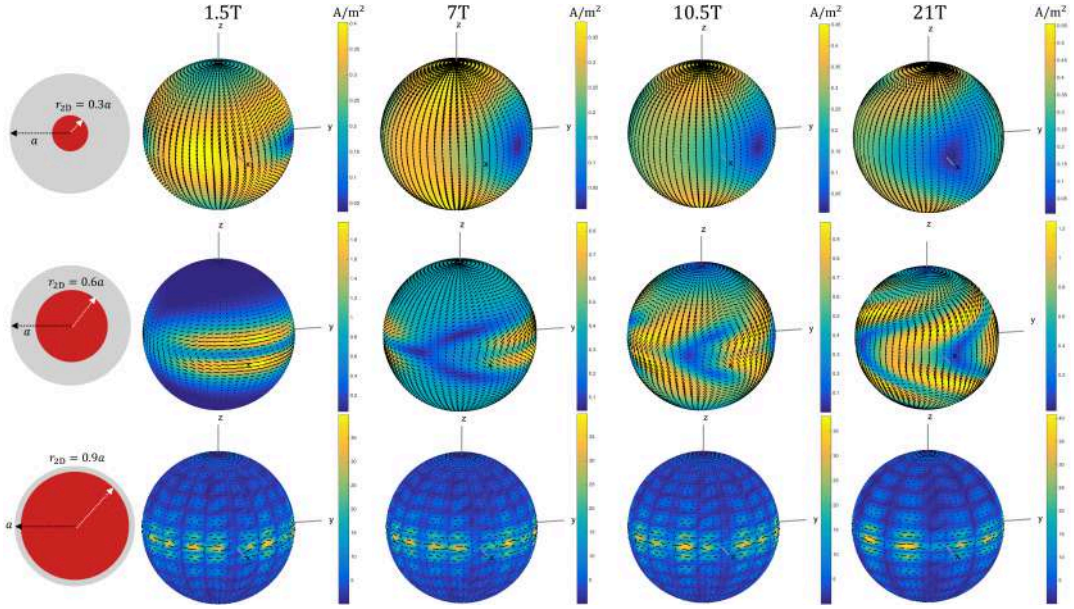

Figure 3.5: Snapshots of ideal current patterns yielding the ultimate transmit efficiency, for various sizes of the two-dimensional excitation ROI and different main magnetic field strengths. The magnitude of ideal current patterns at $\omega t = 0$ is shown for a spherical sample with radius $a = 10\text{cm}$, for circular disk ROIs with increasing size ($r_{2\text{D}} = 0.3a, 0.6a, 0.9a$). The corresponding 2D ROIs can be seen at a schematic at the first column. The other columns show ideal current patterns for increasing field strength $B_0 = 1.5, 7, 10.5, 21\text{T}$. The shape and magnitude of the ideal current patterns differ significantly as the 2D ROI size changes. Specifically, at $r_{2\text{D}} = 0.3a$, they resemble two compressed distributed loops of elliptical shape on opposite sides of the sphere precessing at Larmor frequency. As the size of the 2D ROI increases, the eccentricity of the elliptical shape increases, too, and the ideal current patterns become strongly localized around the excitation plane. As the magnetic field strength increases, their shape also changes and becomes more complex, where wave and propagation delay effects are observed.

UITXE in 2D ROIs

Similar observations and patterns arise when we compute UITXE in 2D ROIs. Figure 3.4 illustrates UITXE as a function of the size of the 2D ROI, where the trend that UITXE decreases with increasing field strength is validated here again, except for small object and ROI sizes. It is worth noting that UITXE remains stable for lower field strengths (0.5T, 1.5T, 3T), until the size of the ROI is between 0.6a and 0.7a, but then increases double-exponentially since the contributions of the superficial voxels in the averaged UITXE are order of magnitudes greater than the central or intermediate, as seen in Figure 3.2. This pattern holds for higher field strengths, too, however, in such strengths, UITXE presents global minima for intermediate ROI sizes. Specifically, the global minima of UITXE for $a = 10\text{cm}$ and $a = 15\text{cm}$ occur at $r_{2\text{D}} = 0.7a, 0.675a, 0.625a, 0.5a$ and at $r_{2\text{D}} = 0.525a, 0.45a, 0.4a, 0.375a$ at 7, 10.5, 14, 21T, respectively. This observation suggests that for higher operating frequencies and object sizes there is a shift towards smaller 2D ROI sizes where the global minimum

arises. Figure B.2 shows the convergence of UITXE for different ROI sizes, object sizes and field strengths and is in exact agreement with the single voxel case (Figure B.1). Particularly, the required basis modes for convergence increase for larger ROI size and for higher field strengths for intermediate ROI sizes (for object size $a = 15\text{cm}$ and ROI size $r_{2\text{D}} = 0.6a$ the number of modes for convergence is 30, 44, 166 for 0.5T, 7T, 21T, respectively). In Figure 3.5, the ICP yielding UITXE in 2D ROIs for various field strengths are depicted. For a small ROI, they resemble large distributed loops precessing at the Larmor frequency and for larger ROIs the patterns become more and more localized around the excitation plane taking the shape of ellipses. As the field strength and the corresponding operating frequency increases, propagation delay and wave phenomena arise altering and perplexing the ICP shape. A last interesting remark is that as the magnetic field strength increases, the elliptical shape of the ICP arises at larger ROIs, which can be seen by comparing ICP at 1.5T, 7T and $r_{2\text{D}} = 0.3a, 0.6a$.

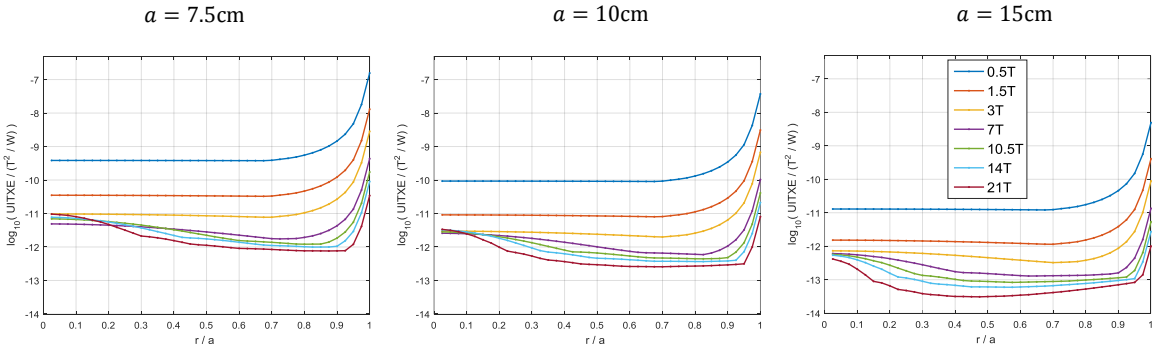

Figure 3.6: Ultimate intrinsic transmit efficiency as a function of the size of the three-dimensional excitation region of interest, for different object size and magnetic field strengths. UITXE is presented in logarithmic scale for spherical samples with radii $a = 7.5, 10, 15\text{cm}$ and brain-mimicking electrical properties at the corresponding magnetic field strengths $B_0 = 0.5, 1.5, 3, 7, 10.5, 14, 21\text{T}$ for increasing radius of the 3D spherical ROI that is concentric to the sample. It can be seen that UITXE is higher for smaller object sizes and lower field strengths, except for the case of small ROI and object size, where it is higher for ultra-high field strengths. UITXE in 3D ROIs remains constant until the ROI size is almost as large as the sphere section where it increases sharply since the contributions of the edge voxels dictate the value of UITXE in the whole ROI when averaged. The overall behavior of UITXE in 3D ROIs is similar to that of 2D ROIs.

UITXE in 3D ROIs

When optimizing TXE in 3D ROIs with increasing size, the behavior of UITXE is expected to share many common characteristics with the UITXE in 2D ROIs. Figure 3.6 confirms this hypothesis, where we see the lower UITXE for higher field strengths pattern and notice the region where UITXE remains stable for up to 3T field strengths. A subtle difference is that for the 3D ROI case, this region is slightly larger and extends up to 0.7a and 0.8a

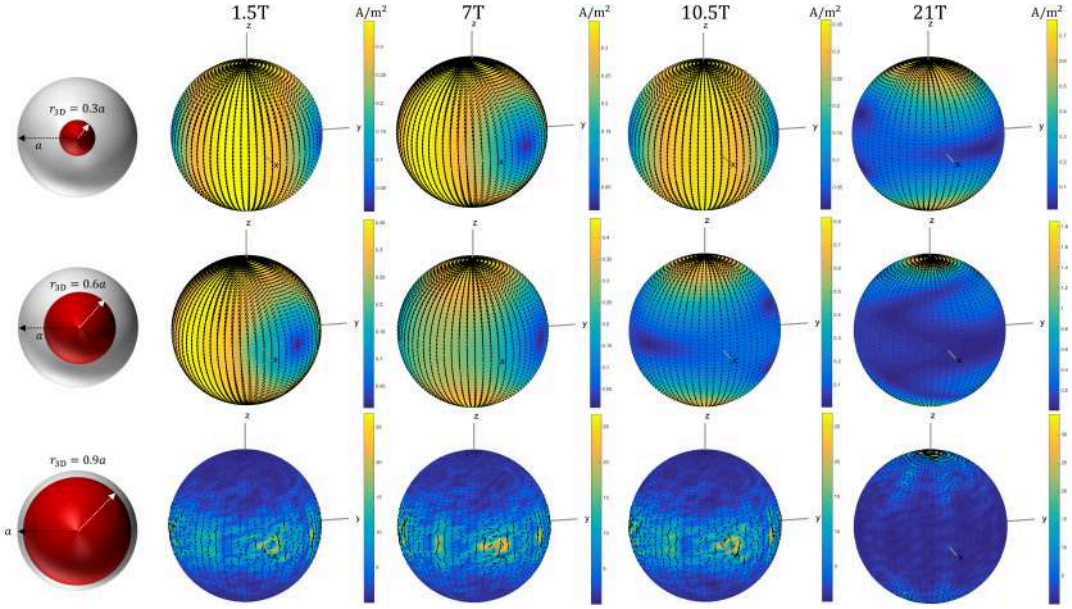

Figure 3.7: Snapshots of ideal current patterns yielding the ultimate transmit efficiency, for various sizes of the three-dimensional excitation ROI and different main magnetic field strengths. The magnitude of ideal current patterns at $\omega t = 0$ is shown for a spherical sample with radius $a = 10\text{cm}$, for spherical 3D ROIs concentric to the object with increasing size ($r_{3D} = 0.3a, 0.6a, 0.9a$). The corresponding 3D ROIs can be seen at a schematic at the first column. The other columns show ideal current patterns for increasing field strength $B_0 = 1.5, 7, 10.5, 21\text{T}$. The shape and magnitude of the ideal current patterns differ as the 3D ROI size changes, but not so significantly as in the case of voxel or 2D ROI optimization, especially for lower field strengths. Specifically, at $r_{3D} = 0.3a$ up to 10.5T and $r_{3D} = 0.6a$ up to 7T, they resemble two large distributed loops on opposite sides of the sphere precessing at Larmor frequency. As the size of the 3D ROI or the magnetic field strength increases, the ideal current patterns become strongly localized around the poles of the sphere. This observation hints to a correlation between the size of the 3D ROI and the operating frequency for the determination of the shape of the ideal current patterns.

ROI sizes, followed by the double-exponential increase associated with the edge voxels contributions. Furthermore, the global minima and their shift with increasing operating frequency are still observed but only for the sample with $a = 15\text{cm}$. Specifically, they arise at $r_{3D} = 0.625a, 0.575a, 0.55a, 0.475a$ at 7T, 10.5T, 14T, 21T, respectively. Interestingly, UITXE for 3D ROIs with intermediate size, as seen in Figure B.3, converges much faster than for the corresponding 2D ROIs, even at UHF. Specifically, for object size $a = 15\text{cm}$ and ROI size $r_{3D} = 0.6a$ the number of modes for convergence is only 1, 5, 30 for 0.5T, 7T, 21T, respectively, requiring 3.33%, 11.36%, 18.07% of the corresponding modes for UITXE convergence in 2D ROIs with the same size. The effect of requiring less modes for convergence appears in the shape of the ICP yielding UITXE in 3D ROIs as demonstrated in Figure 3.7. There, we note that at 7T and $r_{3D} = 0.3a$ they take the form of large distributed loops similar to the ICP shape for a center single voxel optimization, as in Figure 3.3, where

only 1 mode is required for convergence. It is also interesting to emphasize the similarity of the ICP shape for $r_{3D} = 0.3a$ at 21T and $r_{3D} = 0.6a$ at 10.5T where the required modes for convergence are 11 and 19, respectively. This similarity suggests that the ICP localization around the poles arises at smaller 3D ROIs as the field strength increases.

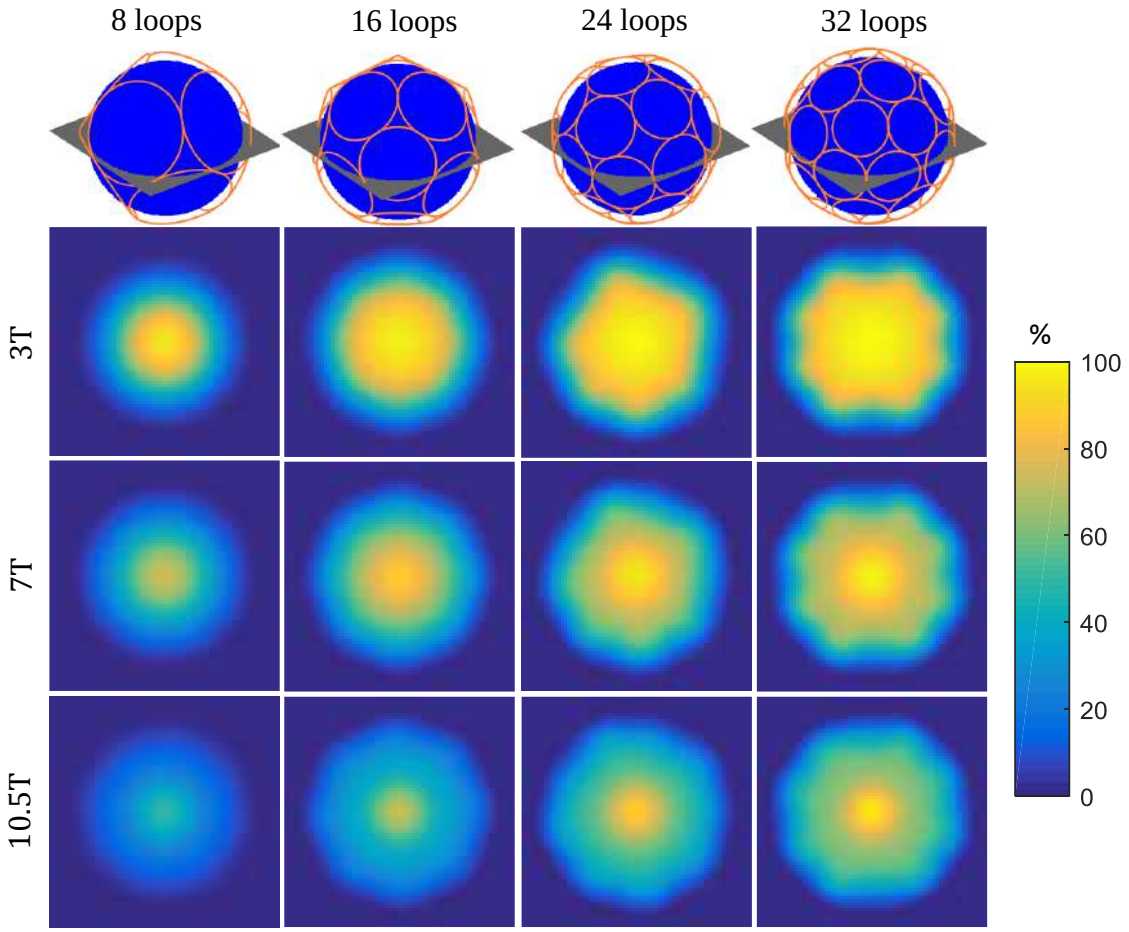

Figure 3.8: Absolute transmit performance of finite arrays with an increasing number of elements encircling the sample, at different main magnetic field strengths. Finite arrays performance maps at each single voxel of the central axial plane of the spherical sample with $a = 10\text{cm}$ and for magnetic field strengths 3T, 7T, 10.5T are presented. The fully encircling arrays consist of rotated loops with 8, 16, 24, and 32 number of channels/loops, schematics of which can be seen at the first row of the figure. Absolute transmit performance increases and covers a broader field of view for an increasing number of loops in the array, but becomes more localized and decreases for higher main magnetic field strengths.

Approaching UITXE with Finite Coil Arrays

UITXE can also be used as an absolute performance metric to assess transmit arrays and evaluate RF shimming algorithms and such assessment of various arrays composed of loops with different configurations is presented in Figure 3.8 and Figure 3.9. Figure 3.8 presents how fully encircling arrays, with increasing number of loops, approach UITXE at single

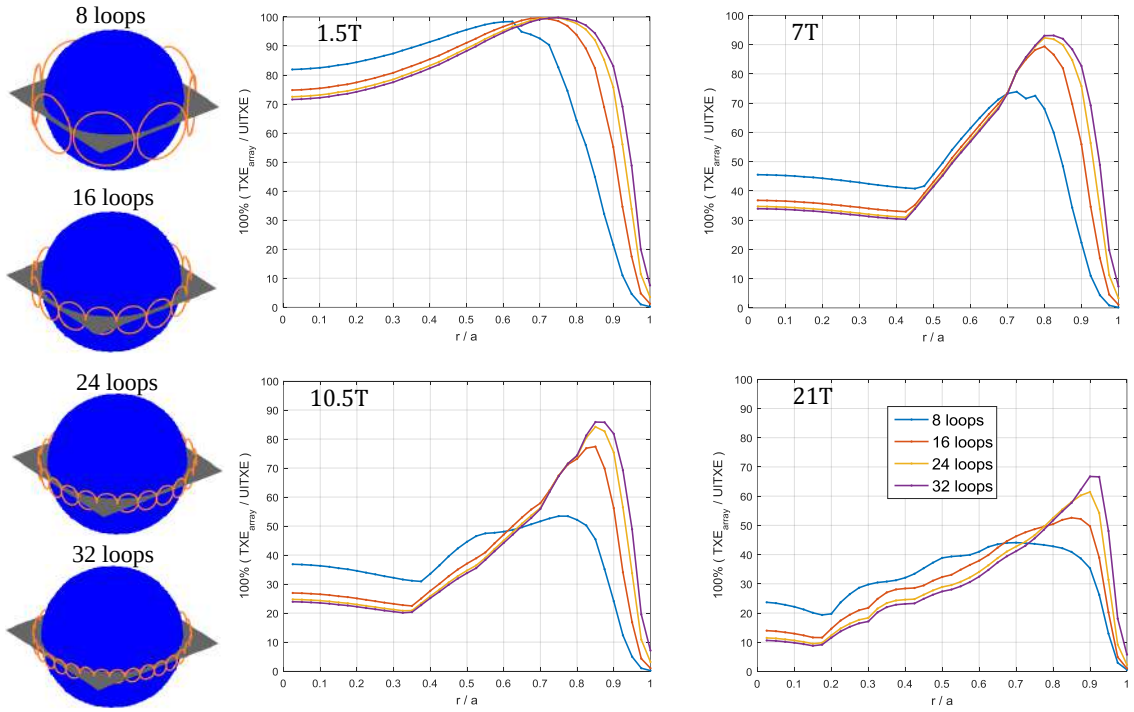

Figure 3.9: Absolute transmit performance of finite arrays with an increasing number of elements arranged like a belt around the central plane, as a function of the size of the 2D excitation ROI. Finite arrays performance for increasing size of the 2D circular disk ROI on the central axial plane of the spherical sample with $a = 10\text{cm}$ and for magnetic field strengths 1.5T, 7T, 10.5T, 21T are presented. The belt-shaped arrays consist of rotated loops with 8, 16, 24, and 32 number of channels/loops, schematics of which can be seen at the first column of the figure. Absolute transmit performance is higher when the coil configuration is consistent with the shape of the ideal current patterns (Figure 3.5). Similarly to the case of fully encircling arrays for single voxel optimization (Figure 3.8), belt-shaped arrays for 2D ROI optimization, reach a higher performance for lower fields and the performance increases as the number of elements increases.

voxels in the central axial plane of the sample. First, we note the qualitative pattern that as magnetic field strength decreases and number of element increases, the voxel performance gets closer to UITXE and in broader regions, too. Quantitatively, at the center voxel, at 3T, 8 and 32 loops yield 94.53% and 99.43% performance, respectively, while at 10.5T, the same number of loops reaches 49.89% and 95.81%. The performance drops significantly at an intermediate voxel with $r_{\text{vox}} = 0.5a$, where at 3T, 8 and 32 loops yield 30.82% and 80.11% performance, respectively, while at 10.5T, the same number of loops reaches only 15.58% and 56.17%. It is also interesting to note that performance is larger than 70% in voxels inside circular disk regions with radii 0.25a and 0.625a at 3T for 8 and 32 loops arrays, while at 10.5T, 8 loops nowhere reach such performance and 32 loops only up to a 0.25a radius.

Figure 3.9 explores the performance of belt-shaped arrays with increasing number of elements for 2D ROI optimization with increasing size. Here, the inverse relationship between

field strength and performance remains, as well as, the direct one between number of elements and performance. Specifically, at ROIs with size $r_{2\mathrm{D}} = 0.75a$, at 1.5T, 8 and 32 loops yield 82.67% and 99.8% performance, respectively, while at 21T, the same number of loops reaches 43.67% and 45.54%. We also notice that for a certain size of the 2D excitation ROI the array performance is higher. This can be explained from the ICP (Figure 3.5), where we see that for small ROIs they look like large distributed loops that are not captured by the array design, while at larger ROIs they are very similar to a belt shape, since they become increasingly localized around the excitation central plane. In fact, at 7T, the array with 32 loops reaches at maximum 33.91% of the UITXE at ROIs with size less than $r_{2\mathrm{D}} = 0.4a$. However, the same array at ROIs with size between 0.6a and 0.9a reach a performance up to 93.12%, where the global maximum is at $r_{2\mathrm{D}} = 0.825a$. Also, a shift in the global maxima location can be seen with increasing field strength, which can also be explained from the ICP in Figure 3.5, where the localization of the ICP around the excitation plane happens at larger ROIs as the field strength increases. Specifically, for a finite array with 32 elements, at 1.5T, 7T, 10.5T, 21T, the global maximum occurs at $r_{2\mathrm{D}} = 0.75a, 0.825a, 0.875a, 0.925$, respectively, and the corresponding performance is 99.8%, 93.12%, 85.76%, 66.6%.

Discussion

In this chapter, we introduced a new theoretical performance upper-bound, namely, the UITXE which is the best achievable TXE from all possible excitations that can provide insight into the design of transmit arrays via ICP and be used to evaluate existing coil designs and RF shimming algorithms. We investigated its behavior in spherical objects with uniform frequency-dependent electrical properties for different sphere radii, magnetic field strengths, and target excitation profiles (single voxels, 2D, and 3D ROIs). A key observation was that the behavior of UITXE for single voxels across the radius of the spherical sample is analogous to that of UISNR [12, 67]. In particular, the minimum of both UITXE and UISNR is always located in the center of the sphere, UITXE presents rotational symmetry and increases exponentially as the voxel position approaches the surface of the sphere. However, there is a significant difference between transmit and receive case which is related to the dependence of the ultimate metrics on the magnetic field strength. UISNR was found to be approximately linear in B_0, for low B_0, while changing to higher power growth for higher B_0 [12]. However, UITXE decreases, as B_0 increases, for most voxel positions and sample sizes, except for the case of smaller sample size and center voxel locations, where it gradually increases again at UHF strengths. Furthermore, UISNR can be solely evaluated in single voxels, whereas UITXE provides the additional degree of freedom of being computed in different target excitations, namely, in 2D and 3D ROIs offering the possibility of a more compact and general evaluation of transmit arrays. It was found that the behavior of UITXE is similar for both 2D and 3D ROIs maintaining a stable value for ROI sizes al-

most as large as the radius of the sample and then increasing sharply since the superficial voxel contributions dictate the ultimate value in the whole ROI making the center and intermediate contributions negligible. Another interesting observation was that UITXE in ROIs has a non-monotonic behavior at high field strengths and large sample sizes. UITXE in all excitation profiles, with its distinct characteristics, provides an absolute performance bound independent of any particular array design that can be readily used for the assessment of coil designs and RF shimming techniques.

Except for offering an absolute performance reference, UITXE also provides insight into the design of RF transmit coils through its associated ICP, which can be used as guidelines to design the position and shape of the conductors. First, we investigated the ICP yielding UITXE in single voxels, where again, there arise similar patterns with the ICP associated with UISNR [15]. In agreement with the UISNR case, at low field strengths, ICP (Figure 3.3) consist of distributed current loops which precess around the direction of the main magnetic field at Larmor frequency. Thus, in the transmit case, too, the field should track as closely as possible the precession of central spins. In practice, in deep-tissue positions, this can be achieved by quadrature birdcage coils [194]. However, in locations closer to the surface of the object, ICP take the form of single loops alternating with figure-eight shapes, resembling the UISNR case and suggesting that surface quadrature coils [195] could be a better fit. However, this is only true for lower field strengths, since ICP become increasingly complex at higher field strengths suggesting that asymmetric quadrature coils might perform better than traditional closed loops. Indeed, there are studies [196–198] suggesting that transmit/receive coils that take into account the asymmetry of the EM fields in higher frequencies achieve higher performance when compared against traditional designs used in lower field. Similarly, ICP associated with UITXE in 2D and 3D ROIs, follow this pattern, where asymmetries and wave phenomena occur with increasing field strength and their magnitude gets localized around the excitation plane.

Furthermore, similarly to previous studies [26–28], we investigated the performance of finite loop coils configurations, inspired by the shape of the ICP, with respect to the theoretical performance limits of TXE for different ROIs and field strengths. As seen in Figure 3.8, increasing the elements of a fully encircling loop-composed array, both in lower and higher field strengths, leads to an increase in the performance mainly in center and close-to-the-center voxels. There, the corresponding ICP take the form of large distributed loops (Figure 3.3), and as the number of loops increases, the coil current patterns resemble more and more the ICP shape. However, performance saturates for voxels close to the surface, especially for higher field strengths, and there is no or negligible improvement in increasing the coil elements. This can be attributed to the fact that the rate and extent at which UITXE is approached depends less on the number of the elements than on the similarity of the array itself to the ICP shape and how closely it can mimic them, for a specific sample and exci-

tation surface combination, similarly to the UISNR case [15, 21, 26]. In Figure 3.8, it was also observed that at higher field strengths, even at the center or close-to-the-center voxels, there are required more coil elements for converging closer to the ultimate values and the farther the voxel from the center the smaller the performance is. This is associated to the fact that electric-dipole components emerge in ICP when optimizing TXE at high field strengths. Thus, it is not expected that an array of loops will approach the UITXE closely in regions where the ICP have significant electric-dipole components, no matter how much the number of loops increases. This effect has been investigated in previous comprehensive studies whose aim was to approach UISNR in spherical [26] and cylindrical [28] samples, where it has been suggested that the combination of loops and electric dipoles could be more effective at UHF. The effect that the performance of an array mostly depends on its similarity with the corresponding ICP yielding UITXE rather than the number of the elements, is further validated in Figure 3.9. There, it is observed that even at UHF strengths (7T and 10.5T) the array performance approaches the ultimate for 2D ROI sizes at which the ICP shape is captured (Figure 3.5) by the belt-shaped design of the array.

In this chapter, we introduced UITXE for RF shimming, but our approach could be generalized to parallel transmission, too. This would require adding the time dependence to the transmit and electric field equations, in order for the phase and amplitude of the different channels to be able to change at each time instant. It would also require using a local SAR matrix [186] instead of the covariance matrix that we used in this chapter. However, the focal point of this study was revolving around TXE for RF shimming rather than parallel transmission because in the former, the power correlation matrix can be measured experimentally [172–174] more easily than the local SAR one. Furthermore, in RF shimming the weights are fixed, so there is a single ultimate value and a single set of ICP associated with each excitation task, leading to more comprehensible and applicable results.

Another limitation of this study, is the use of a uniform sphere as an approximated model of the human head. However, this choice allows to calculate the corresponding full-wave EM fields analytically with a simulation framework based on DGF which enables to rapidly execute simulations and explore dependencies on various parameters. Moreover, it allows to easily and intuitively plot ICP on the surrounding spherical surface from the weighted sum of the current basis modes. Finally, previous work on realistic head models [67] demonstrated that the sphere is a good approximation and even if there would be small differences, the general trends, regarding how UITXE behaves with respect to field strength, target excitation profiles, and number of coil elements, presented in this chapter would not change significantly, as we further illustrate in Chapter 5. Thus, the main mechanisms and principles governing UITXE in spherical samples can provide useful physical insight for the case of realistic head models, too.

An additional advantage that TXE metric offers is that it can be measured experimentally. In particular, we can measure TXE for a transmit array using a spherical phantom of known electrical properties and compare it with the UITXE calculated for an object with the same geometry and properties, to assess the transmit performance of actual coils. Compared to coil performance maps for SNR [199], this approach would not require to scale UITXE by sequence related parameters. However, it would require the proper hardware to measure the power correlation matrix [171–174] and accurate B_1^+ maps [175].

3.2.3 Conclusions

In conclusion, in this chapter we introduced a novel performance metric, namely the UITXE, which is the largest possible TXE that can be achieved for a specific object and field strength consistent with electrodynamic principles. We investigated its behavior for different magnetic field strengths, target excitation ROIs, and spherical sample sizes and computed its associated ICP on spherical surfaces surrounding the samples. Its main mechanisms and behavior for single voxels resemble that of UISNR [12]. We also evaluated the performance of transmit arrays with increasing number of loops and different designs, for various field strengths and ROIs, illustrating how UITXE can be used to assess coil designs and RF shimming algorithms. Our results demonstrated how ICP can provide useful insight into the design of RF transmit arrays and validated previous observations [15, 27, 28] that the ultimate performance is approached more closely when the shape of the array resembles that of ICP rather than when the number of the elements increases. At UHF, transmit performance can be approached only at the center of the sample suggesting that more elements or the combination of loops and electric dipoles could be more effective. In Chapter 5, we study the behavior of UITXE in realistic head models and future work could include the experimental coil performance evaluation with suitable hardware/software for RF power measurements with respect to the UITXE in spherical phantoms, the study of the contributions of dipole arrays and dielectric pads to UITXE, the investigation of the correlation between B_1^+ homogeneity and UITXE, and whether the electric field distribution that corresponds to UITXE respects local SAR aspects.

4 Integral Equations Methods for Electromagnetic Fields Computations in MRI

As we showed in the previous chapter, analytical techniques yield great insight into expected and observed trends in MR signal, noise, and safety. However, to analyze more realistic and complex scenarios, numerical methods have to be employed in order to solve Maxwell equations, compute the 3D local SAR distribution and monitor whether or not it violates local SAR aspects, in particular, in the presence of extremely inhomogeneous objects and objects with high contrast, e.g., anatomical realistic body models. Over the last decades, a plethora of numerical algorithms and computational methods has been developed for applications, not only in the MR field, but also for wireless communications, microwave instrumentation, and remote sensing. The MR modeling case is a particularly challenging problem and modeling the interactions between EM waves and biological tissue is of great relevance for the determination of the deposited RF power inside the human body and the associated safety considerations at UHF MRI. Specifically, at high and UHF strengths, the operating frequency of the associated RF coils increases linearly. Hence, the wavelength becomes comparable to or even smaller than the effective dimension of the human body, potentially increasing the SAR and deteriorating the magnetic field homogeneity and thus the image quality. Therefore, the accurate estimation of the local distribution of the EM fields, generated by an external RF source, as well as the absorbed power, described by SAR, calls for the implementation of novel and efficient electrodynamic solvers, to achieve a reliable numerical solution. Developing such precise simulation tools poses a great challenge since from a computational EM perspective the human body is highly inhomogeneous and presents great geometrical complexity.

Regarding the numerical techniques for computing EM fields in inhomogeneous dielectrics, such as the human body, there is a vast amount of literature and a rich investigative activity. On one hand, there are methods based on the partial differential form of Maxwell equations, such as FDTD and FEM, which are known for their generality and versatility in many application areas. On the other hand, there are methods that start from Maxwell equations in their integro-differential form, such as the IE methods, which offer great flexibility in exploiting certain problem properties by customization of the method. IE methods, despite

being complicated and computationally expensive, have proven to be the method of choice for modeling inhomogeneous objects by dividing the arbitrary scatterer into simple volumetric tessellations, with piecewise homogeneous properties. Furthermore, a VIE-based solver can be effortlessly embedded into a SIE solver to calculate the EM field distributions and RF transmit and receive coils interactions in the presence of realistic human body models [65]. SIE methods [61–63] can be applied to model the homogeneous conductors (e.g., the RF coils) whose radiated EM fields can be computed by applying the appropriate free-space DGF and they are typically combined with the discretization of the surface of homogeneous body models where there is no need to discretize the surrounding air which characteristic reduces the dimensionality of the problem, compared against FDTD or FEM. However, SIE methods can only be applied to piece-wise homogeneous media leading to a not accurate representation of the EM field and SAR distribution for the case of the highly inhomogeneous biological tissue. In order to handle such inhomogeneous scatterers, VIE methods have to be applied where the inhomogeneous medium is discretized with volumetric elements (voxels) with PWC approximations of the electrical properties. The dense matrices that IE methods involve, have hindered their application in large and complex structures, however, the regular discretization of human body models in MRI applications, where tissue parameters (i.e, electrical properties, T_1, T_2) are usually provided in a voxelized form, along with the translation invariance property of the Green's function kernels has allowed for the application of FFT for the matrix-vector product implementation in combination with iterative solvers [60]. Finally, in contrast with partial differential methods, IE methods do not require the introduction of ABCs or PMLs to bound the domain, since the fundamental solution is applied to each discretized element. All these considerations have recently advanced research and development of VIE methods [60, 64, 65] which can also be directly combined with SIE methods for RF coil modeling.

In this chapter, we first describe the vector EM wave equation and the associated Green's functions for a homogeneous medium, then briefly mention important characteristics of SIE methods and how the electric and magnetic field integral equations are formulated and discretized with the Rao-Wilton-Glisson (RWG) basis functions, and finally the focus shifts on VIE methods for EM scattering from inhomogeneous media, where we introduce our novel higher-order current-based VIE solver [76, 77] and show its application within the MR field.

4.1 Dyadic Green's Functions for Homogeneous Media

4.1.1 Electromagnetic Wave Equations

Maxwell equations in 2.20 are a coupled pair of equations and in many applications their decoupling is advantageous. By dividing Eq. 2.20a with $\dot{\mu}_r$, taking its curl and using Eq. 2.20b

we end up with the most general form of the electric field wave equation for an isotropic medium [109]:

$$\nabla \times \left(\frac{1}{\dot{\mu}_r} \nabla \times \boldsymbol{E} \right) - k_0^2 \dot{\epsilon}_r \boldsymbol{E} = -j\omega\mu_0 \boldsymbol{J}_i - \nabla \times \left(\frac{\boldsymbol{M}_i}{\dot{\mu}_r} \right), \tag{4.1}$$

where $k_0 = \omega\sqrt{\mu_0\epsilon_0}$. Similarly, the corresponding magnetic field wave equation takes the form:

$$\nabla \times \left(\frac{1}{\dot{\epsilon}_r} \nabla \times \boldsymbol{H} \right) - k_0^2 \dot{\mu}_r \boldsymbol{H} = -j\omega\epsilon_0 \boldsymbol{M}_i + \nabla \times \left(\frac{\boldsymbol{J}_i}{\dot{\epsilon}_r} \right). \tag{4.2}$$

The EM wave equations, for the case of a homogeneous medium, can be simplified, since the spatial derivatives of the relative permittivity and permeability are zero, as follows:

$$\nabla \times \nabla \times \boldsymbol{E} - k^2 \boldsymbol{E} = -j\omega\dot{\mu}\boldsymbol{J}_i - \nabla \times \boldsymbol{M}_i, \tag{4.3a}$$

$$\nabla \times \nabla \times \boldsymbol{H} - k^2 \boldsymbol{H} = \nabla \times \boldsymbol{J}_i - j\omega\dot{\epsilon}\boldsymbol{M}_i, \tag{4.3b}$$

where $k = \omega\sqrt{\dot{\mu}\dot{\epsilon}}$. Then, by making use of Eqs. 2.20c, 2.20d, and the vector calculus identity $\nabla \times \nabla \times \boldsymbol{A} = \nabla(\nabla \cdot \boldsymbol{A}) - \nabla^2 \boldsymbol{A}$ we can rewrite the above equations as:

$$\nabla^2 \boldsymbol{E} + k^2 \boldsymbol{E} = j\omega\dot{\mu}\boldsymbol{J}_i - \frac{\nabla(\nabla \cdot \boldsymbol{J}_i)}{j\omega\dot{\epsilon}} + \nabla \times \boldsymbol{M}_i, \tag{4.4a}$$

$$\nabla^2 \boldsymbol{H} + k^2 \boldsymbol{H} = -\nabla \times \boldsymbol{J}_i + j\omega\dot{\epsilon}\boldsymbol{M}_i - \frac{\nabla(\nabla \cdot \boldsymbol{M}_i)}{j\omega\dot{\mu}}, \tag{4.4b}$$

which, by making use of the continuity equations in 2.18, can be rewritten as:

$$\nabla^2 \boldsymbol{E} + k^2 \boldsymbol{E} = j\omega\dot{\mu}\boldsymbol{J}_i + \frac{1}{\dot{\epsilon}} \nabla \rho_{e,i} + \nabla \times \boldsymbol{M}_i, \tag{4.5a}$$

$$\nabla^2 \boldsymbol{H} + k^2 \boldsymbol{H} = -\nabla \times \boldsymbol{J}_i + j\omega\dot{\epsilon}\boldsymbol{M}_i + \frac{1}{\dot{\mu}} \nabla \rho_{m,i}. \tag{4.5b}$$

In all the above equations we have used the subscript i to indicate impressed sources and formulated the EM wave equations for incident fields, produced by the impressed sources, that propagate in a homogeneous medium taking into account all losses (dielectric, magnetic, conductive), hence the dotted permittivity and permeability. Furthermore, from now on we drop the subscript i and the dots from the permittivity and the permeability for generality, since, the same equations can be applied either for impressed sources yielding incident fields or for equivalent sources yielding scattered fields. Finally, it should be noted that the electric current/charge densities can represent either real (impressed) or fictitious (equivalent) sources, but the magnetic current/charge densities always represent fictitious sources (either impressed or equivalent).

4.1.2 Dyadic Green's Functions

The EM wave equations can be solved with the help of Green's functions [191, 200–202]. The Green's function method is a generalization of a technique presented by George Green [203] for the solution of the electrostatic scalar potential Poisson equation. Green's functions represent the impulse response of a linear differential equation operator where for the vector wave case impulse responses are the fundamental electric and magnetic dipole current sources. Green's functions are exact propagators of the EM field from a source point $\boldsymbol{r}'$ to an observation point $\boldsymbol{r}$, hence, grid dispersion error that arises on partial differential equation methods does not exist for IE methods [16, 30]. Hence, EM fields at an observation point can be expressed as superposition integrals of the electric/magnetic current sources multiplied by the corresponding Green's function, where the integration is carried out over the domain that the sources are immersed, as a direct consequence of the linearity of Maxwell equations.

In particular, Eq. 4.3 can be solved if we consider the dyadic equation:

$$\nabla \times \nabla \times \bar{\boldsymbol{G}}(\boldsymbol{r}, \boldsymbol{r}') - k^2 \bar{\boldsymbol{G}}(\boldsymbol{r}, \boldsymbol{r}') = \bar{\boldsymbol{I}} \delta(\boldsymbol{r} - \boldsymbol{r}'), \tag{4.6}$$

where $\bar{\boldsymbol{I}}$ is the unit dyadic and $\bar{\boldsymbol{G}}$ is the DGF for a homogeneous medium that satisfies the radiation condition to infinity:

$$\lim_{r \to \infty} r \left[jk\bar{\boldsymbol{G}} + \hat{\boldsymbol{r}} \times (\nabla \times \bar{\boldsymbol{G}}) \right] = 0. \tag{4.7}$$

Then, the DGF takes the form [109]:

$$\bar{\boldsymbol{G}}(\boldsymbol{r}, \boldsymbol{r}') = \left(\bar{\boldsymbol{I}} + \frac{\nabla\nabla}{k^2} \right) g(\boldsymbol{r}, \boldsymbol{r}'), \tag{4.8}$$

where

$$g(\boldsymbol{r}, \boldsymbol{r}') = \frac{e^{-jk|\boldsymbol{r} - \boldsymbol{r}'|}}{4\pi |\boldsymbol{r} - \boldsymbol{r}'|}, \tag{4.9}$$

is the scalar wave Green's function in a homogeneous medium that is the fundamental solution of the scalar wave equation:

$$\nabla^2 g(\boldsymbol{r}, \boldsymbol{r}') + k^2 g(\boldsymbol{r}, \boldsymbol{r}') = -\delta(\boldsymbol{r} - \boldsymbol{r}'), \tag{4.10}$$

which also satisfies the radiation condition:

$$\lim_{r \to \infty} r \left[jkg + \frac{\partial g}{\partial r} \right] = 0. \tag{4.11}$$

Subsequently, the EM fields can be expressed as superposition integrals of the DGF multi-

plied by the corresponding terms in Eq. 4.3 as:

$$\boldsymbol{E}(\boldsymbol{r}) = -j\omega\mu \int\limits_{V'} \bar{\boldsymbol{G}}(\boldsymbol{r},\boldsymbol{r}') \cdot \boldsymbol{J}(\boldsymbol{r}')dV' - \int\limits_{V'} \nabla \times \bar{\boldsymbol{G}}(\boldsymbol{r},\boldsymbol{r}') \cdot \boldsymbol{M}(\boldsymbol{r}')dV', \tag{4.12a}$$

$$\boldsymbol{H}(\boldsymbol{r}) = \int\limits_{V'} \nabla \times \bar{\boldsymbol{G}}(\boldsymbol{r},\boldsymbol{r}') \cdot \boldsymbol{J}(\boldsymbol{r}')dV' - j\omega\epsilon \int\limits_{V'} \bar{\boldsymbol{G}}(\boldsymbol{r},\boldsymbol{r}') \cdot \boldsymbol{M}(\boldsymbol{r}')dV', \tag{4.12b}$$

and of the scalar Green's function multiplied by the corresponding terms in Eq. 4.5, as:

$$\boldsymbol{E}(\boldsymbol{r}) = -j\omega\mu \int\limits_{V'} g(\boldsymbol{r},\boldsymbol{r}')\boldsymbol{J}(\boldsymbol{r}')dV' - \frac{1}{\epsilon}\nabla \int\limits_{V'} g(\boldsymbol{r},\boldsymbol{r}')\rho_e(\boldsymbol{r}')dV' - \nabla \times \int\limits_{V'} g(\boldsymbol{r},\boldsymbol{r}')\boldsymbol{M}(\boldsymbol{r}')dV', \tag{4.13a}$$

$$\boldsymbol{H}(\boldsymbol{r}) = \nabla \times \int\limits_{V'} g(\boldsymbol{r},\boldsymbol{r}')\boldsymbol{J}(\boldsymbol{r}')dV' - j\omega\epsilon \int\limits_{V'} g(\boldsymbol{r},\boldsymbol{r}')\boldsymbol{M}(\boldsymbol{r}')dV' - \frac{1}{\mu}\nabla \int\limits_{V'} g(\boldsymbol{r},\boldsymbol{r}')\rho_m(\boldsymbol{r}')dV'. \tag{4.13b}$$

Here, by using the continuity equations in 2.18, the electric/magnetic charges can be eliminated and we end up having only electric/magnetic currents as follows:

$$\boldsymbol{E}(\boldsymbol{r}) = -j\omega\mu \int\limits_{V'} g(\boldsymbol{r},\boldsymbol{r}')\boldsymbol{J}(\boldsymbol{r}')dV' + \frac{1}{j\omega\epsilon}\nabla \int\limits_{V'} g(\boldsymbol{r},\boldsymbol{r}')\nabla' \cdot \boldsymbol{J}(\boldsymbol{r}')dV' - \nabla \times \int\limits_{V'} g(\boldsymbol{r},\boldsymbol{r}')\boldsymbol{M}(\boldsymbol{r}')dV', \tag{4.14a}$$

$$\boldsymbol{H}(\boldsymbol{r}) = \nabla \times \int\limits_{V'} g(\boldsymbol{r},\boldsymbol{r}')\boldsymbol{J}(\boldsymbol{r}')dV' - j\omega\epsilon \int\limits_{V'} g(\boldsymbol{r},\boldsymbol{r}')\boldsymbol{M}(\boldsymbol{r}')dV' - \frac{1}{j\omega\mu}\nabla \int\limits_{V'} g(\boldsymbol{r},\boldsymbol{r}')\nabla' \cdot \boldsymbol{M}(\boldsymbol{r}')dV'. \tag{4.14b}$$

Furthermore, the individual matrix components of the DGF are defined as [109]:

$$\bar{\boldsymbol{G}}(\boldsymbol{r},\boldsymbol{r}') = \frac{1}{k^2}\begin{bmatrix} k^2 + \frac{\partial^2}{\partial x^2} & \frac{\partial^2}{\partial x \partial y} & \frac{\partial^2}{\partial x \partial z} \\ \frac{\partial^2}{\partial y \partial z} & k^2 + \frac{\partial^2}{\partial y^2} & \frac{\partial^2}{\partial y \partial z} \\ \frac{\partial^2}{\partial z \partial x} & \frac{\partial^2}{\partial z \partial y} & k^2 + \frac{\partial^2}{\partial z^2} \end{bmatrix} g(\boldsymbol{r},\boldsymbol{r}'), \tag{4.15a}$$

$$\nabla \times \bar{\boldsymbol{G}}(\boldsymbol{r},\boldsymbol{r}') = \begin{bmatrix} 0 & -\frac{\partial}{\partial z} & \frac{\partial}{\partial y} \\ \frac{\partial}{\partial z} & 0 & -\frac{\partial}{\partial x} \\ -\frac{\partial}{\partial y} & \frac{\partial}{\partial x} & 0 \end{bmatrix} g(\boldsymbol{r},\boldsymbol{r}'), \tag{4.15b}$$

where the first partial derivative of the scalar Green's function is given as:

$$\frac{\partial g}{\partial a} = -(a - a')\left(\frac{1}{|\boldsymbol{r} - \boldsymbol{r}'|^2} + \frac{jk}{|\boldsymbol{r} - \boldsymbol{r}'|}\right) g(\boldsymbol{r},\boldsymbol{r}'), \tag{4.16}$$

the second as:

$$\frac{\partial^2 g}{\partial a^2} = \left[3\frac{(a-a')^2}{|\boldsymbol{r}-\boldsymbol{r}'|^4} + 3jk\frac{(a-a')^2}{|\boldsymbol{r}-\boldsymbol{r}'|^3} - \frac{1+k^2(a-a')^2}{|\boldsymbol{r}-\boldsymbol{r}'|^2} - \frac{jk}{|\boldsymbol{r}-\boldsymbol{r}'|}\right] g(\boldsymbol{r},\boldsymbol{r}'), \tag{4.17}$$

where $a \in \{x, y, z\}$, and the mixed derivative as:

$$\frac{\partial^2 g}{\partial a \partial b} = \left[3\frac{(a-a')(b-b')}{|\boldsymbol{r}-\boldsymbol{r}'|^4} + 3jk\frac{(a-a')(b-b')}{|\boldsymbol{r}-\boldsymbol{r}'|^3} - k^2\frac{(a-a')(b-b')}{|\boldsymbol{r}-\boldsymbol{r}'|^2}\right] g(\boldsymbol{r},\boldsymbol{r}'), \tag{4.18}$$

where $\{a, b\} \in \{x, y, z\}$ and $a \neq b$. Many times, however, the DGF are written in a more compact form as [109]:

$$\begin{aligned}\bar{\boldsymbol{G}}(\boldsymbol{r},\boldsymbol{r}') = \bar{\boldsymbol{I}}\left(-\frac{1}{k^2|\boldsymbol{r}-\boldsymbol{r}'|^2} - \frac{j}{k|\boldsymbol{r}-\boldsymbol{r}'|} + 1\right) g(\boldsymbol{r},\boldsymbol{r}') \\ + (\boldsymbol{r}-\boldsymbol{r}')(\boldsymbol{r}-\boldsymbol{r}')\left(\frac{3}{k^2|\boldsymbol{r}-\boldsymbol{r}'|^4} + \frac{3j}{k|\boldsymbol{r}-\boldsymbol{r}'|^3} - \frac{1}{|\boldsymbol{r}-\boldsymbol{r}'|^2}\right) g(\boldsymbol{r},\boldsymbol{r}'),\end{aligned} \tag{4.19}$$

$$\nabla \times \bar{\boldsymbol{G}}(\boldsymbol{r},\boldsymbol{r}') = \nabla g(\boldsymbol{r},\boldsymbol{r}') \times \bar{\boldsymbol{I}} = -(\boldsymbol{r}-\boldsymbol{r}') \times \bar{\boldsymbol{I}}\left(\frac{1}{|\boldsymbol{r}-\boldsymbol{r}'|^2} + \frac{jk}{|\boldsymbol{r}-\boldsymbol{r}'|}\right) g(\boldsymbol{r},\boldsymbol{r}'). \tag{4.20}$$

From the above equations, it can be clearly seen that DGF are singular when the source and observation points coincide. Specifically, $\bar{\boldsymbol{G}}$ has a $1/|\boldsymbol{r}-\boldsymbol{r}'|^3$ singularity, while $\nabla \times \bar{\boldsymbol{G}}$ is smoother with $1/|\boldsymbol{r}-\boldsymbol{r}'|^2$ singularity. In the next sections, we will discuss in detail how to treat the Green's functions kernels singularity and compute the associated strongly and weakly singular integrals in a Galerkin MoM and in Chapter 5, we will exploit the smoothing property of the Green's function for remote source and observation points interactions [66, 145], use this property for generating a numerical EM fields basis and present how such basis can be used to extract performance bounds for MR RF coils inside realistic head models and ICP for arbitrary coil substrates. Finally, simply by substituting $k = k_0$ the free-space Green's functions are derived and by setting $\mu = \mu_0$ and $\epsilon = \epsilon_0$ the corresponding EM fields that propagate in free-space can be computed from Eq. 4.12, 4.13, or 4.14.

4.2 Surface Integral Equations

4.2.1 Electric and Magnetic Field Integral Equations

SIE methods can be primarily used for modeling impenetrable scatterers, i.e., perfect electric conductors (PEC) or perfect magnetic conductors (PMC), which are structures into which no EM energy penetrates when irradiated by a source placed in the exterior space [204]. SIE methods can also be applied for penetrable objects [205–208], however, such methods are outside the scope of this thesis, since the RF coils of an MR scanner are metallic scatterers

and are considered PEC.

Solving a scattering problem with the help of IE methods, starts with the separation of the total EM fields into incident and scattered fields, where the incident fields are EM fields due to the impressed sources/excitations in the absence of the scatterer and the scattered fields are fields due to the equivalent current sources. The incident fields can be computed by applying Eq. 4.12 and the scattered EM fields again by the same equation where instead of impressed current sources one has to use equivalent current sources. For the case of EM scattering from an infinitesimal conducting surface S, the equivalent current sources are defined onto a "mathematical" surface S^+ that surrounds the conducting surface S. In the limiting case, as the surface S^+ surrounds more tightly the conducting surface S and eventually coincides with it and by applying the appropriate boundary conditions and the extinction theorem [109, 116, 204], the equivalent current sources on surface S^+ take the form [204]:

$$\boldsymbol{J}_{\mathrm{eq}} = \hat{\boldsymbol{n}} \times \boldsymbol{H}, \tag{4.21a}$$

$$\boldsymbol{M}_{\mathrm{eq}} = -\hat{\boldsymbol{n}} \times \boldsymbol{E}, \tag{4.21b}$$

and these currents produce scattered fields such as the total fields are $\boldsymbol{E}$ and $\boldsymbol{H}$ outside S^+ and zero inside S^- [109]. On the surface of a PEC $\hat{\boldsymbol{n}} \times \boldsymbol{E} = 0$, so no equivalent magnetic currents exist and only the equivalent electric currents are sufficient to represent the electric field as:

$$\left.\begin{array}{ll} \boldsymbol{r} \in V_1, & \boldsymbol{E}(\boldsymbol{r}) \\ \boldsymbol{r} \in V_2, & 0 \end{array}\right\} = \boldsymbol{E}_{\mathrm{inc}}(\boldsymbol{r}) - j\omega\mu \int\limits_{S^+} \bar{\boldsymbol{G}}(\boldsymbol{r}, \boldsymbol{r}') \cdot \boldsymbol{J}_{\mathrm{eq}}(\boldsymbol{r}') dS', \tag{4.22}$$

where V_1 is the volume outside surface S and V_2 is the volume that the surface S encloses, as seen in Figure 4.1. The corresponding equation for the magnetic filed is given by taking the curl of the above equation as:

$$\left.\begin{array}{ll} \boldsymbol{r} \in V_1, & \boldsymbol{H}(\boldsymbol{r}) \\ \boldsymbol{r} \in V_2, & 0 \end{array}\right\} = \boldsymbol{H}_{\mathrm{inc}}(\boldsymbol{r}) + \int\limits_{S^+} \nabla \times \bar{\boldsymbol{G}}(\boldsymbol{r}, \boldsymbol{r}') \cdot \boldsymbol{J}_{\mathrm{eq}}(\boldsymbol{r}') dS', \tag{4.23}$$

Then it is straightforward to derive the SIE for scattering by applying the extinction theorem for the electric and magnetic field respectively as [204]:

$$\boldsymbol{E}_{\mathrm{inc}}(\boldsymbol{r}) = j\omega\mu \int\limits_{S^+} \bar{\boldsymbol{G}}(\boldsymbol{r}, \boldsymbol{r}') \cdot \boldsymbol{J}_{\mathrm{eq}}(\boldsymbol{r}') dS, \tag{4.24a}$$

$$\boldsymbol{H}_{\mathrm{inc}}(\boldsymbol{r}) = -\int\limits_{S^+} \nabla \times \bar{\boldsymbol{G}}(\boldsymbol{r}, \boldsymbol{r}') \cdot \boldsymbol{J}_{\mathrm{eq}}(\boldsymbol{r}') dS', \tag{4.24b}$$

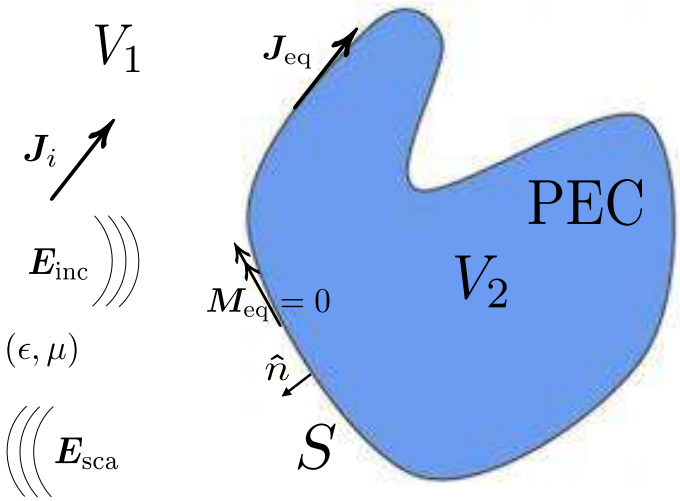

Figure 4.1: Scattering by a perfect electric conductor immersed in a homogeneous medium.

where $\boldsymbol{r} \in S$. Since the tangential component of the electric field is zero for a PEC it is sufficient to include only the tangential components of the above equations and by substituting the equivalent EM fields as in Eq. 4.14 we derive [209]:

$$\hat{\boldsymbol{n}} \times \boldsymbol{E}_{\text{inc}}(\boldsymbol{r}) = \hat{\boldsymbol{n}} \times \left\{ j\omega\mu \int_{S'} g(\boldsymbol{r}, \boldsymbol{r}') \boldsymbol{J}_{\text{eq}}(\boldsymbol{r}') dS' - \frac{1}{j\omega\epsilon} \nabla \int_{S'} g(\boldsymbol{r}, \boldsymbol{r}') \nabla' \cdot \boldsymbol{J}_{\text{eq}}(\boldsymbol{r}') dS' \right\}, \tag{4.25a}$$

$$\hat{\boldsymbol{n}} \times \boldsymbol{H}_{\text{inc}}(\boldsymbol{r}) = -\hat{\boldsymbol{n}} \times \int_{S'} \nabla g(\boldsymbol{r}, \boldsymbol{r}') \times \boldsymbol{J}_{\text{eq}}(\boldsymbol{r}') dS'. \tag{4.25b}$$

These equations are the so-called electric field integral equation (EFIE) and magnetic field integral equation (MFIE) for a PEC. It should be noted that EFIE is valid for both open and closed surfaces while MFIE can only be written for closed surfaces [204] hence when modeling flat surfaces, such as for the case of the RF coils, EFIE is the only suitable choice and then the total surface current is the sum of the surface currents on both sides of the open surface. Another differentiating factor that is connected with the previous is that the currents on the PEC produce a discontinuous magnetic field across the surface whereas the electric field is continuous. Additionally, MFIE has a $1/|\boldsymbol{r} - \boldsymbol{r}'|^2$ singularity according to Eq. 4.25, and usually the principal value of the integral is used [204, 210, 211] and MFIE is rewritten as:

$$\hat{\boldsymbol{n}} \times \boldsymbol{H}_{\text{inc}}(\boldsymbol{r}) = \left(1 - \frac{\Omega_0(\boldsymbol{r})}{4\pi}\right) \boldsymbol{J}_{\text{eq}}(\boldsymbol{r}) - \hat{\boldsymbol{n}} \times \text{P.V.} \int_{S'} \nabla g(\boldsymbol{r}, \boldsymbol{r}') \times \boldsymbol{J}_{\text{eq}}(\boldsymbol{r}') dS', \tag{4.26}$$

where Ω_0 is the solid angle [210, 211] which for the case of a smooth surface is 2π and the coefficient in front of the current is $1/2$. According to the above equation, MFIE is

characterized as a second-kind integral equation, since the unknown current appears both inside and outside of the integral, whereas EFIE is characterized as a first-kind integral equation since the current only appears inside the integral. Finally, both EFIE and MFIE break down when the operating frequency is close to the internal resonance frequencies of the PEC cavity.

4.2.2 Discretization Considerations

Rao-Wilton-Glisson Basis Functions

In order to numerically solve an IE the most commonly used method is the MoM [61], where the continuous integral equation is transformed into a discrete system of equations. The first step of the MoM is to expand the unknown function, which for the case of both EFIE and MFIE are the equivalent electric currents, into a finite set of vector basis/expansion functions:

$$\boldsymbol{J}_{\mathrm{eq}}(\boldsymbol{r}) \approx \sum_{n=1}^{N} j_n \boldsymbol{f}_n(\boldsymbol{r}), \tag{4.27}$$

where j_n are the unknown coefficients that are sought after, $\boldsymbol{f}_n(\boldsymbol{r})$ are the known vector basis/expansion functions, that ideally have to be orthonormal to each other, and N is the dimension of the basis that corresponds to the number of degrees of freedom for a discretized IE. The most commonly known basis functions that are broadly used in the numerical solution of EFIE and MFIE over triangular grids are the RWG [62] basis functions. Each RWG basis function is defined for a pair of adjacent triangular elements of the grid and corresponds to this pair's internal, common edge n. In this way, it is identically zero outside of triangles that share a common edge and it yields an accurate representation of the equivalent current, free of line or point charges. In particular, RWG are defined as [62]:

$$\boldsymbol{f}_n(\boldsymbol{r}) = \begin{cases} \frac{l_n}{2A_n^+}\boldsymbol{\rho}_n^+, & \boldsymbol{r} \in T_n^+ \\ \frac{l_n}{2A_n^-}\boldsymbol{\rho}_n^-, & \boldsymbol{r} \in T_n^- \\ 0, & \text{otherwise} \end{cases}, \tag{4.28}$$

where l_n is the length of the common edge, $A_n^{\pm}$ is the area of the triangular element $T_n^{\pm}$, and $\boldsymbol{\rho}_n^{\pm}$ is the position vector defined with respect to the free vertex of $T_n^{\pm}$ (Figure 4.2).

RWG basis functions approximate the continuous electric and magnetic surface current densities and have the following characteristics [62]: The current does not have a normal component to the boundary of the surface formed by the pair of triangles, except their common edge, and hence no line charges arise. The normal to the common edge current component is continuous across the edge since the normal component of $\boldsymbol{\rho}_n^{\pm}$ is equal to the height of each triangle, as seen in Figure 4.2. That is the reason why in Eq. 4.28 the normalization factor

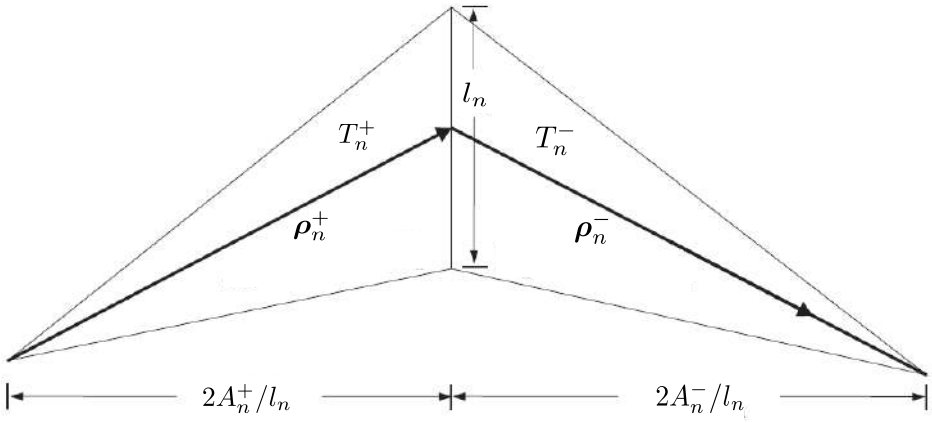

Figure 4.2: Rao-Wilton-Glisson basis function on a pair of adjacent triangular elements [4].

$l_n/2A_n^{\pm}$ is introduced in order for the normal current component to be equal to 1. Finally, the surface divergence of RWG, which is proportional to the surface charge density according to the continuity equations 2.18, is given as:

$$\nabla_s \cdot \boldsymbol{f}_n(\boldsymbol{r}) = \begin{cases} +\frac{l_n}{A_n^+}, & \boldsymbol{r} \in T_n^+ \\ -\frac{l_n}{A_n^-}, & \boldsymbol{r} \in T_n^- \\ 0, & \text{otherwise} \end{cases} . \tag{4.29}$$

In this way, the surface charge density is constant in each triangular element and the total surface charge density in a pair of elements is zero. All these properties have made RWG basis functions a very popular choice for discretizing EFIE, where the equivalent current density can be expressed with the aid of Eq. 4.27, where N now is the number of internal edges of the surface and the unknown coefficients j_n represent the normal current component that flows through this particular edge, which for the boundary edges of open surfaces is zero.

Method of Moments Matrix

Having defined the basis/expansion functions, the next step for the MoM is to find an appropriate set of testing/weight functions w_m. Depending on the choice of the basis/expansion and testing/weight functions, MoM can be formulated with the following variations. Point matching method, where the testing functions of choice are Dirac delta functions and in this way the residual between the exact and approximate solution is enforced to be zero at a specific discrete set of arbitrary points. Collocation method, where the unknown function is approximated by N piece-wise basis functions, usually PWC, that are nonzero only inside a specific subdomain. Galerkin method, where the basis and testing functions are the same and the residual between the exact and approximate solution is enforced to be zero in an average/weighted sense, over the subdomain that the testing functions are defined. Subse-

quently, in order to formulate a Galerkin MoM for SIE methods, the following symmetric inner product has to be defined:

$$\langle \boldsymbol{f}, \boldsymbol{g} \rangle_S = \int_S \boldsymbol{f}^*(\boldsymbol{r}) \cdot \boldsymbol{g}(\boldsymbol{r}) dS. \tag{4.30}$$

Then, the Galerkin MoM with RWG basis functions of the EFIE in Eq. 4.24 will take the following form:

$$\langle \boldsymbol{f}_m(\boldsymbol{r}), \hat{\boldsymbol{n}} \times \boldsymbol{E}_{\text{inc}}(\boldsymbol{r}) \rangle_S = j\omega\mu \sum_{n=1}^{N} j_n \langle \boldsymbol{f}_m(\boldsymbol{r}), \int_{S'} \hat{\boldsymbol{n}} \times \bar{\boldsymbol{G}}(\boldsymbol{r}, \boldsymbol{r}') \cdot \boldsymbol{f}_n(\boldsymbol{r}') dS' \rangle_S, \tag{4.31}$$

where $m = \{1, ..., N\}$, $\boldsymbol{f}_m = \boldsymbol{f}_n$ are the RWG basis functions and in this way a linear system of equations is formulated with j_n as the unknowns. It should be noted that the above equation is mentioned for illustrating how the Galerkin MoM is derived and usually the EFIE impedance matrix tested and expanded with RWG functions for a PEC is given in a more computationally convenient form by using Eq. 4.25, the div-conforming property of RWG basis function, and vector calculus identities [4, 62, 109]:

$$Z_{mn}^E = j\omega\mu \int_S \boldsymbol{f}_m(\boldsymbol{r}) \cdot \int_{S'} \boldsymbol{f}_n(\boldsymbol{r}') g(\boldsymbol{r}, \boldsymbol{r}') dS' dS + \frac{1}{j\omega\epsilon} \int_S \nabla_s \cdot \boldsymbol{f}_m(\boldsymbol{r}) \int_{S'} \nabla'_s \cdot \boldsymbol{f}_n(\boldsymbol{r}') g(\boldsymbol{r}, \boldsymbol{r}') dS' dS, \tag{4.32a}$$

$$b_m = \int_S \boldsymbol{f}_m(\boldsymbol{r}) \cdot \boldsymbol{E}_{\text{inc}}(\boldsymbol{r}) dS, \tag{4.32b}$$

where b_m is the right-hand side and now the $\nabla\nabla$ dyadic operator does not act on the scalar Green's function but on the RWG functions. Hence, we obtain a linear system of equations, $\mathbf{Z}^E\mathbf{j} = \mathbf{b}$, which presents weak singularity ($1/|\boldsymbol{r} - \boldsymbol{r}'|$), governed by g, for triangular elements that coincide or are adjacent. However, MFIE presents strong singularity ($1/|\boldsymbol{r} - \boldsymbol{r}'|^2$), governed by ∇g, and its impedance matrix is given as:

$$Z_{mn}^M = \frac{1}{2} \int_S \boldsymbol{f}_m(\boldsymbol{r}) \cdot \boldsymbol{f}_n(\boldsymbol{r}) dS - \int_S \hat{\boldsymbol{n}} \times \boldsymbol{f}_m(\boldsymbol{r}) \cdot \int_{S'} \nabla g(\boldsymbol{r}, \boldsymbol{r}') \times \boldsymbol{f}_n(\boldsymbol{r}') dS' dS. \tag{4.33}$$

Singular Integrals

Thankfully, in the literature there has been a rich investigative activity that has led to the development of well-established sophisticated cubatures [146–150, 153–160] that compute accurately both weakly and strongly singular and near-singular integrals over triangular planar or curvilinear patches that arise in SIE methods. The surface-surface integrals for non-

coinciding and non-adjacent triangular elements can be computed by means of standard Gauss quadrature rules. Additionally, discretizing MFIE with RWG basis functions does not necessarily yield an accurate approximation, as in the EFIE case, thus, there have been suggested alternative schemes in the literature [212–218], including its testing with $\hat{\boldsymbol{n}} \times \boldsymbol{f}_m$.

Internal Resonance Problem

Except for the singular integrals that arise in SIE methods, EFIE also suffers from an internal resonance problem. In particular, since it is imposed on the surface of the scatterer, it cannot differentiate whether the scatterer is a solid or a shell PEC object, and the latter is a resonance cavity whose resonance modes can be excited. In fact, this happens due to the approximation of the continuous shell with a triangular grid, hence, EM energy leaks into the shell that gives rise to resonance phenomena, when the operating frequency is close to the object's resonance frequency, which is purely real for a lossless medium. Such internal resonance, generates a spurious equivalent current and leaks energy into the exterior space that further generates erroneous scattered fields in the exterior space [204]. Additionally, since the arising spurious current, due to the internal resonance, belongs to the null space of EFIE, the MoM matrix becomes ill-conditioned, hindering the convergence of an iterative solver. A solution to this problem is to formulate EFIE in way that the EM fields in the exterior space remain the same but the interior EM fields correspond to a lossy medium resonance with a complex resonance frequency [219, 220] which does not coincide with the real operating frequency and in this way the internal resonances naturally attenuate. Another alternative is to formulate the problem in terms of a combined field integral equation (CFIE),

$$\text{CFIE} = a\text{EFIE} + \sqrt{\mu/\epsilon}(1-a)\text{MFIE}, \tag{4.34}$$

in a way that an effective lossy boundary condition is applied [220, 221] and subsequently the null space of CFIE occurs at a complex frequency. Special care should be taken when formulating CFIE in order to entail a lossy and non reactive boundary condition, otherwise real resonance frequencies arise with their associated ill-conditioning.

Low Frequency Breakdown

Finally, EFIE suffers from the so-called low frequency breakdown problem that also occurs when the maximum dimension of the scatterer is much smaller than the operating wavelength and is a broader problem that arises not only to IE methods but also to partial differential equation methods that it is associated with the behavior of EM fields when $\omega \to 0$ [204, 209]. As it can be immediately seen from Eqs. 4.13, 4.14, and 4.25, the electric field due to the electric current $\boldsymbol{J}$ is directly proportional to the frequency whereas the electric field due to the electric charge, or equivalently due to $\nabla \cdot \boldsymbol{J}$, is inversely proportional to

the frequency, according to the continuity equation. Consequently, as $\omega \to 0$, the scattered electric field mainly originates from electric charges and the contribution of the electric current goes to zero, due to the limited machine precision of a computer. As a result, the MoM matrix becomes ill-conditioned [209], and in the limiting case, when $\omega = 0$, singular, leading to a slow or non at all convergence of an iterative solver. The same phenomenon happens when EFIE is h-refined and the size of the elements of the computational grid becomes increasingly smaller than the operating wavelength, leading to an increase in the condition number and a slower convergence of an iterative solver. However, MFIE does not suffer from such ill-conditioning, since it is a second-kind integral equation and the identity operator added in front of the strongly singular integral operator prevents the eigenvalues of the impedance matrix to go zero, as the grid is refined.

According to Maxwell equations, as $\omega \to 0$, the electric and the magnetic fields become decoupled and this is reflected to the currents behavior, as well. In particular, the current that produces the magnetic field becomes divergence-free or solenoid ($\boldsymbol{J}_{\text{sol}}$), whereas the current that produces the charges, and, hence, the corresponding electric field, becomes curl-free or irrrotational ($\boldsymbol{J}_{\text{irr}}$) and its divergence should tend linearly to zero, in order for the charge to be bounded, according to the continuity equation [222]. This procedure is called Helmholtz decomposition [223] and such decoupling can be used to tackle the low frequency breakdown problem. RWG basis functions do not account for such behavior and EFIE breaks down at low frequencies, however, in the literature there have been suggested plenty of solutions for this problem including the loop-star basis functions [224, 225], the loop-patch basis functions [226], basis functions with separated Fourier spectra where diagonal precondinioters significantly reduce the condition number [227], and a natural multiplicative Calderón precondinioter [228].

Summary

At this point, it may seem that we have somehow deviated from the main goal this thesis aims to tackle, i.e., modeling the RF coils and biological tissue interactions and computing RF coils performance bounds, but SIE methods and in particular EFIE is an excellent choice for modeling the flat coil conductors [65] with its associated natural coupling with VIE methods, as we have described at the beginning of this chapter and in Chapter 2 and as it have been incorporated in MARIE [64]. Furthermore, RWG basis functions can be used in order to discretize a fully enclosed spherical shell and generate a complete numerical EM fields basis, as we will show in Chapter 5. Finally, the main physical principles and numerical problems that arise in SIE methods e.g., complicated singular integrals, low frequency breakdown, correct choice of the function space that the basis and testing functions should span, slower convergence with h-refinement, internal resonances at the eigenfrequencies of the scatterer, among others, are relevant at VIE methods, too, and they are carefully taken into account

and discussed in the next section as we describe the development of our novel current-based PWL solver [76, 77] for computing EM scattering from highly inhomogeneous media such as the biological tissue.

4.3 Volume Integral Equations

Unlike SIE methods, that can be applied to compute EM scattering from homogeneous media or when the inhomogeneity is PWC, VIE methods are usually used for computing EM scattering from highly inhomogeneous media, such as the human body. The development, however, of an efficient and stable numerical EM simulation solver based on VIE methods is far from being a trivial task. Towards that direction, there has been a recent contribution [60], where a stable current-based VIE solver with PWC basis functions has been developed and incorporated into MARIE [229] for the fast EM analysis of MR coils. However, in the MR modeling case, there is an internal limitation with respect to the spatial resolution and thus the grid refinements in a numerical solver. This naturally leads to the exploitation of p-refinement techniques for achieving more reliable solutions in a VIE-based solver, too.

In this section, we modify the aforementioned current-based VIE solver [60] and equip it with higher-order basis functions, that yield more accurate results for modeling highly inhomogeneous and high contrast objects, without the need of refining the mesh. Namely, discontinuous PWL [230, 231] basis and testing functions are utilized and defined with support a single voxel of a uniform grid that allows for the fast calculation of the associated matrix-vector products with the help of FFT, exploiting the block Toeplitz structure of the system's matrix, since the arising integral kernels are translationally invariant. Plenty of research studies exist in the literature regarding this problem [33–57, 232]. Furthermore, the aforementioned equivalent volumetric currents must not necessarily satisfy any continuity conditions between neighboring elements, voxels in our case, allowing for the use of basis and testing functions that span $\mathcal{L}^2$, when employing the Galerkin MoM. This way, the finite-energy conditions are respected and the spectral properties of the operators are preserved, as it has been shown in recent studies [58, 59]. Moreover, the resulting formulation calls for the numerical integration of singular volume-volume Galerkin inner products, but as it has been shown in previous work [76, 233–236], there exist readily available formulas that reduce both the dimensionality and singularity order of the kernels, allowing for the fast and precise numerical evaluation of the singular integrals by means of well-established sophisticated cubatures [146–150, 153–160], originally developed for SIE formulations. Recent contributions have also expanded the analysis for arbitrary quadrilateral patches [151, 152, 158].

Through numerical experiments, we illustrate that the resulting discretized formulation is well-conditioned and has superior convergence properties than the discretized version with PWC approximations and than a more standard VIE formulation based on electric flux den-

sities [57]. Specifically, the number of iterations of the iterative solver remains practically the same as with the case of PWC basis functions and is much smaller than that of the flux-based solver, for highly inhomogeneous scatterers. Another favorable feature of the proposed scheme is its superior accuracy. To demonstrate that, we present a comparative analysis between the PWC and the PWL basis solver for a homogeneous sphere, comparing both solvers with analytical results obtained with Mie series [78], and for realistic head models from the Virtual Family Population [5]. Even when numerically treating the case of dielectric shimming [79], where high-permittivity dielectric pads are placed in the vicinity of a realistic head model, the suggested solver performs effectively. However, naturally, this comes with an increase in the computational cost and in the required memory footprint. Thankfully, the arising Green's function tensors in FFT-based VIEs preserve low multilinear rank properties [237, 238], thus, we can overcome this limiting factor and accelerate the solution of the linear system of equations by combining tensor decompositions and parallel programming techniques of GPUs [163].

The remainder of this section is organized as follows. First, we set up the current-based VIE formulation and describe its superior properties in comparison with other VIE formulations. Then, we introduce the novel discretization scheme with PWL basis functions, formulate the linear system by means of MoM, and represent the system in a tensor format for a better comprehension. Right after, we describe the procedure to accelerate the matrix-vector product and develop a fast FFT-based solver. Finally, we validate the proposed solver by comparison with the analytical solution for spheres and demonstrate its accuracy and convergence properties when modeling the EM scattering from realistic head models.

4.3.1 Volume Integral Equation Formulations for Inhomogeneous Media

We consider the scattering of time-harmonic EM waves by a penetrable, inhomogeneous object, occupying the bounded domain Ω in 3D Euclidean space, $\mathbb{R}^3$. The working angular frequency is $\omega \in \mathbb{R}^+$ and the electrical properties are defined as:

$$\begin{aligned} \dot{\epsilon} &= \epsilon_0, & \dot{\mu} &= \mu_0 & \text{in} \quad & \mathbb{R}^3 \backslash \Omega, \\ \dot{\epsilon} &= \epsilon_0 \dot{\epsilon}_r(\boldsymbol{r}), & \dot{\mu} &= \mu_0 \dot{\mu}_r(\boldsymbol{r}) & \text{in} \quad & \Omega, \end{aligned} \tag{4.35}$$

as seen in Figure 4.3.

Similarly to SIE methods, the total time harmonic fields $(\boldsymbol{E}, \boldsymbol{H})$ in the presence of an isotropic and inhomogeneous object can be decomposed into incident $(\boldsymbol{E}_{\text{inc}}, \boldsymbol{H}_{\text{inc}})$ and scat-

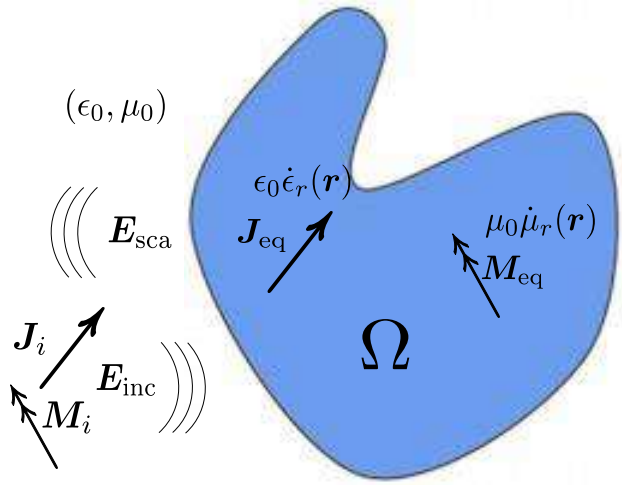

Figure 4.3: Scattering by an inhomogeneous object immersed in free-space.

tered $(\boldsymbol{E}_{\text{sca}}, \boldsymbol{H}_{\text{sca}})$ fields,

$$\begin{pmatrix} \boldsymbol{E} \\ \boldsymbol{H} \end{pmatrix} = \begin{pmatrix} \boldsymbol{E}_{\text{inc}} \\ \boldsymbol{H}_{\text{inc}} \end{pmatrix} + \begin{pmatrix} \boldsymbol{E}_{\text{sca}} \\ \boldsymbol{H}_{\text{sca}} \end{pmatrix}, \tag{4.36}$$

where the incident fields are the fields generated by the impressed currents or the sources in the absence of the scatterer and the scattered fields are given by the induced or equivalent currents due to the presence of the scatterer. Such equivalent volumetric polarization and magnetization currents, according to the volume equivalence principle [109], are defined as:

$$\begin{aligned} \boldsymbol{J}_{\text{eq}}(\boldsymbol{r}) &\triangleq c_e\dot{\chi}_e(\boldsymbol{r})\boldsymbol{E}(\boldsymbol{r}), \\ \boldsymbol{M}_{\text{eq}}(\boldsymbol{r}) &\triangleq c_m\dot{\chi}_m(\boldsymbol{r})\boldsymbol{H}(\boldsymbol{r}), \end{aligned} \tag{4.37}$$

with $\{c_e, c_m\} = \{j\omega\epsilon_0, j\omega\mu_0\}$ and the electric and magnetic susceptibilities are respectively given by

$$\begin{aligned} \dot{\chi}_e(\boldsymbol{r}) &\triangleq \dot{\epsilon}_r(\boldsymbol{r}) - 1, \\ \dot{\chi}_m(\boldsymbol{r}) &\triangleq \dot{\mu}_r(\boldsymbol{r}) - 1. \end{aligned} \tag{4.38}$$

Then according to Eqs. 4.12 and 4.36 and we can derive:

$$\boldsymbol{E}(\boldsymbol{r}) = \boldsymbol{E}_{\text{inc}}(\boldsymbol{r}) - c_m \int_{V'} \bar{\boldsymbol{G}}(\boldsymbol{r}, \boldsymbol{r}') \cdot \boldsymbol{J}_{\text{eq}}(\boldsymbol{r}')dV' - \int_{V'} \nabla \times \bar{\boldsymbol{G}}(\boldsymbol{r}, \boldsymbol{r}') \cdot \boldsymbol{M}_{\text{eq}}(\boldsymbol{r}')dV', \tag{4.39a}$$

$$\boldsymbol{H}(\boldsymbol{r}) = \boldsymbol{H}_{\text{inc}}(\boldsymbol{r}) + \int_{V'} \nabla \times \bar{\boldsymbol{G}}(\boldsymbol{r}, \boldsymbol{r}') \cdot \boldsymbol{J}_{\text{eq}}(\boldsymbol{r}')dV' - c_e \int_{V'} \bar{\boldsymbol{G}}(\boldsymbol{r}, \boldsymbol{r}') \cdot \boldsymbol{M}_{\text{eq}}(\boldsymbol{r}')dV', \tag{4.39b}$$

which is rewritten in a more compact notation commonly used in IE methods [49, 60] as:

$$\begin{pmatrix} \boldsymbol{E} \\ \boldsymbol{H} \end{pmatrix} = \begin{pmatrix} \boldsymbol{E}_{\text{inc}} \\ \boldsymbol{H}_{\text{inc}} \end{pmatrix} + \begin{pmatrix} \frac{1}{c_e}\mathcal{L} & -\mathcal{K} \\ \mathcal{K} & \frac{1}{c_m}\mathcal{L} \end{pmatrix} \begin{pmatrix} \boldsymbol{J}_{\text{eq}} \\ \boldsymbol{M}_{\text{eq}} \end{pmatrix}, \tag{4.40}$$

where the associated continuous integro-differential operators are:

$$\mathcal{L}\boldsymbol{u} \triangleq (k_0^2 + \nabla\nabla\cdot) \int\limits_{\Omega} g(\boldsymbol{r}, \boldsymbol{r}')\boldsymbol{u}(\boldsymbol{r}')d\boldsymbol{r}' = k_0^2 \int\limits_{\Omega} \bar{\boldsymbol{G}}(\boldsymbol{r}, \boldsymbol{r}') \cdot \boldsymbol{u}(\boldsymbol{r}')d\boldsymbol{r}', \tag{4.41a}$$

$$\mathcal{K}\boldsymbol{u} \triangleq \nabla \times \int\limits_{\Omega} g(\boldsymbol{r}, \boldsymbol{r}')\boldsymbol{u}(\boldsymbol{r}')d\boldsymbol{r}' = \int\limits_{\Omega} \nabla \times \bar{\boldsymbol{G}}(\boldsymbol{r}, \boldsymbol{r}') \cdot \boldsymbol{u}(\boldsymbol{r}')d\boldsymbol{r}'. \tag{4.41b}$$

In the literature [40], except for these operators, there has been introduced an additional operator that contains curls instead of divergences:

$$\mathcal{N}\boldsymbol{u} \triangleq \nabla \times \nabla \times \int\limits_{\Omega} g(\boldsymbol{r}, \boldsymbol{r}')\boldsymbol{u}(\boldsymbol{r}')d\boldsymbol{r}' = \int\limits_{\Omega} \nabla \times \nabla \times \bar{\boldsymbol{G}}(\boldsymbol{r}, \boldsymbol{r}') \cdot \boldsymbol{u}(\boldsymbol{r}')d\boldsymbol{r}', \tag{4.42}$$

and its dyadic tensor is given as:

$$\nabla \times \nabla \times \bar{\boldsymbol{G}}(\boldsymbol{r}, \boldsymbol{r}') = \begin{bmatrix} -\frac{\partial^2}{\partial y^2} - \frac{\partial^2}{\partial z^2} & \frac{\partial^2}{\partial x \partial y} & \frac{\partial^2}{\partial x \partial z} \\ \frac{\partial^2}{\partial y \partial x} & -\frac{\partial^2}{\partial x^2} - \frac{\partial^2}{\partial z^2} & \frac{\partial^2}{\partial y \partial z} \\ \frac{\partial^2}{\partial z \partial x} & \frac{\partial^2}{\partial z \partial y} & -\frac{\partial^2}{\partial x^2} - \frac{\partial^2}{\partial y^2} \end{bmatrix} g(\boldsymbol{r}, \boldsymbol{r}'), \tag{4.43}$$

where the partial derivatives are given at Eqs. 4.17 and 4.18. $\mathcal{N}$ operator is also connected with $\mathcal{L}$ operator according to the following identity [40]:

$$\mathcal{L}\boldsymbol{u} = \mathcal{N}\boldsymbol{u} - \boldsymbol{u}, \tag{4.44}$$

which is proven to be useful for both expanding the unknowns in curl-conforming basis functions for the electric field-based VIE [49] and for leaving the identity operator in front of the integral operator in the current-based VIE that allows for the use of a natural preconditioner, as we will describe in the next subsection.

For the case of EM scattering from inhomogeneous media, there exist 3 different formulations [49,51] that we describe below and are derived by combining the constitutive equations 2.13, Eq. 4.37, and Eq. 4.40. First, we define $\mathcal{I}$ as the identity operator and $\mathcal{M}_\phi$ as a multiplication operator that multiplies with the function ϕ as:

$$\mathcal{M}_{\epsilon_r}\boldsymbol{E} = \dot{\epsilon}_r(\boldsymbol{r})\boldsymbol{E}(\boldsymbol{r}), \tag{4.45a}$$

$$\mathcal{M}_{\chi_e}\boldsymbol{E} = \dot{\chi}_e(\boldsymbol{r})\boldsymbol{E}(\boldsymbol{r}), \tag{4.45b}$$

$$\mathcal{M}_{1/\epsilon_r}\boldsymbol{E} = \frac{1}{\dot{\epsilon}_r(\boldsymbol{r})}\boldsymbol{E}(\boldsymbol{r}), \tag{4.45c}$$

where the multiplication operators for the case of the permeability are equivalently defined as $\mathcal{M}_{\mu_r}$, $\mathcal{M}_{\chi_m}$, and $\mathcal{M}_{1/\mu_r}$, thus our notation can be simplified.

The most broadly used formulation is the electric/magnetic flux-based VIE (DB-VIE) formulation [56, 57] having as unknowns the flux densities $\boldsymbol{D}$ and $\boldsymbol{B}$ and takes the form:

$$\begin{pmatrix} \mathcal{I} - \mathcal{L}\mathcal{M}_{\chi_e} & c_e\mathcal{K}\mathcal{M}_{\chi_m} \\ -c_m\mathcal{K}\mathcal{M}_{\chi_e} & \mathcal{I} - \mathcal{L}\mathcal{M}_{\chi_m} \end{pmatrix} \begin{pmatrix} \mathcal{M}_{1/\epsilon_r}\boldsymbol{D} \\ \mathcal{M}_{1/\mu_r}\boldsymbol{B} \end{pmatrix} = \begin{pmatrix} \epsilon_0\boldsymbol{E}_{\text{inc}} \\ \mu_0\boldsymbol{H}_{\text{inc}} \end{pmatrix}. \tag{4.46}$$

The electric/magnetic field-based VIE (EH-VIE) formulation [40,41] has unknowns the field intensities $\boldsymbol{E}$ and $\boldsymbol{H}$ and takes the form:

$$\begin{pmatrix} \mathcal{M}_{\epsilon_r} - \mathcal{N}\mathcal{M}_{\chi_e} & c_m\mathcal{K}\mathcal{M}_{\chi_m} \\ -c_e\mathcal{K}\mathcal{M}_{\chi_e} & \mathcal{M}_{\mu_r} - \mathcal{N}\mathcal{M}_{\chi_m} \end{pmatrix} \begin{pmatrix} \boldsymbol{E} \\ \boldsymbol{H} \end{pmatrix} = \begin{pmatrix} \boldsymbol{E}_{\text{inc}} \\ \boldsymbol{H}_{\text{inc}} \end{pmatrix}. \tag{4.47}$$

Finally, the polarization and magnetization current-based VIE (JM-VIE) formulation [42, 60] has as unknowns the equivalent currents $\boldsymbol{J}_{\text{eq}}$ and $\boldsymbol{M}_{\text{eq}}$ and is written as:

$$\begin{pmatrix} \mathcal{M}_{\epsilon_r} - \mathcal{M}_{\chi_e}\mathcal{N} & c_e\mathcal{M}_{\chi_e}\mathcal{K} \\ -c_m\mathcal{M}_{\chi_m}\mathcal{K} & \mathcal{M}_{\mu_r} - \mathcal{M}_{\chi_m}\mathcal{N} \end{pmatrix} \begin{pmatrix} \boldsymbol{J}_{\text{eq}} \\ \boldsymbol{M}_{\text{eq}} \end{pmatrix} = \begin{pmatrix} c_e\mathcal{M}_{\chi_e}\boldsymbol{E}_{\text{inc}} \\ c_m\mathcal{M}_{\chi_m}\boldsymbol{H}_{\text{inc}} \end{pmatrix}. \tag{4.48}$$

All the above formulations are equivalent to each other with respect to the uniqueness and existence of the solution provided that the permittivity and permeability functions are bounded and coercive [58], however, the convergence of their numerical solution in an iterative solver differs from one another, especially for media with high contrast/inhomogeneity and when one performs h-refinement, as it has been demonstrated in [51] and we further demonstrate in the next subsection. Furthermore, each formulation requires a specific choice of basis and testing functions. Basis functions should respect the continuity conditions of the unknowns across material interfaces and not enforce any additional continuities. Specifically, basis functions for DB-VIE should be div-conforming [53], for EH-VIE curl-conforming [40,239], and for JM-VIE no continuity should be imposed, since the equivalent currents are naturally discontinuous [49]. Testing functions should span the $\mathcal{L}^2$ dual of the range space of the associated operator [49, 58, 59, 240], in order to guarantee convergence in the norm of the solution, hence, it is instructive to examine the mapping properties of each formulation. In particular, the domain and range vector spaces for the 3 formulations read

as:

$$\text{DB-VIE:} \quad \mathcal{H}(div, \mathbb{R}^3) \rightarrow \mathcal{H}(curl, \mathbb{R}^3), \tag{4.49a}$$

$$\text{EH-VIE:} \quad \mathcal{H}(curl, \mathbb{R}^3) \rightarrow \mathcal{H}(div, \mathbb{R}^3), \tag{4.49b}$$

$$\text{JM-VIE:} \quad \left[\mathcal{L}^2(\mathbb{R}^3)\right]^3 \rightarrow \left[\mathcal{L}^2(\mathbb{R}^3)\right]^3, \tag{4.49c}$$

where $\left[\mathcal{L}^2(\mathbb{R}^3)\right]^3$ is the space of square-integrable functions and

$$\mathcal{H}(div, \mathbb{R}^3) = \left\{ \boldsymbol{f} | \boldsymbol{f} \in \left[\mathcal{L}^2(\mathbb{R}^3)\right]^3 \wedge \nabla \cdot \boldsymbol{f} \in \left[\mathcal{L}^2(\mathbb{R}^3)\right]^3 \right\}, \tag{4.50a}$$

$$\mathcal{H}(curl, \mathbb{R}^3) = \left\{ \boldsymbol{f} | \boldsymbol{f} \in \left[\mathcal{L}^2(\mathbb{R}^3)\right]^3 \wedge \nabla \times \boldsymbol{f} \in \left[\mathcal{L}^2(\mathbb{R}^3)\right]^3 \right\}. \tag{4.50b}$$

$\mathcal{H}(div)$ and $\mathcal{H}(curl)$ are $\mathcal{L}^2$ dual to each other and $\mathcal{L}^2$ is dual to itself. Therefore, by applying a Galerkin MoM to the corresponding basis functions, described in the previous paragraph, then the testing functions span the dual of the range space of each formulation.

The focal point of this dissertation revolves around the interactions between EM waves and biological tissue, which can be considered purely dielectric. Therefore, the equivalent magnetization currents are identically zero and the 3 formulations reduce to the following:

$$\text{DVIE:} \quad \left(\mathcal{I} - \mathcal{L}\mathcal{M}_{\chi_e}\right) \mathcal{M}_{1/\epsilon_r} \boldsymbol{D} = \epsilon_0 \boldsymbol{E}_{\text{inc}}, \tag{4.51a}$$

$$\text{EVIE:} \quad \left(\mathcal{M}_{\epsilon_r} - \mathcal{N}\mathcal{M}_{\chi_e}\right) \boldsymbol{E} = \boldsymbol{E}_{\text{inc}}, \tag{4.51b}$$

$$\text{JVIE:} \quad \left(\mathcal{M}_{\epsilon_r} - \mathcal{M}_{\chi_e}\mathcal{N}\right) \boldsymbol{J}_{\text{eq}} = c_e \mathcal{M}_{\chi_e} \boldsymbol{E}_{\text{inc}}. \tag{4.51c}$$

For the case of JVIE the associated EM fields can be computed according to Eq. 4.40, therefore, $\mathcal{K}$ operator should be discretized, as we describe below. Additionally, at JVIE one can notice that the susceptibility multiplication operator $\mathcal{M}_{\chi_e}$ has moved in front of the integro-differential operator, therefore, its numerical differentiation is avoided.

Finally, since biological tissue presents not only high inhomogeneity but high contrast, as well, it is of interest to examine how these 3 VIE formulations behave when $\dot{\epsilon}_r \rightarrow \infty$. Specifically, in the limiting case we get:

$$\lim_{\dot{\epsilon}_r \rightarrow \infty} \text{DVIE:} \; -\mathcal{L}\boldsymbol{D} = \epsilon_0 \boldsymbol{E}_{\text{inc}}, \tag{4.52a}$$

$$\lim_{\dot{\epsilon}_r \rightarrow \infty} \text{EVIE:} \; \left(\mathcal{I} - \mathcal{N}\right) \boldsymbol{E} = 0, \tag{4.52b}$$

$$\lim_{\dot{\epsilon}_r \rightarrow \infty} \text{JVIE:} \; \left(\mathcal{I} - \mathcal{N}\right) \boldsymbol{J}_{\text{eq}} = c_e \boldsymbol{E}_{\text{inc}}. \tag{4.52c}$$

From the above we can notice the following. DVIE becomes a first-kind integral equation with its associated convergence problems with grid refinement. At EVIE the contribution of the incident field vanishes and we end up solving a system of the form $\mathbf{Ax} = 0$ which is physically correct since the electric field should be zero but nontrivial solutions arise due to the existence of null-space. Only JVIE remains a second-kind integral equation therefore it can be considered a well-conditioned formulation as shown in recent studies [49, 51]. It is interesting to note that for the case of free-space, where we set $\dot{\epsilon}_r = 1$, the right-hand side in JVIE becomes zero but the system matrix is diagonal and the problem well-posed [49].

4.3.2 Discretization Scheme

Piece-wise Linear Basis Functions on Voxels

As demonstrated in recent studies and discussed in the previous subsection, the current-based formulation has well-conditioned spectral properties when compared with the other alternatives, i.e., flux- and field-based formulations [49, 58–60]. In order to achieve this superior performance and guarantee convergence in the norm of the solution, when employing a Galerkin projection method, the function space of the basis and testing functions should be carefully chosen [240, 241]. Specifically, the testing functions should span the $\mathcal{L}^2$ dual of the range space of the associated operator and the basis functions should not enforce any continuity condition across the material interfaces or the discretization elements (since the scatterer is inhomogeneous). Therefore, the natural function space of choice both for the basis and testing functions is that of square integrable functions $[\mathcal{L}^2(\mathbb{R}^3)]^3$. All these prerequisites are in accordance with previous work for a current-based VIE with PWC basis functions [60]. However, the nature of the application at hand within the MR field, often requires higher accuracy, especially by means of p-refinement, i.e., using a higher-order approximation of the VIE's unknown which is expected to yield reliable results even for coarser grid resolutions.

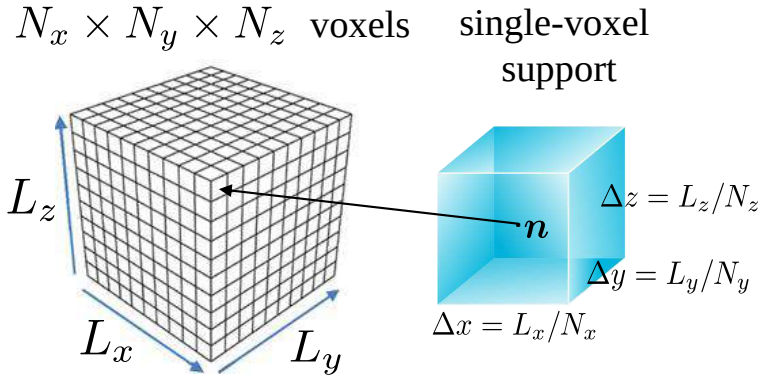

Figure 4.4: Computational domain and volumetric element over which each basis function is defined.

We begin the development of our solver by defining the computational domain and the associated discretization grid. We use a rectangular parallelepiped that encloses the inhomogeneous scatterer but does not have to extend any farther than that, since the radiation conditions at infinity are satisfied by the Green's function. By denoting the dimensions of this rectangular box as L_x, L_y and L_z, we can now discretize it with $N_V = N_x \times N_y \times N_z$ number of voxels (Figure 4.4), which in the general case may be non-uniform and have side length $\Delta x = L_x/N_x$, $\Delta y = L_y/N_y$, and $\Delta z = L_z/N_z$. Having defined the grid, we expand the unknown equivalent polarization and magnetization currents in terms of suitable vector basis functions. The equivalent currents are unlikely to satisfy any continuity conditions because of the material discontinuities and as a result the function space of choice in a Galerkin discretization scheme should be the $[\mathcal{L}^2(\mathbb{R}^3)]^3$. Without loss of generality, we proceed in the following with the expansion only for the polarization currents, since for the magnetization currents the basis functions would be identical,

$$\boldsymbol{J}_{\text{eq}}(\boldsymbol{r}) = J_x(\boldsymbol{r})\hat{\boldsymbol{x}} + J_y(\boldsymbol{r})\hat{\boldsymbol{y}} + J_z(\boldsymbol{r})\hat{\boldsymbol{z}}, \tag{4.53}$$

where each component of the current can be expanded in some discrete set of appropriate basis functions. In this work, we utilize the PWL basis functions, hence the current approximation reads:

$$J_q(\boldsymbol{r}) \approx \sum_{\boldsymbol{n}=(1,1,1)}^{(N_x,N_y,N_z)} \sum_{l=1}^{4} N_{\boldsymbol{n}}^l(\boldsymbol{r}) a_{\boldsymbol{n}}^{ql}, \tag{4.54}$$

where $q \in \{x, y, z\}$ indicates the components of the current, $\boldsymbol{n} = n_x\hat{\boldsymbol{x}} + n_y\hat{\boldsymbol{y}} + n_z\hat{\boldsymbol{z}}$ is a compound index denoting the centers of the voxels in the grid, $N_{\boldsymbol{n}}^l(\boldsymbol{r})$ are the 4 basis functions per current component per voxel, and $a_{\boldsymbol{n}}^{ql}$ are the unknown coefficients. In detail, the scalar basis functions are defined as:

$$N_{\boldsymbol{n}}^1(\boldsymbol{r}) = P_{\boldsymbol{n}}(\boldsymbol{r}), \tag{4.55a}$$

$$N_{\boldsymbol{n}}^2(\boldsymbol{r}) = \frac{x - x_n}{\Delta x} P_{\boldsymbol{n}}(\boldsymbol{r}), \tag{4.55b}$$

$$N_{\boldsymbol{n}}^3(\boldsymbol{r}) = \frac{y - y_n}{\Delta y} P_{\boldsymbol{n}}(\boldsymbol{r}), \tag{4.55c}$$

$$N_{\boldsymbol{n}}^4(\boldsymbol{r}) = \frac{z - z_n}{\Delta z} P_{\boldsymbol{n}}(\boldsymbol{r}), \tag{4.55d}$$

where $\boldsymbol{r}_{\boldsymbol{n}} = (x_n, y_n, z_n)$ is the center of each voxel, $P_{\boldsymbol{n}}(\boldsymbol{r})$ is a volumetric pulse which is equal to 1 inside voxel $\boldsymbol{n}$ and 0 otherwise. From the above, it follows that the PWL basis functions have support a single element (voxel in our case) of the grid (Figure 4.4) allowing for discontinuities between neighboring voxels. The vector-valued basis function at voxel $\boldsymbol{n}$

is:

$$\boldsymbol{f}_{\boldsymbol{n}}(\boldsymbol{r}) = \sum_{q\in\{x,y,z\}} \sum_{l=1}^{4} \boldsymbol{f}_{\boldsymbol{n}}^{ql}(\boldsymbol{r}), \tag{4.56a}$$

$$\boldsymbol{f}_{\boldsymbol{n}}^{ql}(\boldsymbol{r}) = N_{\boldsymbol{n}}^{l}(\boldsymbol{r})\hat{\boldsymbol{q}}, \tag{4.56b}$$

resulting in 12 unknowns per voxel. Finally, the electrical properties of the scatterer are modeled by means of PWC approximations:

$$\dot{\epsilon}_r(\boldsymbol{r}) \approx \sum_{\boldsymbol{n}=(1,1,1)}^{(N_x,N_y,N_z)} \dot{\epsilon}_r(\boldsymbol{r}_{\boldsymbol{n}}) P_{\boldsymbol{n}}(\boldsymbol{r}). \tag{4.57}$$

Utilizing PWL approximations of the electrical properties and studying their potential benefits for highly inhomogeneous scatterers or for the case of absorbers with higher-order polynomial conductivity profiles in photonics simulation with VIE methods [242] could be a subject of future work. However, it is not a part of this work since the linear terms of their approximation would not be able to move outside the testing volume integral, significantly complicating the reduction procedure of the volume-volume integrals to surface-surface integrals [76], that it is described in Appendix C and is a critical and necessary step to compute the singular integrals of the kernels, and they would also interfere with the Toeplitz structure of the operators.

Galerkin Inner Products and Linear System Formalism

In what follows, we describe the required steps to numerically solve the current-based formulation of Eq. 4.51c by means of Galerkin MoM, where the equivalent volumetric currents are expanded in the vector-valued square-integrable basis function of Eq. 4.56 and tested with the same function. At this point, we can form the linear system $\mathbf{A}\mathbf{x} = \mathbf{b}$ with $\mathbf{x}, \mathbf{b} \in \mathbb{C}^N$ and $\mathbf{A} \in \mathbb{C}^{N\times N}$ with $N = 12N_V$. More specifically, the matrix and the right-hand side are given by:

$$\mathbf{A} = \mathbf{M}_{\epsilon_r}\mathbf{G} - \mathbf{M}_{\chi_e}\mathbf{N}, \tag{4.58a}$$

$$\mathbf{b} = c_e\mathbf{M}_{\chi_e}\mathbf{e}_{\mathrm{inc}}, \tag{4.58b}$$

with

$$N_{\boldsymbol{m},\boldsymbol{n}}^{pl,ql'} = \langle \boldsymbol{f}_{\boldsymbol{m}}^{pl}(\boldsymbol{r}), \mathcal{N}\boldsymbol{f}_{\boldsymbol{n}}^{ql'}(\boldsymbol{r})\rangle_V, \tag{4.59a}$$

$$K_{\boldsymbol{m},\boldsymbol{n}}^{pl,ql'} = \langle \boldsymbol{f}_{\boldsymbol{m}}^{pl}(\boldsymbol{r}), \mathcal{K}\boldsymbol{f}_{\boldsymbol{n}}^{ql'}(\boldsymbol{r})\rangle_V, \tag{4.59b}$$

where $p, q \in \{x, y, z\}$, l,$l' \in \{1, 2, 3, 4\}$, $\boldsymbol{m} = m_x\hat{\mathbf{x}} + m_y\hat{\mathbf{y}} + m_z\hat{\mathbf{z}}$ denotes the observation voxel and $\boldsymbol{n}$ the source voxel. Each voxel interacts with each other so $n_x, m_x = 1 : N_x, n_y, m_y = 1 : N_y$ and $n_z, m_z = 1 : N_z$ resulting in the dense matrices $\mathbf{N}, \mathbf{K} \in \mathbb{C}^{N\times N}$, where $\mathcal{K}$ operator is discretized for the computation of the magnetic field, too. Furthermore, $\mathbf{G} \in \mathbb{R}^{N\times N}$ is the associated Gram matrix, which is diagonal, since non-overlapping basis functions are used:

$$G^{pl,ql'}_{\boldsymbol{m},\boldsymbol{n}} = \langle \boldsymbol{f}^{pl}_{\boldsymbol{m}}(\boldsymbol{r}), \boldsymbol{f}^{ql'}_{\boldsymbol{n}}(\boldsymbol{r})\rangle_V. \tag{4.60}$$

Also, $\mathbf{M}_{\epsilon_r}, \mathbf{M}_{\chi_e} \in \mathbb{C}^{N\times N}$ are diagonal matrices for isotropic materials with the nonzero values being equal to the material properties at the corresponding voxels. Finally, the "tested" incident electric field that arises in the right-hand side is given as:

$$e^{pl}_{\mathrm{inc},\boldsymbol{m}} = \langle \boldsymbol{f}^{pl}_{\boldsymbol{m}}(\boldsymbol{r}), \boldsymbol{E}_{\mathrm{inc}}(\boldsymbol{r})\rangle_V. \tag{4.61}$$

In the above equations, we use the following definition for the inner products:

$$\langle \boldsymbol{f}, \boldsymbol{g}\rangle_V = \int_V \boldsymbol{f}^*(\boldsymbol{r}) \cdot \boldsymbol{g}(\boldsymbol{r}) dV. \tag{4.62}$$

Tensor Representation of the Linear System

The various components of the VIE linear system admit a convenient and intuitive representation in tensor format (multidimensional arrays) when we employ a uniform discretization grid. First, we construct the tensors of the dielectric properties of the scatterer, $\underline{\mathbf{M}}_{\epsilon_r}$,$\underline{\mathbf{M}}_{\chi_e} \in \mathbb{C}^{N_x\times N_y\times N_z}$, as follows:

$$\underline{\mathbf{M}}_{\epsilon_r}(\boldsymbol{m}) = \dot{\epsilon}_r(\boldsymbol{r}_{\boldsymbol{m}}), \tag{4.63a}$$

$$\underline{\mathbf{M}}_{\chi_e}(\boldsymbol{m}) = \dot{\epsilon}_r(\boldsymbol{r}_{\boldsymbol{m}}) - 1. \tag{4.63b}$$

Next, we form the tensor of the unknowns, $\underline{\mathbf{x}}^{pl} \in \mathbb{C}^{N_x\times N_y\times N_z}$, where $p \in \{x, y, z\}$ and $l \in \{1, 2, 3, 4\}$. Similarly, we construct the tensor of the incident fields. More specifically, the associated tensor of the component p and the scalar basis function l reads:

$$\underline{\mathbf{e}}^{pl}_{\mathrm{inc}}(\boldsymbol{m}) = \int_V \boldsymbol{f}^{pl}_{\boldsymbol{m}}(\boldsymbol{r}) \cdot \boldsymbol{E}_{\mathrm{inc}}(\boldsymbol{r}) dV = \int_V N^l_{\boldsymbol{m}}(\boldsymbol{r}) E^p_{\mathrm{inc}}(\boldsymbol{r}) dV, \tag{4.64}$$

resulting in $\underline{\mathbf{e}}^{pl}_{\mathrm{inc}} \in \mathbb{C}^{N_x\times N_y\times N_z}$. Naturally, the tensor of the right-hand side is given by

$$\underline{\mathbf{b}}^{pl}(\boldsymbol{m}) = c_e \underline{\mathbf{M}}_{\chi_e} \odot \underline{\mathbf{e}}^{pl}_{\mathrm{inc}}, \tag{4.65}$$

where $\odot$ denotes the element-wise multiplication. Additionally, in order to calculate the interactions between the testing and basis functions, we have to calculate the integrals:

$$G^{pl,ql'}_{\boldsymbol{m},\boldsymbol{n}} = \int\limits_V \boldsymbol{f}^{pl}_{\boldsymbol{m}}(\boldsymbol{r}) \cdot \boldsymbol{f}^{ql'}_{\boldsymbol{n}}(\boldsymbol{r}) dV = \hat{\mathbf{p}} \cdot \hat{\mathbf{q}} \int\limits_V N^{l}_{\boldsymbol{m}}(\boldsymbol{r}) P_{\boldsymbol{m}}(\boldsymbol{r}) N^{l'}_{\boldsymbol{n}}(\boldsymbol{r}) P_{\boldsymbol{n}}(\boldsymbol{r}) dV \tag{4.66}$$

for n_x,$m_x = 1 : N_x$, n_y,$m_y = 1 : N_y$ and n_z,$m_z = 1 : N_z$, p,$q \in \{x, y, z\}$ and l,$l' \in \{1, 2, 3, 4\}$ which can be uniquely expressed by an $\mathbb{R}^{N_x \times N_y \times N_z}$ tensor, since non-overlapping basis functions are used, as:

$$\underline{\mathbf{G}}^{pl}(\boldsymbol{m}) = \int\limits_V \left(P_{\boldsymbol{m}}(\boldsymbol{r}) N^{l}_{\boldsymbol{m}}(\boldsymbol{r}) \right)^2 dV = \begin{cases} P_{\boldsymbol{m}}(\boldsymbol{r}) \Delta V & l = 1 \\ P_{\boldsymbol{m}}(\boldsymbol{r}) \frac{\Delta V}{12} & l = 2, 3, 4 \end{cases}, \tag{4.67}$$

where $\Delta V = \Delta x \Delta y \Delta z$ is the volume of the voxel. It is interesting to note that if the basis function at Eq. 4.55a, corresponding to the constant term, is multiplied by $1/\sqrt{\Delta V}$ and the basis functions at 4.55b - 4.55d, corresponding to the slopes, are multiplied by $\sqrt{12}/\sqrt{\Delta V}$, Gram matrix reduces to the identity matrix facilitating the implementation of the solver.

Volume-Volume Integrals

Finally, the most challenging part in the assembly of the tensors is the calculation of the six-dimensional (6D) volume-volume integrals that arise from the associated, discretized integro-differential $\mathcal{N}$ and $\mathcal{K}$ operators with kernels that exhibit strongly singular ($1/|\boldsymbol{r} - \boldsymbol{r}'|^3$) and weakly singular ($1/|\boldsymbol{r} - \boldsymbol{r}'|^2$) behavior, respectively, when the observation voxels coincide or are adjacent with the source voxels. Note that, here the singularity order is different from SIE methods since the integration is performed over volumetric and not surface elements. More specifically, these integrals, according to Eq. 4.59 can be written as:

$$N^{pl,ql'}_{\boldsymbol{m},\boldsymbol{n}} = \int\limits_V \int\limits_{V'} \boldsymbol{f}^{pl}_{\boldsymbol{m}}(\boldsymbol{r}) \cdot \nabla \times \nabla \times (g(\boldsymbol{r}, \boldsymbol{r}') \boldsymbol{f}^{ql'}_{\boldsymbol{n}}(\boldsymbol{r}')) dV' dV, \tag{4.68a}$$

$$K^{pl,ql'}_{\boldsymbol{m},\boldsymbol{n}} = \int\limits_V \int\limits_{V'} \boldsymbol{f}^{pl}_{\boldsymbol{m}}(\boldsymbol{r}) \cdot \nabla \times (g(\boldsymbol{r}, \boldsymbol{r}') \boldsymbol{f}^{ql'}_{\boldsymbol{n}}(\boldsymbol{r}')) dV' dV. \tag{4.68b}$$

The far interactions are calculated by means of a standard 6D quadrature rule, where the components of the DGF kernels are symmetric and anti-symmetric for $\mathcal{N}$ and $\mathcal{K}$ operator, respectively, resulting in 6 and 3 unique dyadic components, as can be seen from Eqs. 4.15 and 4.43. Also, the unique interactions of the scalar part of the basis and testing functions with a kernel of the form $K(\boldsymbol{r}, \boldsymbol{r}') = K(\boldsymbol{r} - \boldsymbol{r}')$ are 10 instead of 16, when discretized on a

uniform grid. These internal symmetries significantly reduce the overall memory footprint required for storing the tensors of both operators to 90 unique entries. However, simple quadrature rules cannot be applied when calculating the nearby interactions, since for coinciding or adjacent voxels the 6D integrals are singular. The main idea for tackling these cases is to reduce the dimensionality of the 6D volume-volume integrals to four-dimensional (4D) surface-surface integrals step-by-step, as it has been shown in [76, 233, 236] (see Appendix C). As a result, the initial volume-volume integral boils down to a sum of 4 closed surface-surface integrals over the faces of the interacting voxels (Figure 4.5), which have smoother kernels and can be calculated by modern algorithms, originally developed for Galerkin SIE methods over quadrilateral patches [152, 158, 160].

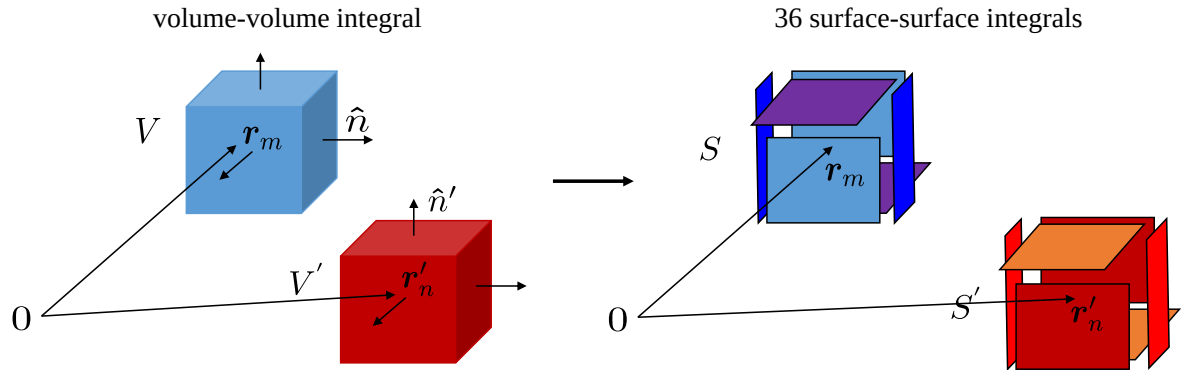

Figure 4.5: Decomposition of a volume-volume integral into a sum of 36 surface-surface integrals over the face-face interactions of the observation and source voxels.

However, we should note that the formulas presented in Appendix C and in [76, 233] suffer from the low-frequency breakdown problem that was mentioned in the previous section and the sum of the 36 face-face integrals is prone to numerical cancellation errors for fine resolutions and/or low frequencies, in general, when $k_0 dx \to 0$. In order for this problem to be resolved, the singularity subtraction method [243, 244] should be employed where the odd, singular terms are added and subtracted from the Taylor expansion series of the scalar Green's function,

$$g = \underbrace{g - \frac{1}{4\pi|\boldsymbol{r}-\boldsymbol{r}'|} + \frac{k_0^2}{8\pi}|\boldsymbol{r}-\boldsymbol{r}'|}_{\text{smooth}} + \underbrace{\frac{1}{4\pi|\boldsymbol{r}-\boldsymbol{r}'|} - \frac{k_0^2}{8\pi}|\boldsymbol{r}-\boldsymbol{r}'|}_{\text{non-smooth}}, \tag{4.69}$$

where the smooth part has 2 continuous derivatives and can be computed with standard 6D quadrature rules and for the non-smooth part new reduced surface-surface static kernels should be derived for which the corresponding singular integrals can be computed with readily available packages for SIE methods. Such procedure has been implemented for the scalar Green's function and incorporated into the assembly of VoxHenry, an inductance extraction tool for voxelized structures accelerated with the help of FFT [245, 246]. However,

the current-based VIE is associated with the curls of g, as seen in Eq. 4.68, and to our knowledge such formulas do not exist in the literature and their derivation, implementation, and convergence analysis could be the subject of future work.

In order to exploit the operators internal symmetries that are mentioned before, as well as, the translation invariance property of the convolutional discrete kernels,

$$N_{\boldsymbol{m},\boldsymbol{n}}^{pl,ql'} = N_{\boldsymbol{m}-\boldsymbol{n}}^{pl,ql'}, \tag{4.70}$$

we choose to use a uniform, voxelized grid, where we can fix the basis function at a specific voxel, say the first with $\boldsymbol{n} = (1,1,1)$, and sweep the testing function over the voxels of the computational domain in order to calculate only the unique volume-volume integrals. Therefore, the above integrals, when expressed in matrix $\in \mathbb{C}^{N_V \times N_V}$ format, will be three-level block-Toeplitz Toeplitz-block matrices, since we are dealing with the 3D case. As a result, it suffices to calculate their Toeplitz defining tensors $\in \mathbb{C}^{N_x \times N_y \times N_z}$ as

$$\underline{\mathbf{N}}^{pl,ql'}(\boldsymbol{m}) = N_{\boldsymbol{m}-\mathbf{1}}^{pl,ql'}, \tag{4.71}$$

where $m_x = 1 : N_x$, $m_y = 1 : N_y$, $m_z = 1 : N_z$, p,$q \in \{x, y, z\}$ and l,$l' \in \{1, 2, 3, 4\}$. The same logic applies to the tensors for $\mathcal{K}$ operator.

Memory Footprint Reduction

Finally, the Green's function has smoothing properties for remote elements interactions, therefore, the off-diagonal blocks of the MoM matrix will be low-rank [66, 145]. In a similar manner, the 3D Toeplitz defining tensors at Eq. 4.71 are expected to present low multilinear ranks [237] and an impressive memory compression factor can be achieved by applying tensor decompositions on the 3D Toeplitz tensors, as demonstrated in [163, 237, 238]. In particular, Tucker decomposition is expected to provide an optimal and a stable approximation for a 3D tensor [247] and can be implemented either with higher-order SVD [248] or with techniques based on cross approximation [249, 250], as it is explained and investigated at [163, 238]. In this way, the overall memory footprint is drastically reduced and the compressed Tucker factors can fit inside a GPU, accelerating the matrix-vector product in an iterative solver and allowing for the solution of linear systems with millions of unknowns (e.g., fine realistic head models with 1mm resolution or whole body EM scattering computation) within reasonable computational time. Similarly, the solution of the VIE for 2D scattering problems for multi-conductor transmission lines [251] has been recently accelerated by the use of tensor train decomposition [252].

Additionally, if we reform the 3D tensors in Eq. 4.71 into a 4D tensor $\in \mathbb{C}^{N_x \times N_y \times N_z \times 60}$, where the fourth dimension corresponds to the unique interactions of the basis and testing

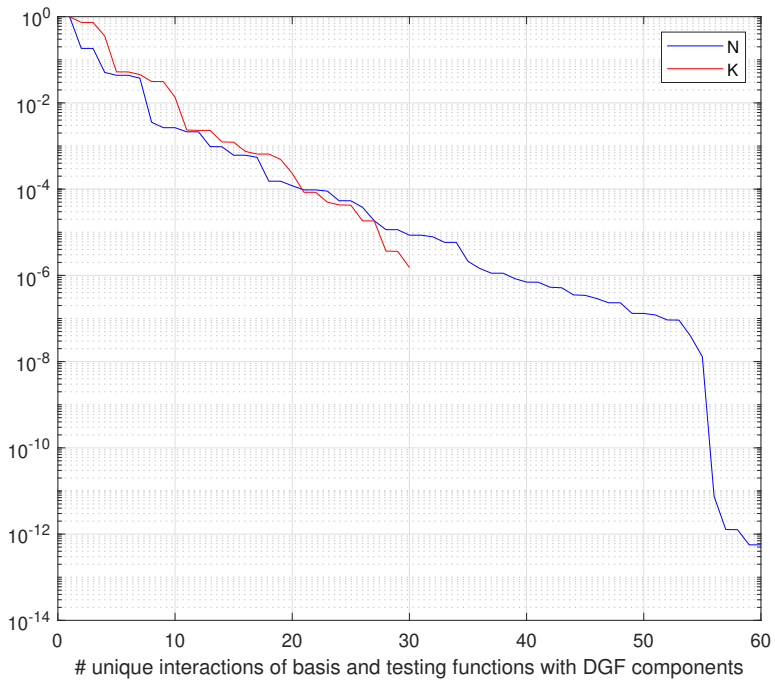

Figure 4.6: Behavior of the ranks along the fourth dimension of $\mathcal{N}$ and $\mathcal{K}$ operator tensors that corresponds to the unique basis and testing functions interactions with the DGF kernels and PWL basis functions.

functions with DGF components of $\mathcal{N}$ operator (this will be 30 for $\mathcal{K}$ operator), then the tensor appears to be low-rank, for the case of PWL basis functions, even along this fourth dimension (see Figure 4.6). Of course, this low-rank property is of different nature than the previously mentioned for the 3D case and originates from the fact that not all linear terms (x, y, z) are physically required to generate a basis with linear functions which implies that a reduced basis representation of the equivalent currents, possibly similar with that of VoxHenry [245, 246], could be employed. However, this is only a speculation and whether it holds true or not, along with the ranks behavior with respect to different choices of basis functions, is open to investigation.

FFT-based Acceleration of the Matrix-Vector Product

In order to numerically solve a discretized VIE, the inversion of a very large and dense matrix is required. Hence, the scientific community has naturally been using iterative solvers. Even with an iterative solver, for which the most time consuming part is the matrix-vector product with $\mathcal{O}(N^2)$ complexity, solving a realistic problem becomes extremely difficult and in many cases prohibitive. However, if uniform, voxelized grids are used, the MoM matrix becomes structured (block Toeplitz with Toeplitz blocks) and the associated matrix-vector product is amenable to acceleration with the help of FFT resulting in $\mathcal{O}(N\log(N))$

complexity for each matrix-vector product.

The first step to that direction is the embedding of the Toeplitz defining tensors for $\mathcal{N}$ and $\mathcal{K}$ operator into their corresponding circulant defining tensors $\underline{\mathbf{N}}_{\text{circ}}^{pl,ql'} \in \mathbb{C}^{2N_x \times 2N_y \times 2N_z}$, with special care to take into account the associated projection signs for the DGF, the basis, and testing functions, as described in a detailed algorithmic analysis, that can be found at the Appendix of [60] and shown here in Table 4.1 for the derivatives of g and for the PWL basis functions. Finally, the circulant matrix-vector product can be computed with the FFT, reducing the computational cost to approximately $\mathcal{O}(N\log(N))$, for number of unknowns that can be expressed as $N = 2^p 3^q 5^r$ [253, 254].

Table 4.1: Projection Signs for the Derivatives of g and for the PWL Basis Functions.

Functions \ Flags	N_x	N_y	N_z	N_xN_y	N_xN_z	N_yN_z	$N_xN_yN_z$
$\partial^2 g/\partial x^2$	+	+	+	+	+	+	+
$\partial^2 g/\partial y^2$	+	+	+	+	+	+	+
$\partial^2 g/\partial z^2$	+	+	+	+	+	+	+
$\partial^2 g/\partial x\partial y$	-	-	+	+	-	-	+
$\partial^2 g/\partial x\partial z$	-	+	-	-	+	-	+
$\partial^2 g/\partial y\partial z$	+	-	-	-	-	+	+
$\partial g/\partial x$	-	+	+	-	-	+	-
$\partial g/\partial y$	+	-	+	-	+	-	-
$\partial g/\partial z$	+	+	-	+	-	-	-
N^1	+	+	+	+	+	+	+
N^2	-	+	+	-	-	+	-
N^3	+	-	+	-	+	-	-
N^4	+	+	-	+	-	-	-

On Preconditioning

Another advantage of using the current-based formulation is that the multiplicative operator with the dielectric susceptibilities is on the left of $\mathcal{N}$ operator, as it can be seen in Eq. 4.51c. Therefore, by multiplying through with the inverse of $\mathcal{M}_{\epsilon_r}$, this equation can be rewritten as

$$(\mathcal{I} - \mathcal{M}_{\chi_e}\mathcal{M}_{1/\epsilon_r}\mathcal{N})\boldsymbol{J}_{\text{eq}} = c_e\mathcal{M}_{\chi_e}\mathcal{M}_{1/\epsilon_r}\boldsymbol{E}_{\text{inc}}, \tag{4.72}$$

where the identity operator is now left alone. In this way, the integral equation is regularized and this regularization can be thought as a natural preconditioning for solving the linear sys-

tem of the discretized current-based VIE, as it has been suggested in [255, 256]. Motivated from these observations, we use a preconditioner of the form $\mathbf{P} = \mathbf{M}_{\epsilon_r}\mathbf{G}$. From a numerical perspective, when using this preconditioner, the iterative solver converges much faster especially in the case of highly inhomogeneous scatterers. Numerical experiments, presented below, indicate the superior convergence properties of the iterative solver when using this preconditioned solver for the case of a realistic head model.

Computation of Electromagnetic Fields and Power

The linear system solution provides us with the equivalent electric and magnetic currents at the center of the voxels and 3 coefficients representing the slopes of the linear terms. However, the equivalent currents are mathematical inventions and do not represent a physical phenomenon or quantity. In what follows, we describe the required steps for the computation of the EM fields and the associated absorbed power.

A fast and efficient way to compute the EM fields is to employ the fast matrix-vector products and calculate the "tested" total fields according to the discrete analogue of Eq. 4.40. Then, in order to calculate the EM fields in a discrete sense, we have to divide the "tested" total fields by the Gram matrix. An advantage of this approach is that no extra memory is required for computing the EM fields, and the complexity is once again governed by the FFT-based matrix-vector product.

Finally, the RF absorbed power can be accurately computed based on [257], where stable and compact vector-matrix-vector formulas are suggested. The only difference here is that we have to replace the Gram matrix, as in Eq. 4.67, to include the contributions of the linear terms of the solution vector and compute the absorbed power, which corresponds also to the global SAR, as:

$$P_{\text{abs}} = \frac{1}{2}\text{Re}\left\{\mathbf{x}^H(c_e\mathbf{M}_{\chi_e})^{-1}\mathbf{G}\mathbf{x}\right\}. \tag{4.73}$$

4.3.3 Electromagnetic Scattering from Inhomogeneous Head Models

Convergence Study for a Uniform Sphere and Solver Validation

To quantitatively validate the proposed framework, we conduct the numerical computation for the scattering of a plane wave from homogeneous dielectric spheres and calculate the absorbed power, as in Eq. 4.73. The results are compared with the Mie series analytical solution [78]. In detail, we model frequency-dependent electrical properties, matched to the average of the gray and white matter according to [67, 258], as they can be seen in Table 4.2, for various B_0 static magnetic field strengths of an MR scanner, where we use the gyromagnetic ratio as $\frac{\gamma}{2\pi} = 42.58\ \text{MHz/T}$ and set the operating frequency as $f = \frac{\gamma}{2\pi}B_0$. Furthermore, the sphere has radius $a = 7.5\text{cm}$ and the excitation is an x-polarized and

z-directed plane wave $\boldsymbol{E}_{\text{inc}} = \hat{\boldsymbol{x}} e^{-jk_0 z}$.

Table 4.2: Electrical Properties of Homogeneous Sphere.

$B_0(\text{T})$	0.5	1.5	3	7
$f(\text{MHz})$	21.29	63.87	127.74	298.06
$\epsilon_r^{'}$	227	141	68	64
$\sigma(\text{S/m})$	0.25	0.35	0.5	0.51

Table 4.3: Degrees of Freedom.

$h(\text{mm})$	5	2.5	1.5	1	0.75
$N_x = N_y = N_z$	31	61	101	151	201
DoFs PWC (million)	0.09	0.68	3.09	10.33	24.36
DoFs PWL (million)	0.36	2.72	12.36	41.32	97.45

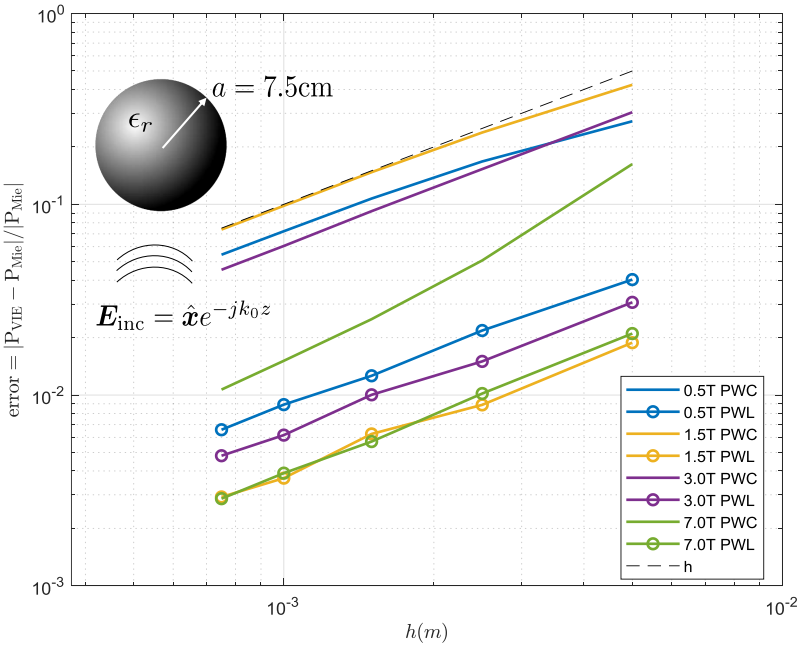

Figure 4.7: Relative error of RF absorbed power with respect to resolution for the PWC and PWL current-based VIE compared with the Mie series solution for homogeneous spheres with $a = 7.5\text{cm}$ and frequency-dependent electrical properties, as seen in Table 4.2, for different B_0 field strengths when irradiated by a plane wave.

Moreover, we calculate the absorbed power, both with the PWC current-based VIE [60] and the proposed solver with PWL basis functions, and compute the relative error for the

power obtained from Mie series, as $\text{error} = |\text{P}_{\text{VIE}} - \text{P}_{\text{Mie}}|/|\text{P}_{\text{Mie}}|$. The iterative solver of choice is the generalized minimum residual (GMRES) with inner iterations 50 and outer 200, and with tolerance 10^{-5}. Finally, we vary the resolution of the discretization, using $h = 5, 2.5, 1.5, 1, 0.75\text{mm}$, and present the results for the relative error of the PWC and PWL solvers, with respect to the resolution in Figure 4.7, along with the Degrees of Freedom (DoFs) for each solver, shown in Table 4.3. Clearly, the discretization with PWL basis functions gives much better accuracy for the same resolution, compared with the PWC discretization. Specifically, it is observed that there is a constant improvement factor of approximately 12 times in the relative error between the PWC and PWL solvers. However, the convergence rate appears to be $\mathcal{O}(h)$, instead of $\mathcal{O}(h^2)$, due to numerical inaccuracies originating from the staircase approximation of a sphere, when discretized with voxels [131].

Convergence Study for the "Billie" Head Model and Comparison with the Flux-Based Formulation

In order to demonstrate the superior convergence properties of the proposed high-order current-based solver, in comparison with the flux-based formulation [56, 57], often used in MRI studies [43, 259], we conduct the computations for the EM scattering of a plane wave for the "Billie" realistic head model from Virtual Family Population [5]. In detail, we operate at $B_0 = 7\text{T}$, hence the corresponding frequency is $f = 298.06\text{MHz}$ and we irradiate the head model with an x-polarized and negative y-directed plane wave $\boldsymbol{E}_{\text{inc}} = \hat{\boldsymbol{x}} e^{jk_0 y}$, so that the plane wavefront is parallel to the coronal plane of the head.

Subsequently, we compute the EM fields and the absorbed power with the current-based formulation with PWC and PWL basis functions and the flux-based (DVIE) formulation with rooftop basis functions [56,57], as we refine the grid, using resolutions $h = 5, 2, 1\text{mm}$. Furthermore, GMRES is utilized with the same tolerance, inner and outer iterations as in the previous example. In Figures 4.8, 4.10, and 4.11 we present the RMS electric field for all 3 resolutions and 3 solvers, where the fields outside the body are masked for enhanced visualization. It is observed that, for coarser resolutions, the PWL solver provides more accurate results, when compared with the lower-order PWC solver. Additionally, both for the case of DVIE and PWC solvers there exist numerical artifacts at regions with high contrast, i.e., at the air-skull and skull-brain interfaces at coarser resolutions (2mm), which is not the case for the proposed higher-order solver. Moreover, we execute the same numerical experiment, utilizing the preconditioner mentioned before, and present the convergence of the iterative solver for all formulations and refinements.

As it can be clearly seen in Figure 4.9, the current-based formulation is well-conditioned, allowing for p-refinement, while the iteration count remains practically the same, when the suggested preconditioner is used. It also allows for h-refinement, since, as we move to finer resolutions, the number of iterations does not change, which is not the case for the flux-based

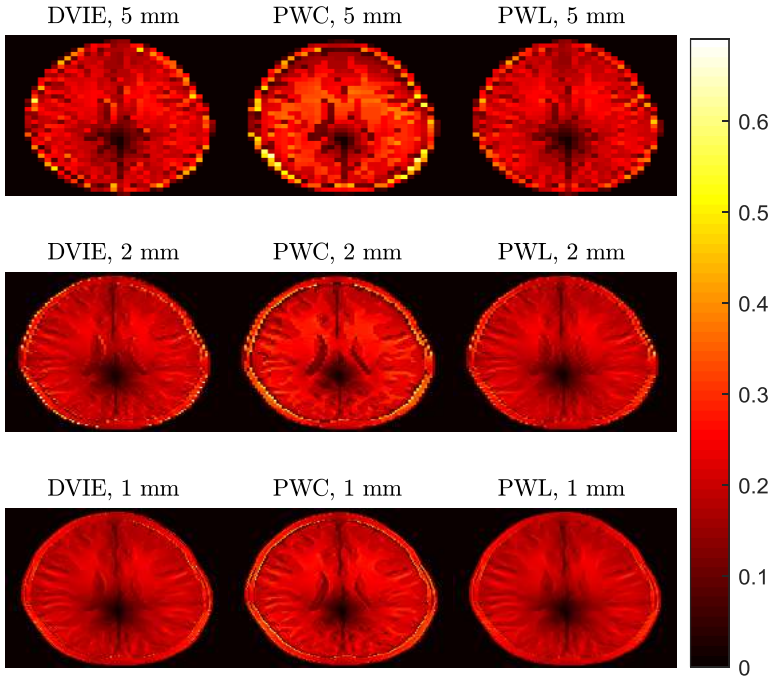

Figure 4.8: Axial views of the RMS value of the electric field in $\mathrm{V/m}$ inside the "Billie" head model, when excited by a plane wave at 7T MRI. From left to right, the electric field values are obtained with the flux-based solver (DVIE), the PWC current-based solver, and the PWL current-based solver for resolutions $h = 5, 2, 1\mathrm{mm}$, as viewed from top to bottom. Fields outside the body are masked to improve the visibility.

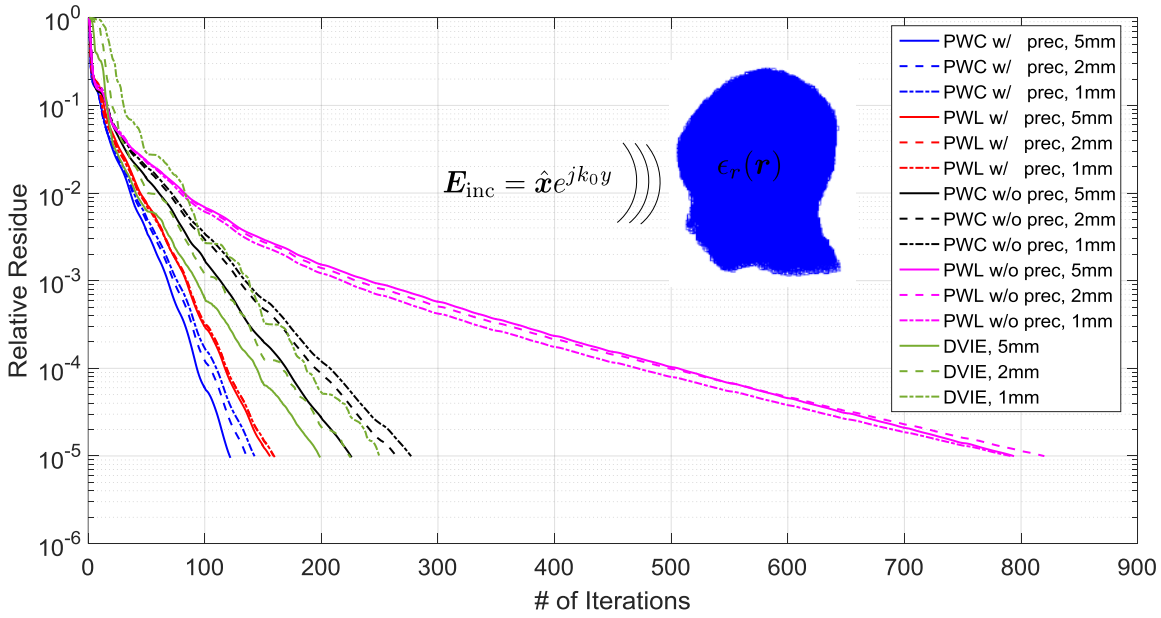

Figure 4.9: Convergence of GMRES iterative solver for the PWC current-based solver, the PWL current-based solver with and without preconditioner, and the flux-based solver (DVIE) for different resolutions $h = 5, 2, 1\mathrm{mm}$, for the calculation of EM scattering of a plane wave from the "Billie" head model at 7T MRI.

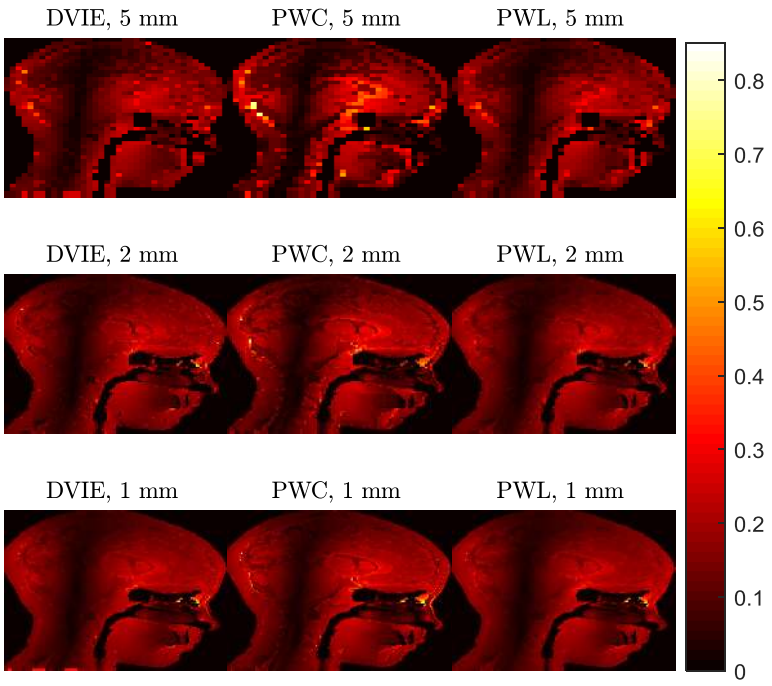

Figure 4.10: Sagittal views of the RMS value of the electric field for the same simulation setup as in Figure 4.8.

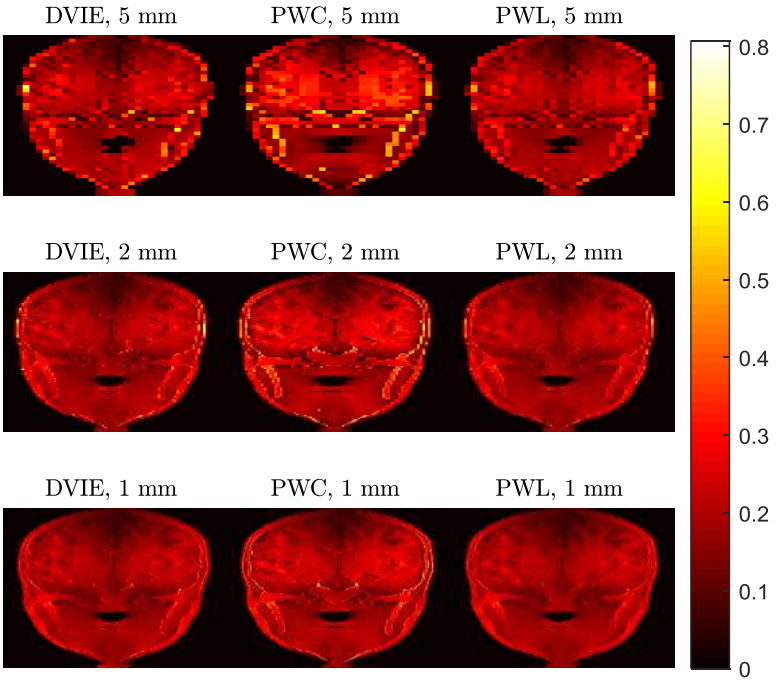

Figure 4.11: Coronal views of the RMS value of the electric field for the same simulation setup as in Figure 4.8.

formulation, where the iteration count diverges, as we refine the grid. This can be attributed to the fact that the flux-based VIE in [57] averages the normalized contrast function with the material properties (since it appears behind $\mathcal{L}$ operator, as seen in Eq. 4.46) and due to the

fact that this formulation is inherently ill-conditioned and the number of iterations increases with h-refinement, as it is demonstrated at [49, 51]. On the contrary, when discretizing the current-based VIE, the spectral properties of the operators are preserved. Finally, the effectiveness of the proposed preconditioner for highly inhomogeneous scatterers can be verified since the iteration count is dramatically reduced when it is utilized, especially for the case of the PWL solver, where the iteration count drops from 800 to 150.

Convergence Study for the "Duke" Head Model with an Attached High-Dielectric Pad and Comparison with FDTD

As it is proposed at [170, 260–268], the use of high-permittivity dielectric materials can effectively address B_1^+ inhomogeneities that arise in high-field MRI, where the effective wavelength is comparable to the dimensions of the subject. By introducing specifically designed dielectric pads between the RF coil and the subject (see geometry in Figure 4.15), B_1^+ becomes more homogeneous, SAR is reduced and SNR increases, a technique called dielectric shimming. An example can be seen in Figure 4.12, where $|B_1^+|$ field becomes localized in the vicinity of the dielectric pad illuminating previously dark regions with $|B_1^+|$ field nulls and improving the SNR at this region. However, from an EM scattering perspective, simulating such setups is very challenging even for the state-of-the-art VIE-based solvers, due to the extremely high contrast and high inhomogeneity of the scatterer.

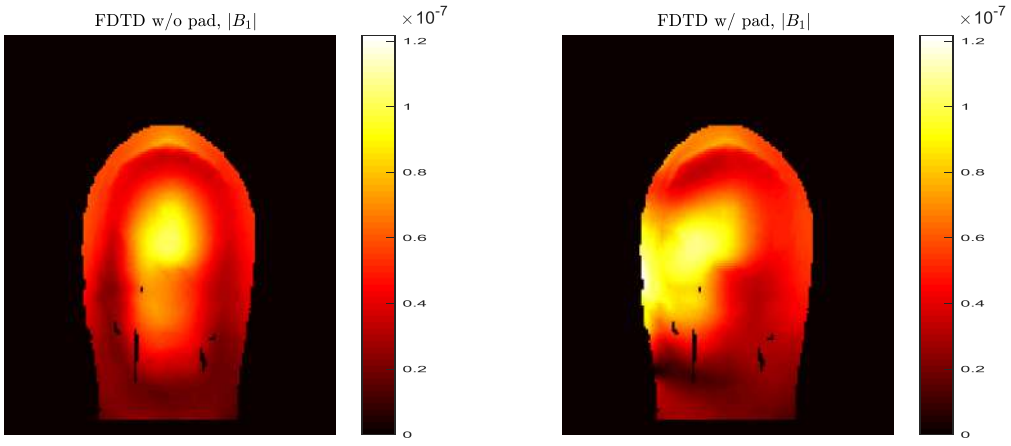

Figure 4.12: $|B_1^+|$ field in T inside "Duke" head model with and without a high-dielectric pad attached to its left-hand side. The localization and shifting of the $|B_1^+|$ field can be seen which can be exploited for dielectric shimming applications.

To demonstrate the superior accuracy of the proposed current-based VIE solver with PWL basis functions, we perform the numerical computation for the EM scattering for the "Duke" head model, where a high-dielectric pad is attached to the left side of the head model and has electrical properties $\epsilon_r^{'} = 300$ and $\sigma = 0.25\mathrm{S/m}$, as seen in Figure 4.13. The geometry and properties of the suspensions, as well as the incident field, which originates from a 16-rung

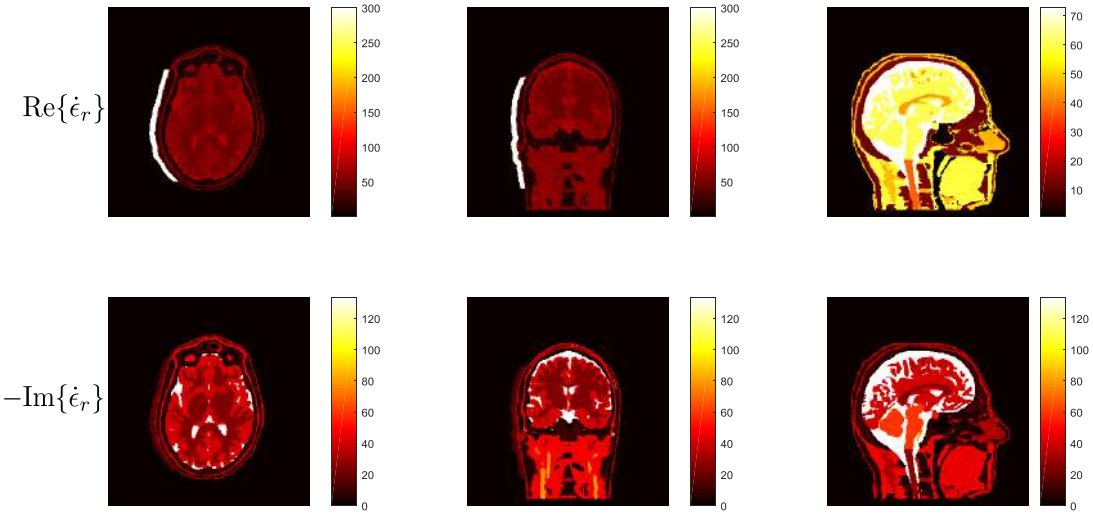

Figure 4.13: Real and imaginary part of relative complex permittivity ($\dot{\epsilon}_r$) of "Duke" realistic head model at 7T with a high-dielectric pad attached to its left-hand side with $\epsilon_r^{'} = 300$ and $\sigma = 0.25\mathrm{S/m}$.

high-pass birdcage coil with sinusoidal excitation tuned and matched at $f = 300\mathrm{MHz}$, are thoroughly explained in [265].

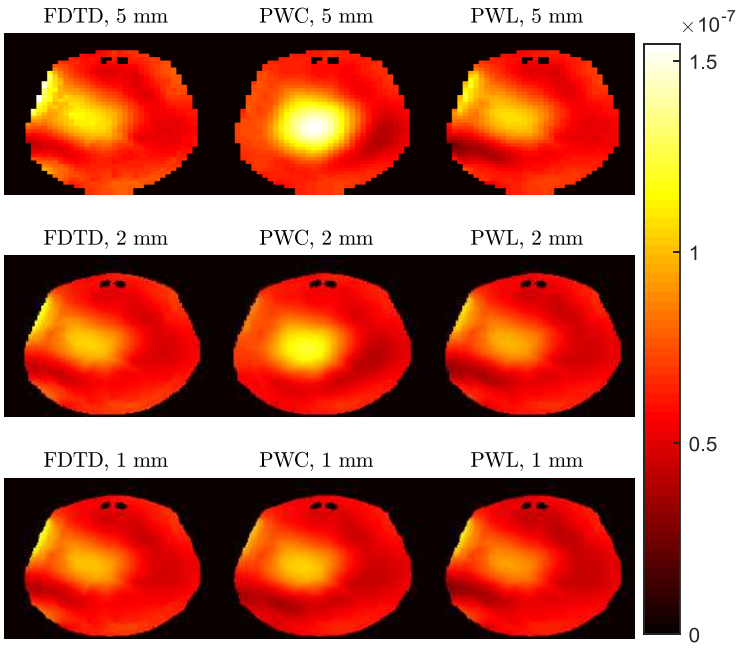

Figure 4.14: Axial views of $|B_1^+|$ in T inside the "Duke" head model with an attached high-dielectric pad, when excited by a tuned birdcage coil at 7T MRI. From left to right, the magnetic field values are obtained with a commercial FDTD package, the PWC current-based solver, and the PWL current-based solver for resolutions $h = 5, 2, 1\mathrm{mm}$, as viewed from top to bottom. Fields outside the body and at the pad are masked to enhance the visibility.

Subsequently, we calculate the EM field distributions over the head and the pad with the current-based VIE formulation with PWC and PWL basis functions, as we refine the resolution of the computational grid, using $h = 5, 2, 1\text{mm}$. Also, GMRES is utilized with the same tolerance, inner and outer iterations as before. The results are qualitatively compared to the EM fields obtained from a commercial software package which employs the FDTD method (xFDTD 7.2, Remcom Inc., State College, Pennsylvania, USA), as it is mentioned at [265], and the $|B_1^+|$ for all 3 resolutions and 3 solvers is presented in Figures 4.14, 4.16, and 4.17 masking the fields outside the body for improved visibility. From these figures, it is clear that, even for this very demanding simulation, the PWL solver yields reliable and accurate EM fields for coarse resolutions, which are in good agreement with the FDTD-based solution, despite the inherent differences in the numerical modeling of the setting. On the contrary, it is necessary to refine the resolution up to 1mm for the PWC solver to converge to an accurate solution.

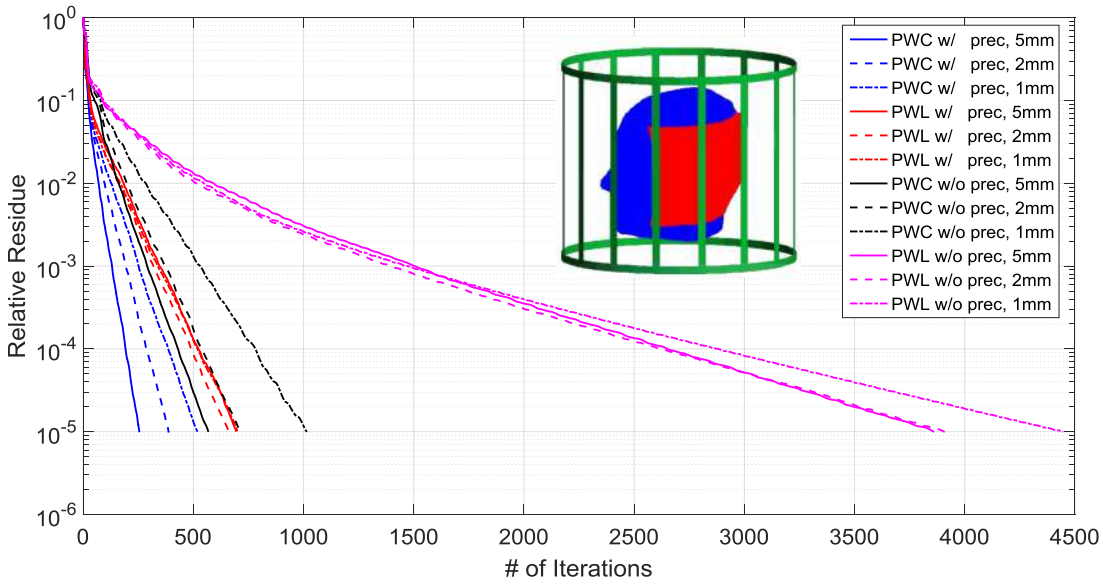

Figure 4.15: Convergence of GMRES iterative solver for the PWC current-based solver and the PWL current-based solver with and without preconditioner for different resolutions $h = 5, 2, 1\text{mm}$, for the calculation of EM scattering from the "Duke" head model with an attached high-dielectric pad irradiated by a tuned birdcage coil at 7T MRI. The simulated geometry with the birdcage coil, the head model, and the attached pad are presented.

Additionally, we execute the same numerical experiment for the PWC and PWL solvers utilizing the preconditioner mentioned in the previous experiment and present the convergence study of the iterative solver in Figure 4.15. Here, the well-conditioned properties of the current-based VIE can be observed, even for this extremely challenging scenario, allowing both for the utilization of higher-order approximations and grid refinements. Furthermore, the remarkable effectiveness of the proposed preconditioner is clearly demonstrated, since when it is utilized the number of iterations significantly drops from 3900 to 700, a value

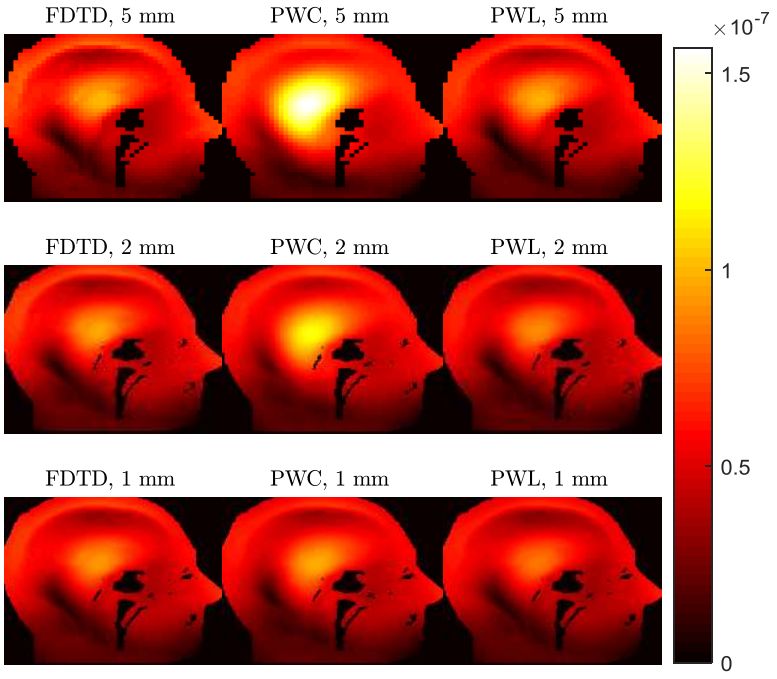

Figure 4.16: Sagittal views of $|B_1^+|$ in T inside the "Duke" head model with an attached high-dielectric pad for the same simulation setup as in Figure 4.14.

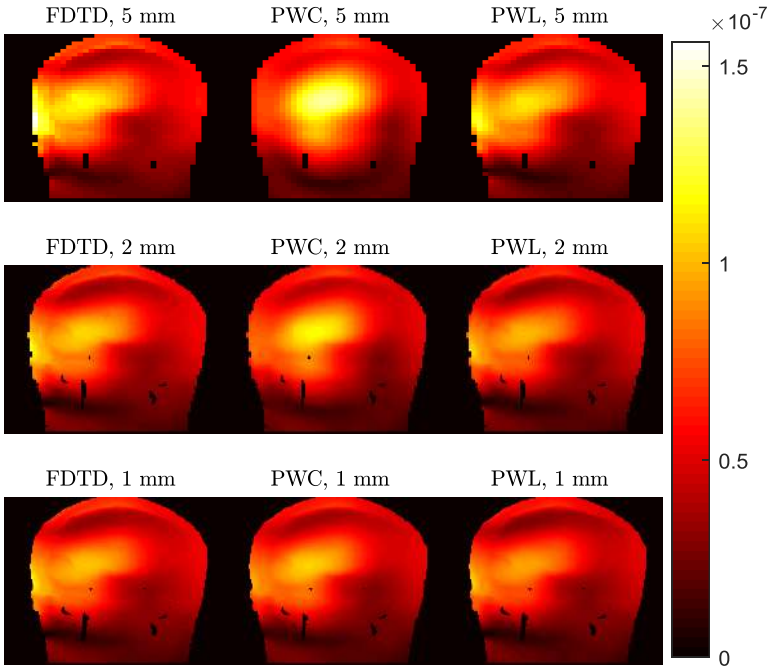

Figure 4.17: Coronal views of $|B_1^+|$ in T inside the "Duke" head model with an attached high-dielectric pad for the same simulation setup as in Figure 4.14.

comparable to the iteration count of the PWC solver, allowing for this solver to be used in practical and demanding applications with manageable computational cost, while simultaneously providing accurate and reliable results. It is worth noting that without the proposed

preconditioner the iteration count of the PWL solver diverges at the finest resolution of 1mm which does not occur when the preconditioner is employed. Finally, for completeness, we show the absorbed power density p_{abs} for all 3 resolutions and 3 solvers in Figures 4.18, 4.19, and 4.20, where similar patterns regarding solver accuracy with respect to the resolution can be observed.

4.3.4 Conclusions

In conclusion, in this chapter, a fast VIE solver based on the equivalent polarization currents with PWL basis functions is derived for the accurate computation of the EM scattering from highly inhomogeneous and/or high contrast objects. The proposed solver has remarkably stable convergence properties and yields reliable EM fields for extremely challenging modeling scenarios and for coarse resolutions without necessarily refining the computational grid. Such stable convergence is not so common for IEs for which the iteration count typically diverges with h-refinement (see the iteration count of the flux-based solver at Figure 4.9). Additionally, the iteration count for the current-based solver with PWL basis functions remains the same as the grid is refined, while for the lower-order PWC scheme it slightly increases which leads to the conclusion that p-refinement stabilizes the iteration count and that the spectral properties of the operators are better preserved. Furthermore, by discretizing the VIE on uniform grids, the matrix-vector product can be performed fast with the help of FFT and when combined with iterative solvers large and complex problems can be solved accurately within reasonable time and computational resources. The proposed framework can be utilized in challenging applications such as the modeling of the interactions between EM fields and biological tissue, including the presence of shimming pads of very high electrical permittivity. In problems with such high contrast, as demonstrated at the numerical experiment with the high-dielectric ($\epsilon_r = 300$) pad attached to the head model, the solver with PWL basis functions provides reliable results comparable to those of a commercial FDTD package. However, the iteration count significantly increases and around 700 iterations are required (Figure 4.15) whereas 160 suffice when the high dielectric pad is not attached (Figure 4.9) to achieve a solution with the same GMRES tolerance. Therefore, it is expected that the higher the contrast the more iterations are required for convergence in an iterative solver similarly to the case of high-frequency problems. Furthermore, the newly developed solver with PWL basis functions has been incorporated into Global Maxwell Tomography [95] for the noninvasive estimation of the electrical properties of the human body based on the MR signal, where it helped by providing to the optimizer solves consistent with each other and thus regularizing the problem and reducing the error of the electrical properties reconstruction [269]. Finally, our higher-order solver will be part of the soon to be released MARIE 2.0 suite. As we mentioned before, future work could include the PWL approximation of the electrical properties for cases where the material profile varies with higher-order polynomial

functions, the derivation, implementation, and convergence study of the subtraction method for the singular kernels of $\mathcal{N}$ and $\mathcal{K}$ operator, and the feasibility, accuracy and convergence properties study of reduced-order linear basis functions.

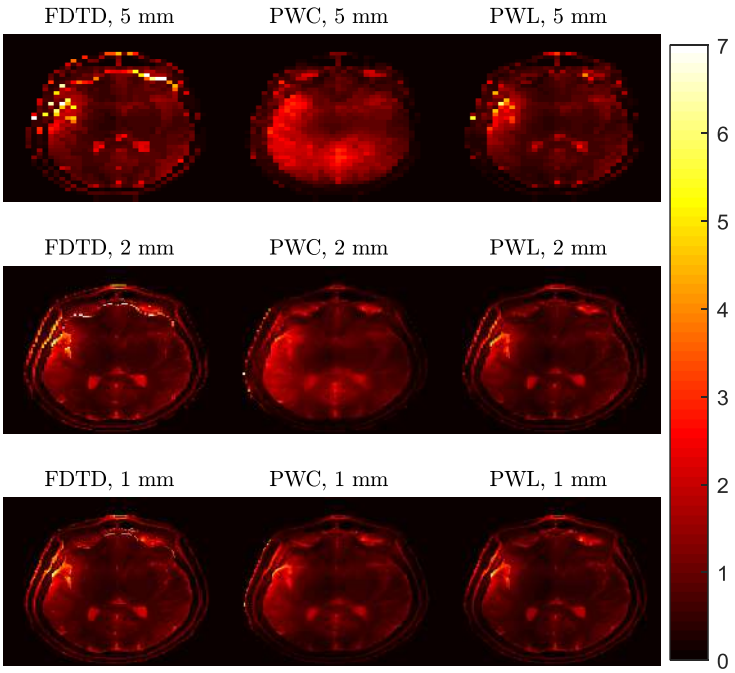

Figure 4.18: Axial views of p_{abs} in W/m^3 inside the "Duke" head model with an attached high-dielectric pad for the same simulation setup as in Figure 4.14.

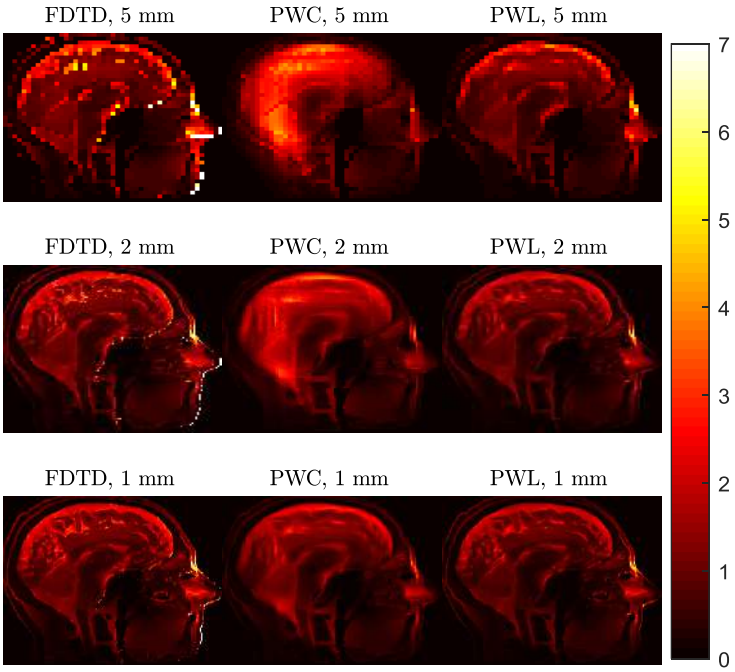

Figure 4.19: Sagittal views of p_{abs} in W/m^3 inside the "Duke" head model with an attached high-dielectric pad for the same simulation setup as in Figure 4.14.

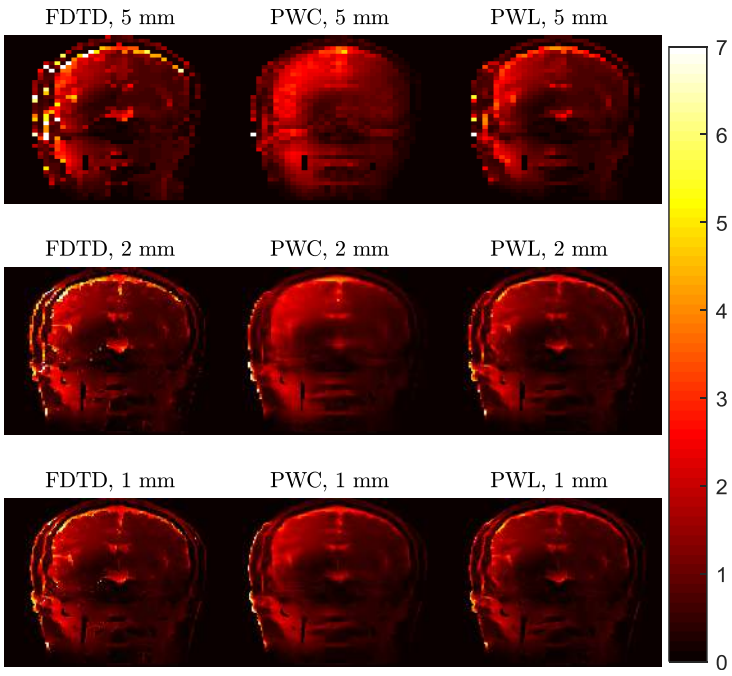

Figure 4.20: Coronal views of p_{abs} in W/m^3 inside the "Duke" head model with an attached high-dielectric pad for the same simulation setup as in Figure 4.14.

5 Numerical Basis of Electromagnetic Fields and MRI Applications

After developing a numerical solver that generates reliable EM fields, the next focal point of this thesis is the description of robust and accurate algorithms for the generation of a numerical EM fields basis, that is consistent with electrodynamics, inside an inhomogeneous, arbitrary scatterer [80]. This step can be considered as generalization of the expansion of EM fields within spherical objects with spherical waves [270] and shares similarities with the characteristic modes theory for arbitrary scatterers [271, 272]. A basis of EM fields can help to understand the currents and EM fields distributions that maximize SNR [67], TXE [75], or SAR amplification factor for RF hyperthermia [71] within the inhomogeneous biological tissue or by calculating the current distributions that yield optimal SNR for arbitrary current-bearing substrates [82]. These currents distributions can inform the non-convex RF coil optimization problem by providing an intuitive initial guess, thus, offering a framework for a truly robust optimization of their design that is a critical step into the design and deployment of next generation high and UHF MRI systems. Additionally, such performance bounds can be used to evaluate and optimize RF coils and MR techniques by assessing existing coil designs and calculating the percentage of the ultimate values they can reach, thus indicating the room for improvement of specific arrays.

In particular, the ultimate SNR, TXE, and SAR are the best possible values that optimization procedures can achieve for any possible coil design. The computation of these ultimate values requires a complete basis of the EM fields in the sample under study, i.e., the human body. Ultimate SNR, TXE, and SAR have been generated and extensively studied based on analytical solutions (such as Mie series and spherical/cylindrical harmonic expansions) for homogeneous spherical and cylindrical geometries [10–19, 74] yielding great insight into expected and observed trends in MRI signal, noise, and safety. Also, important work has been devoted to extract the current excitation patterns and best coil configurations for these relatively simple geometries [15, 20–29]. Despite the useful insight gained from these metrics, MR RF coils are designed for realistic body models. Therefore, results for highly complex inhomogeneous realistic body models can provide useful information for coil array designers, providing an ultimate figure of merit against which they can benchmark their

designs and obtain useful insight and intuition of the best RF excitation patterns.

In this chapter, we investigate how to efficiently generate a low-order subspace basis able to reconstruct all EM fields distributions within a realistic human body model. We present the key points for the basis generation, study the impact that electrical distance has on its generation, demonstrate its ability to reconstruct different EM fields, and compare its numerical accuracy and convergence properties against a complete analytical basis derived in a spherical coordinate system for the TXE and SNR metrics and for different objects. The vectors of the basis can be linearly combined and applied in optimization procedures, as it has been demonstrated for UISNR [67], ultimate SAR amplification factor [71] and we further illustrate for the case of UITXE [75] and such performance bounds can be used to evaluate the performance of existing receive and transmit array designs. Together with these performance bounds, we also compute the associated current distributions on a given arbitrary surface that yield the corresponding EM fields within the inhomogeneous head model that result in the optimal SNR distribution [82]. These numerical ICP can inform the non-convex RF coil optimization problem with an intuitive initial guess and could lead to truly task-optimal coil designs.

5.1 Generation of a Consistent Numerical Basis of Electromagnetic Fields

MRI technology relies on inducing an EM field within the realistic human body model due to impressed/external excitations in the RF coils, which can be calculated according to Eqs. 4.40 and 4.44, where instead of having equivalent sources yielding scattered fields we have impressed sources yielding incident fields within the body, as:

$$\begin{pmatrix} \boldsymbol{E}_{\text{inc}} \\ \boldsymbol{H}_{\text{inc}} \end{pmatrix} = \begin{pmatrix} \frac{1}{c_e}(\mathcal{N}-\mathcal{I}) & -\mathcal{K} \\ \mathcal{K} & \frac{1}{c_m}(\mathcal{N}-\mathcal{I}) \end{pmatrix} \begin{pmatrix} \boldsymbol{J}_{\text{i}} \\ \boldsymbol{M}_{\text{i}} \end{pmatrix}. \tag{5.1}$$

Therefore, for an MRI system, we can hold to the realistic assumption that the excitations are restricted in an arbitrary region (sources region) outside the body (observation region), hence, there are no electric or magnetic sources within the body and the above equation reduces to:

$$\begin{pmatrix} \boldsymbol{E}_{\text{inc}} \\ \boldsymbol{H}_{\text{inc}} \end{pmatrix} = \begin{pmatrix} \frac{1}{c_e}\mathcal{N} & -\mathcal{K} \\ \mathcal{K} & \frac{1}{c_m}\mathcal{N} \end{pmatrix} \begin{pmatrix} \boldsymbol{J}_{\text{i}} \\ \boldsymbol{M}_{\text{i}} \end{pmatrix}. \tag{5.2}$$

5.1.1 Surface Equivalence Principle

The first step in order to generate a numerical basis of incident EM fields inside the human body is to find a way to account for all the possible current excitations outside the human

body, a step that can be computationally demanding unless treated properly. As we mentioned in Chapter 3, we can address this issue by making use of the surface equivalence or Huygens's principle [108, 109, 116] according to which, we can generate an imaginary closed surface around the source-free body, so that any external excitation in the exterior of this surface ($\boldsymbol{J}_i$ and $\boldsymbol{M}_i$) can be reproduced as a combination of sources lying on this surface ($\boldsymbol{J}_{\text{eq}}$ and $\boldsymbol{M}_{\text{eq}}$). Therefore, any EM field distribution inside the devoid-of-sources body can be generated by the tangential equivalent currents flowing on Huygens's surface (Figure 5.1). In this way, Huygens's surface separates the coil domain from the human body domain and allows for the representation of any EM field that originates from coils in the exterior of this surface. It should be noted that there necessarily has to exist a distance between the Huygens's surface and the body in order for the produced EM fields to be smooth and, intuitively, the smaller the distance the less smooth these fields become. In addition, due to computational considerations, a set of discrete points on this surface must be selected to place the equivalent sources. The number of sources required for a sufficiently accurate approximation is problem dependent and depends on the distance between the surface and the observation points. Naturally, the closer two nearby sources are to an observation point, the larger the impact of the distance between them in terms of incident EM fields they generate on the given observation point.

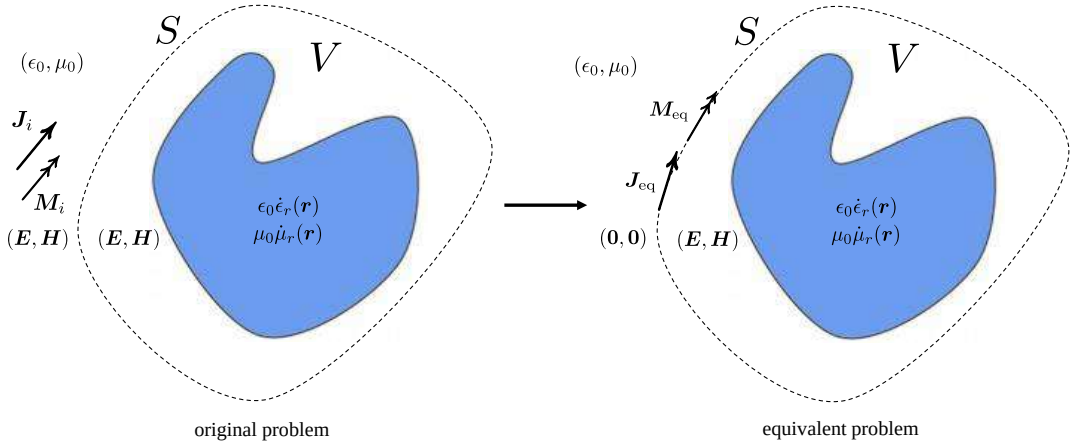

Figure 5.1: Illustration of surface equivalence principle. The arbitrary scatterer within volume V is enclosed with Huygens's surface S where all external current sources $\boldsymbol{J}_i$ and $\boldsymbol{M}_i$ can be represented by the equivalent currents $\boldsymbol{J}_{\text{eq}}$ and $\boldsymbol{M}_{\text{eq}}$ that yield the same EM field.

This coil domain and body domain separation is particularly useful when the RF coils location is not predefined and they can be placed in any position outside the human body. Note, however, that if the RF coils are confined within a volume, we can generate a surface around this RF coil domain, so that any RF coil excitation can be reproduced as a linear combination of the effects of sources lying on this surface, as it has been described at [66] and further demonstrated for the antenna characterization problem [273].

5.1.2 Discretization Schemes and Model-Order Reduction

Discretization Schemes

The second step in order to generate the numerical basis is to chose an appropriate discretization scheme for the equivalent sources lying on the continuous surface that encloses the human body and generate a reduced-order model. Specifically, we use three different discretization schemes. The first involves the representation of the Huygens's surface with a voxelized dipole cloud that entails the discretization of volumetric currents either with PWC [60] or PWL basis functions, as we have introduced them in the previous chapter, over a uniform voxelized grid in a similar manner with [65–67, 71]. Using a uniform voxelized grid leads to approximating the shape of the surface with a staircase or PWC-shaped surface which has nonzero thickness, however, this approach allows for the FFT-based implementation of the matrix-vector product and does not require forming the coupling matrix that maps currents on the surface to fields in the human body. The second employs RWG [62] basis functions on a triangular grid, where the currents are constrained onto a 2D surface [75], respecting the infinitesimal thickness of the Huygens's surface and providing flexibility for coil and surface currents distributions modeling. The third directly applies ideal Hertzian dipoles (the basis functions are Dirac delta functions) which are imposed to be tangential to the 2D surface of interest and has allowed for intuitively visualizing ICP at arbitrary current-bearing surfaces yielding optimal SNR in realistic heterogeneous head models [82] as a linear combination of elementary dipole sources. Additionally, we test the incident EM fields either with PWC or PWL basis functions. Therefore, the discrete form of $\mathcal{N}$ operator in Eq. 5.2 (same considerations hold for $\mathcal{K}$) is calculated for the following five distinct approaches which can be used for different applications within the MR field and are associated with their own numerical and practical considerations that we will describe below.

1. Expansion of volumetric currents with PWC basis functions and testing of the produced EM fields with PWC testing functions over a uniform voxelized grid as in [60]:

$$N_{\boldsymbol{m},\boldsymbol{n}}^{p,q} = \int_V (P_{\boldsymbol{m}}(\boldsymbol{r})\hat{\boldsymbol{p}}) \cdot \int_{V'} \nabla \times \nabla \times \bar{\boldsymbol{G}}(\boldsymbol{r},\boldsymbol{r}') \cdot (P_{\boldsymbol{n}}(\boldsymbol{r})\hat{\boldsymbol{q}}) dV' dV. \tag{5.3}$$

2. Expansion of volumetric currents with PWL basis functions (as in Eq. 4.56) and testing of the produced EM fields with PWL testing functions over a uniform voxelized grid as described in the previous chapter:

$$N_{\boldsymbol{m},\boldsymbol{n}}^{pl,ql'} = \int_V \boldsymbol{f}_{\boldsymbol{m}}^{pl}(\boldsymbol{r}) \cdot \int_{V'} \nabla \times \nabla \times \bar{\boldsymbol{G}}(\boldsymbol{r},\boldsymbol{r}') \cdot \boldsymbol{f}_{\boldsymbol{n}}^{ql'}(\boldsymbol{r}') dV' dV. \tag{5.4}$$

3. Expansion of surface currents with RWG basis functions over a triangular grid (as in Eq.

4.28) and testing of the produced EM fields with PWC basis functions [75]:

$$N^{p}_{\boldsymbol{m},n} = \int\limits_{V} (P_{\boldsymbol{m}}(\boldsymbol{r})\hat{\boldsymbol{p}}) \cdot \int\limits_{S'} \nabla \times \nabla \times \bar{\boldsymbol{G}}(\boldsymbol{r},\boldsymbol{r}') \cdot \boldsymbol{f}_n(\boldsymbol{r}')dS'dV. \tag{5.5}$$

4. Expansion of surface currents with RWG basis functions over a triangular grid and testing of the produced EM fields with PWL basis functions [75]:

$$N^{pl}_{\boldsymbol{m},n} = \int\limits_{V} \boldsymbol{f}^{pl}_{\boldsymbol{m}}(\boldsymbol{r}) \cdot \int\limits_{S'} \nabla \times \nabla \times \bar{\boldsymbol{G}}(\boldsymbol{r},\boldsymbol{r}') \cdot \boldsymbol{f}_n(\boldsymbol{r}')dS'dV. \tag{5.6}$$

5. Expansion of dipole currents with Dirac delta basis functions tangential to an arbitrary surface and testing of the produced EM fields with PWC basis functions [82]:

$$N^{p,q}_{\boldsymbol{m},\boldsymbol{n}} = \int\limits_{V} (P_{\boldsymbol{m}}(\boldsymbol{r})\hat{\boldsymbol{p}}) \cdot \int\limits_{V'} \nabla \times \nabla \times \bar{\boldsymbol{G}}(\boldsymbol{r},\boldsymbol{r}') \cdot \boldsymbol{f}^{q}_{\boldsymbol{n}}(\boldsymbol{r}')dV'dV, \tag{5.7}$$

where the basis function that imposes the ideal Hertzian dipole to be tangential to the surface of interest is defined as

$$\boldsymbol{f}^{q}_{\boldsymbol{n}}(\boldsymbol{r}) = [\hat{\boldsymbol{q}} - (\hat{\boldsymbol{q}} \cdot \hat{\boldsymbol{n}})\hat{\boldsymbol{n}}]\, \delta(\boldsymbol{r} - \boldsymbol{r}_{\boldsymbol{n}}), \tag{5.8}$$

where $q \in \{x, y, z\}$, $\hat{\boldsymbol{n}}$ denotes the normal vector to the surface, and $\boldsymbol{r}_{\boldsymbol{n}}$ the source point where the dipole is immersed. The surface can be meshed with a triangular grid and in the limiting case, as the surface is refined or by assigning a greater number of point dipoles on each triangle, the dipole point cloud becomes denser and the elementary sources approach a continuous surface current distribution.

It should be noted that, here, the basis and testing functions do not necessarily have to be chosen according to a Galerkin scheme, as it can be seen at approaches 3 to 5, since it is not required to solve a linear system in an iterative or direct solver rather we aim at exploring the subspace of the induced EM fields inside the human body model that originate from impressed current sources at the exterior space. The discrete equivalent of Eq. 5.2 for the equivalent sources lying on Huygens's surface can now be expressed for all the above distinct discretization schemes in a unified way as

$$\begin{pmatrix} \mathbf{e}_{\text{inc}} \\ \mathbf{h}_{\text{inc}} \end{pmatrix} = \begin{pmatrix} \frac{1}{c_e}\mathbf{N} & -\mathbf{K} \\ \mathbf{K} & \frac{1}{c_m}\mathbf{N} \end{pmatrix} \begin{pmatrix} \mathbf{j}_{\text{eq}} \\ \mathbf{m}_{\text{eq}} \end{pmatrix}, \tag{5.9}$$

where $\mathbf{j}_{\text{eq}}$ and $\mathbf{m}_{\text{eq}}$ can represent discretized impressed dipole currents on the voxelized version of Huygens's surface for approach 1 and 2, normal current components that flow through each RWG triangle edge for the 2D surface of approach 3 and 4, and tangential-to-

surface current components of each elementary dipole for approach 5. Similarly, matrices $\mathbf{N}$ and $\mathbf{K}$ for approaches 1 to 5 should correspond to Eqs. 5.4 - 5.8.

Low-Rank Property

Independently of the discretization scheme, all the above sources-to-observation points or currents-to-fields coupling matrices are expected to be low-rank due to the smoothing property of Green's functions for remote (well-separated) elements interactions [66, 145]. This holds true for the MRI setup, since the excitations (sources points) are restricted in an arbitrary region outside the body (observation points) and these regions do not intersect with each other, hence, the operator in Eq. 5.9 is compact. In practice, the low-rank property of the coupling matrices means that neighboring current sources yield highly linearly dependent EM fields, or in other words, that there exist several sets of current sources that yield the same EM field at the observation points. Therefore, all possible incident fields that can be excited in the body can be represented by a basis since they are highly restricted and smooth, due to the separating distance. In fact, we can generate a basis for the incident electric $(\mathbf{U}_e)$ and magnetic $(\mathbf{U}_m)$ field that spans the left subspace of the discretized $\mathbf{N}$ and $\mathbf{K}$ matrices, through a principle component analysis of the coupling matrices, as

$$\begin{pmatrix} \mathbf{e}_{\text{inc}} \\ \mathbf{h}_{\text{inc}} \end{pmatrix} = \begin{pmatrix} \mathbf{U}_e \\ \mathbf{U}_m \end{pmatrix} \mathbf{w}. \tag{5.10}$$

Here, $\mathbf{w}$ represents the column vector with the corresponding coefficients that linearly combine the basis fields and the relationship between the incident electric $(\mathbf{U}_e)$ and magnetic field basis $(\mathbf{U}_m)$ will be discussed in detail in the next subsection. In addition, if a principle component analysis based on the SVD factorization of the coupling matrices is applied, then the generated basis can be complete up to a prescribed tolerance so that any incident field in the human body generated by any external source in the exterior of Huygens's surface can be reconstructed with accuracy up to this predefined tolerance. The accuracy monitoring and truncation order of the approximation is determined by keeping the left leading singular vectors that correspond to the Q largest singular values of the SVD factorization and by dropping those below this predefined error tolerance. The SVD truncation enables to generate a reduced-order model providing a stable yet compressed representation of the incident EM fields inside the human body model by any possible excitation with the additional benefit of controlling the error of the approximation, governed by the discarded singular values.

In what follows, we mention some numerical and practical considerations regarding how to chose the appropriate discretization scheme between the above, how to obtain in practice a compressed factorization, and how such reduced-order models can find useful application within the MR field.

Randomized Singular Value Decomposition

As we briefly mentioned before, approach 1 and 2 employs volumetric currents discretized on a uniform voxelized grid (Figure 5.2) that allows to exploit the shift invariance property of the Green's functions kernels and the associated block-Toeplitz with Toeplitz-blocks structure of the matrix, permitting the acceleration of the matrix-vector product with the help of FFT. In this way, there is no need to explicitly form the coupling matrix and, in fact, the knowledge of this fast matrix-vector product suffices to explore the subspace of the coupling matrix by applying RSVD with $\mathcal{O}(MNlog(Q))$ complexity [66, 67, 71, 81] and obtain an approximate rank-Q SVD [274]. This can be particularly useful in cases where the size of the matrices is large (which usually holds for electrically large structures) and thus the application of the SVD factorization becomes computationally expensive and in some cases prohibitive.

RSVD exploits the fact that random vectors can rapidly explore the range of an operator or the principal components of a linear system. In fact, random vectors (in our case random current distributions) produce quite linearly independent EM fields which after being applied many times they become less linearly independent and RSVD converges to SVD [81], hence, the application of random vectors can reveal the structure of the coupling matrices. Specifically, if N_o is the number of the observation voxels and N_i the number of the sources voxels, then $M = 3N_o$, $N = 3N_i$ for the PWC case and $M = 12N_o$, $N = 12N_i$ for the PWL case, and Q is expected to be much smaller than N_i. Finally, when applying RSVD, special care should be taken with regard to the application of the random excitation matrix. In particular, if Q singular values are required, then, the number of the random excitations should be at least twice $(N_r = 2Q)$, in order for the first half to be sufficiently accurate [66, 81].

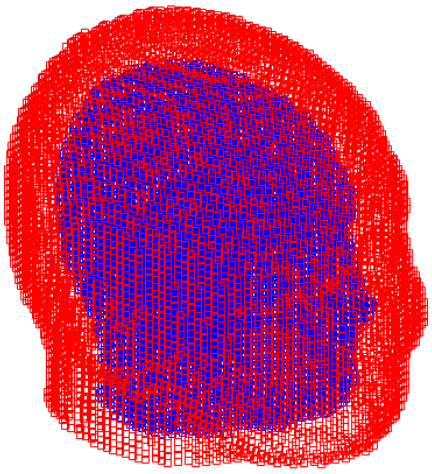

Figure 5.2: Dipole cloud (red) with volumetric currents discretized on a uniform voxelized grid surrounding "Duke" (blue) voxelized and inhomogeneous head model.

Distributed Dipoles in Voxels

Since, we usually have to deal with elementary excitations, such as electric and/or magnetic Hertzian oscillating dipoles, and since our discrete element, in approach 1 and 2, is a single voxel we should find a suitable way to express an elementary dipole within a voxel. The mathematical expression for an electric Hertzian (infinitesimal) dipole (current source) immersed at point $\boldsymbol{r}_n$, oriented along $\hat{\boldsymbol{p}}_n$, and carrying a dipole moment with strength equal to p_n (therefore, its electric dipole moment is $p_n\hat{\boldsymbol{p}}_n$) is given by [275]:

$$\boldsymbol{J}_{n,d}(\boldsymbol{r}) = j\omega p_n \delta(\boldsymbol{r}-\boldsymbol{r}_n)\hat{\boldsymbol{p}}_n, \tag{5.11}$$

where we can introduce vector $\boldsymbol{d}_n = j\omega\boldsymbol{p}_n$ for compactness. The above equation can prove to be problematic since in a discretized VIE the dipole current can at minimum be confined within a single volumetric element, where it has a uniform current distribution. Similarly, from a numerical perspective, the Dirac delta function can at minimum have support a single volumetric element of the discretized grid with volume ΔV and is given as [257]:

$$\delta_{\Delta V}(\boldsymbol{r}-\boldsymbol{r}_n) = \begin{cases} 1/\Delta\mathrm{V}, & \text{if} \quad \boldsymbol{r}-\boldsymbol{r}_n \in \text{supp}(\boldsymbol{f}) \\ 0, & \text{otherwise} \end{cases}, \tag{5.12}$$

where $\boldsymbol{f}$ is the basis function. Motivated by these observations and by the limit $\delta(\boldsymbol{r}) = \lim_{\Delta V\to 0} = \delta_{\Delta V}(\boldsymbol{r})$, we follow the approach of distributed dipole sources, as it has been introduced in [257], where in practice the dipole moment is divided by the volume of the voxel and its action is distributed over the voxel. In particular, the discretized impressed dipole current reads:

$$\mathbf{j}_d = \mathbf{G}^{-1}\mathbf{d}_e, \tag{5.13}$$

which is the discretized version of Eq. 5.11 and the nonzero entries of $\mathbf{d}_e$ are determined by the position $\boldsymbol{r}_n$ where the dipole is immersed and its vector value $\boldsymbol{d}_n$. Similarly, magnetic dipole currents are given as $\mathbf{m}_d = \mathbf{G}^{-1}\mathbf{d}_m$. Therefore, the incident EM fields from dipole excitations for a discretized VIE, according to Eqs. 5.1 and 5.13, are given as [257]:

$$\begin{pmatrix} \mathbf{e}_{\text{inc}} \\ \mathbf{h}_{\text{inc}} \end{pmatrix} = \begin{pmatrix} \frac{1}{c_e}(\mathbf{N}-\mathbf{G}) & -\mathbf{K} \\ \mathbf{K} & \frac{1}{c_m}(\mathbf{N}-\mathbf{G}) \end{pmatrix} \begin{pmatrix} \mathbf{G}^{-1}\mathbf{d}_e \\ \mathbf{G}^{-1}\mathbf{d}_m \end{pmatrix}. \tag{5.14}$$

An advantage of the above discretization scheme is that the dipoles can be immersed within the scatterer. However, this is not required in the MRI setup, where the currents sources from RF coils are at some distance from the human body and the impressed sources are propagated through the free-space DGF. A final remark is that the dipoles necessarily have to be immersed within the discretized computational domain, contrary to approach 5, where

they can be placed at any arbitrary point $\boldsymbol{r}_n$, where of course the field at this point is singular, but the dimensions of the computational domain decrease.

In summary, approaches 1 and 2 with the assistance of RSVD can rapidly explore the subspace of a discretized operator and they constitute an ideal choice when the currents and the scatterer are discretized on a uniform voxelized grid, where the FFT-based matrix-vector product can be performed and the full dense matrix does not have to be formed. However, RSVD is an approximate rank-Q SVD which in some demanding cases does not yield sufficiently accurate results, as we will demonstrate in the next section, and it is associated with voxelized dipole sources which cannot offer great flexibility for RF coil and surface currents modeling. Its usefulness within the MR field has been demonstrated in seemingly different applications such as: the computation of performance bounds for SNR [67] and SAR amplification factor [71] from a complete basis by fully encapsulating the head model (Figure 5.2), the ultra-fast RF coil design [65] with the MR specific Green's function [66,161] where the currents are constrained onto a cylindrical domain around the head model where the arbitrary RF coil must be located, and the regularization of Global Maxwell Tomography [95] by providing orthogonal EM fields excitations. From now on, for simplicity, we will refer to approach 1 as RSVD PWC and to approach 2 as RSVD PWL.

Surface Singular Value Decomposition

Unlike RSVD PWC and RSVD PWL, where the volumetric currents are discretized on a uniform voxelized grid, at approach 3 and 4, the currents are discretized with RWG basis functions on a triangular grid (Figure 5.3). This naturally entails that the currents-to-fields coupling matrix loses its block-Toeplitz with Toeplitz-blocks structure and we can no longer perform the FFT-based matrix-vector product. However, the subspace of the sources-to-observation points coupling matrix can still be calculated fast by adaptive cross approximation of the matrix [83–86] with $\mathcal{O}(Q^2(M+N))$ complexity and we still deal with the storage of compressed matrices. Specifically, similarly to before, for PWC testing we have $M = 3N_o$ and for PWL $M = 12N_o$, but, $N = N_e$ and corresponds to the number of internal edges of the RWG basis functions. Finally, SVD can be directly applied to the coupling matrix when restrictions on memory and computation time permit.

The reasoning behind choosing RWG basis functions for discretizing the currents sources is that they provide a more exact approximation of the Huygens's surface along with a flexibility for RF coil modeling and surface currents distributions representation. Furthermore, since RWG basis functions require fewer DoFs for discretizing the currents sources than the voxelized volumetric currents, it is feasible to directly apply SVD to the coupling matrix and avoid the approximate low-rank representation that RSVD provides which in some cases can be sensitive to numerical inaccuracies, as we will demonstrate in the next section. Similarly to RSVD, as demonstrated at [67,71], a complete basis (up to a specific tolerance)

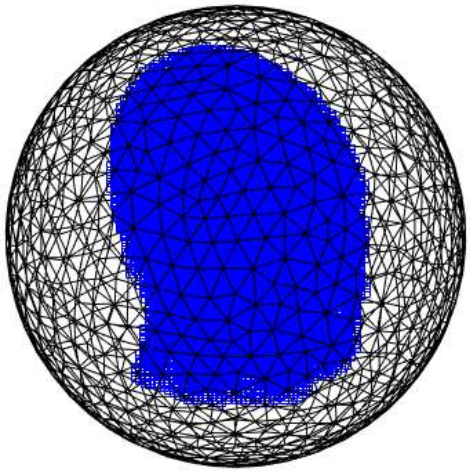

Figure 5.3: 2D shell (black) with surface currents discretized with RWG basis functions on a triangular grid surrounding “Duke” (blue) voxelized and inhomogeneous head model.

can be generated by surrounding the head model with a closed 2D shell (Figure 5.3), hence, performance bounds for MR-related metrics can be computed, as we show for the case of TXE metric [75]. Finally, a recent contribution has demonstrated a way to overcome the loss of the block-Toeplitz with Toeplitz-blocks structure of the coil-to-body coupling matrix by first representing the triangular grid with nearby voxels and then using the FFT to compute the translation invariant interactions between voxels [164]. Hereinafter, we will refer to approach 3 as surface SVD (SSVD) PWC and to approach 4 as SSVD PWL.

Dipole Singular Value Decomposition

An alternative to the distributed dipoles representation for modeling elementary excitations is to treat them directly as point sources and expand them in terms of Dirac delta basis functions, as in approach 5, which idea shares some similarities with the discrete dipole approximation method [276]. Here, special care should be taken in order to impose the dipole vector to be tangential to each element of the discretized arbitrary excitation surface (Figure 5.4), according to Eq. 5.8, hence, Eq. 5.11 takes the form

$$\boldsymbol{J}_{n,t}(\boldsymbol{r}) = [\boldsymbol{d}_n - (\boldsymbol{d}_n \cdot \hat{\boldsymbol{n}})\,\hat{\boldsymbol{n}}]\,\delta(\boldsymbol{r} - \boldsymbol{r}_n). \tag{5.15}$$

In this way, a continuous surface current distribution can be approximated, as the size of the surface element is refined, and the mesh should be sufficiently fine, otherwise the currents might appear to flow outside of the surface if it has high curvature. This approach has the advantage that the representation of the currents sources is imposed to be exact at a specific set of points on an arbitrary surface and no interpolation or projection is required when visualizing SNR-optimizing [12] current distributions, which otherwise is necessary when employing RWG basis functions or with a volumetric representation of the currents.

In fact, approach 5 has allowed for the first time to extract and visualize ICP associated with optimal SNR in heterogeneous head models for arbitrary current-bearing substrates as a linear combination of elementary dipole sources [82]. Here, the surface that encloses the head model is not closed (Figure 5.4) and not all possible EM fields can be represented. Therefore, even if we use all basis vectors in an SNR-optimizing procedure [12], the resulting SNR distribution does not correspond to the UISNR, hence, we refer to such distribution as optimal SNR. Furthermore, the space where the dipoles are immersed does not have to be discretized and the size of the computational domain decreases. Similarly to SSVD, the currents-to-fields coupling matrix is not structured and we cannot perform the FFT-based matrix-vector product but the same considerations hold regarding alternative algorithms for its low-rank representation with the only difference that now $N = 3N_d$, with N_d denoting the number of dipoles. Finally, we note that we test the incident fields with PWC functions and call approach 5 dipole SVD (DSVD) PWC.

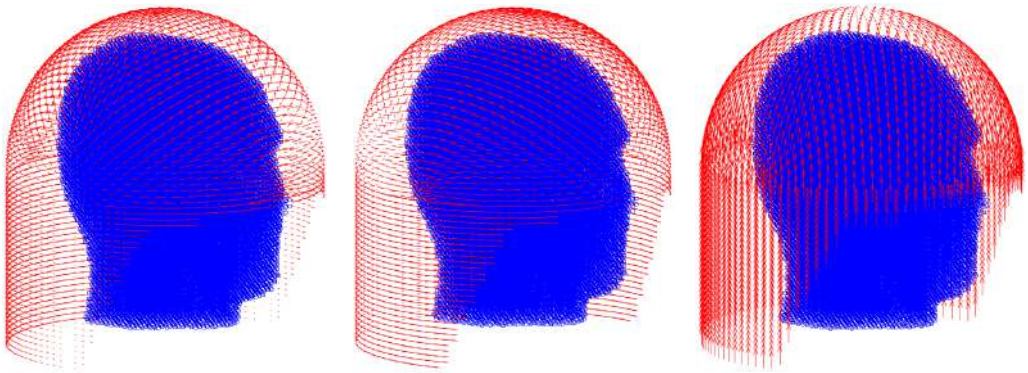

Figure 5.4: Arbitrary current-bearing surface (red) with ideal Hertzian dipoles whose x, y, z components are imposed to be tangential to the 2D surface of interest surrounding "Duke" (blue) voxelized and inhomogeneous head model.

5.1.3 Consistency with Electrodynamic Principles

The third step in order to generate the numerical basis is to impose a relationship between the electric and magnetic field basis in 5.10 which ensures that the electric and magnetic field basis vectors respect electrodynamic principles and are orthogonal to each other. In particular, both the electric and magnetic fields are related by the curl operator, which means that if we want to reconstruct a valid EM field, we must ensure that the reconstructed electric and magnetic fields are related by the same curl operator. This fact also implies that operators $\mathbf{N}$ and $\mathbf{K}$ are orthogonal, in the sense that they generate orthogonal vectors from the same excitation. However, independent bases from each operator, hence, from different kind of currents, do not need to be orthogonal to each other, and, in fact, incident electric fields from electric and magnetic currents are expected to be linearly dependent since

their radiation contributions, particularly for the case of orthogonal complex source point excitations [193, 277], are practically indistinguishable.

Electric Current Excitations

If we assume only electric current excitations outside the body, then each basis can be represented in terms of the left column subspace of the corresponding operator,

$$\mathbf{U}_e \subseteq \text{colspan}(\mathbf{N}), \quad \mathbf{U}_m \subseteq \text{colspan}(\mathbf{K}), \tag{5.16}$$

and in order to guarantee that $\mathbf{U}_e$ and $\mathbf{U}_m$ form a pair of bases that complies with Maxwell equations, the following algorithmic steps should be followed.

First, the incident electric fields due to electric currents, according to Eq. 5.9, are expressed as

$$\mathbf{e}_{\text{inc}} = \frac{1}{c_e}\mathbf{N}\mathbf{j}_{\text{eq}}, \tag{5.17}$$

where distinct sources and observation regions are modeled, hence, the operator is compact and we can compute its SVD as

$$\frac{1}{c_e}\mathbf{N} = \mathbf{U}_{e,N}\mathbf{\Sigma}_{e,N}\mathbf{V}_{e,N}^H. \tag{5.18}$$

Then, SVD can be truncated while controlling the error of the approximation as

$$\frac{1}{c_e}\mathbf{N} \approx \hat{\mathbf{U}}_{e,N}\hat{\mathbf{\Sigma}}_{e,N}\hat{\mathbf{V}}_{e,N}^H, \tag{5.19}$$

where we keep the Q largest singular values, $\sigma_{e,N}^q$, and the corresponding singular vectors are the Q first columns of $\mathbf{U}_{e,N}$ and $\mathbf{V}_{e,N}$, denoted $\hat{\mathbf{U}}_{e,N}$ and $\hat{\mathbf{V}}_{e,N}$, respectively. These matrices form an orthonormal basis of incident electric fields within the human body model and equivalent electric currents at Huygens's surface, respectively. Therefore, all incident electric fields can be expressed as a weighted combination of the orthonormal incident electric fields basis vectors as

$$\mathbf{e}_{\text{inc}} \approx \hat{\mathbf{U}}_{e,N}\mathbf{a}, \tag{5.20}$$

where $\mathbf{a}$ is a column vector with complex coefficients $(\mathbf{a} \in \mathbb{C}^Q)$ which can be approximated in the least square sense as

$$\mathbf{a} = \hat{\mathbf{U}}_{e,N}^H\mathbf{e}_{\text{inc}}. \tag{5.21}$$

Similarly, all possible equivalent electric current sources can be expressed in terms of the same complex coefficients as

$$\mathbf{j}_{\text{eq}} \approx \hat{\mathbf{V}}_{e,N}\hat{\mathbf{\Sigma}}_{e,N}^{-1}\mathbf{a}. \tag{5.22}$$

Finally, in order for the generated magnetic field to comply with Maxwell equations and be

orthogonal to the electric field, it should originate from the same current distribution that induces the corresponding electric field in the human body model, therefore, it takes the form

$$\mathbf{h}_{\text{inc}} = \mathbf{K}\mathbf{j}_{\text{eq}} \approx \mathbf{K}\hat{\mathbf{V}}_{e,N}\hat{\mathbf{\Sigma}}_{e,N}^{-1}\mathbf{a}. \tag{5.23}$$

In summary, if we consider only electric current excitations, Eq. 5.10 boils down to

$$\begin{pmatrix} \mathbf{e}_{\text{inc}} \\ \mathbf{h}_{\text{inc}} \end{pmatrix} = \begin{pmatrix} \mathbf{U}_e \\ \mathbf{U}_m \end{pmatrix} \mathbf{a} \approx \begin{pmatrix} \hat{\mathbf{U}}_{e,N} \\ \mathbf{K}\hat{\mathbf{V}}_{e,N}\hat{\mathbf{\Sigma}}_{e,N}^{-1} \end{pmatrix} \mathbf{a}, \tag{5.24}$$

where $\mathbf{U}_e$ is an orthonormal basis of incident electric fields, each vector of $\mathbf{U}_e$ is orthogonal to the corresponding vector of $\mathbf{U}_m$ in order to be consistent with electrodynamic principles, and $\mathbf{U}_m$ spans a basis of incident magnetic fields which does not necessarily have to be orthogonal.

Magnetic Current Excitations

If we assume only magnetic current excitations outside the body, then

$$\mathbf{U}_e \subseteq \text{colspan}(\mathbf{K}), \quad \mathbf{U}_m \subseteq \text{colspan}(\mathbf{N}). \tag{5.25}$$

The derivation of such a basis is exactly analogous to the case of electric currents and we follow the same steps which we summarize in brief for completeness.

First, the incident electric fields due to magnetic currents are expressed as

$$\mathbf{e}_{\text{inc}} = -\mathbf{K}\mathbf{m}_{\text{eq}}, \tag{5.26}$$

and by performing a truncated SVD and keeping the Q largest singular values we derive

$$-\mathbf{K} \approx \hat{\mathbf{U}}_{e,K}\hat{\mathbf{\Sigma}}_{e,K}\hat{\mathbf{V}}_{e,K}^{H}. \tag{5.27}$$

$\hat{\mathbf{U}}_{e,K}$ and $\hat{\mathbf{V}}_{e,K}$ matrices form an orthonormal basis of incident electric fields within the human body model and of equivalent magnetic currents at Huygens's surface, respectively. Therefore, all incident electric fields can be expressed as a weighted combination of the orthonormal incident electric fields basis vectors as

$$\mathbf{e}_{\text{inc}} \approx \hat{\mathbf{U}}_{e,K}\mathbf{b}, \tag{5.28}$$

and the weighting coefficients are approximated by least squares as

$$\mathbf{b} = \hat{\mathbf{U}}_{e,K}^{H}\mathbf{e}_{\text{inc}}. \tag{5.29}$$

Now, all possible equivalent magnetic sources can be expressed in terms of these different coefficients as

$$\mathbf{m}_{\text{eq}} \approx \hat{\mathbf{V}}_{e,K}\hat{\mathbf{\Sigma}}_{e,K}^{-1}\mathbf{b}, \tag{5.30}$$

and the consistent (orthogonal to electric) magnetic fields should be given as

$$\mathbf{h}_{\text{inc}} = \frac{1}{c_m}\mathbf{N}\mathbf{m}_{\text{eq}} \approx \frac{1}{c_m}\mathbf{N}\hat{\mathbf{V}}_{e,K}\hat{\mathbf{\Sigma}}_{e,K}^{-1}\mathbf{b}. \tag{5.31}$$

In summary, if we consider only magnetic current excitations, Eq. 5.10 boils down to

$$\begin{pmatrix} \mathbf{e}_{\text{inc}} \\ \mathbf{h}_{\text{inc}} \end{pmatrix} = \begin{pmatrix} \mathbf{U}_e \\ \mathbf{U}_m \end{pmatrix}\mathbf{b} \approx \begin{pmatrix} \hat{\mathbf{U}}_{e,K} \\ \frac{1}{c_m}\mathbf{N}\hat{\mathbf{V}}_{e,K}\hat{\mathbf{\Sigma}}_{e,K}^{-1} \end{pmatrix}\mathbf{b}, \tag{5.32}$$

where the same considerations hold as before. Specifically, $\mathbf{U}_e$ is an orthonormal basis of incident electric fields, each vector of $\mathbf{U}_e$ is orthogonal to the corresponding vector of $\mathbf{U}_m$ in order to have a Maxwell-complying basis with electric fields orthogonal to magnetic fields, and $\mathbf{U}_m$ spans a basis of incident magnetic fields which does not necessarily have to be orthogonal.

Electric and Magnetic Current Excitations

If we assume both electric and magnetic current excitations, then

$$\mathbf{U}_e, \mathbf{U}_m \subseteq [\text{colspan}(\mathbf{N}) \cup \text{colspan}(\mathbf{K})], \tag{5.33}$$

and due to linearity we can combine Eqs. 5.24 and 5.32 and derive

$$\begin{pmatrix} \mathbf{e}_{\text{inc}} \\ \mathbf{h}_{\text{inc}} \end{pmatrix} = \begin{pmatrix} \mathbf{U}_e \\ \mathbf{U}_m \end{pmatrix}\mathbf{c} \approx \begin{pmatrix} \hat{\mathbf{U}}_{e,N} & \hat{\mathbf{U}}_{e,K} \\ \mathbf{K}\hat{\mathbf{V}}_{e,N}\hat{\mathbf{\Sigma}}_{e,N}^{-1} & \frac{1}{c_m}\mathbf{N}\hat{\mathbf{V}}_{e,K}\hat{\mathbf{\Sigma}}_{e,K}^{-1} \end{pmatrix}\begin{pmatrix} \mathbf{a} \\ \mathbf{b} \end{pmatrix}. \tag{5.34}$$

Such basis is expected to be ill-conditioned, since the vectors of the electric-field-from-electric-currents basis $(\hat{\mathbf{U}}_{e,N})$ and electric-field-from-magnetic-currents basis $(\hat{\mathbf{U}}_{e,K})$ are linearly dependent [193, 277] and computing the pseudo-inverse to derive the weighting coefficients $\mathbf{c}$ can lead to numerical inaccuracies.

Thankfully, the surface equivalence principle can be formulated based on the use of only electric (or only magnetic) equivalent currents [193, 277] which has as a twofold advantage. First, it alleviates the basis ill-conditioning that is present if we consider both kinds of currents and, second, it halves the number of the incident fields basis vectors and thus the number of solves for total EM fields that are required in optimization procedures and we will describe their derivation in the next subsection.

Another alternative is to seek a compressed representation of the electric-field-from-electric-

currents basis $(\mathbf{U}_{e,N})$ and electric-field-from-magnetic-currents basis $(\mathbf{U}_{e,K})$. In particular, we can form the following electric fields matrix by concatenating the two distinct bases and by scaling their singular vectors with their normalized singular values as

$$\mathbf{E}_{N,K} = \begin{pmatrix} \mathbf{U}_{e,N}\boldsymbol{\Sigma}_{e,N}/\sigma^1_{e,N} & \mathbf{U}_{e,K}\boldsymbol{\Sigma}_{e,K}/\sigma^1_{e,K} \end{pmatrix}, \tag{5.35}$$

with the corresponding magnetic fields matrix similarly taking the form

$$\mathbf{H}_{N,K} = \begin{pmatrix} \mathbf{K}\mathbf{V}_{e,N}/\sigma^1_{e,N} & \frac{1}{c_m}\mathbf{N}\mathbf{V}_{e,K}/\sigma^1_{e,K} \end{pmatrix}. \tag{5.36}$$

Then, in a direct analogy with before we can compute a truncated SVD of the concatenated and scaled basis electric fields in Eq. 5.35 and derive

$$\mathbf{E}_{N,K} \approx \hat{\mathbf{U}}_{e,N,K}\hat{\boldsymbol{\Sigma}}_{e,N,K}\hat{\mathbf{V}}^H_{e,N,K}. \tag{5.37}$$

Therefore, the incident electric field basis that incorporates the contributions of both electric and magnetic currents is now orthonormal and the corresponding consistent incident magnetic field basis can be similarly derived, hence, we end up having

$$\begin{pmatrix} \mathbf{e}_{\text{inc}} \\ \mathbf{h}_{\text{inc}} \end{pmatrix} = \begin{pmatrix} \mathbf{U}_e \\ \mathbf{U}_m \end{pmatrix} \mathbf{d} \approx \begin{pmatrix} \hat{\mathbf{U}}_{e,N,K} \\ \mathbf{H}_{N,K}\hat{\mathbf{V}}_{e,N,K}\hat{\boldsymbol{\Sigma}}^{-1}_{e,N,K} \end{pmatrix} \mathbf{d}. \tag{5.38}$$

In this way, we resolve the ill-conditioning problem of the basis in Eq. 5.34, however, a close inspection on the SV drops (Figure 5.5) reveals that the contributions of the magnetic currents through $\mathbf{K}$ operator are suppressed by the contributions of the electric currents through $\mathbf{N}$ operator, since $\mathbf{N}$ operator generates less smooth EM fields than $\mathbf{K}$ and dictates the SV drop. This is particularly important, since the rate of the SV drop determines the convergence properties of the basis as we will demonstrate in the next section. Additionally, since the surface equivalence principle can be formulated with either only electric or only magnetic currents with its associated speedup in terms of halving the EM scattering problem computations, we suggest that using only one kind of currents should be the method of choice for generating the numerical EM fields basis.

Basis Generation with Respect to Electric or Magnetic Incident Fields

Finally, it is important to note that the generation of the basis requires to obtain a basis for either the incident electric (as we have demonstrated until here) or the incident magnetic field, and the corresponding consistent incident magnetic or incident electric field, respectively, in order to maintain the EM field relation imposed by Maxwell equations.

For completeness, if we chose to derive the basis with respect to incident magnetic fields

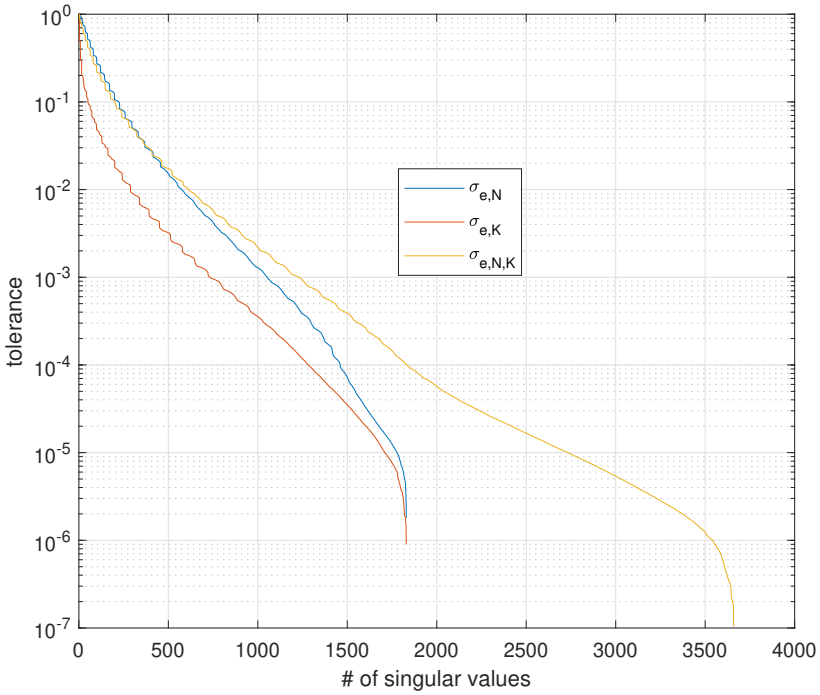

Figure 5.5: Drop of the singular values of $\mathbf{N}$, $\mathbf{K}$, and $\mathbf{E}_{N,K}$ matrices corresponding respectively to Eqs. 5.19, 5.27, and 5.37. The Huygens's surface is discretized with RWG basis functions with 1830 DoFs and it is placed 3cm away from a 10cm-radius sphere. The operating frequency is 298MHz and the spherical scatterer is discretized with PWC basis functions and 5mm resolution resulting in 33401 observation voxels.

from electric currents we get

$$\begin{pmatrix} \mathbf{e}_{\text{inc}} \\ \mathbf{h}_{\text{inc}} \end{pmatrix} = \begin{pmatrix} \mathbf{U}_e \\ \mathbf{U}_m \end{pmatrix} \mathbf{u} \approx \begin{pmatrix} \frac{1}{c_e}\mathbf{N}\hat{\mathbf{V}}_{h,K}\hat{\mathbf{\Sigma}}_{h,K}^{-1} \\ \hat{\mathbf{U}}_{h,K} \end{pmatrix} \mathbf{u}, \tag{5.39}$$

where we compute the truncated SVD of $\mathbf{K}$ as

$$\mathbf{K} \approx \hat{\mathbf{U}}_{h,K}\hat{\mathbf{\Sigma}}_{h,K}\hat{\mathbf{V}}_{h,K}^{H}. \tag{5.40}$$

and now all incident magnetic fields can expressed as a weighted combination of the orthonormal magnetic field basis as

$$\mathbf{h}_{\text{inc}} \approx \hat{\mathbf{U}}_{h,K}\mathbf{u}, \tag{5.41}$$

and the corresponding electric fields have to me consistent to the magnetic fields basis. Of course, $\mathbf{\Sigma}_{h,K}$ and $\mathbf{\Sigma}_{e,K}$ should be equal for the same setup since the singular values are always non-negative real numbers.

Furthermore, if we chose to derive the basis with respect to incident magnetic fields from magnetic currents we get

$$\begin{pmatrix} \mathbf{e}_{\text{inc}} \\ \mathbf{h}_{\text{inc}} \end{pmatrix} = \begin{pmatrix} \mathbf{U}_e \\ \mathbf{U}_m \end{pmatrix} \mathbf{v} \approx \begin{pmatrix} -\mathbf{K}\hat{\mathbf{V}}_{h,N}\hat{\mathbf{\Sigma}}_{h,N}^{-1} \\ \hat{\mathbf{U}}_{h,N} \end{pmatrix} \mathbf{v}, \tag{5.42}$$

where we compute the truncated SVD of $\frac{1}{c_m}\mathbf{N}$ as

$$\frac{1}{c_m}\mathbf{N} \approx \hat{\mathbf{U}}_{h,N}\hat{\mathbf{\Sigma}}_{h,N}\hat{\mathbf{V}}_{h,N}^H. \tag{5.43}$$

and now all incident magnetic fields can expressed as a weighted combination of the orthonormal magnetic field basis as

$$\mathbf{h}_{\text{inc}} \approx \hat{\mathbf{U}}_{h,N}\mathbf{v}, \tag{5.44}$$

and the corresponding electric fields have to me consistent to the magnetic fields basis. Naturally, $\mathbf{\Sigma}_{h,N}$ and $\mathbf{\Sigma}_{e,N}$ should be equal up to scaling factor c_e/c_m.

From the above, it becomes clear that the numerical basis generation and behavior does not directly depend on the kind of the currents (electric or magnetic), rather on the operator ($\mathbf{N}$ or $\mathbf{K}$) through which the EM fields are induced and whose subspace we want to explore and compress. In other words, if we chose to generate the numerical basis with respect to incident electric fields from electric currents it should be analogous to generating the basis with respect to incident magnetic fields from magnetic currents, since the underlying operator that relates such currents and fields in both cases is $\mathbf{N}$. Similarly, if we chose to generate the numerical basis with respect to incident electric fields from magnetic currents, this is analogous to generating the basis with respect to incident magnetic fields from electric currents, since the underlying operator is $\mathbf{K}$. This is directly associated with the duality theorem [109] and the interchangeability of the electric and magnetic fields and the electric and magnetic currents.

Moreover, since operator $\mathbf{K}$ is smoother and, hence, its singular values drop faster (Figure 5.5), the basis from operator $\mathbf{K}$ is expected to require less singular vectors in order to reconstruct any EM field with the same accuracy than the basis from operator $\mathbf{N}$. In this way, less storage and less EM scattering solves are required and this basis converges faster to UISNR and UITXE, as we will demonstrate in the next section, therefore, using operator $\mathbf{K}$ for the basis generation is suggested. Finally, both SNR and TXE are metrics that are sensitive to the magnetic field, while the electric field contributions are averaged over the volume of the sample, hence, it might be beneficial to form the basis with respect to incident magnetic fields (therefore, from electric currents if operator $\mathbf{K}$ is used) in order to have orthonormal incident magnetic fields. However, the study of the convergence properties of the basis with

respect to magnetic fields and its comparison with the one with respect to electric fields is open to investigation. In this thesis, we generate the basis with respect to electric fields for both operators when validating our approach and computing performance bounds. Only for the case of DSVD we build the basis with respect to incident magnetic fields from electric currents (through $\mathbf{K}$), in order for the ICP to correspond to weighted linear combinations of electric dipole currents, since the magnetic dipole moments are associated with small current loops which might prove not so straightforward to model, especially on an arbitrary surface.

5.1.4 Total Electromagnetic Fields Basis

Computation of Total Electromagnetic Fields

The fourth step in order to generate the numerical basis is to compute the total EM fields that correspond to each vector of the Maxwell-consistent pair of electric and magnetic incident fields $(\mathbf{U}_e, \mathbf{U}_m)$ and derive a total EM fields basis. This step can be achieved by exploiting the linearity of Maxwell equations and the fact that the system operator to solve is close to full rank [66], thus the rank of the basis with the total fields is going to be close to the original rank of the basis with the incident fields.

Theoretically, any EM solver can be used to compute the EM scattering problem for each basis incident field pair but we chose to use our in-house current based VIE solver either with PWC [60] or PWL basis functions [77], which is tailor-suited for highly inhomogeneous scatterers such as the human body with fast and stable convergence properties. In the general case, by considering a material with both dielectric and magnetic properties we have to solve the following system:

$$\begin{pmatrix} \mathbf{M}_{\epsilon_r} - \mathbf{M}_{\chi_e}\mathbf{N} & c_e\mathbf{M}_{\chi_e}\mathbf{K} \\ -c_m\mathbf{M}_{\chi_m}\mathbf{K} & \mathbf{M}_{\mu_r} - \mathbf{M}_{\chi_m}\mathbf{N} \end{pmatrix} \begin{pmatrix} \mathbf{x}_e \\ \mathbf{x}_m \end{pmatrix} = \begin{pmatrix} c_e\mathbf{M}_{\chi_e}\mathbf{e}_{\text{inc}} \\ c_m\mathbf{M}_{\chi_m}\mathbf{h}_{\text{inc}} \end{pmatrix}. \tag{5.45}$$

Here, however, instead of using incident fields due to external excitations (i.e., from particular RF coils), we can use the reconstructed EM fields provided by the basis as given by Eq. 5.10, so that the right-hand side to the system can be represented as a weighted combination of the basis incident fields. In this way, we can use the basis of the incident fields as multiple right-hand sides to the system in Eq. 5.45 and then, the set of the polarization/magnetization currents solutions, generated by solving the system for each of the columns of the incident field basis, spans a basis itself able to represent the solution of the scattering problem due to any external excitation,

$$\begin{pmatrix} \mathbf{M}_{\epsilon_r} - \mathbf{M}_{\chi_e}\mathbf{N} & c_e\mathbf{M}_{\chi_e}\mathbf{K} \\ -c_m\mathbf{M}_{\chi_m}\mathbf{K} & \mathbf{M}_{\mu_r} - \mathbf{M}_{\chi_m}\mathbf{N} \end{pmatrix} \begin{pmatrix} \mathbf{X}_e \\ \mathbf{X}_m \end{pmatrix} \mathbf{w} = \begin{pmatrix} c_e\mathbf{M}_{\chi_e}\mathbf{U}_e \\ c_m\mathbf{M}_{\chi_m}\mathbf{U}_m \end{pmatrix} \mathbf{w}. \tag{5.46}$$

The columns of $\mathbf{X}_e$ and $\mathbf{X}_m$ form a valid pair of polarization and magnetization currents solutions of the scattering problem that comply with Maxwell equations. These column vectors form a basis able to represent any scattered EM field inside an inhomogeneous and arbitrary object that can be excited by any external excitation. Then, the "tested" total EM fields can be computed as the sum of incident and scattered fields according to the discrete analogue of Eq. 4.40, again by exploiting linear electromagnetism, as

$$\begin{pmatrix} \mathbf{E}_{\text{tot}} \\ \mathbf{H}_{\text{tot}} \end{pmatrix} \mathbf{w} = \underbrace{\begin{pmatrix} \mathbf{U}_e \\ \mathbf{U}_m \end{pmatrix}}_{\text{incident}} \mathbf{w} + \underbrace{\begin{pmatrix} \frac{1}{c_e}(\mathbf{N}-\mathbf{G}) & -\mathbf{K} \\ \mathbf{K} & \frac{1}{c_m}(\mathbf{N}-\mathbf{G}) \end{pmatrix} \begin{pmatrix} \mathbf{X}_e \\ \mathbf{X}_m \end{pmatrix}}_{\text{scattered}} \mathbf{w}. \tag{5.47}$$

It is important to note that the column vectors of $\mathbf{E}_{\text{tot}}$ and $\mathbf{H}_{\text{tot}}$ contain "tested" or averaged total EM fields within each voxel and each column vector should be divided by the corresponding Gram matrix for the PWC or PWL case in order to get the actual EM fields basis vectors that can be used as basis fields of a hypothetical infinite array in SNR [12], TXE [171], or SAR [278] optimization algorithms:

$$\begin{pmatrix} \mathbf{E}_{\text{tot,p}} \\ \mathbf{H}_{\text{tot,p}} \end{pmatrix} \mathbf{w} = \begin{pmatrix} \mathbf{G}^{-1}\mathbf{E}_{\text{tot}} \\ \mathbf{G}^{-1}\mathbf{H}_{\text{tot}} \end{pmatrix} \mathbf{w}. \tag{5.48}$$

In this way, through Eq. 5.47, we achieve to model an arbitrary, inhomogeneous scatterer by precomputing its response to a set of basis excitations, hence, the response to an arbitrary excitation (originating from the exterior of Huygens's surface) can be represented as a weighted, linear combination of the precomputed responses. This last step of solving for multiple incident EM fields in Eq. 5.47 constitutes the computational bottleneck of the basis generation, which, however, can be expedited by using parallel programming techniques on GPUs or by reducing the number of observation points within the scatterer by applying the discrete empirical interpolation method, as it has been introduced and applied at [279, 280] and [65, 66], respectively.

In summary, the generation of the total EM fields basis in realistic human body models requires two major steps. First, to generate a basis of consistent incident EM fields that can be induced in the body model by any external source and, second, to solve the EM scattering problem for each of the columns of the basis of the incident fields, in order to obtain the equivalent currents solution vectors and then the corresponding total EM fields. The main reasoning for applying these two steps is that generating the incident fields is usually less computational expensive than solving the system, as it only involves evaluating the free-space operator, thus, minimizing the number of solves helps to reduce the computational cost. Also, the system operator to solve is close to full rank [66], and thus the rank of the basis of the solution is going to be close to the original rank of the basis of the incident

fields. Therefore there should be little advantage in trying to directly compute the basis for the solution fields.

MRI Metrics and Optimization Problems

The total basis EM fields at Eq. 5.48 can then be used to compute performance bounds in inhomogeneous head models for SNR [67], SAR amplification factor [71], and TXE [75], among a variety of metrics introduced in the literature, where we only have to solve for the electric polarization currents since the human body is considered non-magnetic. The focal point of this thesis revolves around performance bounds for TXE and SNR, therefore, it is instructive to present formally the metrics of interest and the corresponding optimization problems that have to be solved.

In particular, SNR according to Eqs. 2.7 and 2.9, if we only include imaging sample noise and a circularly polarized RF excitation, takes the form

$$\text{SNR}(\boldsymbol{r}) = \frac{\omega M_0 B_1^-(\boldsymbol{r})}{\sqrt{4\kappa T \int_V' \sigma(\boldsymbol{r}')|\boldsymbol{E}(\boldsymbol{r}')|^2 dV'}}, \tag{5.49}$$

where, V' is the volume of the sample, $\kappa = 1.3807 \cdot 10^{-23}\text{J/K}$ is the Boltzmann constant, $T = 310\text{K}$ is the temperature in Kelvin, and $M_0 = 3.1218 \cdot 10^{-3} B_0$ A/m and these are the exact values we use in the next section for UISNR computations that allow the reproducibility of our numerical experiments. Also, $B_1^- = \mu_0(H_x - jH_y)/2$ is the RF receive magnetic field, rotating against nuclear precession [93, 123].

Similarly to Chapter 3, we exploit the linear superposition principle and SNR can be rewritten in terms of the complex weighting coefficients $\mathbf{w} \in \mathbb{C}^{Q\times 1}$ that linearly combine the vectors of the numerical EM fields basis, hence, Eq. 5.49 boils down to [12, 15, 67]:

$$\text{SNR}(\boldsymbol{r}) = \frac{\omega M_0}{\sqrt{4\kappa T}} \frac{\mathbf{B}_{1-}(\boldsymbol{r})\mathbf{w}}{\sqrt{\mathbf{w}^H \boldsymbol{\Psi} \mathbf{w}}}, \tag{5.50}$$

where,

$$\mathbf{B}_{1-}(\boldsymbol{r}) = \mu_0 \left(\mathbf{H}^x_{\text{tot,p}}(\boldsymbol{r}) - j\mathbf{H}^y_{\text{tot,p}}(\boldsymbol{r})\right)/2, \tag{5.51}$$

is the receive sensitivity matrix $\in \mathbb{C}^{M\times Q}$, $M = N_o$ is the number of the observation voxels and the superscripts in the right-hand side denote the corresponding field component.

$$\boldsymbol{\Psi} = \int_V \sigma(\boldsymbol{r}) \left(\mathbf{E}^{x,H}_{\text{tot,p}}(\boldsymbol{r})\mathbf{E}^x_{\text{tot,p}}(\boldsymbol{r}) + \mathbf{E}^{y,H}_{\text{tot,p}}(\boldsymbol{r})\mathbf{E}^y_{\text{tot,p}}(\boldsymbol{r}) + \mathbf{E}^{z,H}_{\text{tot,p}}(\boldsymbol{r})\mathbf{E}^z_{\text{tot,p}}(\boldsymbol{r})\right) dV, \tag{5.52}$$

is the sample noise covariance matrix $\in \mathbb{C}^{Q\times Q}$ for the basis vectors, where the integral is computed numerically considering PWC or PWL representations of the electric field.

The problem of maximizing Eq. 5.50 is equivalent to minimizing the cost functional $\mathbf{w}^H\mathbf{\Psi}\mathbf{w}$ by variation of the weighting vector $\mathbf{w}$ subject to constant $\mathbf{B}_{1-}(\boldsymbol{r})\mathrm{w}$, which imposes a linear constraint. In practice, the objective of the optimization is to minimize the global SAR within the sample while the receive signal sensitivity should remain equal to one at each position of interest. This problem can be viewed as a convex quadratic programming optimization problem and, according to Appendix A of [12], the optimal weighting coefficients and the corresponding UISNR take the form:

$$\tilde{\mathbf{w}}(\boldsymbol{r}_0) = \mathbf{\Psi}^{-1}\mathbf{B}_{1-}^H(\boldsymbol{r}_0)\left(\mathbf{B}_{1-}(\boldsymbol{r}_0)\mathbf{\Psi}^{-1}\mathbf{B}_{1-}^H(\boldsymbol{r}_0)\right)^{-1}, \tag{5.53a}$$

$$\mathrm{UISNR}(\boldsymbol{r}_0) = \frac{\omega M_0}{\sqrt{4\kappa T\left(\mathbf{B}_{1-}(\boldsymbol{r}_0)\mathbf{\Psi}^{-1}\mathbf{B}_{1-}^H(\boldsymbol{r}_0)\right)^{-1}}}, \tag{5.53b}$$

where $\boldsymbol{r}_0$ is the voxel position where signal reception is maximized, while at the same time global sample losses are considered [14].

Finally, for completeness, we rewrite here the UITXE, while the full derivation can be found in Chapter 3. In particular transmit efficiency is defined (Eq. 3.1) as

$$\mathrm{TXE} = \frac{\mathrm{average}|B_1^+(\boldsymbol{r})|^2}{\frac{1}{2}\int_{V'}\sigma(\boldsymbol{r}')|\boldsymbol{E}(\boldsymbol{r}')|^2 dV'}, \tag{5.54}$$

which is rewritten compactly as

$$\eta = \frac{\mathbf{w}^H\mathbf{\Gamma}\mathbf{w}}{\mathbf{w}^H\mathbf{\Phi}\mathbf{w}}, \tag{5.55}$$

where $\mathbf{\Gamma} = \mathbf{B}_{1+}^H\mathbf{B}_{1+}/M_{\mathrm{ROI}}$, with M_{ROI} denoting the number of voxels inside the ROI over which $\mathbf{B}_{1+}$ is averaged, and $\mathbf{\Phi} = \mathbf{\Psi}/2$. As we mentioned in Chapter 3 and is further explained in [171, 186], the problem of finding the maximum TXE can be treated as a generalized eigenvalue problem [171, 186, 190] which has a closed solution where the largest eigenvalue corresponds to the UITXE and the associated eigenvector gives the corresponding optimal weighting coefficients $(\tilde{\mathbf{w}})$. In practice, the objective of the TXE optimization is to maximize the ratio of the B_1^+ field over an ROI divided by the global SAR within the whole sample without any assumptions or constraints on the behavior of the transmit magnetic field, unlike the SNR case.

Similarly to the analytical case, we increase the number of total basis vectors until UITXE [75] and UISNR [67] converge and such ultimate values can be used as an absolute reference to evaluate existing transmit and receive coil array designs. Finally, the optimal weighting coefficients can be plugged in at Eqs. 5.22 or 5.30 and generate the optimal current patterns that yield UISNR [82], as we will demonstrate in the next section. Such results for highly complex and inhomogeneous realistic body models and arbitrary excitation surfaces can provide useful information for coil array designers, offering an ultimate figure of merit

against which they can benchmark their designs and giving useful insight and intuition for the optimal conductors arrangement through the ideal RF excitation patterns.

Orthonormal Total Electromagnetic Fields Basis

However, in some cases when we use the total basis EM fields from Eq. 5.47 in sensitive optimization procedures whose solution is computed numerically, such as the UITXE case where we have to compute the maximum eigenvalue of a generalized eigenvalue problem, the accuracy of these fields becomes particularly significant. In fact, when solving for the incident basis EM fields and computing the total basis EM fields, especially for higher-order basis vectors where the right-hand side is less uniform, numerical error can accumulate and cause catastrophic results in accuracy, as we will demonstrate in the next section. Driven from such observation, we seek the generation of an orthonormal basis of total EM fields with the hope that it can regularize the problem and smooth the numerically inaccurate total fields. In particular, we compute the SVD factorization of the total electric fields basis matrix in Eq. 5.47 as

$$\mathbf{E}_{\text{tot}} = \mathbf{U}_{e,t}\mathbf{\Sigma}_{e,t}\mathbf{V}_{e,t}^{H}, \tag{5.56}$$

where now $\mathbf{U}_{e,t}$ is an orthonormal basis of total electric fields and we can express all possible total electric fields as $\mathbf{e}_{\text{tot}} = \mathbf{U}_{e,t}\mathbf{q}$. Then, the corresponding basis of total magnetic fields is given as

$$\mathbf{U}_{h,t} = \mathbf{H}_{\text{tot}}\mathbf{V}_{e,t}\mathbf{\Sigma}_{e,t}^{-1}, \tag{5.57}$$

and we can use this new pair of total basis EM fields $(\mathbf{U}_{e,t}, \mathbf{U}_{h,t})$ divided by Gram as input to the optimization algorithm with the aim to improve the numerical accuracy and convergence properties of the basis for sensitive metrics such as the TXE. In fact, such approach yields great results, as we will demonstrate in the next section.

Having computed the above SVD factorization for the total EM fields basis matrix, it is interesting to take a look at the drop of its singular values and verify the expectation that they should drop slow. In fact, Figure 5.6 demonstrates such effect, where we observe that the minimum normalized singular value is around 0.05 and even this relatively small value can be attributed to the fact that we approximate the continuous current-bearing 2D shell with a triangular grid with a finite number of DoFs. Another interesting observation is that, here as well, the drop of the singular values of the total fields matrices follows the previously mentioned pattern of the drop of the singular values of incident fields coupling matrices that is associated with the smoothness of the $\mathbf{N}$, $\mathbf{K}$, and $\mathbf{E}_{N,K}$ matrices, as illustrated in Figure 5.5.

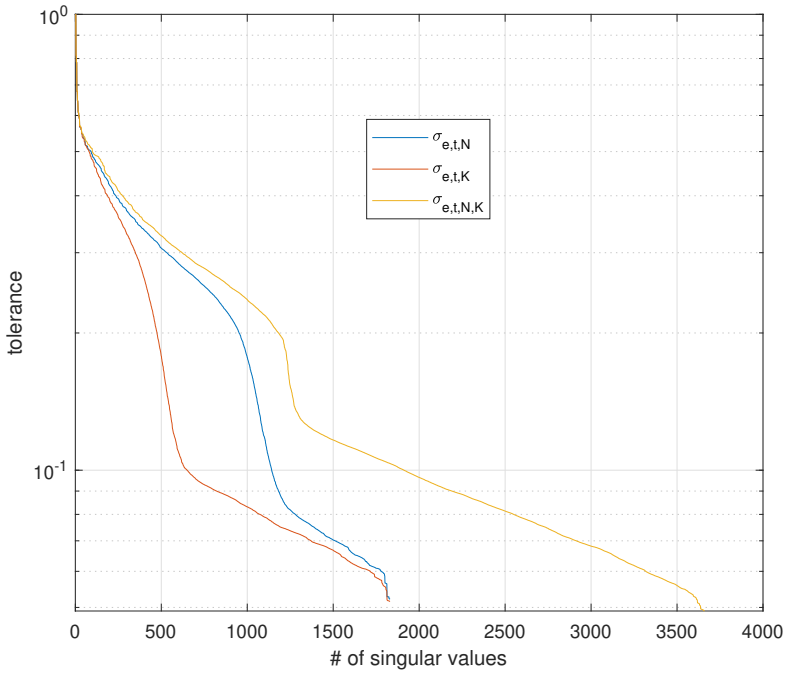

Figure 5.6: Drop of the singular values of the total EM fields matrices $\mathbf{E}_{\text{tot}}$ where the total fields for $\sigma_{e,t,N}$, $\sigma_{e,t,K}$, and $\sigma_{e,t,N,K}$ drop originate from the incident fields at Eqs. 5.24, 5.32, and 5.38, respectively. The Huygens's surface is discretized with RWG basis functions with 1830 DoFs and it is placed 3cm away from a 10cm-radius sphere. The operating frequency is 298MHz, the spherical scatterer has $(\epsilon_r, \sigma) = (20, 0.2\text{S}/\text{m})$ and is discretized with PWC basis functions and 5mm resolution resulting in 33401 observation voxels.

Summary

Similar concepts have been exploited and reduced-order models [66] have been generated for the ultra-fast design of RF coils [65] through the MR specific Green's function [161], for UISNR [67] and ultimate SAR amplification factor [71] computations within inhomogeneous head models, and for fast antenna characterization problems [273]. All these research studies depend on the generation of a numerical basis of EM fields, however, in this section, we have presented an exhaustive study of the best methodologies along with theoretical and numerical considerations when generating such basis. Additionally, in the next section, we study the impact that electrical distance has on the basis generation, the ability of the different numerical basis approaches to reconstruct EM fields and the accuracy and convergence properties of the numerical basis against a complete analytical basis derived in a spherical coordinate system for the TXE and SNR metrics [80]. We further calculate bounds for the case of TXE [75] metric, and demonstrate how they can be used to evaluate the performance of existing transmit array designs. Together with these performance bounds, we also compute the associated ICP on a given arbitrary surface that yield the corresponding EM fields within the inhomogeneous head model that result in the optimal SNR distribution [82].

5.2 Numerical Results and MRI Applications

5.2.1 Impact of Distance and Frequency

In this first subsection, we present the impact of the operating frequency and the distance between the Huygens's surface and the scatterer on the basis generation and, in particular, on the drop of singular values of $\mathbf{N}$ and $\mathbf{K}$ operators. We consider a uniform spherical object with diameter 20cm which is discretized with PWC basis functions resulting in 33401 voxels thus 100203 DoFs in the observation region. In addition, we discretize the Huygens's surface with a voxelized dipole cloud with 15mm thickness resulting in 28440 voxels thus 85320 DoFs in the sources region. We place the voxelized dipole cloud at $D = 1, 2, 3\mathrm{cm}$ distance from the spherical object and energize the dipoles in the cloud with operating frequencies $f = 63.9, 298, 447\mathrm{MHz}$, corresponding to $B_0 = 1.5, 7, 10.5T$, respectively. Since we have a uniform, voxelized domain, we generate the incident EM fields basis by employing RSVD PWC approach with 4000 random excitations, hence, 2000 singular values can be considered sufficiently accurate [66] and, in Figure 5.7, we present the results, where the first thing we notice is the relatively fast decay of the singular values where 2000 column vectors are enough to approximate the matrix (with a 10^{-4} to 10^{-5} truncation error at the fastest singular value decay) instead of 85320.

A closer look reveals the following trends. First, the distance between the dipole sources and the scatterer highly defines the number of singular vectors required for an accurate approximation, and, second, the singular values of $\mathbf{K}$ operator drop faster than the singular values of $\mathbf{N}$ operator. Such behavior can be explained by the underlying $\mathbf{K}$ and $\mathbf{N}$ operators dependence on the first-order and second-order spatial derivatives of g, hence, the near-field power-law drop-off depends on $1/|\boldsymbol{r} - \boldsymbol{r}'|^2$ and $1/|\boldsymbol{r} - \boldsymbol{r}'|^3$, respectively. In this way, $\mathbf{K}$ operator yields smoother fields and, therefore, it has a faster SV drop than $\mathbf{N}$, and the greater the separating distance D, the faster the SV drop. Additionally, the larger the separating distance D, the less the difference of the SV drop between $\mathbf{K}$ and $\mathbf{N}$ operators. Furthermore, it is observed that the operating frequency has a small impact on the SV drop, which is even smaller for the less smooth $\mathbf{N}$ operator and for smaller separating distances D which implies that the actual governing factor of the SV drop is the electrical distance between the sources and the observation region.

Detailed theoretical results on the ranks behavior with respect to the electrical distance of the separated geometry blocks [145], as well as, numerical results on the ranks behavior for the Hermitian part of the self-interactions blocks and for the off-diagonal blocks of the Green's function dedicated to the study of thermal radiation, heat transfer, and fluorescence [281] can be found in the literature, where an interested reader can refer to. Here, we only present in short, in Figure 5.8a, the SV drop of the real and imaginary parts of the

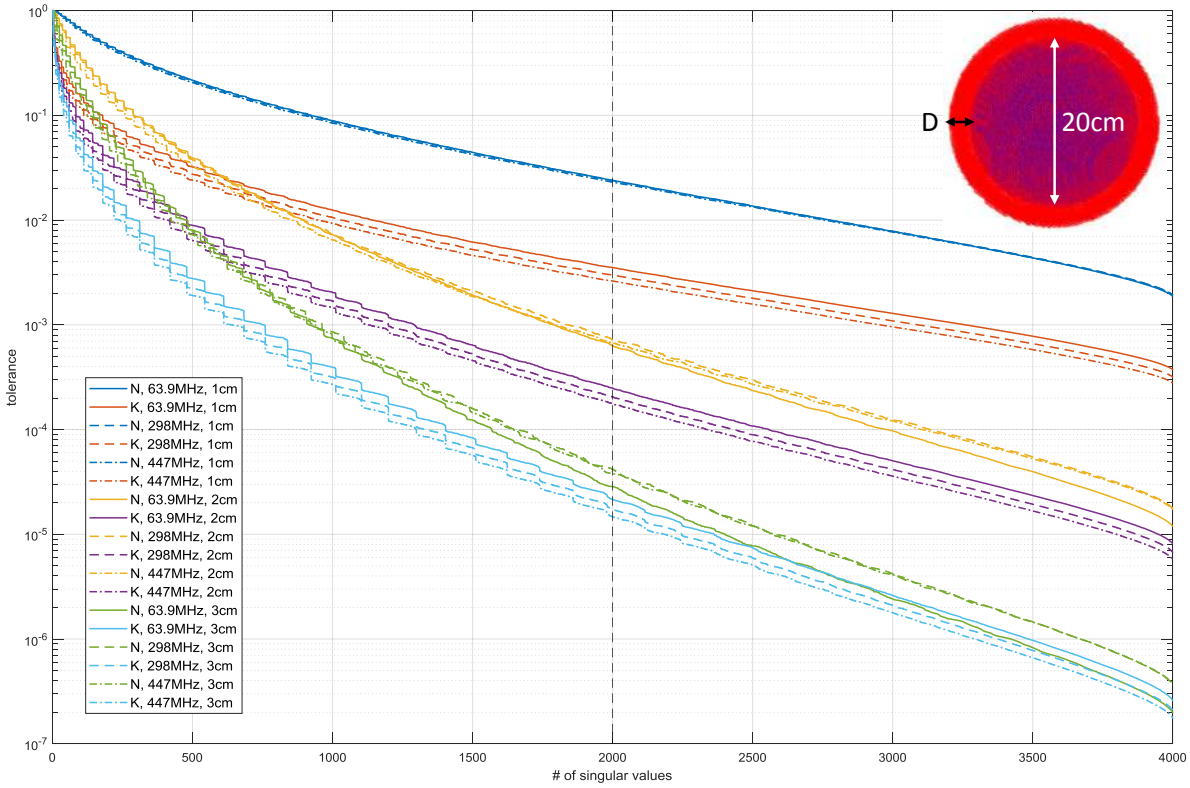

Figure 5.7: Drop of the singular values of $\mathbf{N}$ and $\mathbf{K}$ operators, at operating frequencies $f = 63.9, 298, 447\text{MHz}$, and distances $D = 1, 2, 3\text{cm}$ between the voxelized dipoles sources (red) and the spherical object (blue) with diameter 20cm. The sphere is discretized with 33401 voxels resulting in 100203 DoFs and the dipole cloud with 28440 voxels resulting in 85320 DoFs.

coupling matrices $\mathbf{N}$ and $\mathbf{K}$ at frequency $f = 298\text{MHz}$ and distance $D = 3\text{cm}$, where, in a similar manner, we observe the extremely fast SV drop of the imaginary part of the coupling matrices which is associated with the fact that the imaginary part of g, $\text{Im}\{g\} = -\frac{\sin(k_0|\boldsymbol{r}-\boldsymbol{r}'|)}{4\pi|\boldsymbol{r}-\boldsymbol{r}'|}$, is smooth. However, since we are interested in the near-field radiations of the impressed currents, such results are not to be applied in the MRI setup and they are presented here parenthetically. Finally, in Figure 5.8 we focus on the first 80 singular values of $\mathbf{N}$ operator at frequencies $f = 63.9, 298, 447\text{MHz}$ and distance $D = 3\text{cm}$, where we notice that their power is clustered at intervals with odd length mimicking the clustering of the VSH basis currents and EM fields at Eqs. 3.10 and 3.11, respectively, with degree l. This implies that the numerical basis currents and EM fields are expected to be similar to those of VSH, since our setup is equivalent (spherical shell and spherical object). Furthermore, this Figure illustrates the faster drop of the singular values of coupling matrices that relate separated blocks with larger electrical distance.

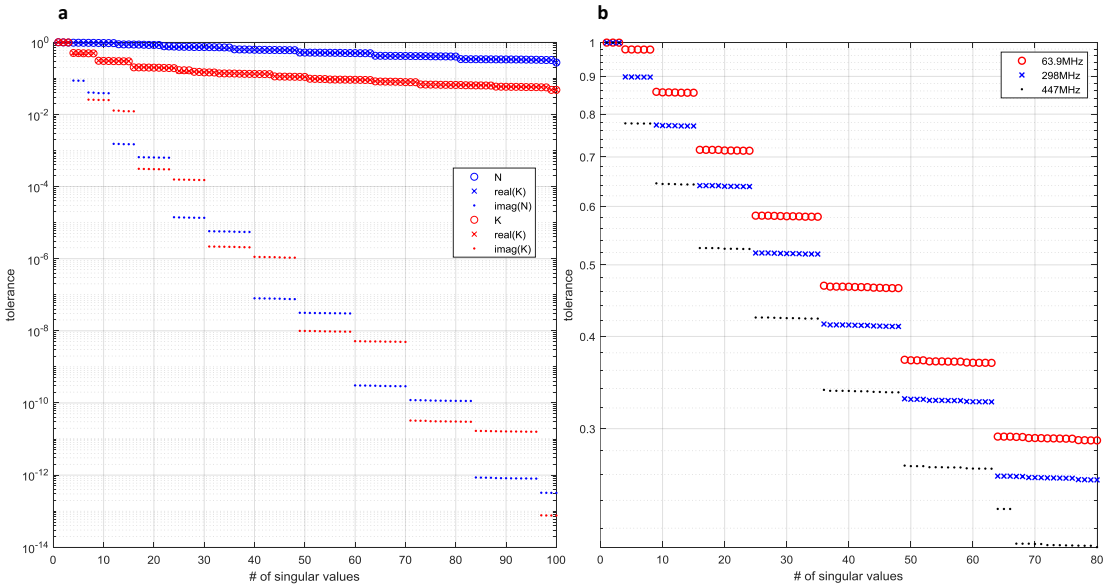

Figure 5.8: (**a**) Drop of the singular values of the real and imaginary part of $\mathbf{N}$ and $\mathbf{K}$ coupling matrices at operating frequency $f = 298\text{MHz}$ and distance $D = 3\text{cm}$ for the same setup as in Figure 5.7. (**b**) Drop of the singular values of $\mathbf{N}$ coupling matrix at operating frequencies $f = 63.9, 298, 447\text{MHz}$ and distance $D = 3\text{cm}$ for the same setup as in Figure 5.7.

5.2.2 Electromagnetic Fields Reconstruction

In this subsection, our attention shifts on investigating the ability of the numerical basis to reconstruct EM fields. In particular, we conduct 3 numerical experiments where we generate the incident EM fields basis with respect to electric fields with all 4 basis generation approaches that were presented in the previous section, i.e., from electric currents (Eq. 5.24 referred as $\mathbf{U}_{e,N}$), from magnetic currents (Eq. 5.32 referred as $\mathbf{U}_{e,K}$), from the linear combination of electric and magnetic currents contributions (Eq. 5.34 referred as $\mathbf{U}_{e,NK}$), and from the orthonormalization of the electric and magnetic currents contributions (Eq. 5.38 referred as $\mathbf{U}_{e,N,K}$). The EM fields that we aim to reconstruct originate from an x-polarized, z-directed plane wave, $\boldsymbol{E}_{\text{inc}} = \hat{\boldsymbol{x}} e^{-jk_0 z}$, from an ideal Hertzian dipole immersed at $\boldsymbol{r}_d = (0.15, 0, 0)\text{m}$ with dipole moment $\boldsymbol{p}_d = (0, 0, 1)\text{C} \cdot \text{m}$, and from a 4cm-radius vertical loop with its center located at $\boldsymbol{r}_l = (0.13, 0, 0)\text{m}$ with constant current equal to 1A and for all the cases the operating frequency is $f = 298\text{MHz}$. The scatterer is a 20cm-diameter spherical object with 5mm resolution, $(\epsilon_r, \sigma) = (20, 0.2\text{S/m})$ electrical properties, is discretized with PWC basis functions resulting in 100203 DoFs, and its distance from the Huygens's surface is 3cm (Figure 5.9).

At the first two experiments, we present the convergence of the root mean square error (RMSE) of the reconstructed by the basis incident EM field ($\hat{\mathbf{e}}_{\text{inc}} \approx \mathbf{U}_e \mathbf{w}$) and the actual

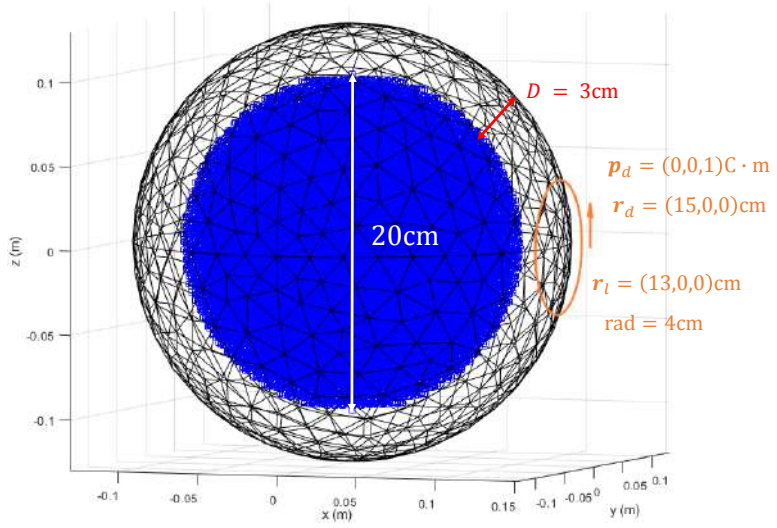

Figure 5.9: Spherical object with diameter 20cm (blue) surrounded by Huygens's surface (black) at 3cm distance, irradiated by a dipole at $\boldsymbol{r}_d = (0.15, 0, 0)\mathrm{m}$ with dipole moment $\boldsymbol{p}_d = (0, 0, 1)\mathrm{C} \cdot \mathrm{m}$, by a 4cm-radius loop with its center at $\boldsymbol{r}_l = (0.13, 0, 0)\mathrm{m}$ with constant current equal to 1A, and by an an x-polarized, z-directed plane wave, $\boldsymbol{E}_{\mathrm{inc}} = \hat{\boldsymbol{x}} e^{-jk_0 z}$.

incident EM field $(\mathbf{e}_{\mathrm{inc}})$, while at the third, we show the RMSE convergence for both the reconstructed incident and total EM fields $(\hat{\mathbf{e}}_{\mathrm{tot}} \approx \mathbf{E}_{\mathrm{tot}}\mathbf{w})$, where the reference total EM fields are computed with the PWC [60] current-based VIE $(\mathbf{e}_{\mathrm{tot}})$. When computing the RMSE convergence for $\mathbf{U}_{e,K}$, $\mathbf{U}_{e,N}$, and $\mathbf{U}_{e,N,K}$ bases, we add a single basis vector each time when we project the incident field onto each orthonormal basis in a least square sense, while at $\mathbf{U}_{e,NK}$ we use the first basis fields vectors of both $\mathbf{U}_{e,K}$ and $\mathbf{U}_{e,N}$ and project the incident field by computing the pseudo-inverse. For all the cases, we use the following RMSE metric:

$$\mathrm{RMSE}(\mathbf{v}) = \frac{\sum_{i=1}^{N_o} \sqrt{\sum_q |\hat{\mathbf{v}}_{q,i} - \mathbf{v}_{q,i}|^2}}{\sum_{i=1}^{N_o} \sqrt{\sum_q |\mathbf{v}_{q,i}|^2}}, \tag{5.58}$$

where N_o is the number of voxels within the spherical object and $q \in \{x, y, z\}$.

At the first numerical experiment, we generate all incident EM fields bases with the SSVD PWC approach, where the Huygens's surface is discretized with a 2D shell with varying number of DoFs, namely, 657, 1830, and 7218. In Figure 5.10, we present the convergence of the RMSE for the incident EM fields (from the plane wave, the dipole, and the loop) reconstruction by all 4 basis generation approaches for varying DoFs in the 2D shell.

At the second numerical experiment, we generate all incident EM fields bases both with the SSVD PWC and RSVD PWC approach, where the Huygens's surface is discretized with a 2D shell with 1830 DoFs and with a voxelized dipole cloud with 85320 DoFs, that results in 3613 basis vectors after RSVD application with 10^{-6} tolerance, respectively. In Figure

5.11, we present the convergence of the RMSE for the incident EM fields (from the plane wave, the dipole, and the loop) reconstruction by all 4 basis generation approaches for the SSVD and RSVD approach.

At the third numerical experiment, we generate all incident EM fields bases with the SSVD PWC approach, where the Huygens's surface is discretized with a 2D shell with 1830 DoFs, and this time we also compute the total EM fields basis. The total EM fields are computed with the PWC current-based VIE [60], the scatterer has $(\epsilon_r, \sigma) = (20, 0.2\mathrm{S/m})$ electrical properties, and is discretized with 5mm resolution. In Figure 5.12, we present the convergence of the RMSE for the incident and total EM fields (from the plane wave, the dipole, and the loop) reconstruction by all 4 basis generation approaches.

In Figure 5.10, we observe that the fastest reconstruction of all the incident EM fields is achieved by the basis that originates from the linear combination of electric and magnetic currents contributions $(\mathbf{U}_{e,NK})$. However, the RMSE convergence from this basis is not stable and diverges at the finest 2D shell case since the higher-order basis fields are close to being linearly dependent, and when computing the pseudo-inverse numerical error arises. The second fastest reconstruction of all incident EM fields is achieved by the basis that originates from the contributions of magnetic currents $(\mathbf{U}_{e,K})$, validating the expectation that the faster rate of the SV drop of $\mathbf{K}$ operator affects the convergence rate of the EM fields reconstruction. Additionally, such basis is orthonormal, hence, its convergence is stable, even for the finest 2D shell. Furthermore, the RMSE convergence achieved by the basis that originates from the orthonormalization of the electric and magnetic currents contributions $(\mathbf{U}_{e,N,K})$ is similar to that from the contributions of electric currents $(\mathbf{U}_{e,N})$, validating the expectation that contributions of $\mathbf{K}$ operator are suppressed when orthonormalizing and the convergence rate is very closely dictated by the SV drop of the less smooth $\mathbf{N}$ operator (Figure 5.5). Therefore, since the basis from magnetic currents $(\mathbf{U}_{e,K})$ provides the second fastest, yet stable, RMSE convergence for all incident EM fields and the surface equivalence principle can be formulated from only one kind of currents [193, 277], we suggest following this approach for generating the numerical basis.

The trends we described in the previous paragraph hold exactly true for the case of the smooth plane wave, however, some interesting local characteristics can be observed for the dipole and loop excitation. Specifically, the loop EM field can be reconstructed equally fast by $\mathbf{U}_{e,K}$ and $\mathbf{U}_{e,NK}$ basis when we focus on the contributions of the first 400 basis fields. On the contrary, the reconstruction by $\mathbf{U}_{e,N}$ basis is much slower than that of $\mathbf{U}_{e,N,K}$. Such behavior can be explained by the fact that, in the limiting case, loop EM fields are associated with magnetic currents, therefore, with the subspace of operator $\mathbf{K}$. Similarly, the dipole EM field can be reconstructed faster by $\mathbf{U}_{e,N}$ and $\mathbf{U}_{e,N,K}$ basis when we focus on the contributions of the few first basis fields (it is clearer for the magnetic field case) and the

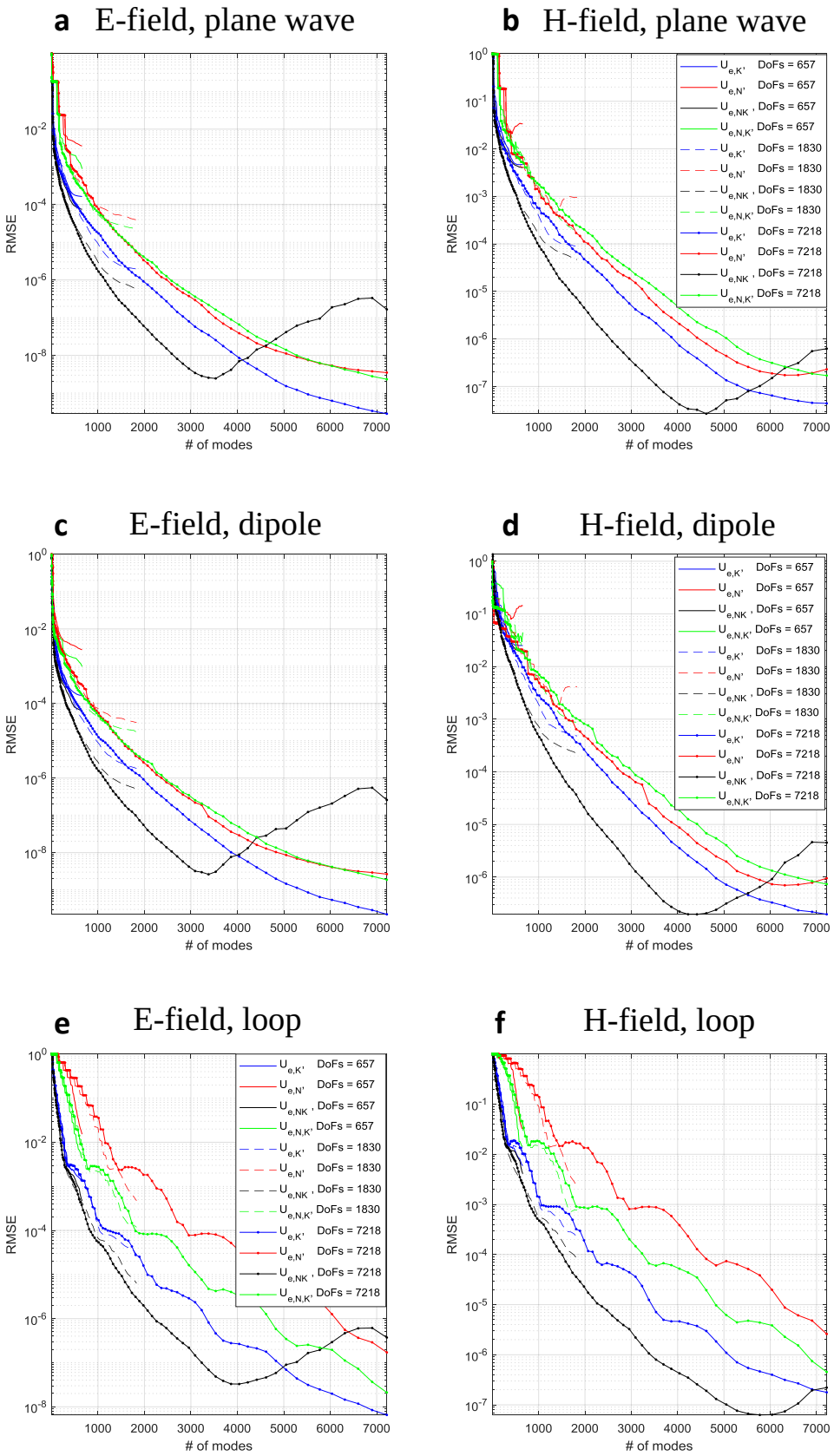

Figure 5.10: RMSE convergence of incident EM fields (plane wave, dipole, loop) reconstruction by all 4 basis generation approaches and for a 2D shell Huygens's surface with 657, 1830, and 7218 number of DoFs.

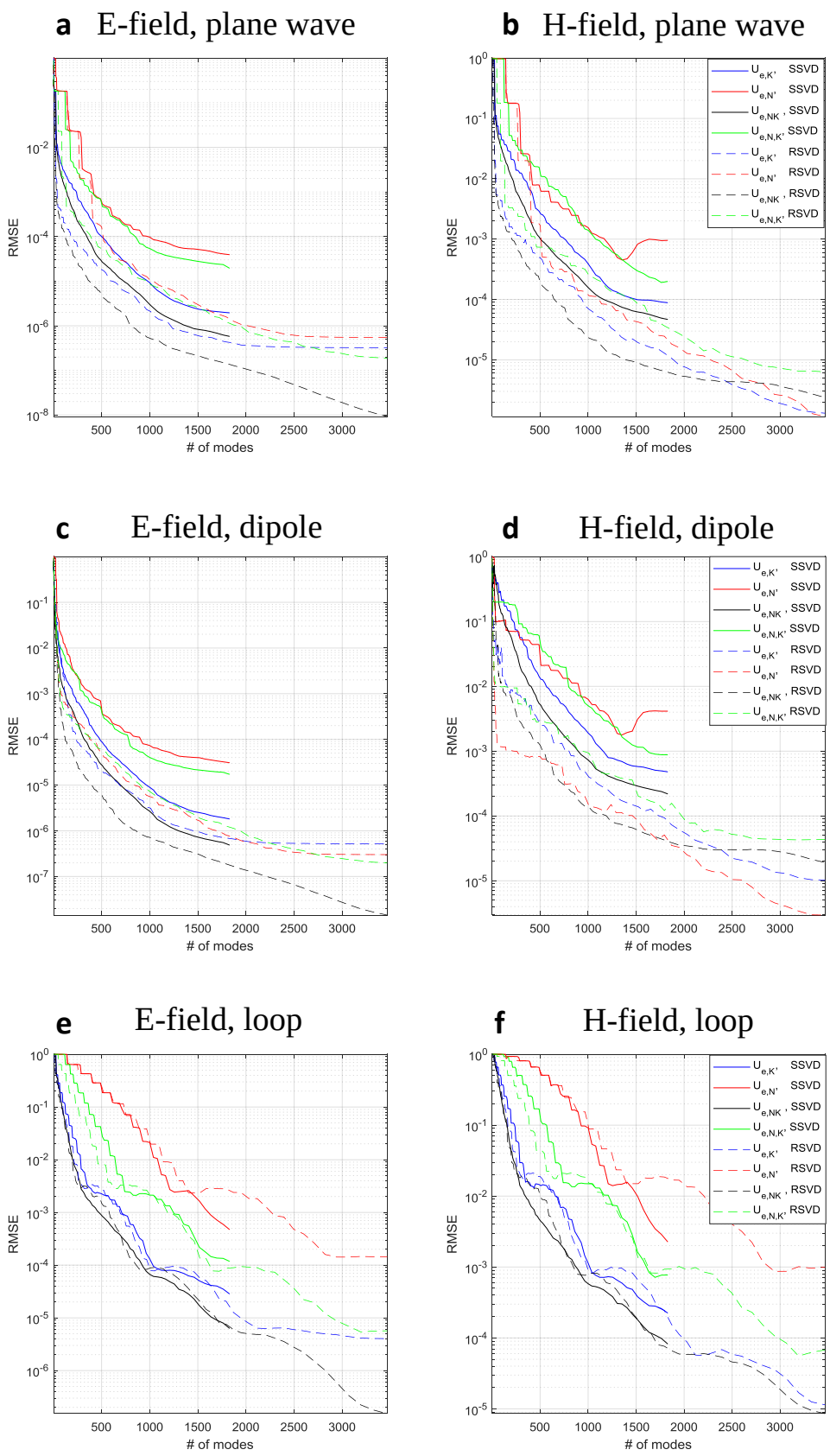

Figure 5.11: RMSE convergence of incident EM fields (plane wave, dipole, loop) reconstruction by all 4 basis generation approaches and for a 2D shell Huygens's surface with 1830 DoFs and for RSVD with 3613 singular vectors.

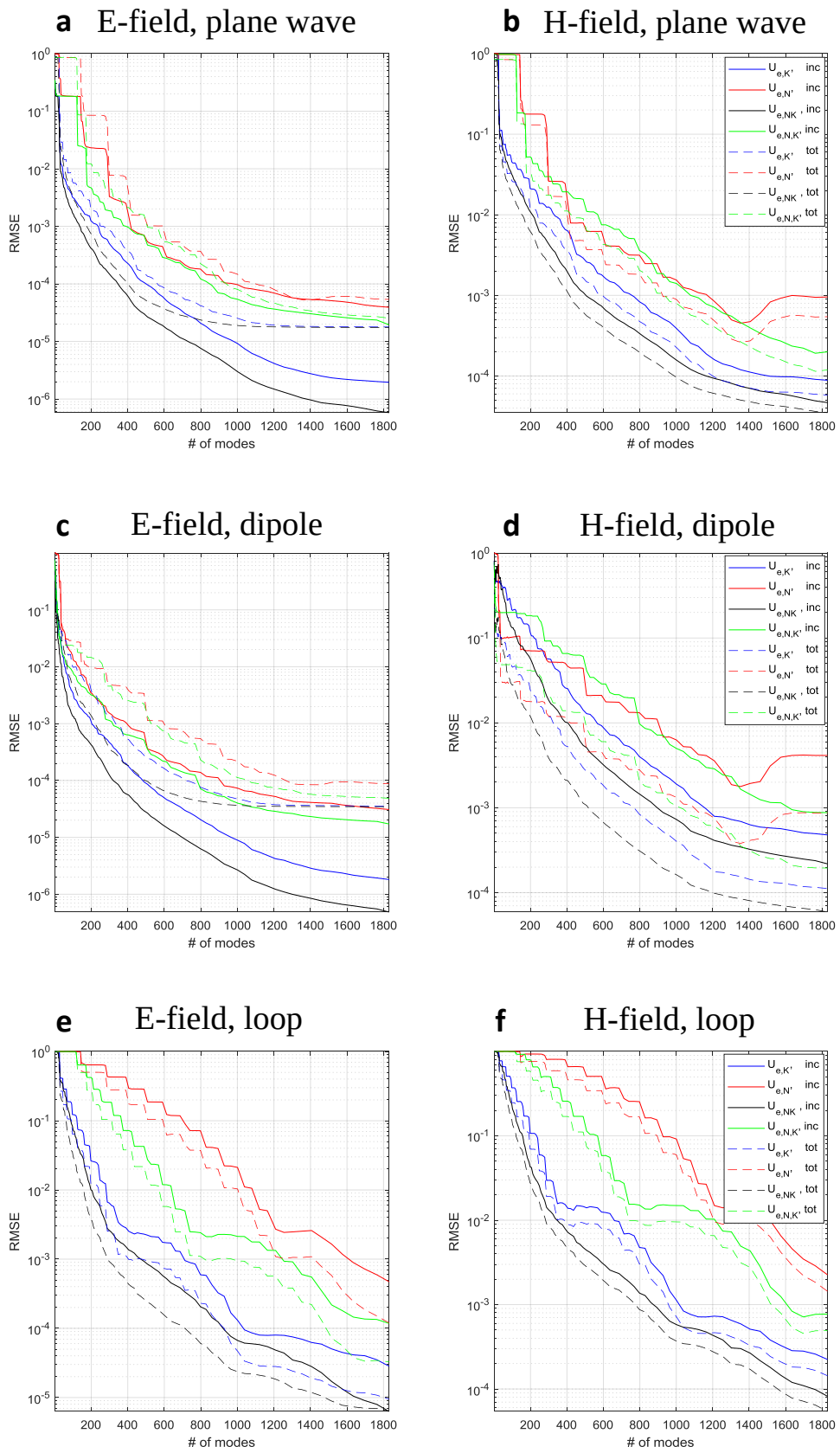

Figure 5.12: RMSE convergence of incident and total EM fields (plane wave, dipole, loop) reconstruction by all 4 basis generation approaches and for a 2D shell Huygens's surface with 1830 number of DoFs.

reconstruction by $\mathbf{U}_{e,K}$ basis is slower than that by $\mathbf{U}_{e,NK}$. Similarly, such behavior can be explained by the fact that, in the limiting case, dipole EM fields are associated with electric currents, therefore, with the subspace of operator $\mathbf{N}$.

The impact of the distance on the EM fields reconstruction is evident, since the EM field from a loop (which is placed the closest to Huygens's surface) has the slowest RMSE convergence and requires the most basis fields for an accurate representation. Furthermore, refinement does not affect significantly the RMSE convergence at the first basis vectors, but, naturally, for a smaller RMSE and a better accuracy more DoFs in the 2D shell are required. In addition, by comparing the RMSE convergence from the 1830-DoFs and the 7218-DoFs shell, we notice that the curves coincide for roughly half the singular vectors (900) of the coarser 2D shell. Therefore, similarly to RSVD, it is suggested that half of singular values in the SSVD approach should be exactly trusted, due to discretization concerns. Finally, for the case of the plane wave and dipole magnetic field reconstruction by $\mathbf{U}_{e,N}$ basis, the RMSE slightly diverges when the last basis fields contributions are included. This can possibly be explained by the fact that the last basis fields, particularly from $\mathbf{N}$ operator, are not accurate and when imposing the orthogonality relationship for the magnetic field, numerical error arises.

In Figure 5.11, similar trends and considerations with respect to the basis generation approaches and the excitation type are observed for the RSVD PWC basis, as well. A differentiating factor is that the RMSE from RSVD PWC converges faster than from SSVD, except for the case of the loop EM field reconstruction. The difference in convergence rate can be explained by the fact that RSVD is generated with tolerance 10^{-6}, hence, all 3613 basis fields can be trusted, whereas the 2D shell has only 1830 DoFs. A more fair numerical experiment would involve the careful choice of tolerance in RSVD that would yield comparable number of basis fields with the DoFs of the 2D shell.

Finally, in Figure 5.12, we present the RMSE convergence for both incident and total EM fields for the basis from the 2D shell with 1830 DoFs. Regarding the RMSE convergence for total EM fields, the trends and considerations with respect to the basis generation approaches and the excitation type remain practically the same with the incident EM fields, as we have discussed them in detail when commenting Figure 5.10. Finally, there is no consistent trend regarding whether total or incident EM fields convergence rate is faster.

5.2.3 Numerical Accuracy and Convergence Properties

In this subsection, we study the convergence properties and accuracy of the numerical basis for UISNR (Eq. 5.53) and UITXE (generalized eigenvalue problem of Eq. 5.54) metrics against an analytical, complete basis from VSH, as it has been defined at Eq. 3.11. Such analytical EM fields basis has been employed for UISNR [12, 15] and UITXE [74, 75] semi-

analytical computations in uniform spherical objects and we compare our numerical results against these calculations, where we use $l_{\max} = 45$ yielding $N = (l_{\max}+1)^2 = 2116$ modes to ensure convergence of the VSH basis.

Simulation Setup and Drop of Singular Values

Specifically, we generate the numerical EM fields basis with 4 approaches, at all of which the operating frequency is $f = 298\mathrm{MHz}$ and the Huygens's surface is placed at 3cm distance from a uniform spherical object with $a = 10\mathrm{cm}$ radius, $(\epsilon_r, \sigma) = (20, 0.2\mathrm{S/m})$ electrical properties, and $dx = 5\mathrm{mm}$ resolution. Furthermore, the numerical basis is generated both from $\mathbf{K}$ and $\mathbf{N}$ operator. At the first approach, Huygens's surface is discretized with a 2D shell with 1830 DoFs and the spherical object with 33401 voxels and PWC basis functions resulting in 100203 DoFs (SSVD PWC). At the second, again Huygens's surface is discretized with a 2D shell with 1830 DoFs and the spherical object with 33401 voxels but PWL basis functions are now used resulting in 400812 DoFs (SSVD PWL). At the third approach, Huygens's surface is discretized with a voxelized dipole cloud with 28440 voxels and RSVD is employed with 10^{-6} tolerance resulting in 3347 and 3611 number of basis fields for $\mathbf{K}$ and $\mathbf{N}$, respectively, and the spherical object has 33401 voxels with PWC basis functions resulting in 100203 DoFs (RSVD PWC). Finally, at the fourth approach, we use again a voxelized dipole cloud with 28440 voxels and RSVD with 10^{-4} tolerance resulting in 1513 and 1789 number of basis fields for $\mathbf{K}$ and $\mathbf{N}$, respectively, and the spherical object has 33401 voxels with PWL basis functions resulting in 400812 DoFs (RSVD PWL). When the scatterer is discretized with PWC or PWL basis functions, we compute the total EM fields with [60] or [77] current-based VIE solvers, respectively, and GMRES iterative solver is employed with inner iterations 50, outer 200, and tolerance 10^{-5}.

First, we present the drop of singular values of both operators for all 4 discretization schemes (Figure 5.13) to develop intuition for the expected convergence rate of UISNR and UITXE. We notice, once again, the faster drop of singular values of $\mathbf{K}$ operator, hence, we expect UISNR and UITXE to converge faster from this basis. In addition, we see that RSVD and SSVD SV drops coincide for the case of the smoother $\mathbf{K}$ operator but they are different for $\mathbf{N}$ operator, even at the first singular values, since the less smooth EM fields possibly affect the approximate RSVD approach. Furthermore, discretizing the scatterer with PWL basis functions does not affect the SV drop, particularly, for SSVD since no additional DoFs are added in the sources regions. However, there exists a difference between PWC and PWL RSVD, since additional DoFs are added in the sources region and this also affects their SV drop, where we can see that PWL RSVD drops somewhat slower than PWC RSVD and more closely to the SV drop of SSVD.

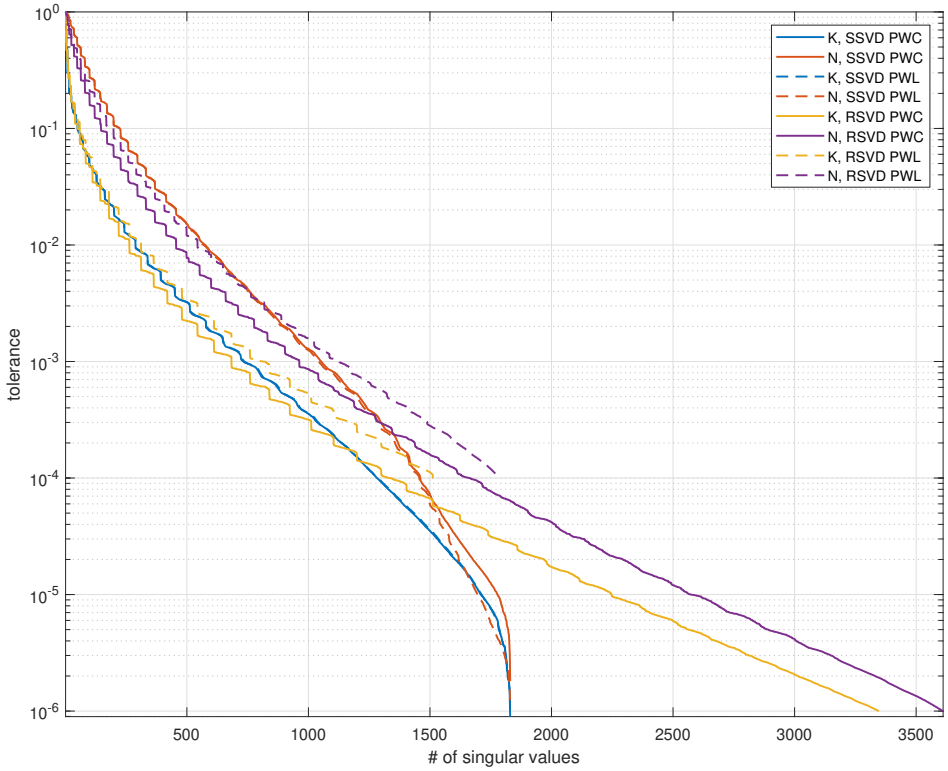

Figure 5.13: Drop of the singular values of $\mathbf{K}$ and $\mathbf{N}$ operator, for SSVD PWC and PWL, and for RSVD PWC and PWL. The Huygens's surface is placed 3cm away from a 10cm-radius sphere, the operating frequency is 298MHz, and the spherical object is discretized with 5mm resolution.

UISNR Convergence in Spherical Objects

Next, we present the convergence of UISNR for different voxel positions for all 4 discretization schemes and both operators (Figure 5.14) against the VSH basis. We can see that all numerical approaches converge to a similar value of UISNR after increasing sufficiently the number of basis vectors, and, naturally, UISNR computed with PWL basis functions is closer to that of VSH. For all voxel positions, VSH basis converges faster than the SVD-based numerical basis from $\mathbf{N}$ operator, since VSH is a basis specifically developed for spherical geometries. However, this difference in convergence rate is significantly mitigated in UISNR convergence computation by the smoother $\mathbf{K}$ operator, where we can observe that, as we move farther away from the center of the sphere and optimize voxels closer to the surface, VSH and SVD basis from $\mathbf{K}$ operator requires almost the same number of basis vectors for convergence. Finally, there is practically no difference in convergence rate between the RSVD and SSVD approach or between the PWC and PWL discretization scheme, particularly for the basis from $\mathbf{K}$ operator, while from $\mathbf{N}$ small differences can be seen.

At this point, we consider it instructive to present the RMS value of the first basis vectors of the incident electric field basis from VSH and SVD over the mask of the spherical object.

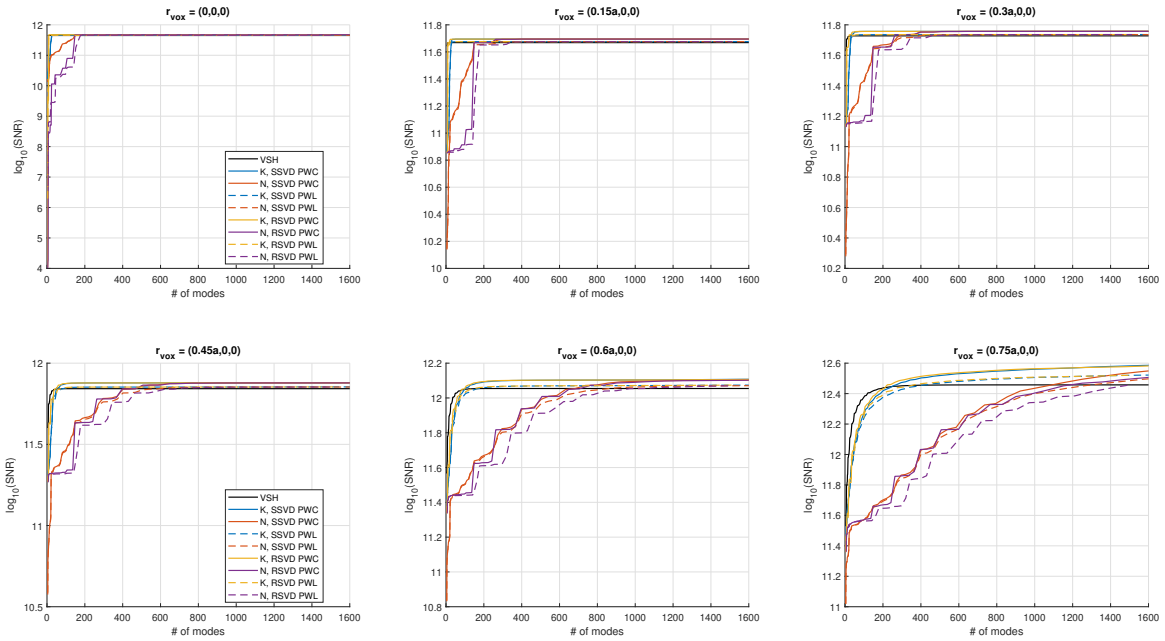

Figure 5.14: Convergence of UISNR for different voxel positions for the numerical bases from $\mathbf{K}$ and $\mathbf{N}$ operator, SSVD PWC and PWL, and RSVD PWC and PWL discretization schemes.

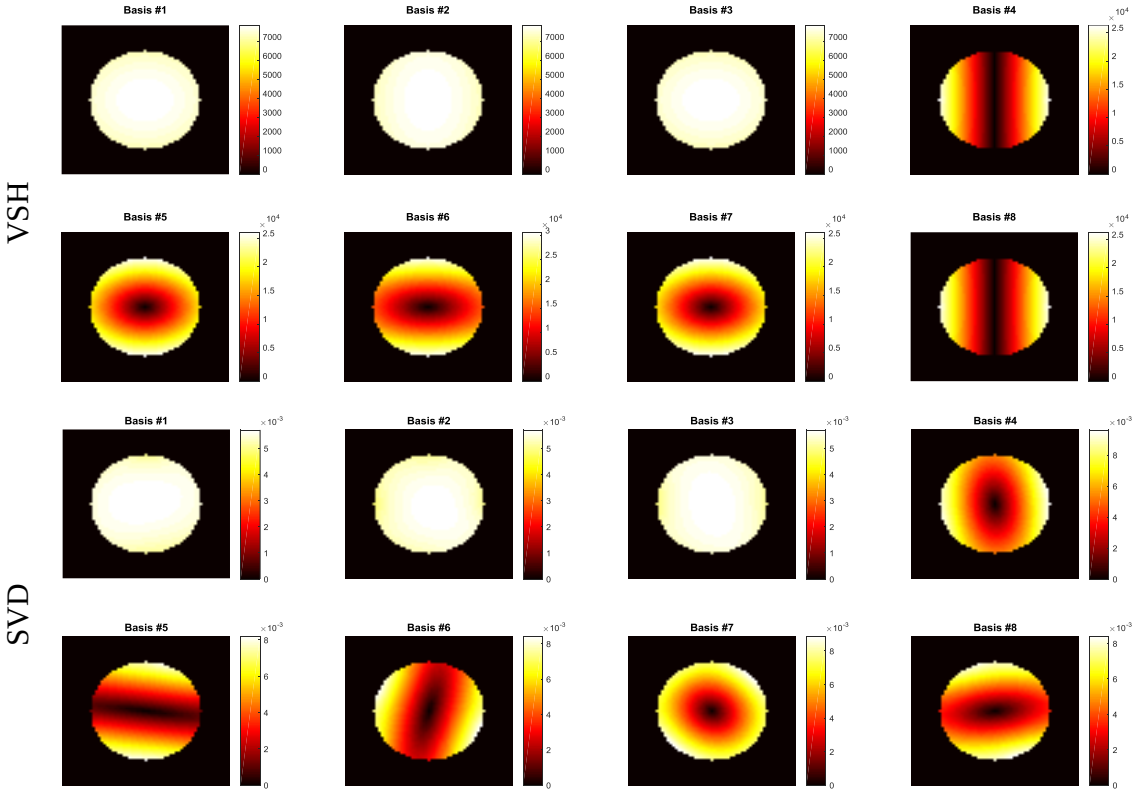

Figure 5.15: RMS value of the 8 first incident electric field basis vectors of the VSH and SVD basis across the central axial plane of the spherical object.

Specifically, in Figure 5.15, we show the 8 first basis vectors over the central axial plane of the spherical object and notice that they are practically the same, up to scaling factor and reordering of the basis fields that correspond to singular vectors with the same power as determined by the clustering of the singular values in Figure 5.8b.

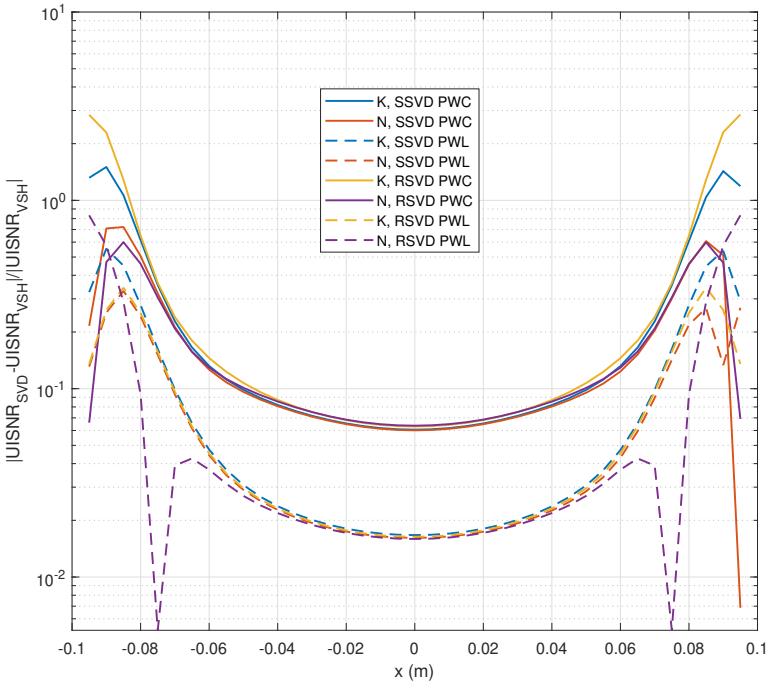

Figure 5.16: Relative error of UISNR across the diameter of the uniform sphere computed with the different numerical basis approaches against analytical calculations from a VSH basis.

Next, we present the relative error of UISNR across the diameter of the uniform sphere from all the above-mentioned numerical approaches, where we include all the available basis fields from each basis, with respect to analytical VSH calculations (Figure 5.16) for a quantitative validation of the proposed algorithms. From this figure, we can notice that the main governing factor that determines accuracy is the choice of the solver for computing the total EM fields. Specifically, at the center of the sphere, the relative error of UISNR, when PWL basis functions are employed, is around 1.5%, while for PWC it is 6%, independently of the choice of the sources discretization scheme (shell or voxelized dipole cloud) or of the compressed operator ($\mathbf{N}$ or $\mathbf{K}$). However, closer to the surface of the spherical object, the error grows fast due to the staircase approximation of the shape of the sphere and such error is usually mitigated with h-refinement of the spherical object, as we will demonstrate in the next subsection [75] and it has been studied at [67] for the RSVD PWC case. Additionally, there is a subtle trend that the relative error from the basis from $\mathbf{N}$ operator tends to be smaller closer to the surface but, in general, such trend is not consistent.

UITXE Convergence in Spherical Objects

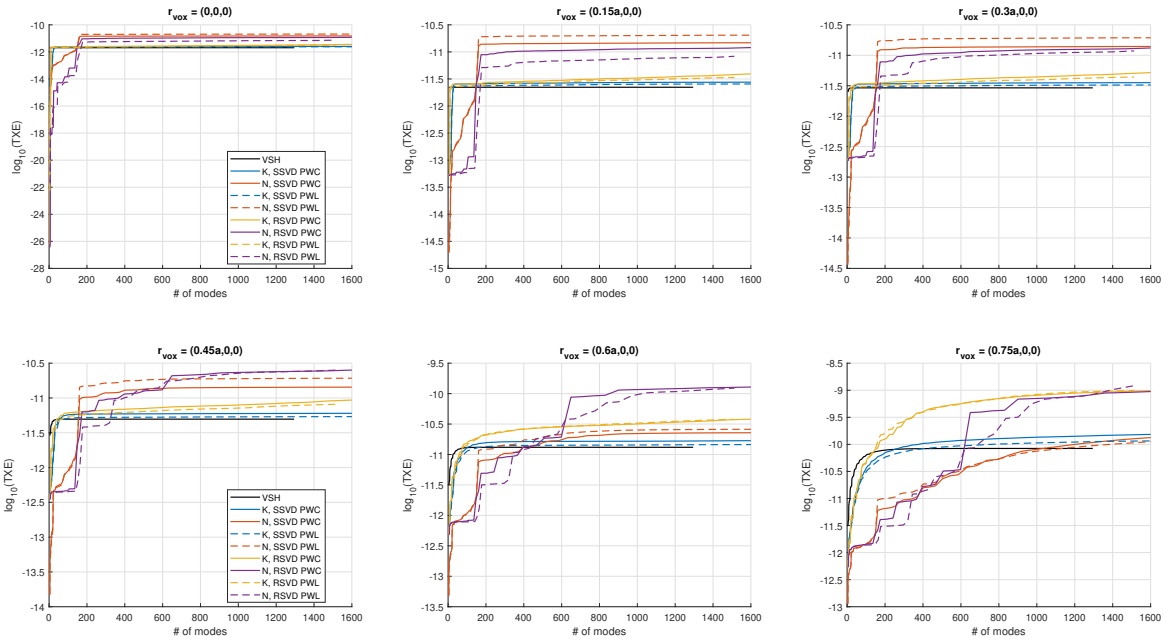

Figure 5.17: Convergence of UITXE for different voxel positions for the numerical bases from $\mathbf{K}$ and $\mathbf{N}$ operator, SSVD PWC and PWL, and RSVD PWC and PWL discretization schemes.

In what follows, our attention shifts on studying the convergence properties and numerical accuracy of UITXE. Similarly to the UISNR case, we first present the convergence of UITXE for different voxel positions for all 4 discretization schemes and for both operators (Figure 5.17) against the VSH basis, however, here, the situation changes dramatically. Although, still UITXE converges to some values, such values differ very significantly from the analytical computations and are not to be trusted. In particular, UITXE computations from $\mathbf{N}$ operator are even less accurate than those from $\mathbf{K}$ for both of the sources discretization schemes (shell or voxelized dipole cloud) and UITXE computations from RSVD are significantly less accurate than SSVD approach for both operators. In fact, the only approach that can be considered marginally admissible (with an 18.5% relative error in the center of the sphere) is the SSVD from $\mathbf{K}$ operator with PWL basis functions which still provide more accurate results than PWC, but not as good as one would expect (see Figure 5.18 for quantitative results).

Such results are somewhat surprising, given the fact that the only factor that has changed between UISNR and UITXE computations is the optimization strategy, and the reason we chose to include them in this thesis is to make the reader aware of the fact that the convergence properties and accuracy of the numerical EM fields basis are problem dependent and should be treated with care. In fact, in this particular example, there are 3 possible underlying factors that could account for such a behavior. The first is associated with the sensitive

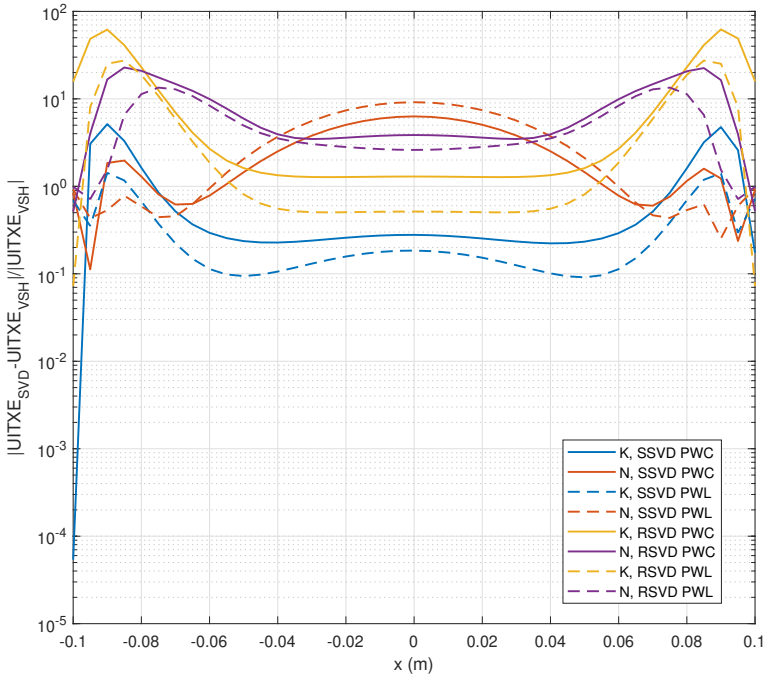

Figure 5.18: Relative error of UITXE across the diameter of the uniform sphere computed with the different numerical basis approaches against analytical calculations from a VSH basis.

optimization procedure of solving the generalized eigenvalue problem, where the largest eigenvalue (UITXE) has to be computed numerically, in contrast with UISNR, where there exists a closed-form expression. In such cases, the accuracy of the total EM fields becomes crucial, especially for higher-order basis incident fields where the right-hand side becomes less smooth, and unless they are particularly accurate, catastrophic results may arise, as in the UITXE case. The second is further connected with the smoothness of the EM fields and this can be seen by the fact that the basis from $\mathbf{N}$ operator provides by far with the least accurate results, accompanied by steep jumps in the convergence curve (Figure 5.17), possibly associated with spurious basis fields contributions. The last is related to the fact that RSVD is an approximate SVD factorization and such hypothesis can be confirmed by comparing the relative error of the basis from $\mathbf{K}$ operator generated from SSVD and RSVD approach (see Figure 5.18), where SSVD gives clearly more accurate results. However, it has been suggested in the literature that the accuracy of RSVD can be improved by power iterations application [81] and it could be worth investigating towards this direction.

In this thesis, however, we follow an alternative approach, namely, that of generating an orthonormal basis of total EM fields (Eq. 5.56), as described in the previous section and, in fact, such approach yields great results and remedies the problem. A second alternative could be to generate directly a total EM fields basis by applying the free-space operator, solving the scattering problem for each random EM field for RSVD or for each column vec-

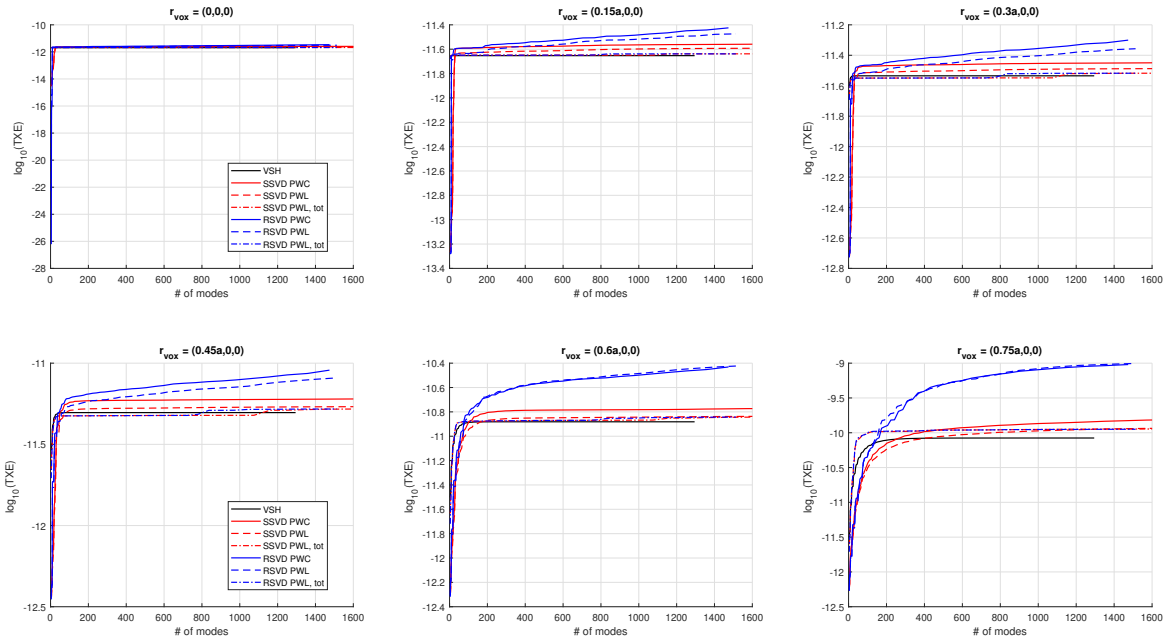

Figure 5.19: Convergence of UITXE for different voxel positions for the numerical bases from $\mathbf{K}$ operator, SSVD PWC and PWL, RSVD PWC and PWL, and for the orthonormal total EM fields basis for PWL SSVD and RSVD.

tor of the coupling matrix for SSVD and DSVD, and then orthonormalizing. This approach is more computationally expensive but might be worth investigating as a future step. Here, we generate an orthonormal basis of total EM fields by computing the SVD factorization of the computed total EM basis fields from the incident basis fields and, indeed, such approach regularizes the problem and smooths the numerically inaccurate total EM fields. Specifically, it has a twofold advantage: first it accelerates and stabilizes the convergence rate of UITXE for all different voxel positions and discretization schemes (RSVD and SSVD) which, in practice, now coincides with the convergence rate of the VSH basis and, second, it significantly increases the numerical accuracy of the converged UITXE value. The first effect can be seen in Figure 5.19, where we include the results only from $\mathbf{K}$ operator, since it provides with the only admissible results without orthonormalizing, hence, from now on, we only compute the basis from this operator for UITXE calculations. In this figure, we can see the stabler and faster convergence rate of the orthonormal total EM fields basis both for RSVD and SSVD, with RSVD being improved significantly more than SSVD.

Quantitative results, demonstrating the accuracy increase (second effect), are presented at Figure 5.20, where we show the relative error of UITXE from the orthonormal total EM fields basis with respect to VSH analytical calculations. Specifically, when optimizing TXE at a single voxel at the center of the sphere without orthonormalizing the total EM fields, the minimum relative error (from SSVD PWL) is 18.5%, whereas, with the suggested approach, it drops to 3.5%, both for SSVD and RSVD PWL, between which there is practically no dif-

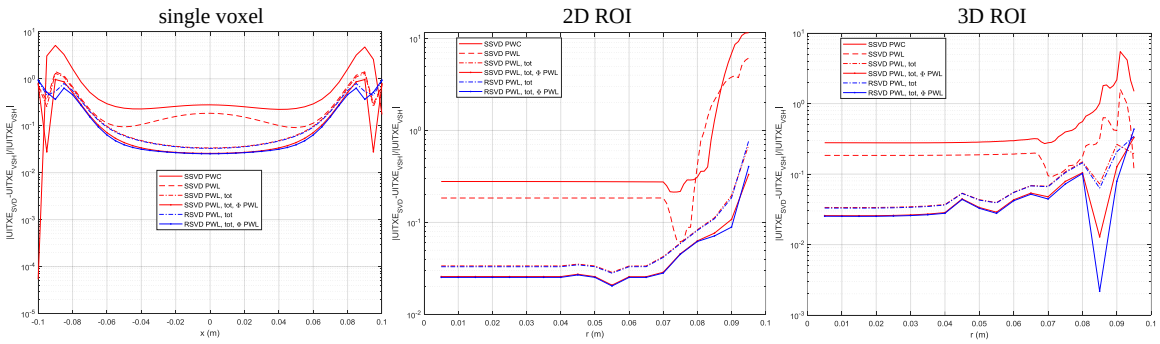

Figure 5.20: Relative error of UITXE for single voxels across the diameter of the uniform sphere, 2D, and 3D ROIs computed with the orthonormal total EM fields basis for PWL SSVD and RSVD against analytical calculations from a VSH basis.

ference. Furthermore, when RF power correlation matrix $\mathbf{\Phi}$ is computed with a numerical integration quadrature scheme that includes the contributions of the PWL terms of the electric field, there is a small improvement in the relative error which drops to 2.5%. This value is similar to the relative error of UISNR (1.5%) for the same voxel position, where no total EM fields orthonormalization is imposed and no PWL terms are included in $\mathbf{\Phi}$ integral. Hence, it is strongly suggested that the orthonormal total EM fields basis from $\mathbf{K}$ operator should be used and, when memory and computation time concerns permit, PWL basis functions should be employed for UITXE computations. In the next subsection, we use this approach (i.e., the orthonormal total EM fields basis with SSVD PWL and covariance matrix including the linear terms) when computing the UITXE in realistic head models [75]. Finally, the relative error of UITXE with respect to VSH for 2D and 3D ROIs presents the same trends with the single voxel case. For ROI sizes with radii up to 70% of the sphere's radius, the best approach yields a 2.5% relative error, while for larger ROI sizes the error grows fast, since the superficial voxel positions with their associated staircase approximation error determine the value of UITXE in the whole ROI, but such error can be mitigated with h-refinement, as we show in the next subsection.

UISNR Convergence in Arbitrary Objects

In terms of convergence, we conduct an additional numerical experiment where we compute UISNR in objects with arbitrary shape, namely, a homogeneous cube and an inhomogeneous head model [80]. Specifically, we compare the convergence rate of the SVD numerical basis and the VSH basis. We generate the numerical basis with respect to electric fields from the linear combination of the electric and magnetic currents contributions (Eq. 5.34) to ensure the fastest convergence and we truncate on-the-fly to ensure stability. The Huygens's surface is discretized with the SSVD approach where the 2D shell completely encapsulates the arbitrary object and we compute UISNR as it has been described in the previous sections. For the VSH basis, we use its free-space incident EM fields (from Eq. 3.11) over the mask

of the cube or the head model and we use $l_{\max} = 55$ yielding $N = (l_{\max}+1)^2 = 3136$ modes. We also account for boundary conditions only at the surface of the surrounding current-bearing spherical surface (by setting $C_l = D_l = 1$ at Eq. A.11) in order to have a setup equivalent to that of the numerical basis. Then, we use these EM fields as right-hand side excitations at our in-house current-based VIE solvers [60, 77] and compute the total EM fields that can be used as basis fields for the computation of UISNR. A similar approach based on the combination of the vector wave eigenfunction expansion of the spherical and cylindrical Helmholtz operator with the above-mentioned ultra-fast VIE solver [60] has recently allowed to obtain ICP in cylindrical and open spherical surfaces that yield optimal SNR in realistic head models [68, 72].

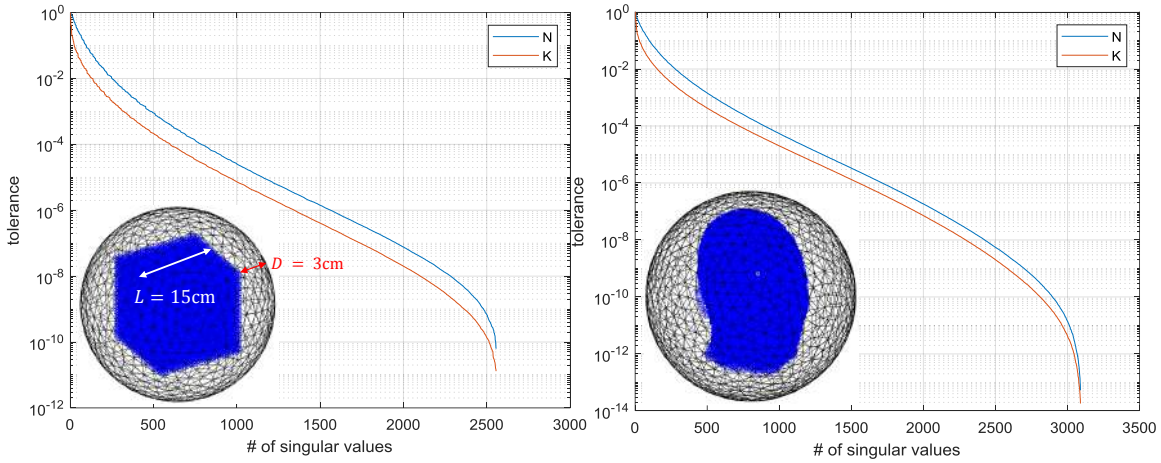

Figure 5.21: Simulation setups for homogeneous cube and "Duke" head model and drop of singular values of the coupling matrices.

The homogeneous cubic object has edge length $L = 15\text{cm}$, $(\epsilon_r, \sigma) = (20, 0.2\text{S/m})$ electrical properties, and it is discretized with $dx = 5\text{mm}$ resolution resulting in 29791 voxels and 89373 or 357492 DoFs for the solver with PWC or PWL basis functions, respectively. Additionally, the 2D shell has 2556 DoFs and its distance from a vertex of the cube is $D = 3\text{cm}$ (Figure 5.21). Finally, the operating frequency is $f = 298\text{MHz}$ and we compute the total EM fields with both PWC and PWL solvers where GMRES iterative solver is employed with inner iterations 50, outer 200, and tolerance 10^{-5}. Similarly, we crop "Duke" realistic human body model with $dx = 5\text{mm}$ resolution and keep the inhomogeneous head resulting in 38770 voxels and 116310 DoFs for the PWC solver and, in this case, the 2D shell has 3090 DoFs (Figure 5.21). The operating frequency is again $f = 298\text{MHz}$ and the total EM fields are computed with the PWC solver and GMRES with the same properties as before. We note that the total EM fields from the incident VSH basis EM fields are calculated with the same EM solvers.

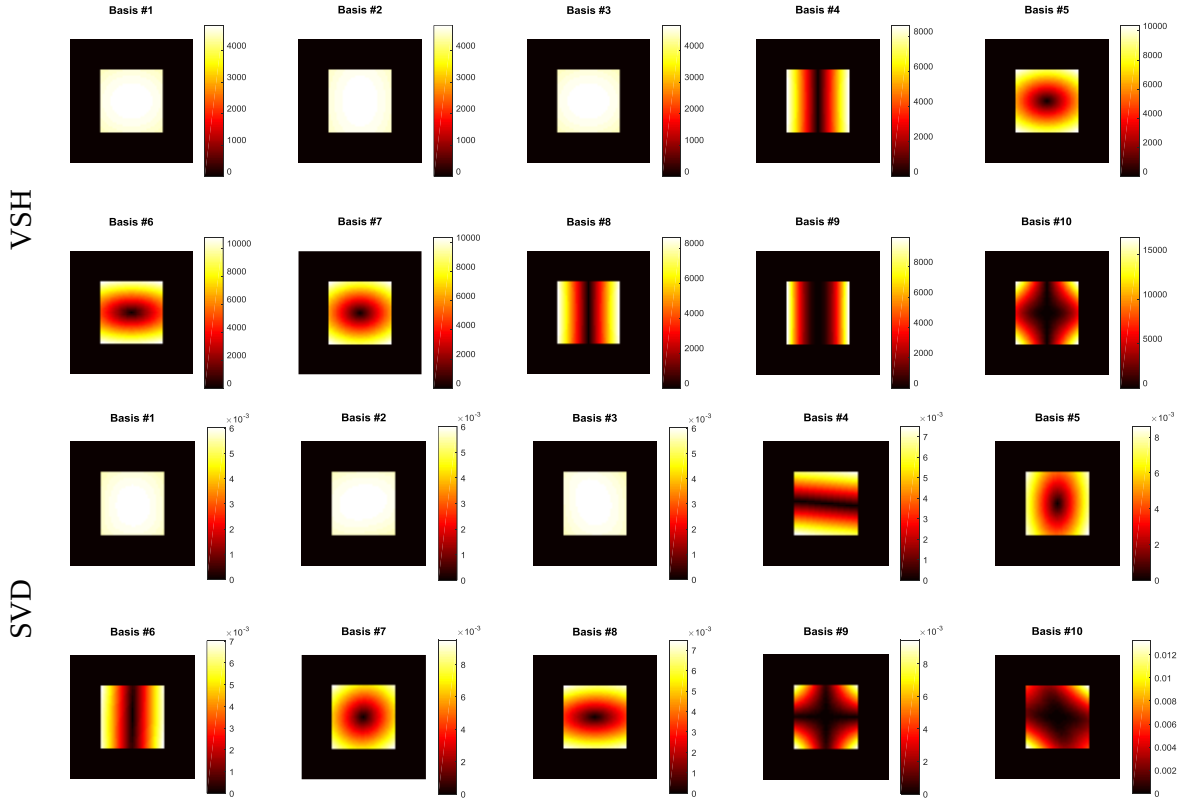

Figure 5.22: RMS value of the 10 first incident electric field basis vectors of the VSH and SVD basis across the central axial plane of the cubic object.

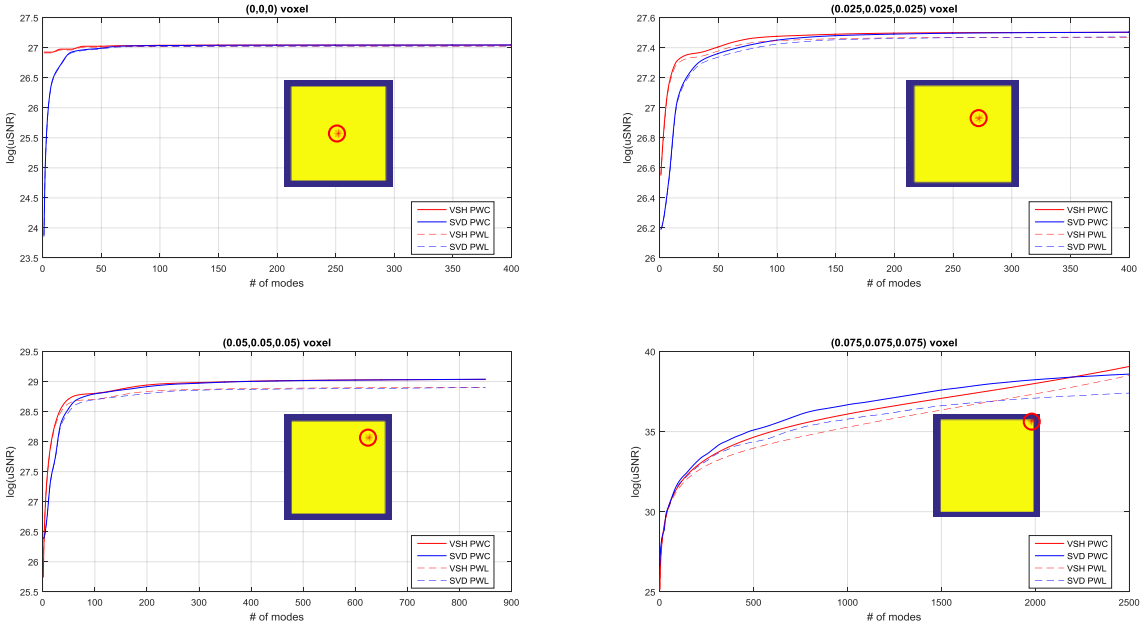

Figure 5.23: Convergence of UISNR for different voxel positions within a uniform cube for VSH and SVD basis where the total EM fields are computed both with PWC and PWL basis functions.

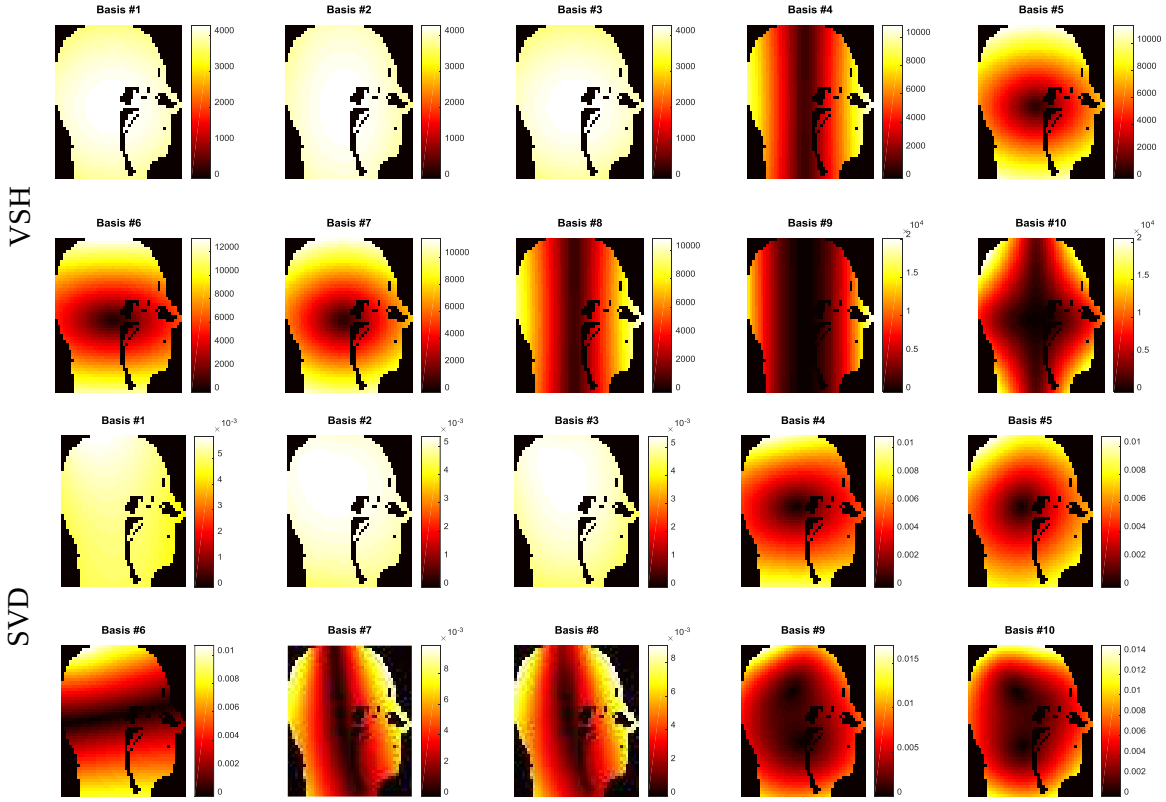

Figure 5.24: RMS value of the 10 first incident electric field basis vectors of the VSH and SVD basis across a sagittal plane at the center of the "Duke" realistic head model.

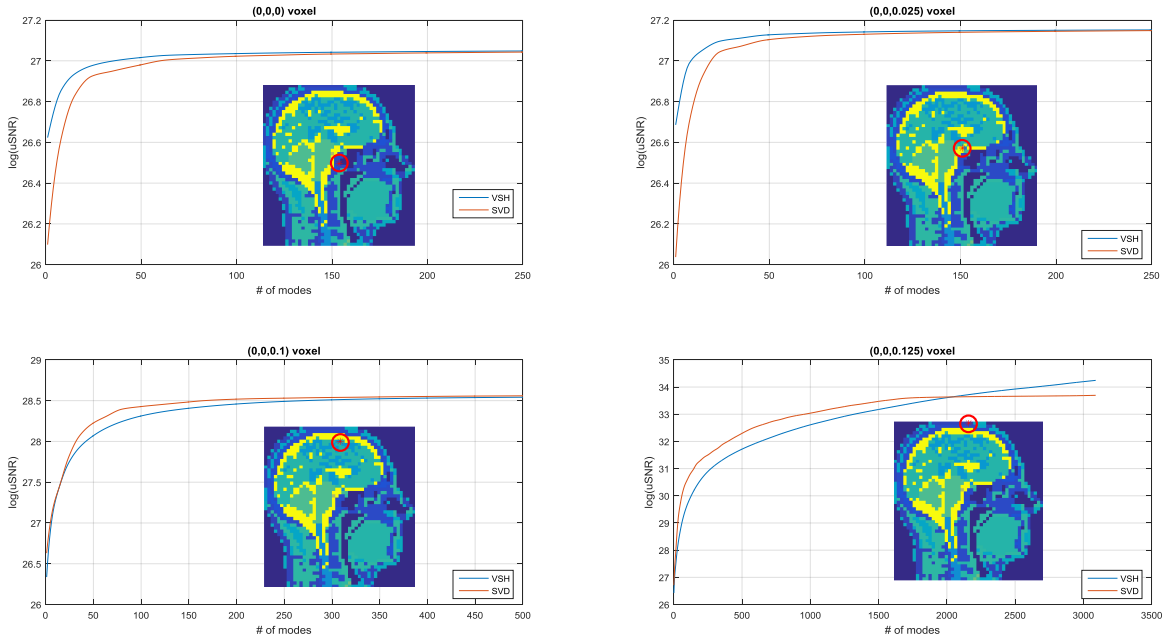

Figure 5.25: Convergence of UISNR for different voxel positions within the "Duke" heterogeneous head model for VSH and SVD basis where the total EM fields are computed with PWC basis functions.

In Figure 5.21, we present the simulation setups along with the SV drops of the associated coupling matrices $\mathbf{N}$ and $\mathbf{K}$ for the PWC case. In addition, in Figures 5.22 and 5.24, we show the RMS value of the first basis vectors of the incident electric fields from VSH and SVD basis at the mask of the cube (at the central axial plane) and the head model (at the central sagittal plane), respectively. Here, we notice their similarities and the fact that the first basis fields are smooth and higher-order basis fields become less uniform, especially for the case of the SVD basis, which can represent more efficiently EM field distributions at corners or volumes with non-smooth boundaries and great geometrical complexity.

Such characteristic, naturally, affects the convergence rate of UISNR in different voxel positions for the SVD and the VSH basis, which we illustrate in Figures 5.23 and 5.25. In particular, when optimizing SNR at interior voxel positions, interestingly, VSH basis converges faster than the SVD basis. However, as the voxel position at which we want to compute UISNR moves closer to the non-smooth boundary of the cube or the head model, the SVD basis converges faster and exactly at the boundary VSH diverges. This is directly associated with the fact that higher-order singular vectors correspond to EM field distributions with higher spatial frequency and such EM fields can be described more efficiently by the SVD basis for arbitrary objects or volumes with non-smooth boundaries. In other words, the representation of the EM fields with the SVD basis can be thought as a numerical eigenfunction expansion which particularly respects the boundary conditions that are imposed by the shape of the arbitrary object, whereas, the analytical eigenfunction expansion with the VSH basis does not conform with such boundary conditions (since it is analytically derived for spherical geometries) and the EM basis fields fail to illuminate regions close to the boundary of the object. Such observations lead to the inviting direction of generating the free-space incident EM fields from the VSH basis over the mask of an arbitrary object and then orthonormalize with SVD, where costly RSVD or SSVD could be avoided, in this way. However, the study of the convergence properties and accuracy of such basis is open to investigation and it also involves the downside that the currents sources necessarily have to be constrained onto a spherical shell preventing the generation of ICP for arbitrary excitation surface that we will show in the last subsection of this chapter. A final remark is that the choice of EM solver does not affect the convergence rate of both VSH and SVD basis and it only changes the converged or diverged UISNR value.

5.2.4 Approaching Performance Bounds with Finite Coil Arrays

In this subsection, we compute the UITXE for different B_0 field strengths in the "Duke" realistic head model and compare these results with the maximum TXE that can be achieved with finite coil arrays [75], illustrating the usefulness of the numerical EM fields basis for coil benchmarking and for assessing the room for improvement of particular arrays. Specifically, we present the TXE of various loop arrays as a percentage of the UITXE for different

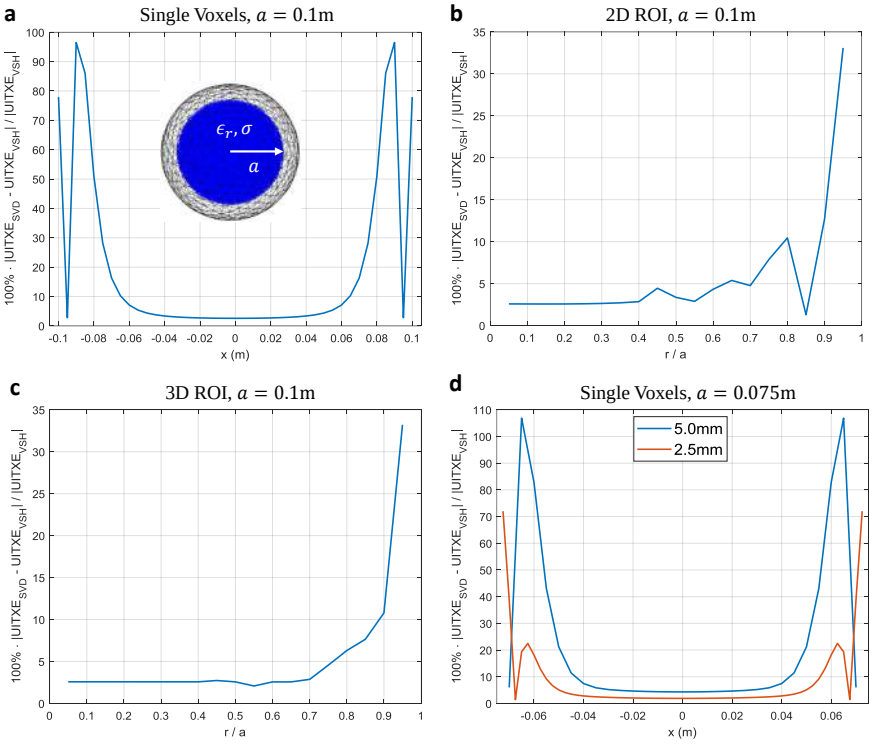

Figure 5.26: (**a**)-(**c**) Relative error of UITXE for single voxels across the diameter of the uniform sphere, 2D, and 3D ROIs computed with the orthonormal total EM fields basis for SSVD PWL from $\mathbf{K}$ operator against analytical calculations from the VSH basis. (**d**) Relative error of UITXE for single voxel ROI showing the accuracy increase with grid refinement.

field strengths $B_0 = 1.5, 7, 10.5\text{T}$, for increasing number of elements (8, 16, 24, 32), and for various arrays designs (fully encircling, helmet-shaped, cylindrical design).

We generate an orthonormal total EM fields basis from SSVD with PWL basis functions and the calculation of the covariance matrix integral includes the linear terms, since according to the laborious analysis of the previous subsection this approach is the one that yields the most accurate results. In Figure 5.26, we summarize the most accurate results from Figure 5.20 for (a) single voxel, (b) 2D, and (c) 3D ROIs from the previous subsection for a reader that is more interested in MRI applications rather than the underlying numerical considerations. At (d) of the same figure, we show the accuracy increase that can be achieved with grid refinement, where, close to the edge of the sphere, the error drops from over 100% to 22.5%, when the grid is refined by 2. Note that we decrease the radius of the spherical object limited by the memory size of our GPU. We generate the basis for operating frequencies $f = 63.9, 298, 447\text{MHz}$ (corresponding to $B_0 = 1.5, 7, 10.5\text{T}$) from a 2D shell with 1830 DoFs and use a truncated SVD with 10^{-6} that yields around 1400 basis fields (Figure 5.27). We also present the RMS value of the 8 first incident electric field basis vectors of the numerical basis across a sagittal plane at the center of the head model and note that their

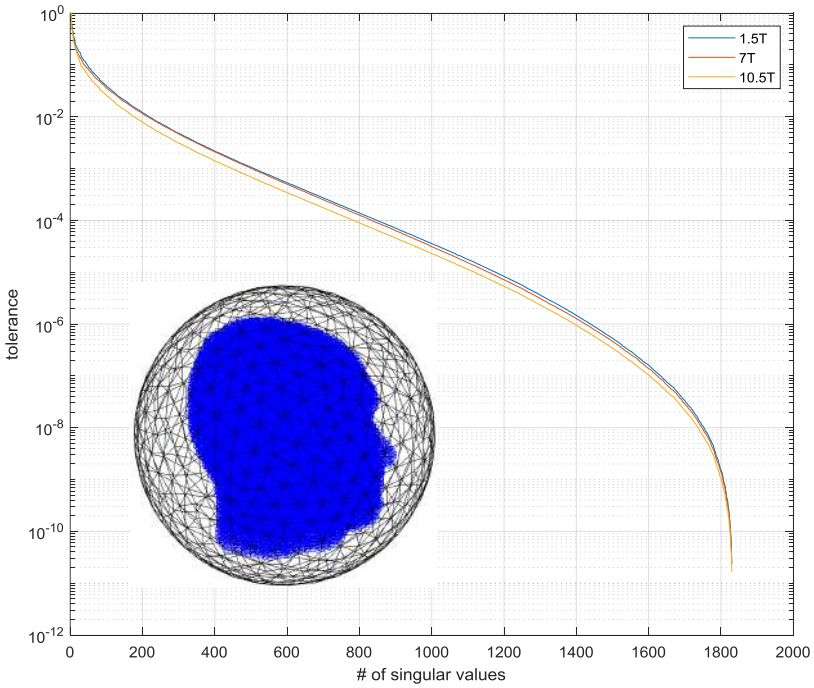

Figure 5.27: Simulation setup for UITXE computations in the "Duke" head model and drop of the singular values of the coupling matrices for different field strengths.

distribution does not change significantly for increasing field strength. Finally, we adjust the electrical properties of the numerical head model, that is discretized with 5mm resolution resulting in 38770 voxels hence 465240 DoFs, to each Larmor frequency and compute the total EM fields with our VIE solver with PWL basis functions and GMRES iterative solver is employed with inner iterations 50, outer 200, and tolerance 10^{-5}.

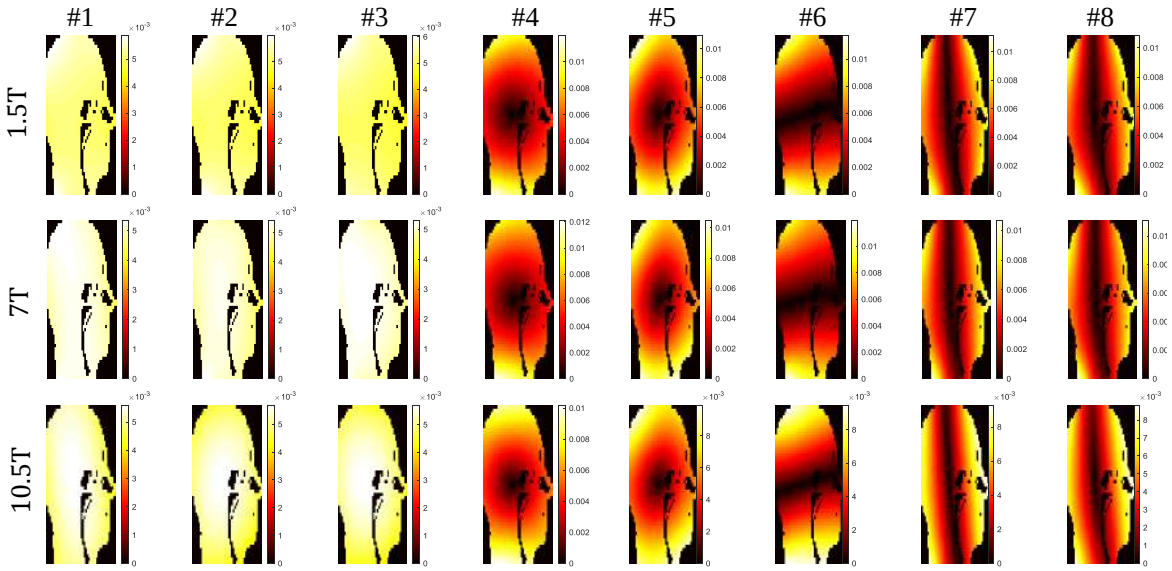

Figure 5.28: RMS value of the 8 first incident electric field basis vectors of the SVD basis across a sagittal plane at the center of the "Duke" head model for $B_0 = 1.5, 7, 10.5\mathrm{T}$.

In Figure 5.29, we compare the spatial distributions of the UITXE in the heterogeneous head model and the uniform sphere at different field strengths. The uniform sphere has radius 10cm to match the dimension of the head model along y-axis and uniform electrical properties of average brain tissue, as in Chapter 3. We notice that at the center of the head, UITXE decreases from $19.5(\mu\mathrm{T})^2/\mathrm{W}$ to $2.95(\mu\mathrm{T})^2/\mathrm{W}$ and $2.69(\mu\mathrm{T})^2/\mathrm{W}$ when the field strength increases from 1.5T to 7T and 10.5T, respectively, corresponding to an 85% and 86% drop. The corresponding UITXE values at the center of the sphere at 1.5T, 7T, and 10.5T are $9.12(\mu\mathrm{T})^2/\mathrm{W}$, $2.57(\mu\mathrm{T})^2/\mathrm{W}$, and $2.82(\mu\mathrm{T})^2/\mathrm{W}$, respectively, showing a similar trend. Additionally, the central UITXE profiles along the 3 Cartesian axes further demonstrate the similar behavior between the head-mimicking sphere and the realistic head model. In particular, along the dimension of the head that matches the diameter of the sphere (i.e., the y-profile), the values of the UITXE in the sphere and head almost overlap (see Figure 5.29). Such observations are in agreement with previous work on UISNR using realistic head models [67] which has demonstrated that the sphere with average brain electrical properties is a good approximation for the head and these results confirms such behavior for the case of the UITXE.

The fact that the sphere is expected to be an accurate approximation, even at the surface voxels, when the diameter of the sphere is equal to the dimension of the head could possibly be explained by the similarities of the incident EM basis fields between the analytical and numerical (via SVD) eigenfunction expansions, particularly for volumes with coinciding boundaries. This is associated with what we have mentioned in the previous subsection, namely, the fact the incident EM fields by the SVD basis conform with the shape of the boundary of the object. Then, in the limiting case, as more total basis EM fields are added while calculating the UITXE, the resulting TXE distributions would become smoother and more similar for the two models, despite the higher inhomogeneity of the realistic head model. This, however, entails that the calculation of the UITXE in the realistic head model would require more basis vectors for convergence, since EM fields with higher degrees of freedom, or higher spatial frequency, would be required for generating the same smooth UITXE distribution, within the inhomogeneous object. A numerical experiment that could prove or disprove this hypothesis could be the computation of the UITXE or UISNR in a homogeneous and a highly inhomogeneous object with exactly the same shape and the comparison of their distributions and convergence rates.

Finally, the incident EM fields of finite coil arrays are modeled with a simplified wire integral equation framework, where each coil segment is assumed to have a constant current, proportional to its length, radiating in free-space and the corresponding total EM fields are computed with the same VIE solver and with the same parameters as for the basis fields. The maximum TXE for each array is computed as for the ultimate case by solving the generalized eigenvalue problem where special care should be taken in order for the array elements

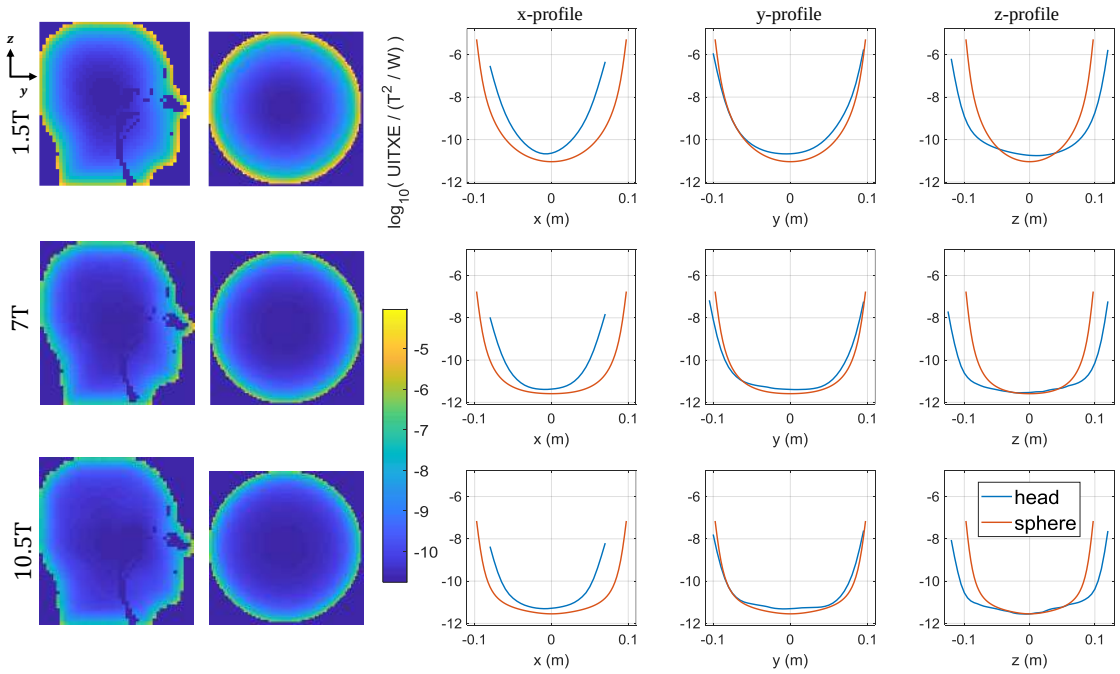

Figure 5.29: Comparison of the UITXE in the heterogeneous head model and the head-mimicking uniform sphere, as a function of voxel position and for different magnetic field strengths. UITXE is plotted in logarithmic scale for the central sagittal plane of the "Duke" head model and the spherical sample with radius $a = 10\text{cm}$, for $B_0 = 1.5, 7, 10.5\text{T}$. UITXE profiles along the x, y, and z axes are in agreement between the two objects, especially for the case of the y-profile, for which the dimension of the head matches the radius of the sphere. UITXE decreased with increasing field strength for both the heterogeneous head model and the uniform sphere.

to be placed in the exterior of Huygens's surface, otherwise their EM fields might not be able to be represented by the basis and the array's performance might be overestimated or even greater than the ultimate.

In Figure 5.30, we present the performance maps of fully encircling loop-arrays, arranged on Huygens's surface, with increasing number of transmit coils (16, 24, 32) and for increasing field strength, where we notice that the general trends of array performance with respect to field strength and number of coil elements are similar to those of the uniform sphere case (Figure 3.8), further supporting the validity of the uniform sphere as an approximation of the head. However, performance maps in the realistic head model are less uniform, when compared against the case of the homogeneous sphere, especially at higher field strengths, reflecting the geometrical complexity and non-uniform tissue electrical properties, which affect the generated EM field distribution by each element of the array and thus its maximum TXE. At UHF, finite arrays with as many as 32 transmit loops can approach UITXE only in the central region of the head, suggesting that more transmit channels or different type of coils may be needed to optimize performance, since it has been suggested that the

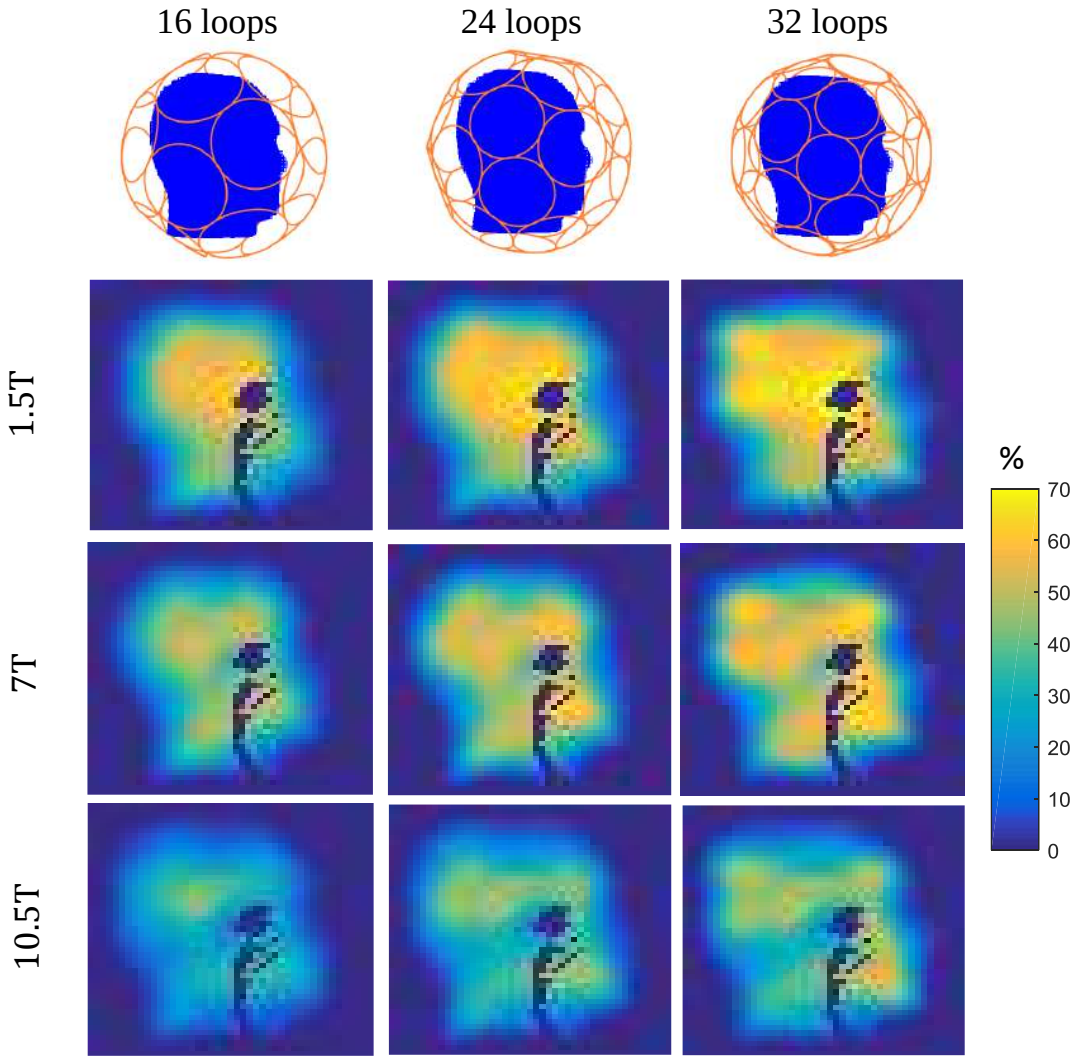

Figure 5.30: Performance maps of fully-encircling arrays displaying their maximum TXE as a percentage of the UITXE at each voxel of the central sagittal plane of "Duke" for increasing number of elements and magnetic field strengths. As for the case of the uniform sphere, absolute transmit performance becomes higher over a broader central region when the number of transmit loops increases.

combination of loops and electric dipoles could be more effective to approach UISNR at UHF [28].

Additionally, in Figure 5.31 we present the maximum SNR as a percentage of UINSR that these same fully-encircling arrays can approach, where we notice similar trends with respect to field strength and number of elements, as with the UITXE case. However, interestingly, the same arrays approach a larger percentage of UISNR, in a broader region, and their performance maps are more uniform. Such difference could possibly be associated with the formulation of each optimization problem, because in practice SNR and TXE differ only in the direction of the $\boldsymbol{B}_1$ field polarization and SNR is additionally scaled by the square of

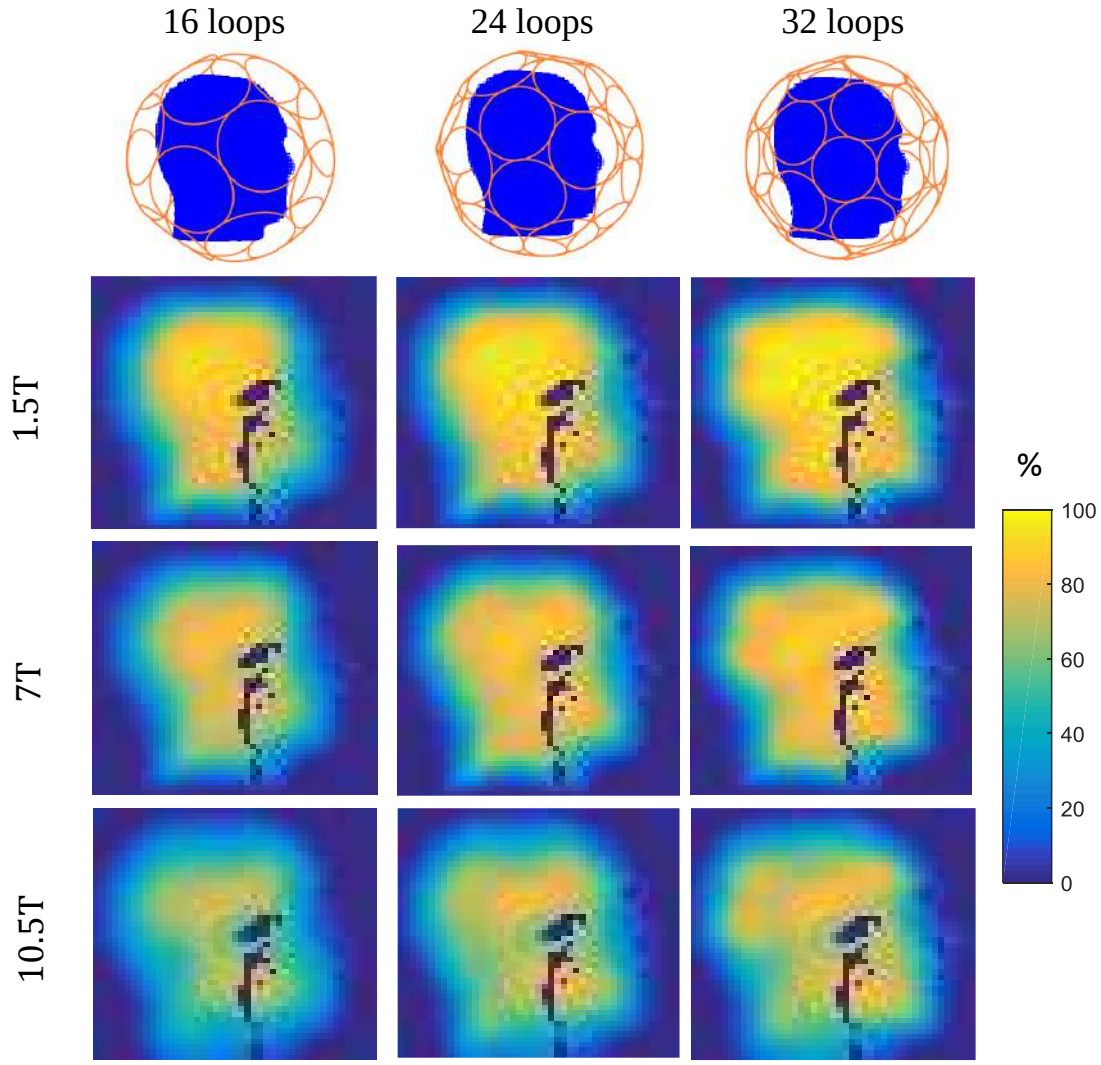

Figure 5.31: Performance maps of fully-encircling arrays displaying their maximum SNR as a percentage of the UISNR at each voxel of the central sagittal plane of "Duke" for increasing number of elements and magnetic field strengths. As for the case of UITXE absolute receive performance becomes higher over a broader central region when the number of receive loops increases.

the B_0 field strength.

Finally, in Figure 5.32, we present the performance maps of realistic loop-arrays with increasing number of transmit coils (8, 16, 24, 32) and for increasing field strength showing similar trends with respect to field strength and number of elements. Specifically, 8 loops can reach a performance of only 45% for a voxel at the center of the brain at 7T, while 32 loops achieve approximately 70% of the UITXE, illustrating the usefulness of the numerical EM fields basis in computing performance bounds that can serve as absolute references to evaluate coil designs and RF shimming algorithms.

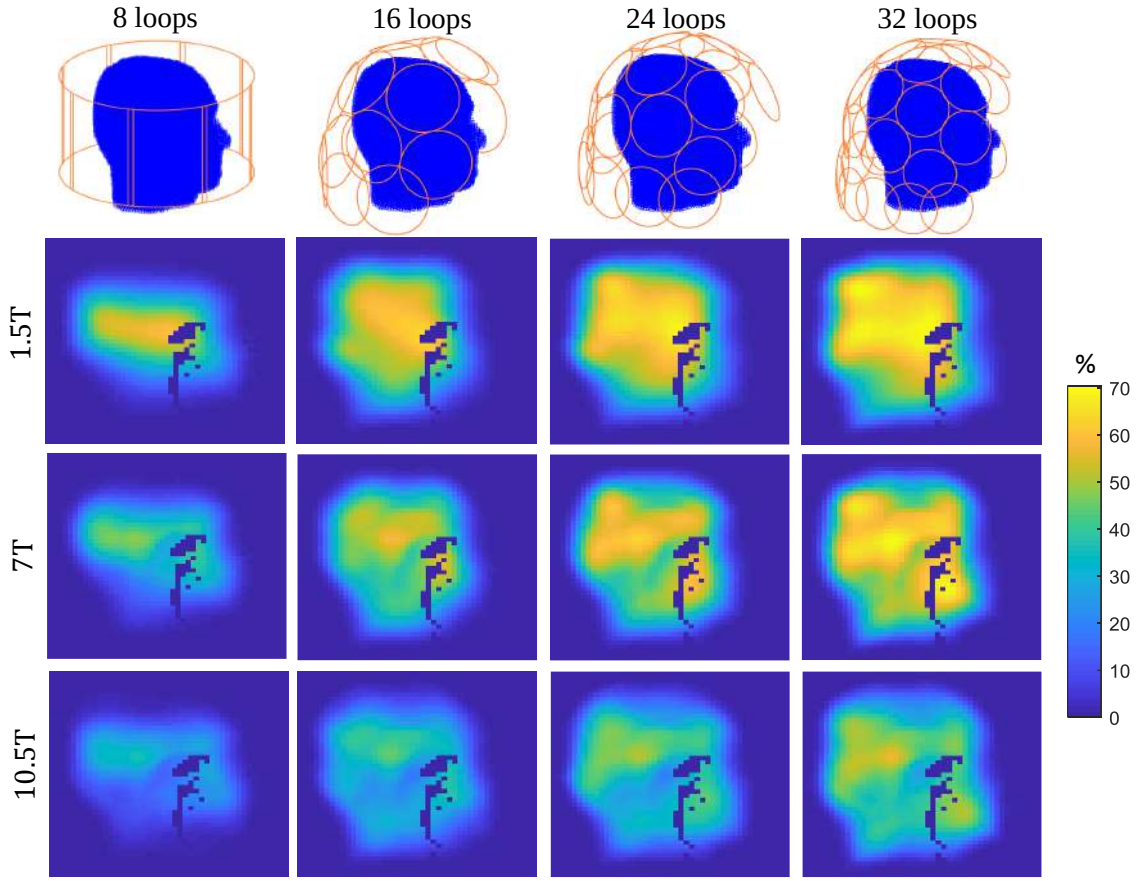

Figure 5.32: Performance maps of realistic cylindrical and helmet-shaped loop arrays displaying their maximum TXE as a percentage of the UITXE at each voxel of the central sagittal plane of "Duke" for increasing number of elements and magnetic field strengths.

5.2.5 Ideal Current Patterns on Arbitrary Excitation Surfaces

In this last subsection, we present the surface current distributions that generate EM fields that result in optimal SNR, commonly known as ICP, within heterogeneous head models for arbitrarily shaped current-bearing surfaces [82]. In particular, we investigate their behavior with respect to field strength ($B_0 = 1.5, 7, 10.5\mathrm{T}$), shape of the realistic head coil substrate (cylinder, helmet, and head-and-neck), and target voxel position (center of brain, cortex of brain, and neck) within "Duke" inhomogeneous head model. In addition, according to the surface equivalence principle, all possible EM fields and, therefore, the corresponding UISNR can be computed only by a closed surface that fully encapsulates the head, which is not a realistic scenario. For this reason, we refer to the best possible SNR from open surfaces as optimal SNR and we calculate the percentage of UISNR that it can be captured by them. ICP can inform non-convex RF coil optimization problems by providing an intuitive initial guess and by translating the optimization problem onto the currents domain, where the full-wave solution and SNR calculation for each new coil shape can be avoided, and could lead to task-optimal RF arrays designs. Their derivation, however, relies on the generation of

a numerical EM fields basis, further emphasizing the numerical EM fields basis usefulness within the MR field.

To compute ICP, we employ DSVD approach and generate the numerical EM fields basis from $\mathbf{K}$ operator with respect to incident magnetic fields, hence, from electric currents, according to the algorithmic steps described in the previous section. The reasoning behind this choice (orthonormal basis of incident magnetic fields from electric currents) has also been mentioned in the previous section, but we consider it instructive to briefly summarize its advantages here again. First, this approach involves $\mathbf{K}$ operator with its associated smoother EM fields, second, the EM fields basis is orthonormal for magnetic fields that SNR is sensitive to while the electric field contributions are averaged over the volume of the sample, and, third, it computes ICP as weighted linear combinations of electric dipole currents which are more straightforward to model on an arbitrary surface than magnetic dipole currents that are associated with small current loops. In fact, DSVD models surface currents with ideal Hertzian dipoles that are imposed to be tangential to each element of the discretized arbitrary excitation surface and, in the limiting case, as the surface is refined or by assigning a greater number of point dipoles on each element, the dipole point cloud becomes denser and the elementary sources approach a continuous surface current distribution. In this way, no interpolation or projection is required when visualizing ICP, since the currents are imposed to be exact at a specific set of points. Therefore, we calculate the optimal SNR, within this framework, by treating each basis EM field from Eq. 5.39 as if generated by a coil of a hypothetical array and we increase the number of basis elements until SNR converges to its optimal value. The corresponding weighting coefficients $(\tilde{\mathbf{u}})$, computed by Eq. 5.53, allow to appropriately combine the tangential Hertzian dipoles and obtain ICP, $\mathbf{j}_{\text{ideal}} = \hat{\mathbf{V}}_{h,K}\hat{\mathbf{\Sigma}}^{-1}_{h,K}\tilde{\mathbf{u}}$, that result in optimal SNR.

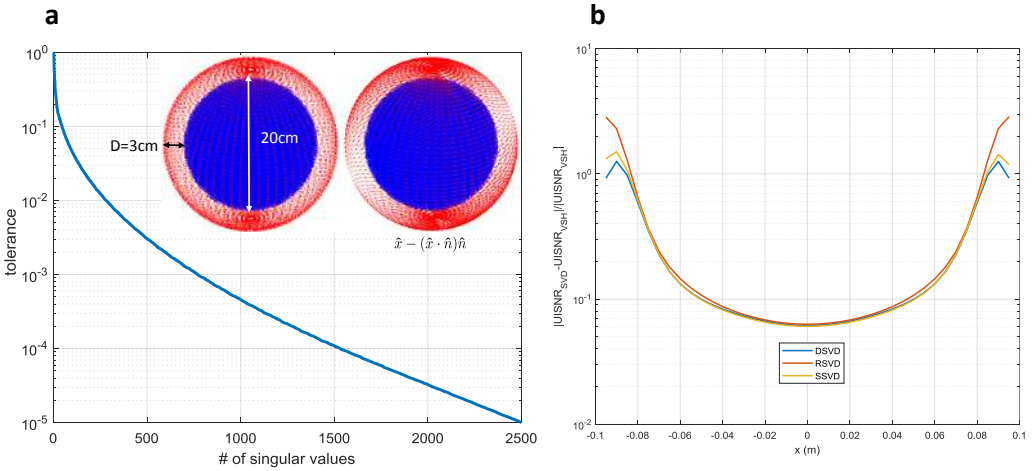

Figure 5.33: (**a**) Simulation setup and drop of the singular values of $\mathbf{K}$ coupling matrix for DSVD approach. (**b**) Relative error of UISNR across the diameter of the uniform sphere computed with DSVD approach against analytical calculations from VSH.

To validate our numerical approach, we calculate ICP yielding UISNR at the center and half-radius voxel of a homogeneous sphere from DSVD approach and compare the results with those obtained from analytical calculations from VSH [28]. Specifically, we place the Huygens's spherical surface at distance $D = 3\mathrm{cm}$ from the uniform sphere with radius $a = 10\mathrm{cm}$ and electrical properties $(\epsilon_r, \sigma) = (20, 0.2\mathrm{S/m})$. Huygens's surface is discretized with 3600 ideal Hertzian dipoles resulting in 10800 DoFs which are tangential to the spherical surface and they are placed on a spherical coordinate system by linearly varying the polar and azimuthal angles (see Figure 5.33a). An alternative could be to place the dipoles on coordinate points associated with Lebedev quadrature scheme [282] for a uniform representation of the currents on a spherical surface. However, here, we use the spherical coordinates to compare numerical ICP at the exact same points obtained from VSH. The sphere is discretized with PWC basis functions and 5mm resolution resulting in 33371 voxels and 100113 DoFs. The operating frequency is 298MHz and we solve for the total EM fields with our VIE solver with PWC basis functions [60], where GMRES iterative solver is employed with inner iterations 50, outer 200, and tolerance 10^{-5}. For the analytical calculations from VSH, we use expansion order $l_{\max} = 45$ yielding $N = (l_{\max} + 1)^2 = 2116$ modes.

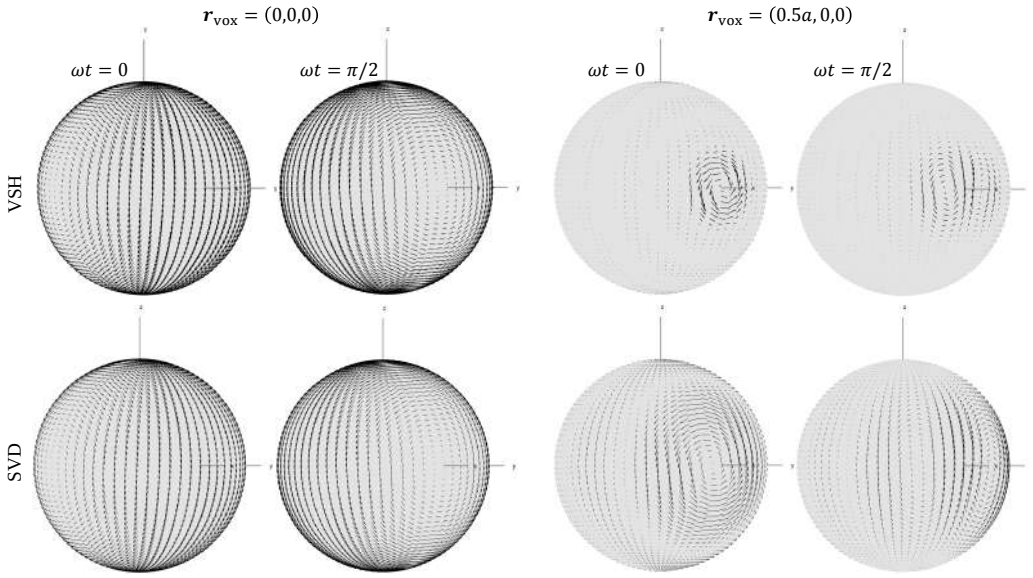

Figure 5.34: Real part of ICP yielding UISNR at the center and half radius voxel of a uniform sphere at $\omega t = 0, \pi/2$.

In Figure 5.33a, we present the simulation setup and the drop of the singular values of the coupling matrix $\mathbf{K}$, where we truncate SVD with 10^{-5} tolerance resulting in 2500 basis incident EM fields and basis dipole currents. Then, after solving the EM scattering problem for the basis fields and computing the UISNR, in Figure 5.33b, we show the relative error of UISNR across the diameter of the uniform sphere from DSVD approach with respect to UISNR analytical calculations from the VSH basis. We notice that the relative error remains practically the same with the corresponding UISNR computations from RSVD and SSVD

approaches (with the same setup). Namely, it is around 6% at the center of the sphere for all approaches, and the mean relative error is 28.3%, 45.9%, and 31.5% from DSVD, RSVD, and SSVD, respectively, since DSVD behaves better closer to the surface of the sphere. Finally, for a qualitative visual validation, in Figure 5.34, we present the real part of ICP that yield UISNR at the center and half-radius voxel of the uniform sphere at $\omega t = 0, \pi/2$ and see that the numerical (SVD) and analytical (VSH) calculations are in agreement.

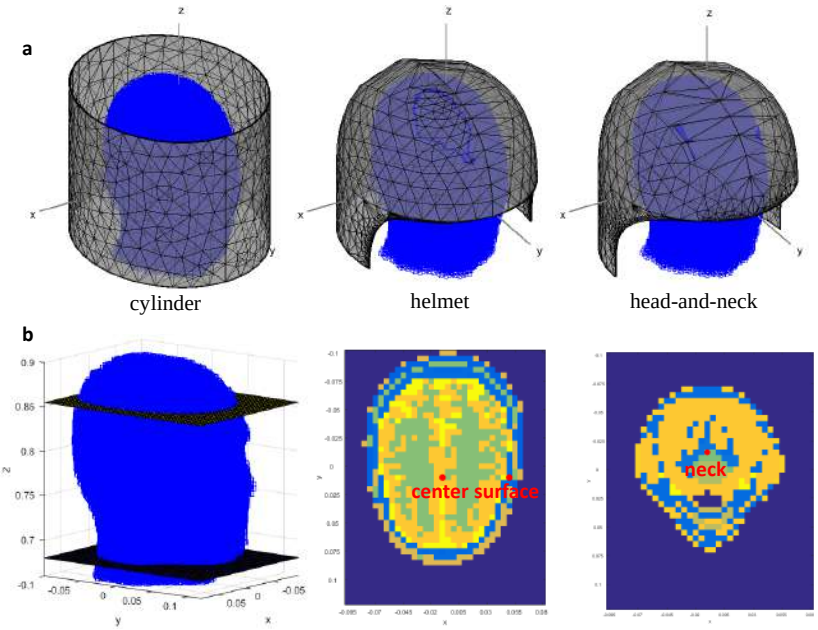

Figure 5.35: (**a**) Cylinder, helmet and head-and-neck coil substrates where the current distributions are constrained loaded with the "Duke" heterogeneous head model. (**b**) Axial planes across the "Duke" model along with the positions of the voxels of interest near the center, the cortex of the brain and in the neck region.

In what follows, we calculate and present ICP for voxels at the center of the brain, near the brain cortex (surface) and in the neck region, using three realistic coil substrates, loaded with "Duke" head model at 1.5T, 7T, and 10.5T (see simulation setup in Figure 5.35). In detail, we adjust the electrical properties of "Duke" head model at each corresponding Larmor frequency ($f = 63.9, 298, 447\text{MHz}$) and discretize it with 5mm resolution that results in 38770 voxels and 116310 DoFs for PWC basis functions. The discretized version of the substrates with the tangential electric dipoles can be seen in Figure 5.36. In particular, the cylinder substrate is discretized with 4500 dipoles (13500 DoFs), the helmet with 8451 dipoles (13500 DoFs), and the head-and-neck with 3621 dipoles (10863 DoFs) and all coupling matrices preserve their low rank nature. Specifically, we truncate SVD with 10^{-5} tolerance (Figure 5.36) and the coupling matrix, e.g., for the cylinder substrate, can be approximated with 1200, 1175, and 1110 singular vectors at 1.5T, 7T, and 10.5T, respectively, where we note the faster drop of the singular values for larger electrical distances. The helmet and head-and-neck substrates behave similarly to the cylinder substrate with respect to

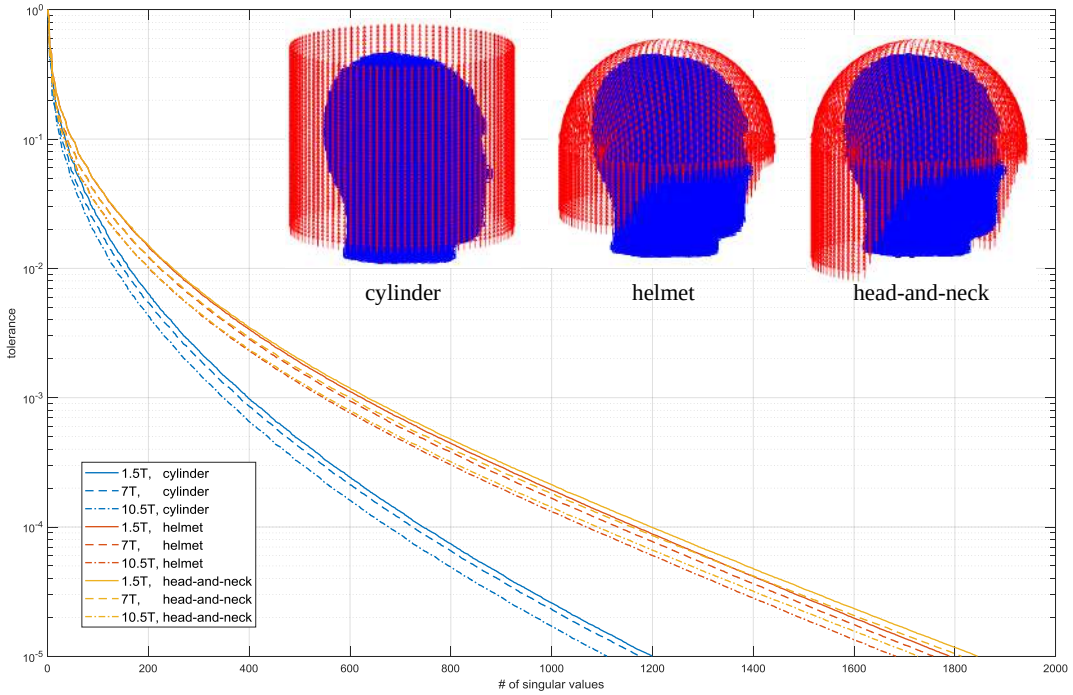

Figure 5.36: Discretized version of realistic coil substrates with tangential electric dipoles and drop of the singular values of coupling matrix $\mathbf{K}$ for the coil substrates and for field strengths 1.5T, 7T, and 10.5T.

increasing frequency, however, their singular values drop slower since these substrates cover the top of the head, hence, more EM fields or surface currents sets can be represented due to the larger constraining topology of the surface. On the contrary, the difference of the SV drops between the helmet and the head-and-neck substrates is negligible, since the elongated section of the surface behind the neck can barely represent additional EM fields or surface currents. Such trends are also reflected on the behavior of the ICP for each substrate and for different field strengths, as well as, on the percentage of UISNR each substrate can capture, as we will illustrate in the next figures.

For completeness and to develop useful intuition, we also present the first and tenth vector of the incident and total EM fields basis, as well as, of the electric dipole currents basis (Figure 5.37) for the helmet substrate loaded with "Duke" at 7T. The total EM fields are computed with the PWC current-based VIE solver where GMRES iterative solver is employed with inner iterations 50, outer 200, and tolerance 10^{-5}. In this figure, it is interesting to note that the higher-order (tenth) basis vectors are associated with less uniform EM fields and more localized surface current distributions. Finally, we use these basis elements and calculate optimal SNR along with its corresponding optimal weights, until convergence is observed, and plug in the optimal weights to appropriately combine the Hertzian dipoles and obtain ICP.

First, we show ICP yielding optimal SNR at the surface voxel (Figure 5.38), where we

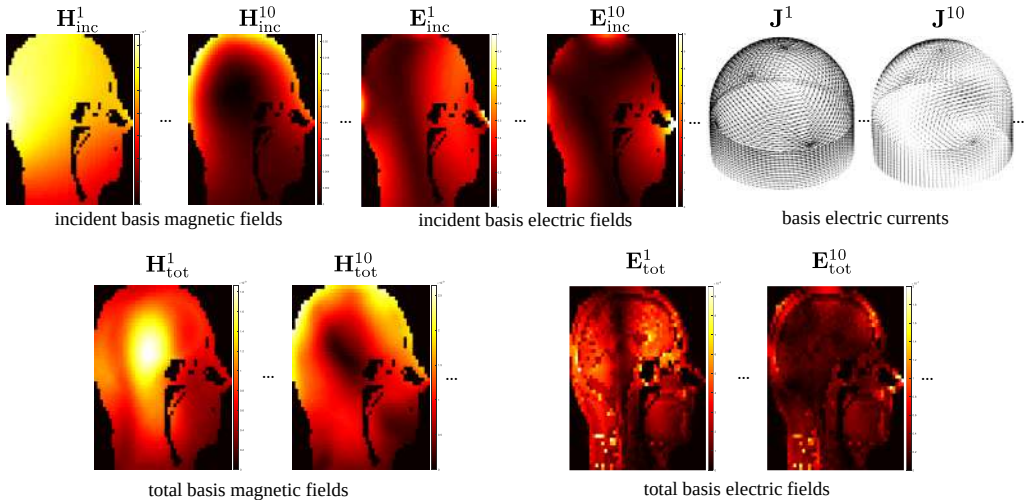

Figure 5.37: Incident EM fields, total EM fields, and electric dipole currents basis vectors for helmet substrate and "Duke" head model at 7T.

observe that the ICP strongly depend on the topology of the current-baring arbitrary surface [73], even though the optimal SNR distribution is similar for different substrates and same field strengths (Figure 5.41). Furthermore, for the substrate with spherical symmetry, ICP tend to concentrate around the target voxel. Then, in Figure 5.39, we show ICP yielding optimal SNR at the center voxel, where we notice that as field strength increases, the ICP change, especially for the cylindrical substrate, where we might be looking at the relative contributions of loops and dipoles. However, for substrates with spherical symmetry loops are more dominant, especially at low field strengths. Similarly to surface voxel SNR optimization, there is a clear dependence of the ICP on the substrate topology, even though the optimal SNR almost overlaps for different substrates and same field strengths at the center voxel (Figure 5.41). Finally, in Figure 5.40, we show ICP yielding optimal SNR at the neck voxel, where for both the head-and-neck and helmet substrate, ICP form small loops at the region of the surface behind the neck showing no particular differences for the same B_0.

Finally, in Figure 5.41, we show the percentage of UISNR that can be captured by the realistic coil substrates at the brain axial plane at 1.5T, 7T, and 10.5T field strengths. We notice that at the center voxel and all field strengths, all substrates can capture UISNR (more than 90%). However, at the brain cortex, the cylinder substrate can only capture on average 55% of UISNR, even with infinite number of coils. Therefore, if the elements of an RF receive array are arranged on a cylinder substrate, as for a birdcage coil, UISNR cannot be reached. This fact is associated with the faster SV drop of the cylinder-to-head coupling matrix, since the top of the head is not covered and less EM fields can be represented by this substrate within the head model. For similar reasons, UISNR is approached less closely at superficial than central voxels. Additionally, at center voxel, UISNR is approached more closely at 10.5T than at 7T for all substrates, but the opposite happens at the surface voxel.

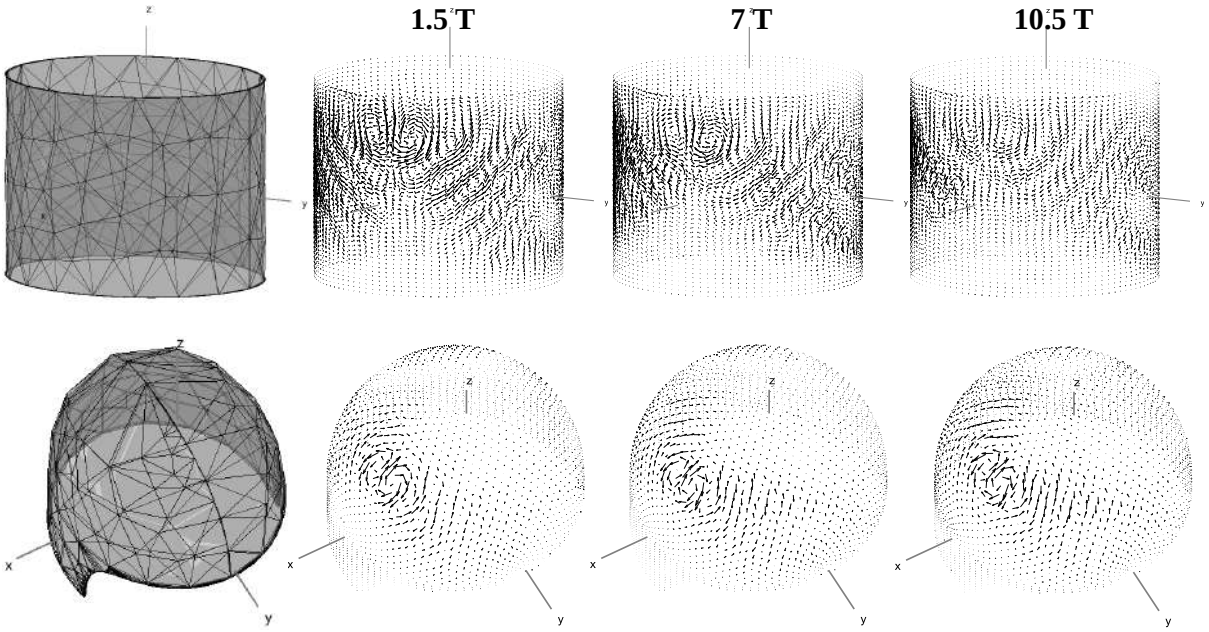

Figure 5.38: ICP yielding optimal SNR near the surface of the brain for the cylindrical and helmet substrates, at 1.5T, 7T, and 10.5T.

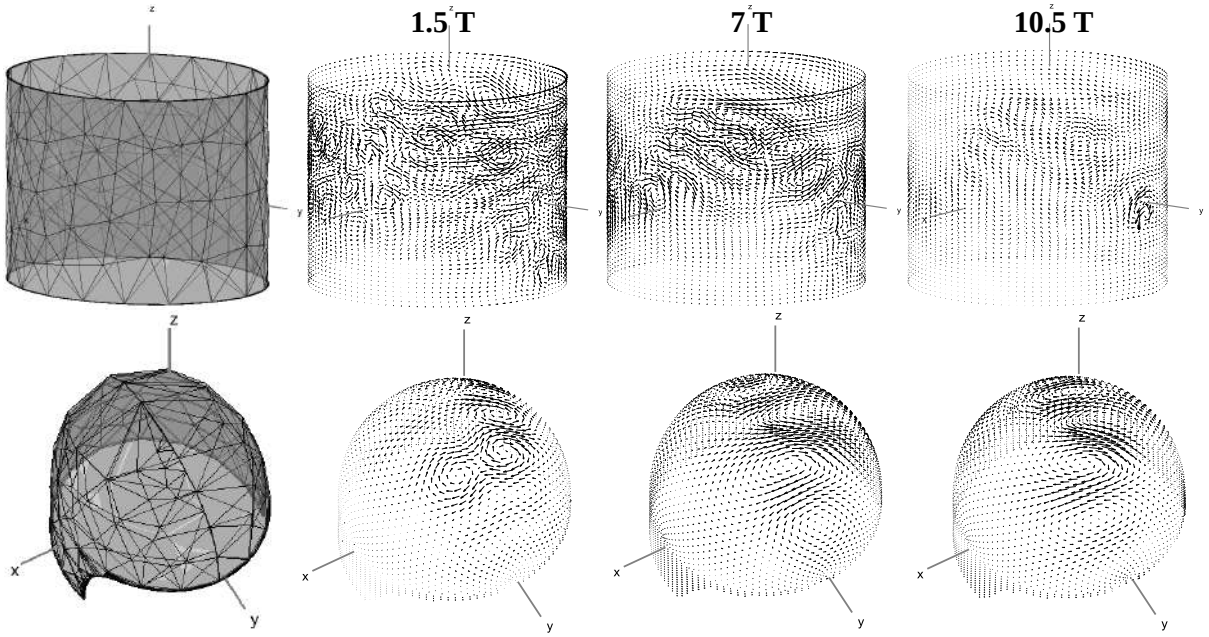

Figure 5.39: ICP yielding optimal SNR near the center of the brain for the cylindrical and helmet substrates, at 1.5T, 7T, and 10.5T.

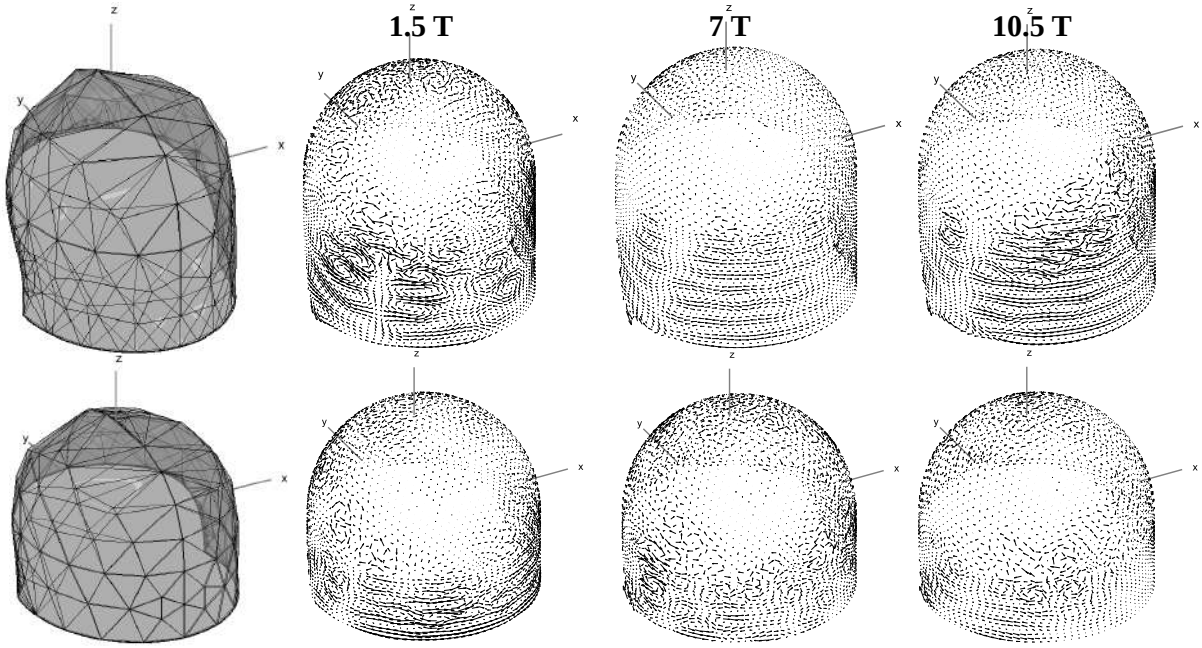

Figure 5.40: ICP yielding optimal SNR at a voxel in the neck for the head-and-neck and helmet substrates at 1.5T, 7T, and 10.5T.

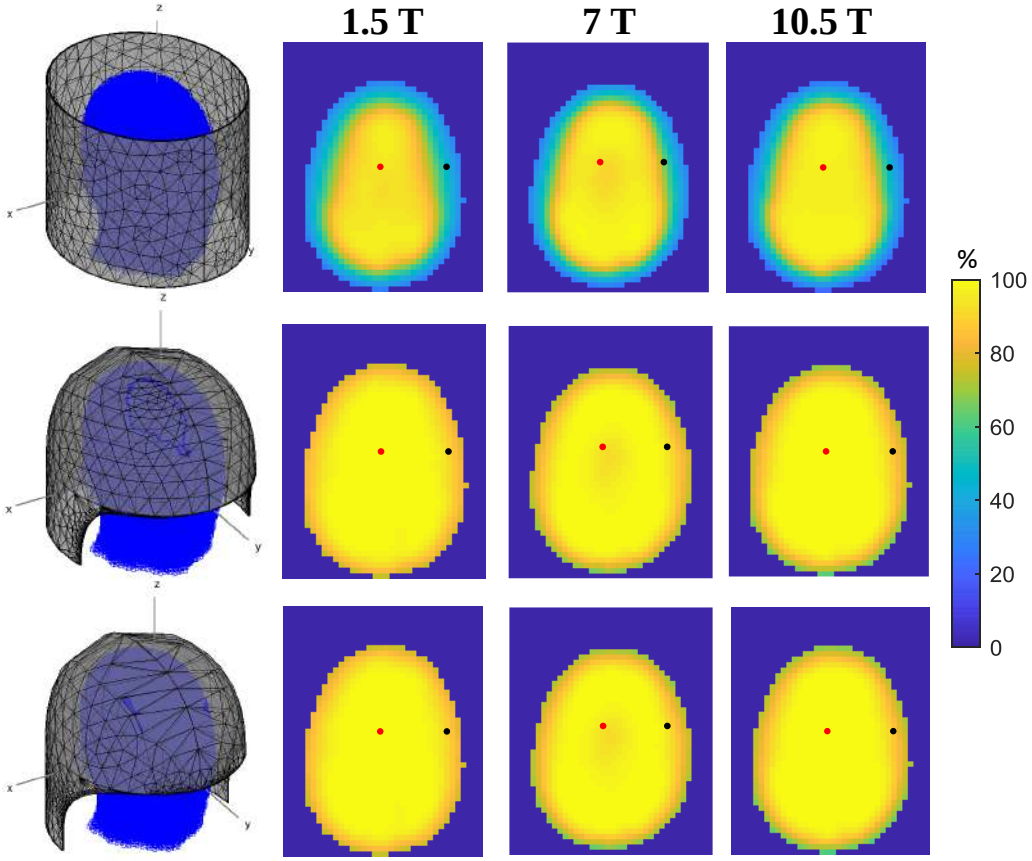

Figure 5.41: Percentage of UISNR captured by the realistic coil substrates at the brain axial plane at 1.5T, 7T, and 10.5T. The center and surface voxel for which we present ICP are highlighted with a red and a black dot, respectively.

Similarly, at neck voxel, as it can be seen in Figure 5.42, UISNR is approached more closely by the head-and-neck substrate since the neck is not covered by the other substrates. Finally, UISNR cannot really be reached expect for a region in the back of the head but, interestingly, it is approached more closely as field strength increases for all substrates.

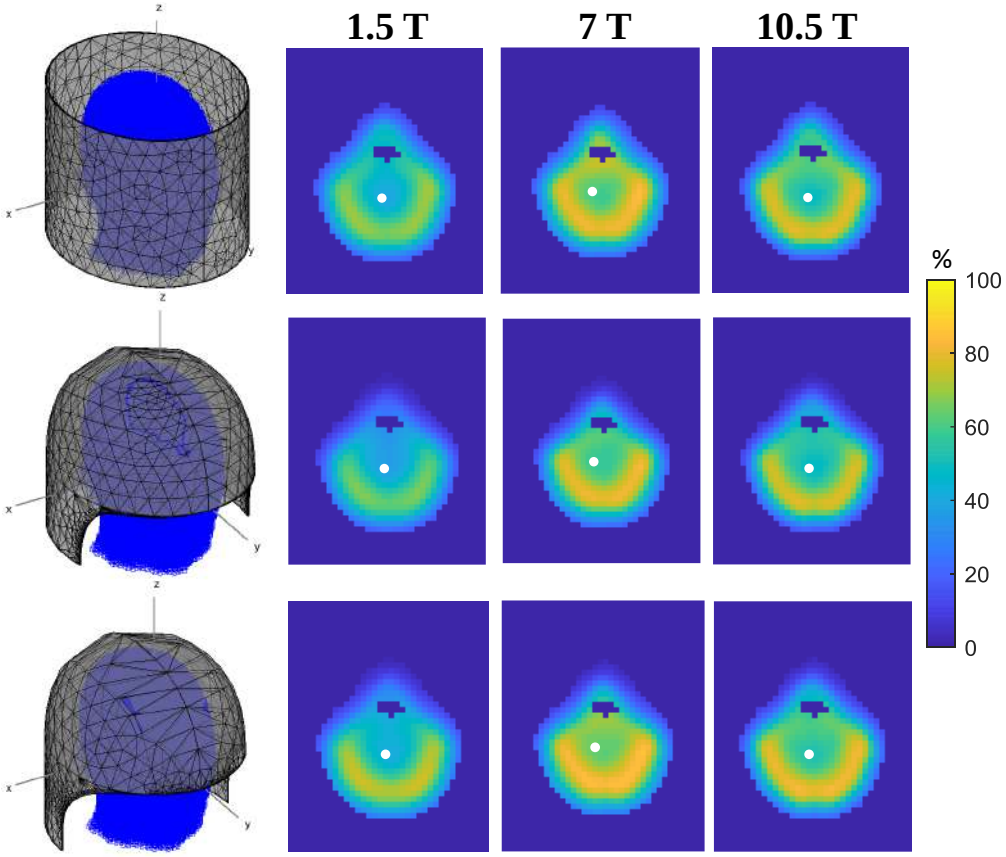

Figure 5.42: Percentage of UISNR captured by the realistic coil substrates at the neck axial plane at 1.5T, 7T, and 10.5T. The neck voxel for which we present ICP is highlighted with white dot.

The exact percentages of the optimal SNR by UISNR ratio are presented in Table 5.1, where UISNR for all field strengths is computed with the same DSVD framework and solver parameters by completely encapsulating the head model. Special care should taken in order for the substrates to be placed in the exterior of Huygens's surface.

Table 5.1: $\mathrm{OSNR}/\mathrm{UISNR} \cdot 100\%$ for Different Voxels, Field Strengths, and Substrates.

	center			surface			neck		
B_0 / substrate	1.5T	7T	10.5T	1.5T	7T	10.5T	1.5T	7T	10.5T
cylinder	94.1	90.6	96.7	45.5	68.3	45.6	39.7	43.5	48.6
helmet	99.6	92.5	99.4	89.6	94.7	86.5	36.9	42.5	47.8
head-and-neck	99.4	92.5	99.4	89.3	94.4	85.5	41.7	46.8	52.5

5.3 Conclusions

In conclusion, in this chapter we described detailed algorithmic steps for the generation of an accurate and stable numerical EM fields basis that is consistent with electrodynamic principles inside an inhomogeneous arbitrary scatterer and demonstrated its application and usefulness within the MR field, where the coil domain and body domain are separated, hence, the operators that relate electric/magnetic currents to EM fields are compact and the corresponding coupling matrices admissible to a low-rank representation based on a truncated SVD.

First, we studied the impact that the separating electrical distance has on the basis generation and demonstrated that the larger the electrical distance the less basis vectors are required for generating the basis with the same prescribed tolerance and that $\mathbf{K}$ operator has a faster SV drop than $\mathbf{N}$ operator which fact affects the convergence rate of EM fields reconstruction error and ultimate metrics computations. Then, we investigated how accurately the numerical basis can represent different EM fields and how fast the reconstruction error from each basis converges. We showed that the fastest convergence rate for all EM fields reconstruction is achieved by the basis from the linear combination of the bases from the subspaces of $\mathbf{N}$ and $\mathbf{K}$ operators, however, such basis is ill-conditioned and unstable, especially when its higher-order basis vectors are involved. The second fastest convergence rate is achieved by the basis from the subspace of $\mathbf{K}$ operator which is well-conditioned and stable, whereas, the basis from the orthonormalized bases from the subspaces of $\mathbf{N}$ and $\mathbf{K}$ operators is practically the same with that from the subspace of $\mathbf{N}$ operator. Therefore, we can conclude that the basis from $\mathbf{K}$ operator combines convergence speed and stability and we suggest that it should be the method of choice, taking into account the fact that the surface equivalence theorem can be formulated with only one kind of currents, which also allows to halve the number of solves for total EM fields. In addition, we compared the numerical accuracy and convergence properties of the numerical basis against a complete analytical basis from VSH. We showed that the faster SV drop of $\mathbf{K}$ operator leads to a faster convergence of UISNR and that different discretization schemes of the Huygens's surface and the scatterer do not affect significantly the convergence rate, however, when computing the total basis EM fields with PWL basis functions, the converged UISNR values are significantly more accurate. We further demonstrated, that in more sensitive optimization problems, e.g., generalized eigenvalue problem for UITXE computation, the incident EM fields basis from the approximate RSVD or from the less smooth $\mathbf{N}$ operator does not provide accurate results, hence, we suggest generating an orthonormal total EM fields basis from $\mathbf{K}$ operator that provides faster convergence, similar to that of VSH, and reliable converged ultimate values. Finally, we showed that the SVD-based numerical EM fields basis can describe more efficiently EM fields within arbitrary objects or volumes with non-smooth boundaries and

UISNR converges even at voxels at the boundary of the arbitrary object, whereas, UISNR computations from VSH basis diverge at such superficial voxels.

With regard to MRI applications, we demonstrated how the vectors of the total EM fields basis can be applied in optimization procedures and used to calculate performance bounds, such as the UITXE, which constitutes a valuable metric for transmit arrays benchmarking and RF shimming algorithms evaluation. Additionally, we showed that the overall behavior of the UITXE within an inhomogeneous head model and a uniform sphere are similar when their dimensions are comparable and that the general trends of transmit array performance with respect to field strength and number of coil elements remain valid between the two models. In fact, more coils can approach UITXE in the head model and the same arrays can achieve a larger performance at lower field strengths, however, at UHF, finite arrays with as many as 32 transmit loops can approach UITXE only in the central region of the head model, suggesting that more transmit channels or different type of coils may be needed to optimize performance. We also computed ICP on a given arbitrary surface yielding optimal SNR within an inhomogeneous head model and found that they depend mostly on the topology of the surface onto which they are constrained, even though optimal SNR is similar for different substrates and that loops are more dominant at lower field strengths for substrates with spherical symmetry. We computed the percentage of UISNR that realistic head coil substrates can capture and showed that UISNR is approached better by the helmet and head-and-neck substrates than by the cylinder substrate, especially at the periphery where cylinder reaches only 55%, leading to the conclusion that helmet coils are better-suited for head imaging. Similarly, UISNR is usually approached better at the central than the superficial voxel positions and for all substrates, at center voxels, is better captured at 10.5T than 7T. In addition to helping to visually understand the origin of optimal RF coil performance, ICP could also help designing the next-generation MR coils, by providing an intuitive initial guess for non-convex coil optimization algorithms and translating the optimization problem onto the currents domain, where the full-wave solution and SNR calculation for each new coil shape can be avoided, and could lead to a truly task-optimal design of RF coils.

Future steps could include the investigation of the convergence properties and numerical accuracy of UISNR and UITXE computed by an orthonormal basis of incident magnetic fields and verify or not the hypothesis that the sensitivity of SNR and TXE to magnetic fields affects such properties. In addition, a direction worth pursuing could be the direct generation of an orthonormal total EM fields basis by applying the free-space operator, solving the scattering problem for each random incident EM field for RSVD or for each column vector of the currents-to-incident-fields coupling matrix for SSVD and DSVD, and then orthonormalizing. This approach is more computationally expensive but might be worth investigating since we showed that an incident EM fields basis does not provide accurate results when generated by the less smooth $\mathbf{N}$ operator or by the approximate RSVD for UITXE com-

putations. Furthermore, it is suggested in the literature that the accuracy of RSVD can be improved by power iterations application [81], therefore, studying such potential improvement on the accuracy of UISNR and UITXE could be an additional future step. Finally, generating a basis by applying SVD factorization to the VSH basis modes over the mask of an arbitrary object could also be an inviting research direction, motivated by the well-behaved UISNR convergence properties of the VSH basis in central voxel positions and the fact that the incident EM fields by the SVD basis conform with the shape of the boundary of the arbitrary object and illuminate regions close to it.

Within the MR field, future work could involve the computation of UITXE in specific ROIs of the realistic head model (e.g., cerebellum) and the investigation of the correlation between B_1^+ homogeneity and UITXE and whether the electric field distribution that corresponds to UITXE respects local SAR aspects in realistic head models. Furthermore, with the aid of ICP, a new research project could involve the implementation of RF coil shape optimization and/or SIE node optimization algorithms, where ICP could serve as an initial guess to the optimizer. Additionally, curvilinear basis functions for the discretization of Huygens's surface could be employed for more accurate coil modeling and ICP representation. Finally, a new promising principle, the optimality principle [73], which allows one to predict rapidly and intuitively ICP for arbitrary dielectric objects and current-bearing surfaces, could be further explored in future work.

6 Conclusions

6.1 Conclusions and Thesis Contributions

The focal point of this dissertation revolved around modeling the interactions between EM waves and biological tissue. We employed analytical methods and introduced a novel performance metric, the UITXE, which is the theoretically largest TXE that can be achieved by any RF coil or RF shimming algorithm in head-mimicking spherical samples, and calculated its associated ideal RF excitation patterns on spherical surfaces. In addition, we developed novel numerical methods based on integral equations for the computation of EM fields distributions and the derivation of performance bounds of modern MR coils within inhomogeneous realistic body models, as well as, ideal RF excitation patterns on arbitrary surfaces. Such reliable EM fields distributions can be used to obtain relevant figures of merit such as B_1^+, B_1^-, and local SAR maps inside the inhomogeneous body, whereas, performance bounds (within either the uniform sphere or the body model) can provide an absolute reference for benchmarking different RF arrays designs. Ideal RF excitation patterns on arbitrary surfaces can further inform the non-convex RF coil optimization problem by providing an intuitive initial guess, thus, offering a framework that could lead to a truly task-optimal design of RF coils. A summary of the contributions and conclusions of each chapter of the thesis is presented below.

In Chapter 2, we described the physical principles that govern the NMR phenomenon and gave an overview of the components of an MRI system, namely, the main magnet, the RF transmit and receive coils, and the gradient coils that are required to appropriately manipulate the magnetic fields in order to generate the MR image. We described the opportunities and challenges that are associated with UHF MRI. Such challenges necessitate the fast and accurate EM modeling of the associated RF coils and EM fields distributions within the body but, simultaneously, they present an opportunity to design the next-generation tunable RF coils that can yield higher SNR and faster image acquisition without compromising patient safety and image quality. We reviewed analytical and numerical methods and tools for the calculation of EM RF fields in MRI, including FDTD, FEM, and IE methods whose distinct characteristics and applicability within the MR field were comparatively analyzed, as well

as, scientific contributions with respect to the calculation of ultimate SNR, SAR, and their associated current distributions which constitute a great source of physical insight into the design of optimal RF coil arrays.

The novel contributions of this thesis started in Chapter 3, where we introduced the UITXE metric [74, 75] which is the theoretically largest TXE that can be achieved by any RF coil or RF shimming algorithm for a given imaging sample, field strength, and target excitation ROI. We investigated its behavior for different magnetic field strengths, target excitation ROIs, and uniform spherical sample sizes and computed its associated ICP on spherical surfaces surrounding the samples, illustrating the power of analytical methods for rapid yet rigorous computations for multiple parameters and configurations. We found that the main mechanisms and behavior of UITXE for single voxels resemble those of UISNR and we further evaluated the performance of transmit arrays with increasing number of loops and different designs, for various field strengths and ROIs, illustrating how UITXE can be used to assess coil designs and RF shimming algorithms. Our results demonstrated how ICP can provide useful insight into the design of RF transmit arrays and were in agreement with other studies showing that the ultimate performance is approached more closely when the shape of the array resembles that of ICP and not necessarily when the number of its elements increases. Finally, we showed that at UHF, transmit performance can be approached only at the center of the sample suggesting that more elements or the combination of loops and electric dipoles could be more effective.

Despite the great insight that analytical methods yield into expected and observed trends in MR signal, noise, and safety, RF coils are designed for realistic body models, therefore, a natural next step into computing performance bounds within such body models was the development of a numerical solver that generates reliable EM fields. In fact, Chapter 4 dealt exactly with this task, where we introduced a fast VIE solver [76, 77] based on equivalent polarization/magnetization currents with discontinuous PWL basis functions for the accurate computation of EM fields distributions within highly inhomogeneous and/or high contrast arbitrary objects, such as the human body. We showed that the matrix of the linear system that arises from the current-based formulation is well-conditioned and the proposed solver has remarkably stable convergence properties in terms of iteration count in an iterative solver, which remains practically the same with the current-based VIE solver with PWC basis functions and is much smaller than that of the flux-based solver, for highly inhomogeneous scatterers. Additionally, we demonstrated that our novel solver yields reliable EM fields which are in good agreement with results from an FDTD-based software package for extremely challenging modeling scenarios and for coarse resolutions without necessarily refining the computational grid. As shown in the literature, by discretizing the VIE on a uniform grid, the matrix-vector product can be performed fast with the help of FFT and, when combined with iterative solvers, our solver can be used to accurately solve large and

complex problems within reasonable time and computational resources. Hence, the proposed framework can be utilized in challenging applications within the MR field such as modeling the interactions between EM fields and biological tissue, including the presence of RF shimming pads of very high electrical permittivity. However, despite the use of PWL basis and testing functions, the convergence rate of our solver at the uniform sphere numerical experiment appears to be $\mathcal{O}(h)$ instead of $\mathcal{O}(h^2)$ which can probably be explained by numerical inaccuracies originating from the staircase approximation of a sphere when discretized with voxels. Finally, our solver was integrated into Global Maxwell Tomography for the MR-signal-based noninvasive estimation of the human body electrical properties, where it provided to the optimizer solves consistent with each other, thus regularized the inverse problem and reduced the error of the electrical properties reconstruction [269] and it will further be part of the soon to be released MARIE 2.0 suite.

After developing a numerical solver that generates reliable EM fields, our focus, in Chapter 5, shifted on the description of robust and accurate algorithms for the generation of a consistent numerical EM fields basis able to reconstruct all EM fields distributions within inhomogeneous, arbitrary objects [80] and an electric/magnetic currents basis in arbitrary excitation surfaces. We demonstrated how such bases can be employed to transition from computing performance bounds in uniform spherical or cylindrical objects to inhomogeneous body models [75] and from computing ICP in comparatively simple surfaces (i.e., spherical or cylindrical shells) to arbitrary excitation surfaces [82]. Such bases can help to understand the currents and EM fields distributions that maximize SNR or TXE and provide ultimate figures of merit against which coil array designers can benchmark their designs and obtain useful insight and intuition of the best RF excitation patterns, offering the framework for a truly robust optimization of next-generation RF coils. We described the necessary algorithmic steps for the basis generation which rely on the surface equivalence principle and the fact that, in the MRI setup, the coil domain and body domain are separated, hence, the operators that relate electric/magnetic currents sources to EM fields in the body are compact and the corresponding coupling matrices admissible to a low-rank representation based on a truncated SVD. The basis generation can be viewed as an extension of the expansion of EM fields within spherical objects with spherical waves to an EM fields expansion within arbitrarily complex objects with the help of the leading singular basis vectors.

With regard to numerical considerations, we showed that for larger separating electrical distances, less basis vectors are required for approximating the EM fields subspace with the same prescribed tolerance and that $\mathbf{K}$ operator has a faster singular value drop than $\mathbf{N}$ operator which significantly affects the convergence rate of EM fields reconstruction error and ultimate metrics computations. In fact, we demonstrated that the basis from the subspace of $\mathbf{K}$ operator combines convergence speed and stability in terms of EM fields reconstruction error and UISNR convergence and we suggest that it should be the method of choice, taking

into account the fact that the surface equivalence theorem can be formulated with only one kind of currents. By comparing the numerical accuracy of the converged UISNR values with analytical calculations from a VSH basis, we showed that computing the total basis EM fields with PWL basis functions yields much more accurate results without significantly affecting the convergence rate, which is also not affected by the different discretization schemes of the Huygens's surface. We further demonstrated, that for UITXE computations, the incident EM fields basis from the approximate RSVD or from the less smooth $\mathbf{N}$ operator does not provide accurate results, hence, we suggest generating an orthonormal total EM fields basis from $\mathbf{K}$ operator that provides faster convergence, similar to that of VSH, and reliable converged values. Finally, we showed that the SVD-based numerical EM fields basis can describe more efficiently EM fields within arbitrary objects or volumes with non-smooth boundaries than a basis from VSH functions [80].

With regard to MRI applications, we demonstrated how the vectors of the total EM fields basis can be applied in optimization procedures and used to calculate performance bounds, such as the UITXE [75], which constitutes a valuable metric for transmit arrays benchmarking and RF shimming algorithms evaluation. We showed that the overall behavior of the UITXE within an inhomogeneous head model and a uniform sphere are similar when their dimensions are comparable and that the general trends of transmit array performance with respect to field strength and number of coil elements remain valid between the two models. We computed ICP on a given arbitrary surface yielding optimal SNR within an inhomogeneous head model [82] and found that they depend mostly on the topology of the surface onto which they are constrained, even though optimal SNR is similar for different substrates. We further computed the percentage of UISNR that realistic head coil substrates can capture and showed that UISNR is approached better by the helmet and head-and-neck substrates than by the cylinder substrate, especially at the periphery, leading to the conclusion that helmet coils are better-suited for head imaging. In addition to helping to visually understand the origin of optimal RF coil performance, ICP could also help designing the next-generation MR coils, by providing an intuitive initial guess for non-convex coil optimization algorithms, setting the scene for a truly task-optimal design of RF coils.

From an imaging perspective and in an attempt to answer to the question of whether the scientific community and potentially the industry should continue pursuing UHF MRI we could say the following, motivated by the findings of this thesis and from state-of-the-art studies reviewed at Chapter 2. Increasing the B_0 field strength above 7T could result in considerable B_1^+ inhomogeneities, particularly if the MR scanner is not operated properly, and one could end up having worse image quality than from a 3T or lower field strength scanner that yields smoother B_1^+ fields. Additionally, a UHF MR scanner may be operated sub-optimally with the fear of excessive heat deposition to the patient. However, a substantial body of research, including both simulation [12, 67, 106, 166] and experimental [87, 124, 171] studies,

demonstrates that pushing the limits to UHF strengths can indeed make the difference. Two characteristic examples that further support this claim is the world's first MRI of the human body at 10.5T [283], where the greater detail of the MR image is clear, and the recent FDA approval of the first 7T MR scanner for clinical application [103]. Therefore, we believe that it is indeed worth pursuing UHF MRI, which effort should be accompanied by substantial research and development that takes into account the UHF challenges and should aim to develop novel, task-optimal RF arrays that respect the underlying EM fields considerations, hence, such arrays could yield higher SNR and faster image acquisition without compromising patient safety and image quality. Finally, there is a recent review article that discusses the question of the evolution of the UHF body MRI, its technology, its applications, and its future directions [284], where an interested reader can refer to for more details.

6.2 Future Work and Research Extensions

In this thesis, among other contributions, a current-based VIE solver with PWL basis functions was developed. Future work that could possibly enhance its overall performance could involve the PWL approximation of the electrical properties for cases where the material profile varies with higher-order polynomial functions, as well as, the derivation, implementation, and convergence study of the subtraction method for the singular kernels of $\mathcal{N}$ and $\mathcal{K}$ operators, and the implementation and convergence properties study of a diagonal preconditioner. Another interesting research direction could be the comparison of the convergence properties of an iterative solver between the current-based formulation with either PWC or PWL basis functions and the discrete dipole approximation formulation for a broad range of permittivities and electrical sizes. Finally, the feasibility, accuracy and convergence properties study of reduced-order linear basis functions could be investigated.

Additionally, we described robust algorithms for the generation of a consistent numerical EM fields basis within an arbitrary, inhomogeneous object and showed how such basis can be used to compute performance bounds for MR-related metrics within realistic body models. From a numerical point of view, future steps could include the investigation of the convergence properties and numerical accuracy of UISNR and UITXE computed by an orthonormal basis of incident magnetic fields and the study of whether the sensitivity of SNR and TXE to magnetic fields affects such properties. Another direction worth pursuing could be the direct generation of an orthonormal total EM fields basis by applying the free-space operator, solving the scattering problem for each random incident EM field for RSVD or for each column vector of the currents-to-incident-fields coupling matrix for SSVD and DSVD, and then orthonormalizing. This approach may be more computationally expensive but might be worth investigating since we showed that an incident EM fields basis does not provide accurate results when generated by the less smooth $\mathbf{N}$ operator or by the approxi-

mate RSVD for UITXE computations. Generating a basis by applying SVD factorization to the VSH basis modes over the mask of an arbitrary object could also be an inviting research direction, motivated by the well-behaved UISNR convergence properties of the VSH basis in central voxel positions and the fact that the incident EM fields by the SVD basis conform with the shape of the boundary of the arbitrary object and illuminate regions close to it. Similar convergence properties comparisons studies for various geometries against other analytical (complete) bases derived in cylindrical or Cartesian coordinate systems could also be performed, during which studies, it should prove useful to view the numerical basis as an extension of spectral methods to arbitrarily shaped domains.

More broadly speaking, we would like to place the numerical basis tool into a greater perspective and highlight that it is a general tool that can be used for seemingly different applications within various fields. In fact, we showed that, within the MR field, the numerical basis can be utilized to compute ideal RF excitation patterns for arbitrary surfaces yielding optimal SNR in inhomogeneous head models [82] or to calculate theoretical transmit performance bounds within these head models [75]. Additionally, it has been applied for the ultra-fast RF coil design [65] through the MR-specific Green's function [161] and, recently, for generating orthogonal excitations in Global Maxwell Tomography [95], for the design of optimal shim bases towards ultimate B_0 shim [285], and for peripheral nerve stimulation constrained gradient coil design [286]. In a slightly different setup, it has been employed for the design of high-permittivity pads for dielectric shimming [287] and it could possibly be used for generating the optimal RF excitation patterns that generate reduced or close-to-null electric field zones inducing minimal electric currents in biodegradable implants [288] that could lead to implant friendly RF coil designs. Furthermore, within the field of optics, similar concepts have been exploited for the design of non-intuitive illumination patterns that maximize optical force or torque [289] and within the antennas and propagation field, since many years, there already exists the characteristic modes theory [271,272] for the expansion of radiated and scattered fields into modes characteristic of the obstacle shape and independent of any specific excitation. Optimal currents on arbitrarily shaped surfaces that extremize various antenna parameters have also been presented [290] and reduced-order models for fast antenna characterization have been generated [273], where all these approaches rely on the idea of expanding EM fields and currents onto an appropriate basis set. Finally, due to similarities between the acoustic and the electrodynamic Green's function, there should be crossover scope for applying analogous ideas within the acoustic field with the goal of designing arrays for high-intensity focused ultrasound.

Future work associated with applications within the MR field could include the experimental coil performance evaluation with suitable hardware/software for RF power measurements with respect to the UITXE in spherical phantoms. In addition, it could include the computation of UITXE in specific ROIs of the realistic head model (e.g., cerebellum), the study

of the contributions of dipole arrays and dielectric pads to UITXE, as well as, whether the electric field distribution that corresponds to UITXE respects local SAR aspects and whether B_1^+ remains homogeneous in realistic head models. It would also be of interest to compute eigenvalues other than the largest and investigate how they compare to it, how their corresponding ICP change, whether B_1^+ homogeneity improves and if local SAR decreases. Furthermore, with the aid of ICP, a new research project could involve the implementation of RF coil shape optimization and/or SIE node optimization algorithms, where ICP could serve as an initial guess to the optimizer. Additionally, curvilinear basis functions for the discretization of Huygens's surface could be employed for more accurate coil modeling and ICP representation. A new promising principle, the optimality principle [73], which allows for the rapid and intuitive prediction of ICP for arbitrary dielectric objects and current-bearing surfaces, could be further explored for the UITXE case. Finally, a comparative study between MR images acquired with arrays driven with the optimal RF shimming coefficients that approach UISNR or UITXE and images acquired with traditional birdcage coils could be of great relevance and interest.

In a broader perspective and in an attempt to describe possible directions that could set the scene for the future of MR research and practice, the following challenges with speculations on how they could be addressed are worth to be mentioned. With regard to MR engineering at UHF, different solutions for the transmit field inhomogeneity due to wavelength/dielectric effects along with the development of standardized methods for SAR monitoring and control are among the most significant challenges. To address these needs, novel and task-optimal RF array designs could be of great relevance and part of the work presented in this thesis could provide a robust framework for optimizing their design. In addition, digital artifact removal pipelines could be employed for smoothening the constructive interference effects associated with the UHF strength, while dielectric shimming approaches already provide a fast and efficient way to tackle the corresponding destructive interferences [260], however, only at superficial regions. Furthermore, image-to-image translation approaches [291] could be of great practical value for generating higher-resolution 7T images at the cost of a 3T MRI and similar approaches based on neural networks could be employed for the regularization of a relevant study that aims at the reconstruction of the tissue electrical properties from MR measurements [95]. Combined Bloch/Maxwell simulations with SNR-optimizing RF excitation sequences could further provide useful insight into the SNR improvement level of the MR images with respect to images acquired with traditional RF excitation sequences, while experimental studies focusing on the MR image acquisition from RF arrays that approach the shape of the ICP, thus the UISNR, and that are driven with the optimal RF shimming weights could give an answer to the question of how the RF detectors would behave given a complex excitation sequence and how the resulting MR image would compare to images acquired with traditional birdcage coils. Finally, the experimental study of the existence of

second-order relaxation effects in biological tissues with increasing B_0 field strength could also be of great relevance towards the development and deployment of the future MR scanners.

A Expansion of Dyadic Green's Function In Vector Spherical Harmonics

We construct the DGF for a dielectric sphere with its center located at the origin of the coordinates system using the method of superposition [15, 191]:

$$\bar{\boldsymbol{G}}_{\mathrm{sph}}(\boldsymbol{r},\boldsymbol{r}') = \begin{cases} \bar{\boldsymbol{G}}(\boldsymbol{r},\boldsymbol{r}') + \bar{\boldsymbol{G}}_{\mathrm{s},1}(\boldsymbol{r},\boldsymbol{r}') & r \geq a \\ \bar{\boldsymbol{G}}_{\mathrm{s},2}(\boldsymbol{r},\boldsymbol{r}') & r \leq a \end{cases}, \tag{A.1}$$

where $\boldsymbol{r}'$ is the position of the current sources, $\boldsymbol{r}$ is the position at which the EM field is observed and a is the radius of the sphere. The free-space DGF is defined as:

$$\bar{\boldsymbol{G}}(\boldsymbol{r},\boldsymbol{r}') = -jk_0 \sum_{l=0}^{\infty}\sum_{m=-l}^{l} \begin{cases} \boldsymbol{M}^{+}_{l,m}(k_0,\boldsymbol{r})\boldsymbol{M}_{l,m}(k_0,\boldsymbol{r}') + \boldsymbol{N}^{+}_{l,m}(k_0,\boldsymbol{r})\boldsymbol{N}_{l,m}(k_0,\boldsymbol{r}') & \boldsymbol{r} \geq \boldsymbol{r}' \\ \boldsymbol{M}_{l,m}(k_0,\boldsymbol{r})\boldsymbol{M}^{+}_{l,m}(k_0,\boldsymbol{r}') + \boldsymbol{N}_{l,m}(k_0,\boldsymbol{r})\boldsymbol{N}^{+}_{l,m}(k_0,\boldsymbol{r}') & \boldsymbol{r} \leq \boldsymbol{r}' \end{cases}, \tag{A.2}$$

the scattering component of the DGF outside the sphere as:

$$\bar{\boldsymbol{G}}_{s,1}(\boldsymbol{r},\boldsymbol{r}') = -jk_0 \sum_{l=0}^{\infty}\sum_{m=-l}^{l} \left[A_l \boldsymbol{M}^{+}_{l,m}(k_0,\boldsymbol{r})\boldsymbol{M}^{+}_{l,m}(k_0,\boldsymbol{r}') + B_l \boldsymbol{N}^{+}_{l,m}(k_0,\boldsymbol{r})\boldsymbol{N}^{+}_{l,m}(k_0,\boldsymbol{r}')\right], \tag{A.3}$$

and inside the sphere as:

$$\bar{\boldsymbol{G}}_{s,2}(\boldsymbol{r},\boldsymbol{r}') = -jk_0 \sum_{l=0}^{\infty}\sum_{m=-l}^{l} \left[C_l \boldsymbol{M}_{l,m}(k_{\mathrm{in}},\boldsymbol{r})\boldsymbol{M}^{+}_{l,m}(k_0,\boldsymbol{r}') + D_l \boldsymbol{N}_{l,m}(k_{\mathrm{in}},\boldsymbol{r})\boldsymbol{N}^{+}_{l,m}(k_0,\boldsymbol{r}')\right], \tag{A.4}$$

where k_0 and k_{in} are the wavenumbers in free-space and inside the sphere, respectively, A_l, B_l, C_l and D_l are calculated by applying the Dirichlet boundary conditions [15], and the spherical vector wave functions are defined as:

$$\begin{aligned} \boldsymbol{M}_{l,m}(k,\boldsymbol{r}) &= \frac{1}{-j\sqrt{l(l+1)}} \nabla \times (\psi_{l,m}(k,\boldsymbol{r})\boldsymbol{r}), \\ \boldsymbol{N}_{l,m}(k,\boldsymbol{r}) &= \frac{1}{k}\frac{1}{-j\sqrt{l(l+1)}} \nabla \times \nabla \times (\psi_{l,m}(k,\boldsymbol{r})\boldsymbol{r}), \end{aligned} \tag{A.5}$$

with k being the appropriate wavenumber at the position of interest and $\psi_{l,m}(k,\boldsymbol{r})$ is the eigenfunction of the scalar wave function $\psi_{l,m}(k,\boldsymbol{r}) = j_l(kr)Y_{l,m}(\theta,\phi)$ with

$$Y_{l,m}(\theta,\phi) = \sqrt{\frac{2l+1}{4\pi}\frac{(l-m)!}{(l+m)!}}P_l^m(\cos\theta)e^{jm\phi}, \tag{A.6}$$

where $P_l^m(\cos\theta)$ is the associated Legendre function of order (l,m) and $j_l(kr)$ is the spherical Bessel function of order l. The $^+$ superscript in Eqs. A.2 - A.4 indicates that the spherical Hankel function of the first kind and order l is used in place of the Bessel of the same order.

The electric field inside the sphere, which is also considered to have the permeability of free-space, can be calculated using Eqs. 3.9, 3.10, A.1, and A.4 (since we are interested in calculating the EM field inside the sphere, we select the second branch) as:

$$\begin{aligned}
\boldsymbol{E}(\boldsymbol{r}) &= -j\omega\mu_0\int_{V'}\bar{\boldsymbol{G}}_{\text{sph}}(\boldsymbol{r},\boldsymbol{r}')\cdot\boldsymbol{J}(\boldsymbol{r}')dV' \\
&= -j\omega\mu_0\int_{S'}\bar{\boldsymbol{G}}_{s,2}(\boldsymbol{r},\boldsymbol{r}')\cdot\boldsymbol{K}(\boldsymbol{r}')dS' \\
&= -\omega\mu_0 k_0\int_{S'}\left\{\sum_{l=0}^{\infty}\sum_{m=-l}^{l}\left[C_l\boldsymbol{M}_{l,m}(k_{\text{in}},\boldsymbol{r})\boldsymbol{M}^+_{l,m}(k_0,\boldsymbol{r}') + D_l\boldsymbol{N}_{l,m}(k_{\text{in}},\boldsymbol{r})\boldsymbol{N}^+_{l,m}(k_0,\boldsymbol{r}')\right]\right\}\cdot \\
&\quad\cdot\left\{\sum_{l'=0}^{\infty}\sum_{m'=-l'}^{l'}-j\sqrt{l'(l'+1)}\left[W^M_{l',m'}\boldsymbol{X}_{l',m'}(\theta',\phi') + W^E_{l',m'}\hat{\boldsymbol{r}}\times\boldsymbol{X}_{l',m'}(\theta',\phi')\right]\right\}dS',
\end{aligned} \tag{A.7}$$

from which we can define the coefficients in 3.11:

$$\begin{aligned}
V^M_{(l,m)(l',m')} &= C_l\int_{S'}\Big[\boldsymbol{M}^+_{l,m}(k_0,\boldsymbol{r}')\cdot\left(-j\sqrt{l'(l'+1)}\boldsymbol{X}_{l',m'}(\theta',\phi')\right)W^M_{l',m'} \\
&+ \boldsymbol{M}^+_{l,m}(k_0,\boldsymbol{r}')\cdot\left(-j\sqrt{l'(l'+1)}\hat{\boldsymbol{r}}\times\boldsymbol{X}_{l',m'}(\theta',\phi')\right)W^E_{l',m'}\Big]dS',
\end{aligned} \tag{A.8}$$

$$\begin{aligned}
V^N_{(l,m)(l',m')} &= D_l\int_{S'}\Big[\boldsymbol{N}^+_{l,m}(k_0,\boldsymbol{r}')\cdot\left(-j\sqrt{l'(l'+1)}\boldsymbol{X}_{l',m'}(\theta',\phi')\right)W^M_{l',m'} \\
&+ \boldsymbol{N}^+_{l,m}(k_0,\boldsymbol{r}')\cdot\left(-j\sqrt{l'(l'+1)}\hat{\boldsymbol{r}}\times\boldsymbol{X}_{l',m'}(\theta',\phi')\right)W^E_{l',m'}\Big]dS',
\end{aligned} \tag{A.9}$$

where the VSH is defined as [192]:

$$\boldsymbol{X}_{l,m}(\theta,\phi) = \frac{1}{j\sqrt{l(l+1)}}(\hat{\boldsymbol{r}}\times\boldsymbol{\nabla})Y_{l,m}(\theta,\phi), \tag{A.10}$$

in which $\hat{\boldsymbol{r}}$ is the unit vector in the radial direction. Then, by applying the orthogonality relations of the VSH [192], the integrals can be solved and the coefficients are calculated as

$\mathbf{v} = \mathbf{T}\mathbf{w}$ with $\mathbf{v} = \left[V_{l,m}^{M}; V_{l,m}^{N}\right]$, $\mathbf{w} = \left[W_{l,m}^{M}; W_{l,m}^{E}\right]$ with the transformation matrix defined as [15]:

$$\mathbf{T} = \begin{bmatrix} -j\sqrt{l(l+1)}h_l^{(1)}(k_0 b)C_l & 0 \\ 0 & \frac{-j\sqrt{l(l+1)}}{k_0 b}\left.\frac{\partial\left[r h_l^{(1)}(k_0 r)\right]}{\partial r}\right|_{r=b} D_l \end{bmatrix}. \tag{A.11}$$

Finally, from Maxwell equation $\boldsymbol{B}(\boldsymbol{r}) = j/\omega\nabla \times \boldsymbol{E}(\boldsymbol{r})$ and the symmetrical relations of the vector wave functions [191], we form the magnetic field as in Eq. 3.11.

Then, the last step is to calculate the transmit sensitivities and electric fields covariance matrices. In order to construct the B_1^+ transmit sensitivity matrix we expand the transmit field at Q spatial locations or voxels with a finite expansion order $l_{\max}$ yielding $N = (l_{\max} + 1)^2$ number of modes which are sufficient to ensure convergence. So, for each mode, we can construct the transmit sensitivity matrix as:

$$B_1^+(\boldsymbol{r}_q) = B_x + jB_y = \sum_{l=0}^{l_{\max}} \sum_{m=-l}^{l} \mathbf{C}_{l,m}(\boldsymbol{r}_q)\mathbf{w}. \tag{A.12}$$

$\mathbf{C}_{l,m}(\boldsymbol{r}_q)$ is a $Q \times 2$ that includes both the divergence-free and curl-free contributions and accounts for the boundary conditions:

$$\mathbf{C}_{l,m}(\boldsymbol{r}_q) = -j\mu_0 k_0 k_{\text{in}} \left[N_{l,m}^{x}(k_{\text{in}}, \boldsymbol{r}_q) + jN_{l,m}^{y}(k_{\text{in}}, \boldsymbol{r}_q) \quad M_{l,m}^{x}(k_{\text{in}}, \boldsymbol{r}_q) + jM_{l,m}^{y}(k_{\text{in}}, \boldsymbol{r}_q)\right]. \tag{A.13}$$

The electric fields covariance matrix for the modes can be calculated as:

$$P_{\text{abs}} = \frac{1}{2}\int_V \sigma(\boldsymbol{r})\boldsymbol{E}^*(\boldsymbol{r}) \cdot \boldsymbol{E}(\boldsymbol{r})dV = \sum_{l=0}^{l_{\max}} \sum_{m=-l}^{l} \mathbf{w}^H \mathbf{\Phi}_{l,m}\mathbf{w}, \tag{A.14}$$

where $\mathbf{\Phi}_{l,m} = \mathbf{T}^H \mathbf{R}_L \mathbf{T}$ is a 2×2 diagonal matrix and $\mathbf{R}_L$ is given by [15]:

$$\mathbf{R}_L = \frac{\sigma(\omega\mu_0 k_0)^2}{2} \begin{bmatrix} \int_0^a |j_l(k_{\text{in}} r)| r^2 dr & 0 \\ 0 & \frac{1}{|k_{\text{in}}|^2}\int_0^a \left[\left|\frac{\partial[r j_l(k_{\text{in}} r)]}{\partial r}\right|^2 + l(l+1)|j_l(k_{\text{in}} r)|^2\right] dr \end{bmatrix}, \tag{A.15}$$

and the electric fields covariance matrix with dimensions $2N \times 2N$ for all the modes is:

$$\mathbf{\Phi}_{\text{mode}} = \begin{bmatrix} \mathbf{\Phi}_{0,0} & 0 & 0 \\ 0 & \ddots & 0 \\ 0 & 0 & \mathbf{\Phi}_{l_{\max}, l_{\max}} \end{bmatrix}. \tag{A.16}$$

B Convergence of Ultimate Intrinsic Transmit Efficiency

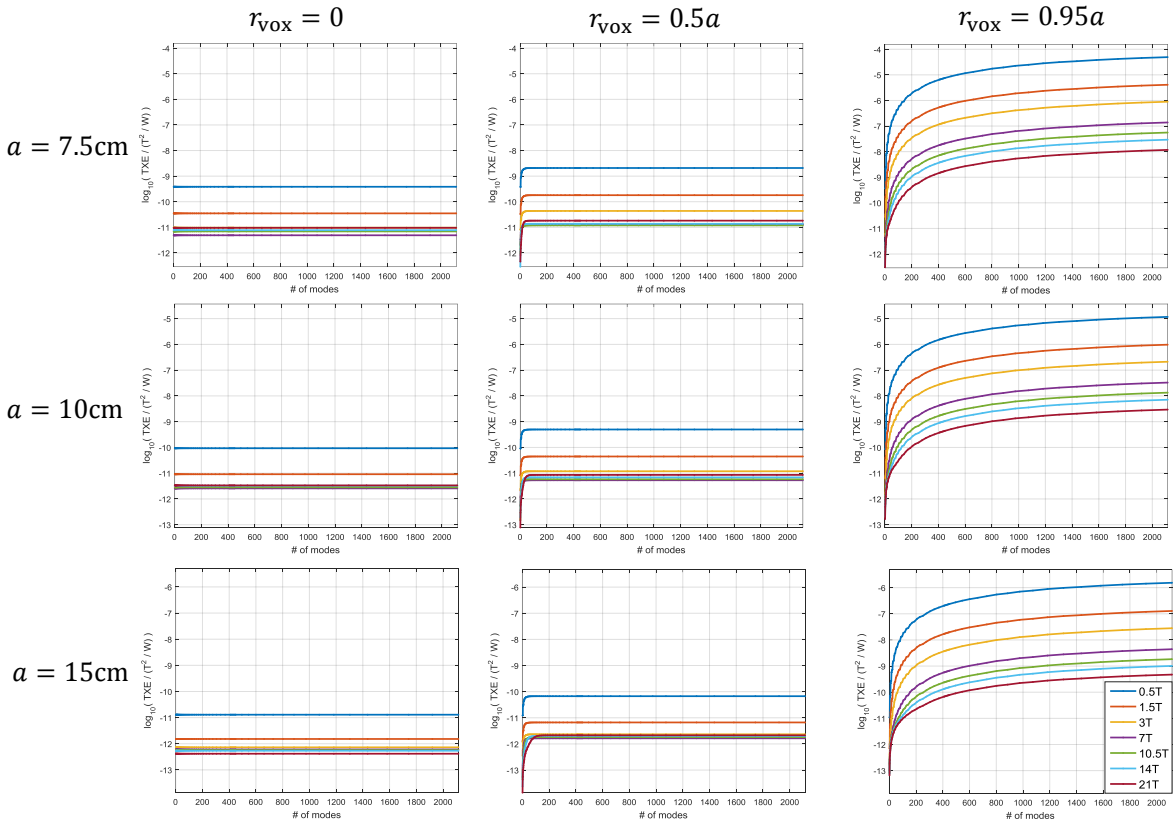

Figure B.1: Convergence of the UITXE as a function of voxel location, for different main magnetic field strengths and object sizes. UITXE convergence is plotted in logarithmic scale for expansion order $l_{\max}$ ranging from 0 to 45, yielding $N = (l_{\max} + 1)^2 = 2116$ modes. Note that each mode includes both the curl-free and divergence-free components in Eq. [10]. Results are shown for sphere radii $a = 7.5, 10, 15\text{cm}$ and uniform brain-mimicking electrical properties adjusted for the corresponding frequency at $B_0 = 0.5, 1.5, 3, 7, 10.5, 14, 21\text{T}$. The convergence was assessed for three voxel locations at $r_{\text{vox}} = 0, 0.5a, 0.95a$. The closer a voxel is to the surface of the sphere the larger the number of modes required for convergence. The convergence is also slower at higher field strengths, which is more evident for larger object sizes and the intermediate voxel location.

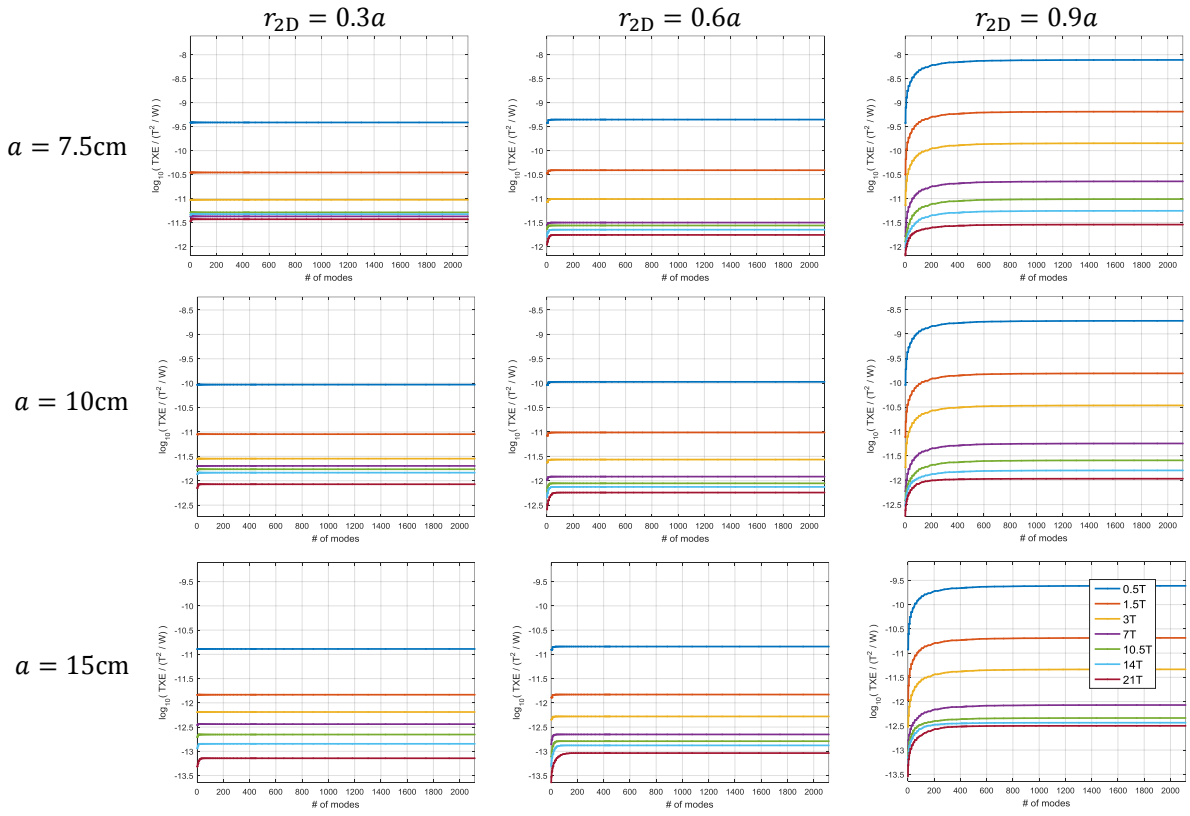

Figure B.2: Convergence of the UITXE as a function of the size of the two-dimensional region of interest, for different main magnetic field strengths and object sizes. UITXE convergence is plotted for the same number of modes, sphere radii and B_0 shown in Figure B.1, for different sizes $(r_{2D} = 0.3a, 0.6a, 0.9a)$ of a 2D circular disk ROI. More modes are required for convergence with larger excitation regions and at higher field strengths. This can be seen more clearly for larger object sizes and especially for the 2D ROI with $r_{2D} = 0.6a$.

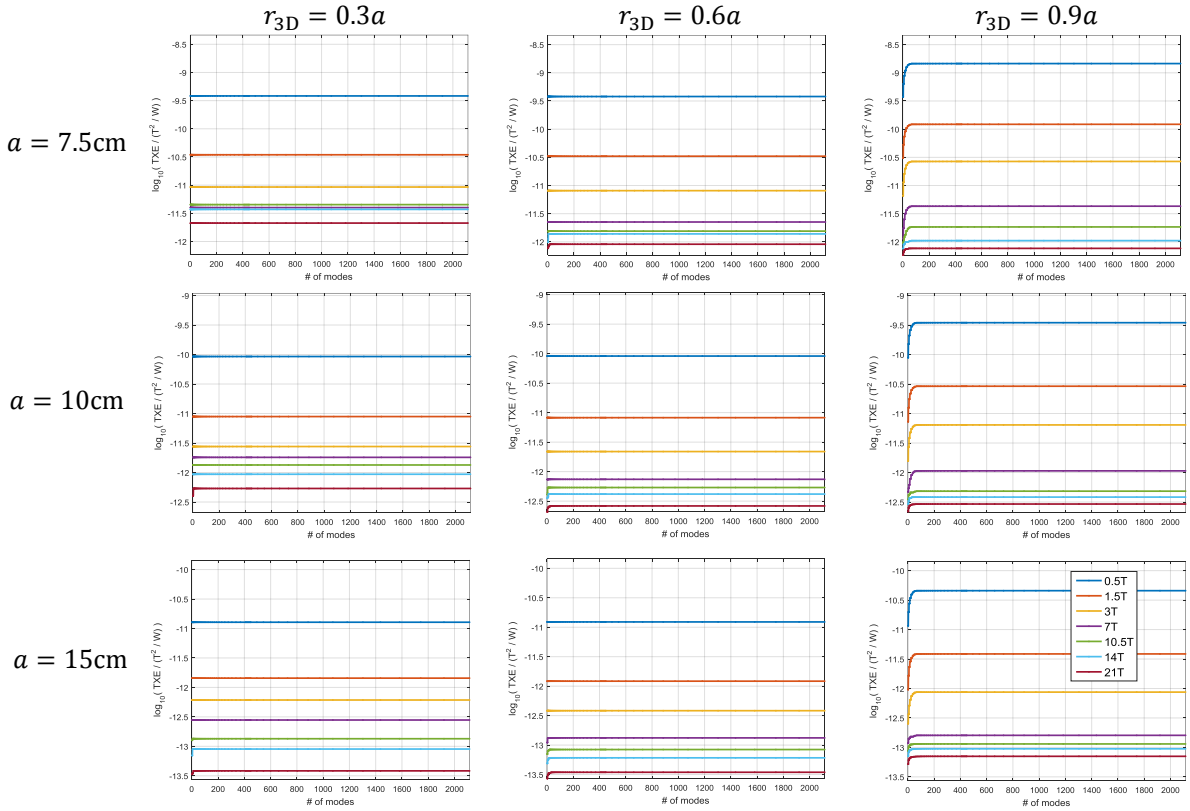

Figure B.3: Convergence of the UITXE calculations as a function of the size of the three-dimensional region of interest, for different main magnetic field strengths and object sizes. UITXE convergence is plotted for different sizes $(r_{3D} = 0.3a, 0.6a, 0.9a)$ of a spherical 3D ROI concentric with the sample. Results are shown for the same range of expansion order, magnetic field strength and object size used in Figure B.1.

C Reduction Procedure of Volume-Volume to Surface-Surface Integrals

C.1 Operator $\mathcal{N}$

We start by Eq. 4.68a which can be rewritten as:

$$\begin{aligned} N_{\boldsymbol{m},\boldsymbol{n}}^{pl,ql'} = & \int_V \int_{V'} \nabla \times \boldsymbol{f}_{\boldsymbol{m}}^{pl} \cdot \nabla \times (g \boldsymbol{f}_{\boldsymbol{n}}^{ql'}) dV' dV \\ & - \int_V \int_{V'} \nabla \cdot (\boldsymbol{f}_{\boldsymbol{m}}^{pl} \times \nabla \times (g \boldsymbol{f}_{\boldsymbol{n}}^{ql'})) dV' dV, \end{aligned} \tag{C.1}$$

and then apply the divergence theorem to it:

$$\begin{aligned} N_{\boldsymbol{m},\boldsymbol{n}}^{pl,ql'} = & - \int_{V'} \oint_S (\hat{\boldsymbol{n}} \times \nabla \times \boldsymbol{f}_{\boldsymbol{m}}^{pl}) \cdot g \boldsymbol{f}_{\boldsymbol{n}}^{ql'} dS dV' \\ & - \int_{V'} \oint_S (\hat{\boldsymbol{n}} \times \boldsymbol{f}_{\boldsymbol{m}}^{pl}) \cdot \nabla \times (g \boldsymbol{f}_{\boldsymbol{n}}^{ql'}) dS dV'. \end{aligned} \tag{C.2}$$

Since the curl of a linear function is a constant vector, we can move it outside the inner integral:

$$\begin{aligned} N_{\boldsymbol{m},\boldsymbol{n}}^{pl,ql'} = & - \oint_S (\hat{\boldsymbol{n}} \times \nabla \times \boldsymbol{f}_{\boldsymbol{m}}^{pl}) \cdot \underbrace{\int_{V'} g \boldsymbol{f}_{\boldsymbol{n}}^{ql'} dV'}_{\boldsymbol{I}_1'} dS \\ & - \oint_S (\hat{\boldsymbol{n}} \times \boldsymbol{f}_{\boldsymbol{m}}^{pl}) \cdot \underbrace{\int_{V'} \nabla \times (g \boldsymbol{f}_{\boldsymbol{n}}^{ql'}) dV'}_{\boldsymbol{I}_2'} dS. \end{aligned} \tag{C.3}$$

We can further simplify $\boldsymbol{I}_2'$ by using the fact that $\nabla g = -\nabla' g$ and subsequently $\nabla \times (g\boldsymbol{f}_{\boldsymbol{n}}^{ql'}) = g\nabla' \times \boldsymbol{f}_{\boldsymbol{n}}^{ql'} - \nabla' \times (g\boldsymbol{f}_{\boldsymbol{n}}^{ql'})$ and write it down as:

$$\boldsymbol{I}_2' = \nabla' \times \boldsymbol{f}_{\boldsymbol{n}}^{ql'} \int\limits_{V'} g dV' - \int\limits_{V'} \nabla' \times (g\boldsymbol{f}_{\boldsymbol{n}}^{ql'}) dV'. \tag{C.4}$$

The first integral in the right-hand side above requires special treatment. As shown in [233], with the help of powerful techniques presented in [235], we can get the following expression:

$$g = \nabla \cdot \boldsymbol{F} = -\nabla' \cdot \boldsymbol{F}, \tag{C.5}$$

where

$$\boldsymbol{F} = \frac{1}{(jk_0)^2} \nabla (g - g_0) = -\frac{1}{(jk_0)^2} \nabla' (g - g_0), \tag{C.6}$$

with $g_0 = g|_{k_0=0}$ denoting the static Green's function and by calculating the gradients, $\boldsymbol{F}$ can be rewritten as:

$$\boldsymbol{F} = -\frac{(\boldsymbol{r} - \boldsymbol{r}')}{(jk_0)^2} \left(jk_0 \frac{g}{|\boldsymbol{r} - \boldsymbol{r}'|} + \frac{g - g_0}{|\boldsymbol{r} - \boldsymbol{r}'|^2} \right). \tag{C.7}$$

Then, by combining the above we get:

$$\boldsymbol{I}_2' = -\nabla' \times \boldsymbol{f}_{\boldsymbol{n}}^{ql'} \oint\limits_{S'} \hat{\boldsymbol{n}}' \cdot \boldsymbol{F} dS' - \oint\limits_{S'} (\hat{\boldsymbol{n}}' \times \boldsymbol{f}_{\boldsymbol{n}}^{ql'}) g dS'. \tag{C.8}$$

Similarly, for $\boldsymbol{I}_1'$ we have:

$$\begin{aligned} \boldsymbol{I}_1' &= \int\limits_{V'} g \boldsymbol{f}_{\boldsymbol{n}}^{ql'} dV' = -\sum_{q \in \{x,y,z\}} \int\limits_{V'} \nabla' \cdot \boldsymbol{F} f_{\boldsymbol{n}}^{ql'} \hat{\boldsymbol{q}} dV' \\ &= \sum_{q \in \{x,y,z\}} \left(-\int\limits_{V'} \nabla' \cdot (\boldsymbol{F} f_{\boldsymbol{n}}^{ql'}) \hat{\boldsymbol{q}} dV' + \hat{\boldsymbol{q}} \nabla' f_{\boldsymbol{n}}^{ql'} \cdot \int\limits_{V'} \boldsymbol{F} dV' \right). \end{aligned} \tag{C.9}$$

Next, by substituting Eq. C.6 and applying again the divergence theorem, we get:

$$\begin{aligned} \boldsymbol{I}_1' = &-\sum_{q \in \{x,y,z\}} \oint\limits_{S'} \hat{\boldsymbol{n}}' \cdot \boldsymbol{F} f_{\boldsymbol{n}}^{ql'} \hat{\boldsymbol{q}} dS' \\ &- \sum_{q \in \{x,y,z\}} \hat{\boldsymbol{q}} \nabla' f_{\boldsymbol{n}}^{ql'} \cdot \oint\limits_{S'} \hat{\boldsymbol{n}}' \frac{g - g_0}{(jk_0)^2} dS'. \end{aligned} \tag{C.10}$$

Finally, the original 6D integral Eq. C.1 is reduced to the sum of four closed 4D integrals over the faces of the volumetric elements:

$$N_{\boldsymbol{m},\boldsymbol{n}}^{pl,ql'} = N_1 + N_2 + N_3 + N_4, \tag{C.11}$$

where

$$N_1 = \oint_S (\hat{\boldsymbol{n}} \times \boldsymbol{f}_{\boldsymbol{m}}^{pl}) \cdot \oint_{S'} (\hat{\boldsymbol{n}}' \times \boldsymbol{f}_{\boldsymbol{n}}^{ql'}) g dS' dS, \tag{C.12a}$$

$$N_2 = -\oint_S (\hat{\boldsymbol{n}} \times \nabla' \times \boldsymbol{f}_{\boldsymbol{n}}^{ql'}) \cdot \boldsymbol{f}_{\boldsymbol{m}}^{pl} \oint_{S'} \hat{\boldsymbol{n}}' \cdot \boldsymbol{F} dS' dS, \tag{C.12b}$$

$$N_3 = \oint_S (\hat{\boldsymbol{n}} \times \nabla \times \boldsymbol{f}_{\boldsymbol{m}}^{pl}) \cdot \oint_{S'} \boldsymbol{f}_{\boldsymbol{n}}^{ql'} \hat{\boldsymbol{n}}' \cdot \boldsymbol{F} dS' dS, \tag{C.12c}$$

$$N_4 = \sum_{q \in \{x,y,z\}} \oint_S (\hat{\boldsymbol{n}} \times \nabla \times \boldsymbol{f}_{\boldsymbol{m}}^{pl}) \cdot \hat{\boldsymbol{q}} \nabla' f_{\boldsymbol{n}}^{ql'} \cdot \oint_{S'} \hat{\boldsymbol{n}}' \frac{g - g_0}{(jk_0)^2} dS' dS. \tag{C.12d}$$

It is clear from the final expressions that the resulting 4D integrals have kernels that are smoother than the original 6D integral. In particular, only N_1 has a $1/|\boldsymbol{r} - \boldsymbol{r}'|$ weak singularity and the rest are non-singular with singular derivatives. Therefore, they are amenable to well-established integration techniques in the most challenging case where the elements have common points [148–150, 159, 160]. It is also worth noting that the final expression reduces to the single term N_1 for PWC functions, since the rest are identically zero.

C.2 Operator $\mathcal{K}$

Next, we proceed with the integral Eq. 4.68b, which assumes the following form:

$$\begin{aligned} K_{\boldsymbol{m},\boldsymbol{n}}^{pl,ql'} &= \int_V \int_{V'} \boldsymbol{f}_{\boldsymbol{m}}^{pl}(\boldsymbol{r}) \cdot \nabla \times (g \boldsymbol{f}_{\boldsymbol{n}}^{ql'}(\boldsymbol{r}')) dV' dV \\ &= \int_V \boldsymbol{f}_{\boldsymbol{m}}^{pl} \cdot \underbrace{\int_{V'} \nabla \times (g \boldsymbol{f}_{\boldsymbol{n}}^{ql'}) dV'}_{\boldsymbol{I}_2'} dV. \end{aligned} \tag{C.13}$$

By substituting again Eq. C.8 into the above equation and by reordering the integrals we derive:

$$
\begin{aligned}
K_{\boldsymbol{m},\boldsymbol{n}}^{pl,ql'} = &- \oint_{S'} \hat{\boldsymbol{n}}' \cdot \underbrace{\int_{V} \boldsymbol{F} \boldsymbol{f}_{\boldsymbol{m}}^{pl} \cdot \nabla' \times \boldsymbol{f}_{\boldsymbol{n}}^{ql'} dV}_{\boldsymbol{I}_3} \, dS' \\
&- \oint_{S'} (\hat{\boldsymbol{n}}' \times \boldsymbol{f}_{\boldsymbol{n}}^{ql'}) \cdot \underbrace{\int_{V} g \boldsymbol{f}_{\boldsymbol{m}}^{pl} dV}_{\boldsymbol{I}_1} \, dS'.
\end{aligned}
\tag{C.14}
$$

One can notice that $\boldsymbol{I}_1$ is similar to $\boldsymbol{I}_1'$, hence it is straightforward to obtain:

$$
\begin{aligned}
\boldsymbol{I}_1 = &\sum_{p \in \{x,y,z\}} \oint_{S_m} \hat{\boldsymbol{n}} \cdot \boldsymbol{F} f_{\boldsymbol{m}}^{pl} \hat{\boldsymbol{p}} dS \\
&- \sum_{p \in \{x,y,z\}} \hat{\boldsymbol{p}} \nabla f_{\boldsymbol{m}}^{pl} \cdot \hat{\boldsymbol{n}} \oint_{S_m} \frac{g - g_0}{(jk_0)^2} dS.
\end{aligned}
\tag{C.15}
$$

While handling $\boldsymbol{I}_3$, for simplicity we denote the linear scalar function $h = \boldsymbol{f}_{\boldsymbol{m}}^{pl} \cdot \nabla' \times \boldsymbol{f}_{\boldsymbol{n}}^{ql'}$, and we write:

$$
\begin{aligned}
\boldsymbol{I}_3 &= \int_V \frac{1}{(jk_0)^2} \nabla (g - g_0) h dV \\
&= \frac{1}{(jk_0)^2} \int_V \nabla \left[(g - g_0) h \right] dV - \frac{\nabla h}{(jk_0)^2} \int_V (g - g_0) dV.
\end{aligned}
\tag{C.16}
$$

Next, taking into account that $\nabla \cdot \frac{(\boldsymbol{r} - \boldsymbol{r}')g_0}{2} = g_0$ and applying the divergence theorem, we get

$$
\begin{aligned}
\boldsymbol{I}_3 = &\frac{1}{(jk_0)^2} \oint_S \hat{\boldsymbol{n}} (g - g_0) h dS \\
&- \frac{\nabla h}{(jk_0)^2} \oint_S \hat{\boldsymbol{n}} \cdot \left(\boldsymbol{F} - \frac{(\boldsymbol{r} - \boldsymbol{r}')g_0}{2} \right) dS.
\end{aligned}
\tag{C.17}
$$

Finally, putting all the above together we can write the original 6D integral in terms of 4D integrals, as follows:

$$
K_{\boldsymbol{m},\boldsymbol{n}}^{pl,ql'} = K_1 + K_2 + K_3 + K_4, \tag{C.18}
$$

where

$$
K_1 = - \oint_{S'} (\hat{\boldsymbol{n}}' \times \boldsymbol{f}_{\boldsymbol{n}}^{ql'}) \cdot \oint_{S_m} \boldsymbol{f}_{\boldsymbol{m}}^{pl} \hat{\boldsymbol{n}} \cdot \boldsymbol{F} dS dS', \tag{C.19a}
$$

$$K_2 = \sum_{p\in\{x,y,z\}} \oint_{S'} (\hat{\boldsymbol{n}}' \times \boldsymbol{f}_{\boldsymbol{n}}^{ql'}) \cdot \hat{\boldsymbol{p}} \nabla f_{\boldsymbol{m}}^{pl} \cdot \oint_{S_m} \hat{\boldsymbol{n}} \frac{g - g_0}{(jk_0)^2} dS dS', \tag{C.19b}$$

$$K_3 = -\oint_{S'} \hat{\boldsymbol{n}}' \cdot \oint_{S} \hat{\boldsymbol{n}} \boldsymbol{f}_{\boldsymbol{m}}^{pl} \cdot \nabla' \times \boldsymbol{f}_{\boldsymbol{n}}^{ql'} \frac{g - g_0}{(jk_0)^2} dS dS', \tag{C.19c}$$

$$K_4 = \frac{1}{(jk_0)^2} \oint_{S'} \hat{\boldsymbol{n}}' \cdot \nabla (\boldsymbol{f}_{\boldsymbol{m}}^{pl} \cdot \nabla' \times \boldsymbol{f}_{\boldsymbol{n}}^{ql'}) \oint_{S} \hat{\boldsymbol{n}} \cdot \left(\boldsymbol{F} - \frac{(\boldsymbol{r} - \boldsymbol{r}')g_0}{2} \right) dS dS'. \tag{C.19d}$$

Again, in the case of PWC functions the only nonzero term in the final expression is K_1. Finally, it is interesting to note that the kernels of the final expressions for $\mathcal{K}$ operator are non-singular that however have singular derivatives, similarly to the three kernels for $\mathcal{N}$ operator.

Bibliography

[1] C. M. Collins, *Electromagnetics in magnetic resonance imaging: physical principles, related applications, and ongoing developments*. Morgan & Claypool Publishers, 2016.

[2] D. G. Nishimura, *Principles of magnetic resonance imaging*. Stanford University, 1996.

[3] J.-M. Jin, "Electromagnetics in magnetic resonance imaging," *IEEE Antennas and Propagation Magazine*, vol. 40, no. 6, pp. 7–22, 1998.

[4] A. G. Polimeridis, "Resolution of scattering and radiation problems in planar stratified media via the method of integral equations," 2008.

[5] A. Christ, W. Kainz, E. G. Hahn, K. Honegger, M. Zefferer, E. Neufeld, W. Rascher, R. Janka, W. Bautz, J. Chen *et al.*, "The Virtual Family-development of surface-based anatomical models of two adults and two children for dosimetric simulations," *Physics in medicine and biology*, vol. 55, no. 2, p. N23, 2009.

[6] C. M. Collins and Z. Wang, "Calculation of radiofrequency electromagnetic fields and their effects in MRI of human subjects," *Magnetic resonance in medicine*, vol. 65, no. 5, pp. 1470–1482, 2011.

[7] P. A. Bottomley, R. W. Redington, W. A. Edelstein, and J. F. Schenck, "Estimating radiofrequency power deposition in body NMR imaging," *Magnetic resonance in medicine*, vol. 2, no. 4, pp. 336–349, 1985.

[8] J. Keltner, J. Carlson, M. Roos, S. Wong, T. Wong, and T. Budinger, "Electromagnetic fields of surface coil in vivo NMR at high frequencies," *Magnetic resonance in medicine*, vol. 22, no. 2, pp. 467–480, 1991.

[9] F. Liu and S. Crozier, "Electromagnetic fields inside a lossy, multilayered spherical head phantom excited by MRI coils: models and methods," *Physics in Medicine & Biology*, vol. 49, no. 10, p. 1835, 2004.

[10] W. Schnell, W. Renz, M. Vester, and H. Ermert, "Ultimate signal-to-noise-ratio of surface and body antennas for magnetic resonance imaging," *IEEE Transactions on Antennas and Propagation*, vol. 48, no. 3, pp. 418–428, 2000.

[11] M. A. Ohliger, A. K. Grant, and D. K. Sodickson, "Ultimate intrinsic signal-to-noise ratio for parallel MRI: electromagnetic field considerations," *Magnetic Resonance in Medicine: An Official Journal of the International Society for Magnetic Resonance in Medicine*, vol. 50, no. 5, pp. 1018–1030, 2003.

[12] F. Wiesinger, P. Boesiger, and K. P. Pruessmann, "Electrodynamics and ultimate SNR in parallel MR imaging," *Magnetic Resonance in Medicine: An Official Journal of the International Society for Magnetic Resonance in Medicine*, vol. 52, no. 2, pp. 376–390, 2004.

[13] R. Lattanzi, "Coil performance evaluation based on electrodynamics: tools for hardware design and validation in magnetic resonance imaging," Ph.D. dissertation, Massachusetts Institute of Technology, 2008.

[14] R. Lattanzi, D. K. Sodickson, A. K. Grant, and Y. Zhu, "Electrodynamic constraints on homogeneity and radiofrequency power deposition in multiple coil excitations," *Magnetic Resonance in Medicine: An Official Journal of the International Society for Magnetic Resonance in Medicine*, vol. 61, no. 2, pp. 315–334, 2009.

[15] R. Lattanzi and D. K. Sodickson, "Ideal current patterns yielding optimal signal-to-noise ratio and specific absorption rate in magnetic resonance imaging: computational methods and physical insights," *Magnetic resonance in medicine*, vol. 68, no. 1, pp. 286–304, 2012.

[16] H.-H. Lee, D. K. Sodickson, and R. Lattanzi, "An analytic expression for the ultimate intrinsic SNR in a uniform sphere," *Magnetic resonance in medicine*, vol. 80, no. 5, pp. 2256–2266, 2018.

[17] N. Avdievich, A. Pfrommer, I. Giapitzakis, and A. Henning, "Analytical modeling provides new insight into complex mutual coupling between surface loops at ultrahigh fields," *NMR in Biomedicine*, vol. 30, no. 10, p. e3759, 2017.

[18] A. Pfrommer and A. Henning, "On the superlinear increase of the ultimate intrinsic signal-to-noise ratio with regard to main magnetic field strength in a spherical sample," in *2017 International Conference on Electromagnetics in Advanced Applications (ICEAA)*. IEEE, 2017, pp. 684–687.

[19] ——, "On the contribution of curl-free current patterns to the ultimate intrinsic signal-to-noise ratio at ultra-high field strength," *NMR in Biomedicine*, vol. 30, no. 5, p. e3691, 2017.

[20] F. Wiesinger, N. De Zanche, and K. Pruessmann, "Approaching ultimate SNR with finite coil arrays," in *Proceedings of the 13th Annual Meeting of ISMRM*, 2005, p. 672.

[21] R. Lattanzi, A. Grant, and D. Sodickson, "Approaching ultimate SNR and ideal current patterns with finite surface coil arrays on a dielectric cylinder," in *Proceedings of the 16th Annual Meeting of ISMRM, Toronto, Ontario, Canada*, 2008, p. 1074.

[22] G. C. Wiggins, B. Zhang, R. Lattanzi, G. Chen, and D. Sodickson, "The electric dipole array: an attempt to match the ideal current pattern for central SNR at 7 Tesla," in *Proceedings of the 20th Annual Meeting of ISMRM, Melbourne, Australia*, vol. 541, 2012.

[23] G. Chen, M. Cloos, R. Lattanzi, D. Sodickson, and G. Wiggins, "Bent electric dipoles: a novel coil design inspired by the ideal current pattern for central SNR at 7 Tesla," *Proc. Int. Soc. Magh. Reson. Med*, vol. 22, p. 402, 2014.

[24] G. Chen, R. Lattanzi, D. Sodickson, and G. Wiggins, "Approaching the ultimate intrinsic SNR with dense arrays of electric dipole antennas," in *Proc. ISMRM*, 2016, p. 168.

[25] R. Lattanzi, A. K. Grant, J. R. Polimeni, M. A. Ohliger, G. C. Wiggins, L. L. Wald, and D. K. Sodickson, "Performance evaluation of a 32-element head array with respect to the ultimate intrinsic SNR," *NMR in Biomedicine: An International Journal Devoted to the Development and Application of Magnetic Resonance In vivo*, vol. 23, no. 2, pp. 142–151, 2010.

[26] M. V. Vaidya, D. K. Sodickson, and R. Lattanzi, "Approaching ultimate intrinsic SNR in a uniform spherical sample with finite arrays of loop coils," *Concepts in Magnetic Resonance Part B: Magnetic Resonance Engineering*, vol. 44, no. 3, pp. 53–65, 2014.

[27] C. M. Deniz, M. V. Vaidya, D. K. Sodickson, and R. Lattanzi, "Radiofrequency energy deposition and radiofrequency power requirements in parallel transmission with increasing distance from the coil to the sample," *Magnetic resonance in medicine*, vol. 75, no. 1, pp. 423–432, 2016.

[28] R. Lattanzi, G. C. Wiggins, B. Zhang, Q. Duan, R. Brown, and D. K. Sodickson, "Approaching ultimate intrinsic signal-to-noise ratio with loop and dipole antennas," *Magnetic resonance in medicine*, vol. 79, no. 3, pp. 1789–1803, 2018.

[29] L. Alon, R. Lattanzi, K. Lakshmanan, R. Brown, C. M. Deniz, D. K. Sodickson, and C. M. Collins, "Transverse slot antennas for high field MRI," *Magnetic resonance in medicine*, vol. 80, no. 3, pp. 1233–1242, 2018.

[30] A. Taflove and S. C. Hagness, *Computational electrodynamics: the finite-difference time-domain method*. Artech house, 2005.

[31] J.-M. Jin, *The finite element method in electromagnetics*. John Wiley & Sons, 2015.

[32] P. P. Silvester and R. L. Ferrari, *Finite elements for electrical engineers*. Cambridge university press, 1996.

[33] F. Wei and A. E. Yılmaz, "A 2-D decomposition based parallelization of AIM for 3-D BIOEM problems," in *Antennas and Propagation (APSURSI), 2011 IEEE International Symposium on*. IEEE, 2011, pp. 3158–3161.

[34] G. Rubinacci and A. Tamburrino, "A broadband volume integral formulation based on edge-elements for full-wave analysis of lossy interconnects," *IEEE transactions on antennas and propagation*, vol. 54, no. 10, pp. 2977–2989, 2006.

[35] C.-C. Lu, "A fast algorithm based on volume integral equation for analysis of arbitrarily shaped dielectric radomes," *IEEE transactions on antennas and propagation*, vol. 51, no. 3, pp. 606–612, 2003.

[36] N. A. Ozdemir and J.-F. Lee, "A nonconformal volume integral equation for electromagnetic scattering from anisotropic materials," in *Antennas and Propagation Society International Symposium 2006, IEEE*. IEEE, 2006, pp. 2889–2892.

[37] ——, "A nonconformal volume integral equation for electromagnetic scattering from penetrable objects," *IEEE Transactions on Magnetics*, vol. 43, no. 4, pp. 1369–1372, 2007.

[38] M. F. Catedra, E. Gago, and L. Nuno, "A numerical scheme to obtain the RCS of three-dimensional bodies of resonant size using the conjugate gradient method and the fast Fourier transform," *IEEE transactions on antennas and propagation*, vol. 37, no. 5, pp. 528–537, 1989.

[39] H. Gan and W. C. Chew, "A discrete BCG-FFT algorithm for solving 3D inhomogeneous scatterer problems," *Journal of Electromagnetic Waves and Applications*, vol. 9, no. 10, pp. 1339–1357, 1995.

[40] L. Sun and W. Chew, "A novel formulation of the volume integral equation for electromagnetic scattering," *Waves in Random and Complex Media*, vol. 19, no. 1, pp. 162–180, 2009.

[41] M. Li and W. C. Chew, "Applying divergence-free condition in solving the volume integral equation," *Progress In Electromagnetics Research*, vol. 57, pp. 311–333, 2006.

[42] W. C. Chew, E. Michielssen, J. Song, and J.-M. Jin, *Fast and efficient algorithms in computational electromagnetics*. Artech House, Inc., 2001.

[43] J. Jin, J. Chen, W. Chew, H. Gan, R. Magin, and P. Dimbylow, "Computation of electromagnetic fields for high-frequency magnetic resonance imaging applications," *Physics in Medicine & Biology*, vol. 41, no. 12, p. 2719, 1996.

[44] M. Costabel, E. Darrigrand, and E. Koné, "Volume and surface integral equations for electromagnetic scattering by a dielectric body," *Journal of Computational and Applied Mathematics*, vol. 234, no. 6, pp. 1817–1825, 2010.

[45] L.-M. Zhang and X.-Q. Sheng, "Discontinuous Galerkin volume integral equation solution of scattering from inhomogeneous dielectric objects by using the SWG basis function," *IEEE Transactions on Antennas and Propagation*, vol. 65, no. 3, pp. 1500–1504, 2017.

[46] D. Borup and O. Gandhi, "Fast-Fourier-transform method for calculation of SAR distributions in finely discretized inhomogeneous models of biological bodies," *IEEE transactions on microwave theory and techniques*, vol. 32, no. 4, pp. 355–360, 1984.

[47] C. S. Geyik, F. Wei, J. W. Massey, and A. E. Yilmaz, "FDTD vs. AIM for bioelectromagnetic analysis," in *Antennas and Propagation Society International Symposium (APSURSI), 2012 IEEE*. IEEE, 2012, pp. 1–2.

[48] J. Markkanen, C.-C. Lu, X. Cao, and P. Yla-Oijala, "Analysis of volume integral equation formulations for scattering by high-contrast penetrable objects," *IEEE Transactions on Antennas and Propagation*, vol. 60, no. 5, pp. 2367–2374, 2012.

[49] J. Markkanen, P. Yla-Oijala, and A. Sihvola, "Discretization of volume integral equation formulations for extremely anisotropic materials," *IEEE Transactions on Antennas and Propagation*, vol. 60, no. 11, pp. 5195–5202, 2012.

[50] J. Markkanen, "Volume potential-integral-equation formulation for electromagnetic scattering by dielectric objects," in *Electromagnetic Theory (EMTS), 2016 URSI International Symposium on*. IEEE, 2016, pp. 468–471.

[51] P. Yla-Oijala, J. Markkanen, S. Jarvenpaa, and S. P. Kiminki, "Surface and volume integral equation methods for time-harmonic solutions of Maxwell's equations," *Progress in electromagnetics Research*, vol. 149, pp. 15–44, 2014.

[52] S. Antenor de Carvalho and L. de Souza Mendes, "Scattering of EM waves by inhomogeneous dielectrics with the use of the method of moments and 3-D solenoidal basis functions," *Microwave and Optical Technology Letters*, vol. 23, no. 1, pp. 42–46, 1999.

[53] D. Schaubert, D. Wilton, and A. Glisson, "A tetrahedral modeling method for electromagnetic scattering by arbitrarily shaped inhomogeneous dielectric bodies," *IEEE Transactions on Antennas and Propagation*, vol. 32, no. 1, pp. 77–85, 1984.

[54] C. Y. Shen, K. J. Glover, M. I. Sancer, and A. D. Varvatsis, "The discrete Fourier transform method of solving differential-integral equations in scattering theory," *IEEE Transactions On Antennas and Propagation*, vol. 37, no. 8, pp. 1032–1041, 1989.

[55] M. I. Sancer, K. Sertel, J. L. Volakis, and P. Van Alstine, "On volume integral equations," *IEEE transactions on antennas and propagation*, vol. 54, no. 5, pp. 1488–1495, 2006.

[56] P. Zwanborn and P. M. van den Berg, "A weak form of the conjugate gradient FFT method for plate problems," *IEEE Transactions on antennas and propagation*, vol. 39, no. 2, pp. 224–228, 1991.

[57] P. Zwamborn and P. M. Van Den Berg, "The three dimensional weak form of the conjugate gradient FFT method for solving scattering problems," *IEEE Transactions on Microwave Theory and Techniques*, vol. 40, no. 9, pp. 1757–1766, 1992.

[58] M. Van Beurden and S. Van Eijndhoven, "Gaps in present discretization schemes for domain integral equations," in *Electromagnetics in Advanced Applications, 2007. ICEAA 2007. International Conference on*. IEEE, 2007, pp. 673–675.

[59] ——, "Well-posedness of domain integral equations for a dielectric object in homogeneous background," *Journal of Engineering Mathematics*, vol. 62, no. 3, pp. 289–302, 2008.

[60] A. G. Polimeridis, J. F. Villena, L. Daniel, and J. K. White, "Stable FFT-JVIE solvers for fast analysis of highly inhomogeneous dielectric objects," *Journal of Computational Physics*, vol. 269, pp. 280–296, 2014.

[61] R. F. Harrington, *Field Computation by Moment Methods*. Wiley-IEEE Press, 1993.

[62] S. Rao, D. Wilton, and A. Glisson, "Electromagnetic scattering by surfaces of arbitrary shape," *IEEE Transactions on antennas and propagation*, vol. 30, no. 3, pp. 409–418, 1982.

[63] M. H. Reid, A. W. Rodriguez, J. White, and S. G. Johnson, "Efficient computation of Casimir interactions between arbitrary 3D objects," *Physical review letters*, vol. 103, no. 4, p. 040401, 2009.

[64] J. F. Villena, A. G. Polimeridis, L. L. Wald, E. Adalsteinsson, J. K. White, and L. Daniel, "MARIE–a MATLAB-based open source software for the fast electromagnetic analysis of MRI systems," in *Proceedings of the 23rd Annual Meeting of ISMRM, Toronto, Canada*, 2015, p. 709.

[65] J. F. Villena, A. G. Polimeridis, Y. Eryaman, E. Adalsteinsson, L. L. Wald, J. K. White, and L. Daniel, "Fast electromagnetic analysis of MRI transmit RF coils based on accelerated integral equation methods," *IEEE Transactions on Biomedical Engineering*, vol. 63, no. 11, pp. 2250–2261, 2016.

[66] A. Hochman, J. F. Villena, A. G. Polimeridis, L. M. Silveira, J. K. White, and L. Daniel, "Reduced-order models for electromagnetic scattering problems," *IEEE Transactions on Antennas and Propagation*, vol. 62, no. 6, pp. 3150–3162, 2014.

[67] B. Guérin, J. F. Villena, A. G. Polimeridis, E. Adalsteinsson, L. Daniel, J. K. White, and L. L. Wald, "The ultimate signal-to-noise ratio in realistic body models," *Magnetic resonance in medicine*, vol. 78, no. 5, pp. 1969–1980, 2017.

[68] A. Pfrommer and A. Henning, "The ultimate intrinsic signal-to-noise ratio of loop- and dipole-like current patterns in a realistic human head model," *Magnetic resonance in medicine*, vol. 80, no. 5, pp. 2122–2138, 2018.

[69] ——, "Comparison of the ultimate intrinsic SNR in a spherical phantom vs a realisitc human head model at 9.4 T," 2016.

[70] A. Pfrommer, N. Avdievich, and A. Henning, "About the ultimate SNR for cylindrical and spherical RF arrays in a realistic human head model," 2016.

[71] B. Guérin, J. F. Villena, A. G. Polimeridis, E. Adalsteinsson, L. Daniel, J. K. White, B. R. Rosen, and L. L. Wald, "Computation of ultimate SAR amplification factors for radiofrequency hyperthermia in non-uniform body models: impact of frequency and tumour location," *International Journal of Hyperthermia*, vol. 34, no. 1, pp. 87–100, 2018.

[72] A. Pfrommer and A. Henning, "About the ideal receive array for human head MRI," in *Joint Annual Meeting ISMRM-ESMRMB 2018*, 2018.

[73] D. K. Sodickson, R. Lattanzi, M. Vaidya, G. Chen, D. S. Novikov, C. M. Collins, and G. C. Wiggins, "The optimality principle for MR signal excitation and reception: New physical insights into ideal radiofrequency coil design," *arXiv preprint arXiv:1808.02087*, 2018.

[74] I. P. Georgakis, A. G. Polimeridis, and R. Lattanzi, "Ultimate intrinsic transmit efficiency for RF shimming," in *Proceedings of Joint Annual Meeting ISMRM-ESMRMB, Paris, France*, 2018, p. 0139.

[75] ——, "Ultimate intrinsic transmit efficiency for radiofrequency shimming," *(submitted)*.

[76] I. P. Georgakis and A. G. Polimeridis, "Reduction of volume-volume integrals arising in Galerkin JM-VIE formulations to surface-surface integrals," in *11th European Conference on Antennas and Propagation (EuCAP)*. IEEE, 2017, pp. 324–326.

[77] I. P. Georgakis, I. I. Giannakopoulos, M. S. Litsarev, and A. G. Polimeridis, "A fast volume integral equation solver with linear basis functions for the accurate computation of electromagnetic fields in MRI," *(submitted), arXiv preprint arXiv:1902.02196*.

[78] G. Mie, "Beiträge zur optik trüber medien, speziell kolloidaler metallösungen," *Annalen der physik*, vol. 330, no. 3, pp. 377–445, 1908 (in german).

[79] J. Van Gemert, W. Brink, A. Webb, and R. Remis, "An efficient methodology for the analysis of dielectric shimming materials in magnetic resonance imaging," *IEEE transactions on medical imaging*, vol. 36, no. 2, pp. 666–673, 2017.

[80] I. P. Georgakis, J. F. Villena, L. Daniel, J. K. White, and A. G. Polimeridis, "Consistent numerical basis of electromagnetic fields in realistic human body models for MRI system design and optimization," in *International Conference on Electromagnetics in Advanced Applications (ICEAA), Verona, Italy*, 2017, p. 1063.

[81] N. Halko, P.-G. Martinsson, and J. A. Tropp, "Finding structure with randomness: Probabilistic algorithms for constructing approximate matrix decompositions," *SIAM review*, vol. 53, no. 2, pp. 217–288, 2011.

[82] I. P. Georgakis, A. G. Polimeridis, and R. Lattanzi, "Ideal current patterns for optimal SNR in realistic heterogeneous head models," in *Proceedings of ISMRM 27th Annual Meeting and Exhibition, Montreal, Canada*, 2019, p. 1036.

[83] E. Tyrtyshnikov, "Incomplete cross approximation in the mosaic-skeleton method," *Computing*, vol. 64, no. 4, pp. 367–380, 2000.

[84] M. Bebendorf, "Approximation of boundary element matrices," *Numerische Mathematik*, vol. 86, no. 4, pp. 565–589, 2000.

[85] Kezhong Zhao, M. N. Vouvakis, and Jin-Fa Lee, "The adaptive cross approximation algorithm for accelerated method of moments computations of EMC problems," *IEEE Transactions on Electromagnetic Compatibility*, vol. 47, no. 4, pp. 763–773, Nov 2005.

[86] S. Kurz, O. Rain, and S. Rjasanow, "The adaptive cross-approximation technique for the 3D boundary-element method," *IEEE Transactions on Magnetics*, vol. 38, no. 2, pp. 421–424, March 2002.

[87] B. L. Edlow, A. Mareyam, A. L. Horn, J. Polimeni, M. D. Tisdall, J. Augustinack, J. P. Stockman, B. R. Diamond, A. Stevens, L. S. Tirrell *et al.*, "7 Tesla MRI of the ex vivo human brain at 100 micron resolution," *BioRxiv*, p. 649822, 2019.

[88] F. Bloch, "Nuclear induction," *Physical review*, vol. 70, no. 7-8, p. 460, 1946.

[89] E. M. Purcell, H. C. Torrey, and R. V. Pound, "Resonance absorption by nuclear magnetic moments in a solid," *Physical review*, vol. 69, no. 1-2, p. 37, 1946.

[90] P. C. Lauterbur, "Image formation by induced local interactions: Examples employing nuclear magnetic resonance," *Nature*, vol. 242, pp. 190–191, 1973.

[91] X. Chen and M. Steckner, "Electromagnetic computation and modeling in MRI," *Medical physics*, vol. 44, no. 3, pp. 1186–1203, 2017.

[92] E. M. Haacke, R. W. Brown, M. R. Thompson, R. Venkatesan *et al.*, *Magnetic resonance imaging: physical principles and sequence design*. Wiley-Liss New York:, 1999, vol. 82.

[93] D. Hoult, "The principle of reciprocity in signal strength calculations—a mathematical guide," *Concepts in Magnetic Resonance: An Educational Journal*, vol. 12, no. 4, pp. 173–187, 2000.

[94] H. Vesselle and R. E. Collin, "The signal-to-noise ratio of nuclear magnetic resonance surface coils and application to a lossy dielectric cylinder model. I. Theory," *IEEE transactions on biomedical engineering*, vol. 42, no. 5, pp. 497–506, 1995.

[95] J. E. Serralles, I. Giannakopoulos, B. Zhang, C. Ianniello, M. A. Cloos, A. G. Polimeridis, J. K. White, D. K. Sodickson, L. Daniel, and R. Lattanzi, "Noninvasive estimation of electrical properties from magnetic resonance measurements via Global Maxwell Tomography and match regularization," *IEEE Transactions on Biomedical Engineering*, 2019.

[96] J. Liu, Y. Wang, U. Katscher, and B. He, "Electrical properties tomography based on B1+ maps in MRI: Principles, applications, and challenges," *IEEE Transactions on Biomedical Engineering*, vol. 64, no. 11, pp. 2515–2530, 2017.

[97] J. Liu, X. Zhang, P.-F. Van de Moortele, S. Schmitter, and B. He, "Determining electrical properties based on B1 fields measured in an MR scanner using a multi-channel transmit/receive coil: a general approach," *Physics in Medicine & Biology*, vol. 58, no. 13, p. 4395, 2013.

[98] E. Balidemaj, C. A. van den Berg, J. Trinks, A. L. van Lier, A. J. Nederveen, L. J. Stalpers, H. Crezee, and R. F. Remis, "CSI-EPT: a contrast source inversion approach

for improved MRI-based electric properties tomography," *IEEE transactions on medical imaging*, vol. 34, no. 9, pp. 1788–1796, 2015.

[99] D. K. Sodickson, L. Alon, C. M. Deniz, R. Brown, B. Zhang, G. C. Wiggins, G. Y. Cho, N. B. Eliezer, D. S. Novikov, R. Lattanzi *et al.*, "Local Maxwell tomography using transmit-receive coil arrays for contact-free mapping of tissue electrical properties and determination of absolute RF phase," in *Proceedings of the 20th Annual Meeting of ISMRM*. ISMRM Concord, California, USA, 2012, p. 388.

[100] C. M. Collins, "Numerical field calculations considering the human subject for engineering and safety assurance in MRI," *NMR in Biomedicine: An International Journal Devoted to the Development and Application of Magnetic Resonance In vivo*, vol. 22, no. 9, pp. 919–926, 2009.

[101] C. Ham, J. Engels, G. Van de Wiel, and A. Machielsen, "Peripheral nerve stimulation during MRI: effects of high gradient amplitudes and switching rates," *Journal of Magnetic Resonance Imaging*, vol. 7, no. 5, pp. 933–937, 1997.

[102] A. A. Obi, "A Method of Moments approach for the design of RF coils for MRI," 2008.

[103] FDA. (2017) FDA clears first 7T magnetic resonance imaging device. [Online]. Available: https://www.fda.gov/news-events/press-announcements/fda-clears-first-7t-magnetic-resonance-imaging-device

[104] P. Jezzard and R. S. Balaban, "Correction for geometric distortion in echo planar images from B0 field variations," *Magnetic resonance in medicine*, vol. 34, no. 1, pp. 65–73, 1995.

[105] P. Van Gelderen, J. De Zwart, P. Starewicz, R. Hinks, and J. Duyn, "Real-time shimming to compensate for respiration-induced B0 fluctuations," *Magnetic Resonance in Medicine: An Official Journal of the International Society for Magnetic Resonance in Medicine*, vol. 57, no. 2, pp. 362–368, 2007.

[106] Z. Cao, J. Park, Z.-H. Cho, and C. M. Collins, "Numerical evaluation of image homogeneity, signal-to-noise ratio, and specific absorption rate for human brain imaging at 1.5, 3, 7, 10.5, and 14T in an 8-channel transmit/receive array," *Journal of Magnetic Resonance Imaging*, vol. 41, no. 5, pp. 1432–1439, 2015.

[107] T. M. Fiedler, M. E. Ladd, and A. K. Bitz, "SAR simulations & safety," *Neuroimage*, vol. 168, pp. 33–58, 2018.

[108] C. A. Balanis, *Advanced engineering electromagnetics*. John Wiley & Sons, 1999.

[109] J. Volakis, *Integral equation methods for electromagnetics*. The Institution of Engineering and Technology, 2012.

[110] A. Herczyński, "Bound charges and currents," *American Journal of Physics*, vol. 81, no. 3, pp. 202–205, 2013.

[111] S. Grimnes and O. Martinsen, "Bioimpedance and bioelectricity basics academic press," *New York*, 2000.

[112] A. Barchanski, "Simulations of low-frequency electromagnetic fields in the human body," Ph.D. dissertation, Technische Universität, 2007.

[113] S. Gabriel, R. Lau, and C. Gabriel, "The dielectric properties of biological tissues: III. Parametric models for the dielectric spectrum of tissues," *Physics in Medicine & Biology*, vol. 41, no. 11, p. 2271, 1996.

[114] C. A. Gonano, R. E. Zich, and M. Mussetta, "Definition for polarization P and magnetization M fully consistent with Maxwell's equations," *Progress In Electromagnetics Research*, vol. 64, pp. 83–101, 2015.

[115] K. T. McDonald, "Poynting's theorem with magnetic monopoles," 2015.

[116] A. Ishimaru, *Wave propagation and scattering in random media*. Academic press New York, 1978, vol. 2.

[117] C. M. Collins, B. Yang, Q. X. Yang, and M. B. Smith, "Numerical calculations of the static magnetic field in three-dimensional multi-tissue models of the human head," *Magnetic resonance imaging*, vol. 20, no. 5, pp. 413–424, 2002.

[118] H. Bassen *et al.*, "IEEE recommended practice for measurements and computations of radio frequency electromagnetic fields with respect to human exposure to such fields, 100 kHz-300 GHz (IEEE std c95. 3-2002)," *The Institute of Electrical and Electronics Engineers, New York*, 2003.

[119] J. C. Lin, "A new IEEE standard for safety levels with respect to human exposure to radio-frequency radiation," *IEEE Antennas and Propagation Magazine*, vol. 48, no. 1, pp. 157–159, 2006.

[120] I. E. Commission *et al.*, "Medical electrical equipment-part 2-33: Particular requirements for the basic safety and essential performance of magnetic resonance equipment for medical diagnosis," *IEC 60601-2-33 Ed. 3.0*, 2010.

[121] D. Hoult and P. C. Lauterbur, "The sensitivity of the zeugmatographic experiment involving human samples," *Journal of Magnetic Resonance (1969)*, vol. 34, no. 2, pp. 425–433, 1979.

[122] D. I. Hoult, "Sensitivity and power deposition in a high-field imaging experiment," *Journal of Magnetic Resonance Imaging*, vol. 12, no. 1, pp. 46–67, 2000.

[123] M. V. Vaidya, C. M. Collins, D. K. Sodickson, R. Brown, G. C. Wiggins, and R. Lattanzi, "Dependence of and field patterns of surface coils on the electrical properties of the sample and the MR operating frequency," *Concepts in Magnetic Resonance Part B: Magnetic Resonance Engineering*, vol. 46, no. 1, pp. 25–40, 2016.

[124] J. T. Vaughan, M. Garwood, C. Collins, W. Liu, L. DelaBarre, G. Adriany, P. Andersen, H. Merkle, R. Goebel, M. Smith *et al.*, "7T vs. 4T: RF power, homogeneity, and signal-to-noise comparison in head images," *Magnetic Resonance in Medicine: An Official Journal of the International Society for Magnetic Resonance in Medicine*, vol. 46, no. 1, pp. 24–30, 2001.

[125] T. S. Ibrahim, R. Lee, B. A. Baertlein, A. M. Abduljalil, H. Zhu, and P.-M. L. Robitaille, "Effect of RF coil excitation on field inhomogeneity at ultra high fields: a field optimized TEM resonator," *Magnetic resonance imaging*, vol. 19, no. 10, pp. 1339–1347, 2001.

[126] F. Seifert, G. Wübbeler, S. Junge, B. Ittermann, and H. Rinneberg, "Patient safety concept for multichannel transmit coils," *Journal of Magnetic Resonance Imaging: An Official Journal of the International Society for Magnetic Resonance in Medicine*, vol. 26, no. 5, pp. 1315–1321, 2007.

[127] A. Massire, M. A. Cloos, M. Luong, A. Amadon, A. Vignaud, C. J. Wiggins, and N. Boulant, "Thermal simulations in the human head for high field MRI using parallel transmission," *Journal of Magnetic Resonance Imaging*, vol. 35, no. 6, pp. 1312–1321, 2012.

[128] Z. Wang, J. C. Lin, W. Mao, W. Liu, M. B. Smith, and C. M. Collins, "SAR and temperature: simulations and comparison to regulatory limits for MRI," *Journal of Magnetic Resonance Imaging: An Official Journal of the International Society for Magnetic Resonance in Medicine*, vol. 26, no. 2, pp. 437–441, 2007.

[129] L. P. Panych and B. Madore, "The physics of MRI safety," *Journal of Magnetic Resonance Imaging*, vol. 47, no. 1, pp. 28–43, 2018.

[130] D. J. Panagopoulos, O. Johansson, and G. L. Carlo, "Polarization: a key difference between man-made and natural electromagnetic fields, in regard to biological activity," *Scientific Reports*, vol. 5, p. 14914, 2015.

[131] A. Farjadpour, D. Roundy, A. Rodriguez, M. Ibanescu, P. Bermel, J. Joannopoulos, S. G. Johnson, and G. Burr, "Improving accuracy by subpixel smoothing in the finite-difference time domain," *Optics letters*, vol. 31, no. 20, pp. 2972–2974, 2006.

[132] S. Dey and R. Mittra, "A locally conformal finite-difference time-domain (FDTD) algorithm for modeling three-dimensional perfectly conducting objects," *IEEE Microwave and Guided Wave Letters*, vol. 7, no. 9, pp. 273–275, 1997.

[133] B. Krietenstein, R. Schuhmann, P. Thoma, and T. Weiland, "The perfect boundary approximation technique facing the big challenge of high precision field computation," in *Proceedings of the XIX International Linear Accelerator Conference (LINAC 98), Chicago, USA*, 1998, pp. 860–862.

[134] K. Yee, "Numerical solution of initial boundary value problems involving Maxwell's equations in isotropic media," *IEEE Transactions on antennas and propagation*, vol. 14, no. 3, pp. 302–307, 1966.

[135] M. Kozlov and R. Turner, "Fast MRI coil analysis based on 3-D electromagnetic and RF circuit co-simulation," *Journal of magnetic resonance*, vol. 200, no. 1, pp. 147–152, 2009.

[136] J. Chi, F. Liu, E. Weber, Y. Li, and S. Crozier, "GPU-accelerated FDTD modeling of radio-frequency field–tissue interactions in high-field MRI," *IEEE Transactions on Biomedical Engineering*, vol. 58, no. 6, pp. 1789–1796, 2011.

[137] C. Cimala, M. Clemens, N. Gödel, J. Streckert, M. Zang, and F. Wolfheimer, "GPU-accelerated time domain electromagnetic field simulations for numerical EMC testing applications," in *2011 International Conference on Electromagnetics in Advanced Applications*. IEEE, 2011, pp. 1017–1018.

[138] M. I. Iacono, N. Makris, L. Mainardi, L. M. Angelone, and G. Bonmassar, "MRI-based multiscale model for electromagnetic analysis in the human head with implanted DBS," *Computational and mathematical methods in medicine*, vol. 2013, 2013.

[139] G. Mur, "Absorbing boundary conditions for the finite-difference approximation of the time-domain electromagnetic-field equations," *IEEE transactions on Electromagnetic Compatibility*, no. 4, pp. 377–382, 1981.

[140] Z.-F. LIAO, K.-l. Huang, B.-p. Yang, and Y.-F. YUAN, "A transmitting boundary for transient wave analyses," *Science in China Series A-Mathematics, Physics, Astronomy & Technological Science*, vol. 27, no. 10, pp. 1063–1076, 1984.

[141] J.-P. Berenger, "A perfectly matched layer for the absorption of electromagnetic waves," *Journal of computational physics*, vol. 114, no. 2, pp. 185–200, 1994.

[142] S. Wolf, D. Diehl, M. Gebhardt, J. Mallow, and O. Speck, "SAR simulations for high-field MRI: how much detail, effort, and accuracy is needed?" *Magnetic resonance in medicine*, vol. 69, no. 4, pp. 1157–1168, 2013.

[143] B. Guerin, M. I. Iacono, M. Davids, D. D. Dougherty, L. M. Angelone, and L. L. Wald, "The "virtual DBS population": five realistic computational models of deep brain stimulation patients for electromagnetic MR safety studies," *Physics in medicine and biology*, 2019.

[144] B. Guerin, P. Serano, M. I. Iacono, T. M. Herrington, A. S. Widge, D. D. Dougherty, G. Bonmassar, L. M. Angelone, and L. L. Wald, "Realistic modeling of deep brain stimulation implants for electromagnetic MRI safety studies," *Physics in Medicine & Biology*, vol. 63, no. 9, p. 095015, 2018.

[145] W. Chai and D. Jiao, "Theoretical study on the rank of integral operators for broadband electromagnetic modeling from static to electrodynamic frequencies," *IEEE Transactions on Components, Packaging and Manufacturing Technology*, vol. 3, no. 12, pp. 2113–2126, 2013.

[146] A. G. Polimeridis and T. V. Yioultsis, "On the direct evaluation of weakly singular integrals in Galerkin mixed potential integral equation formulations," *IEEE Transactions on Antennas and Propagation*, vol. 56, no. 9, pp. 3011–3019, 2008.

[147] A. G. Polimeridis and J. R. Mosig, "Complete semi-analytical treatment of weakly singular integrals on planar triangles via the direct evaluation method," *International journal for numerical methods in engineering*, vol. 83, no. 12, pp. 1625–1650, 2010.

[148] A. G. Polimeridis, J. M. Tamayo, J. M. Rius, and J. R. Mosig, "Fast and accurate computation of hypersingular integrals in Galerkin surface integral equation formulations via the direct evaluation method," *IEEE transactions on antennas and propagation*, vol. 59, no. 6, pp. 2329–2340, 2011.

[149] A. Polimeridis, S. Järvenpää, P. Ylä-Oijala, L. Gray, S. Kiminki, and J. Mosig, "On the evaluation of hyper-singular double normal derivative kernels in surface integral equation methods," *Engineering Analysis with Boundary Elements*, vol. 37, no. 2, pp. 205–210, 2013.

[150] A. G. Polimeridis, F. Vipiana, J. R. Mosig, and D. R. Wilton, "DIRECTFN: Fully numerical algorithms for high precision computation of singular integrals in Galerkin SIE methods," *IEEE Transactions on Antennas and Propagation*, vol. 61, no. 6, pp. 3112–3122, 2013.

[151] A. Tambova, G. Guryev, and A. G. Polimeridis, "On the fully numerical evaluation of singular integrals over coincident quadrilateral patches," in *Antennas and Propagation (EUCAP), 2017 11th European Conference on*. IEEE, 2017, pp. 3205–3208.

[152] A. A. Tambova, M. S. Litsarev, G. Guryev, and A. G. Polimeridis, "On the generalization of DIRECTFN for singular integrals over quadrilateral patches," *IEEE Transactions on Antennas and Propagation*, vol. 66, no. 1, pp. 304–314, 2018.

[153] F. Vipiana and D. R. Wilton, "Numerical evaluation via singularity cancellation schemes of near-singular integrals involving the gradient of Helmholtz-type potentials," *IEEE Transactions on Antennas and Propagation*, vol. 61, no. 3, pp. 1255–1265, 2012.

[154] F. Vipiana and D. Wilton, "Numerical evaluation of near strongly singular integrals via singularity cancellation techniques," in *Proceedings of the 5th European Conference on Antennas and Propagation (EUCAP)*. IEEE, 2011, pp. 2705–2707.

[155] F. Vipiana, D. R. Wilton, and W. A. Johnson, "Advanced numerical schemes for the accurate evaluation of 4-D reaction integrals in the method of moments," *IEEE Transactions on Antennas and Propagation*, vol. 61, no. 11, pp. 5559–5566, 2013.

[156] F. Vipiana and D. R. Wilton, "Direct numerical evaluation of near strongly-singular integrals," in *2011 IEEE International Symposium on Antennas and Propagation (APSURSI)*. IEEE, 2011, pp. 3200–3202.

[157] ——, "Optimized numerical evaluation of singular and near-singular potential integrals involving junction basis functions," *IEEE Transactions on Antennas and Propagation*, vol. 59, no. 1, pp. 162–171, 2010.

[158] D. R. Wilton, F. Vipiana, and W. A. Johnson, "Evaluating singular, near-singular, and non-singular integrals on curvilinear elements," *Electromagnetics*, vol. 34, no. 3-4, pp. 307–327, 2014.

[159] "DEMCEM package," 2016. [Online]. Available: `https://github.com/thanospol/DEMCEM`

[160] "DIRECTFN package," 2016. [Online]. Available: `https://github.com/thanospol/DIRECTFN`

[161] J. F. Villena, A. Polimeridis, A. Hochman, J. White, and L. Daniel, "Magnetic resonance specific integral equation solver based on precomputed numerical Green functions," in *2013 International Conference on Electromagnetics in Advanced Applications (ICEAA)*. IEEE, 2013, pp. 724–727.

[162] D. Jiao and J.-M. Jin, "Fast frequency-sweep analysis of RF coils for MRI," *IEEE transactions on biomedical engineering*, vol. 46, no. 11, pp. 1387–1390, 1999.

[163] I. I. Giannakopoulos, M. S. Litsarev, and A. G. Polimeridis, "Memory footprint reduction for the FFT-based volume integral equation method via tensor decompositions," *arXiv preprint arXiv:1811.00484*, 2018.

[164] G. Guryev, A. G. Polimeridis, E. Adalsteinsson, L. Wald, and J. White, "Fast field analysis for complex coils and metal implants in MARIE 2.0," p. 1035, 2019.

[165] T. Stöcker, K. Vahedipour, D. Pflugfelder, and N. J. Shah, "High-performance computing MRI simulations," *Magnetic Resonance in Medicine*, vol. 64, no. 1, pp. 186–193, 2010.

[166] Z. Cao, S. Oh, C. T. Sica, J. M. McGarrity, T. Horan, W. Luo, and C. M. Collins, "Bloch-based MRI system simulator considering realistic electromagnetic fields for calculation of signal, noise, and specific absorption rate," *Magnetic resonance in medicine*, vol. 72, no. 1, pp. 237–247, 2014.

[167] O. Ocali and E. Atalar, "Ultimate intrinsic signal-to-noise ratio in MRI," *Magnetic resonance in medicine*, vol. 39, no. 3, pp. 462–473, 1998.

[168] H. Çelik, Y. Eryaman, A. Altıntaş, I. Abdel-Hafez, and E. Atalar, "Evaluation of internal MRI coils using ultimate intrinsic SNR," *Magnetic Resonance in Medicine: An Official Journal of the International Society for Magnetic Resonance in Medicine*, vol. 52, no. 3, pp. 640–649, 2004.

[169] Y. Gao, W. Chen, and X. Zhang, "Investigating the influence of spatial constraints on ultimate receive coil performance for monkey brain MRI at 7 T," *IEEE transactions on medical imaging*, vol. 37, no. 7, pp. 1723–1732, 2018.

[170] G. G. Haemer, M. Vaidya, C. M. Collins, D. K. Sodickson, G. C. Wiggins, and R. Lattanzi, "Approaching ultimate intrinsic specific absorption rate in radiofrequency shimming using high-permittivity materials at 7 Tesla," *Magnetic resonance in medicine*, vol. 80, no. 1, pp. 391–399, 2018.

[171] C. M. Deniz, R. Brown, R. Lattanzi, L. Alon, D. K. Sodickson, and Y. Zhu, "Maximum efficiency radiofrequency shimming: Theory and initial application for hip imaging at 7 Tesla," *Magnetic resonance in medicine*, vol. 69, no. 5, pp. 1379–1388, 2013.

[172] Y. Zhu, "In vivo RF power and SAR calibration for multi-port RF transmission," in *Proceedings of the 17th Scientific Meeting, ISMRM*, 2009, p. 2585.

[173] L. Alon, C. M. Deniz, R. Lattanzi, G. Wiggins, R. Brown, D. K. Sodickson, and Y. Zhu, "An automated method for subject specific global SAR prediction in parallel transmission," in *Proceedings of the 18th Scientific Meeting, ISMRM*, 2010, p. 780.

[174] Y. Zhu, L. Alon, C. M. Deniz, R. Brown, and D. K. Sodickson, "System and SAR characterization in parallel RF transmission," *Magnetic resonance in medicine*, vol. 67, no. 5, pp. 1367–1378, 2012.

[175] H. Fautz, M. Vogel, P. Gross, A. Kerr, and Y. Zhu, "B1 mapping of coil arrays for parallel transmission," in *Proceedings of the 16th Annual Meeting of ISMRM, Toronto, Canada*, 2008, p. 1247.

[176] U. Katscher, P. Börnert, C. Leussler, and J. S. Van Den Brink, "Transmit sense," *Magnetic Resonance in Medicine: An Official Journal of the International Society for Magnetic Resonance in Medicine*, vol. 49, no. 1, pp. 144–150, 2003.

[177] Y. Zhu, "Parallel excitation with an array of transmit coils," *Magnetic Resonance in Medicine: An Official Journal of the International Society for Magnetic Resonance in Medicine*, vol. 51, no. 4, pp. 775–784, 2004.

[178] F. Padormo, A. Beqiri, J. V. Hajnal, and S. J. Malik, "Parallel transmission for ultrahigh-field imaging," *NMR in Biomedicine*, vol. 29, no. 9, pp. 1145–1161, 2016.

[179] G. J. Metzger, C. Snyder, C. Akgun, T. Vaughan, K. Ugurbil, and P.-F. Van de Moortele, "Local B1+ shimming for prostate imaging with transceiver arrays at 7T based on subject-dependent transmit phase measurements," *Magnetic Resonance in Medicine: An Official Journal of the International Society for Magnetic Resonance in Medicine*, vol. 59, no. 2, pp. 396–409, 2008.

[180] W. Mao, M. B. Smith, and C. M. Collins, "Exploring the limits of RF shimming for high-field MRI of the human head," *Magnetic Resonance in Medicine: An Official Journal of the International Society for Magnetic Resonance in Medicine*, vol. 56, no. 4, pp. 918–922, 2006.

[181] B. van den Bergen, C. A. Van den Berg, L. W. Bartels, and J. J. Lagendijk, "7 T body MRI: B1 shimming with simultaneous SAR reduction," *Physics in Medicine & Biology*, vol. 52, no. 17, p. 5429, 2007.

[182] C. M. Deniz, L. Alon, R. Brown, D. K. Sodickson, and Y. Zhu, "Specific absorption rate benefits of including measured electric field interactions in parallel excitation pulse design," *Magnetic resonance in medicine*, vol. 67, no. 1, pp. 164–174, 2012.

[183] S. Orzada, S. Maderwald, B. A. Poser, A. K. Bitz, H. H. Quick, and M. E. Ladd, "RF excitation using time interleaved acquisition of modes (TIAMO) to address B1 inhomogeneity in high-field MRI," *Magnetic resonance in medicine*, vol. 64, no. 2, pp. 327–333, 2010.

[184] P. Balchandani, M. Khalighi, S. Hsieh, K. Setsompop, J. Pauly, and D. Spielman, "Adiabatic B1 shimming algorithm for multiple channel transmit at 7T," in *Proceedings of the 19th Scientific Meeting, ISMRM. Montreal*, 2011, p. 2907.

[185] K. Setsompop, L. Wald, and E. Adalsteinsson, "Reduced-voltage RF shimming for adiabatic pulse design in parallel transmission," in *Proceedings of the 15th Scientific Meeting, ISMRM. Berlin*, 2007, p. 1687.

[186] Y. Zhu, C. Deniz, L. Alon, H. Fautz, and D. Sodickson, "Undestanding parallel transmit array efficiency," *ISMRM. Stockholm*, p. 1518, 2010.

[187] W. Grissom, C.-y. Yip, Z. Zhang, V. A. Stenger, J. A. Fessler, and D. C. Noll, "Spatial domain method for the design of RF pulses in multicoil parallel excitation," *Magnetic Resonance in Medicine: An Official Journal of the International Society for Magnetic Resonance in Medicine*, vol. 56, no. 3, pp. 620–629, 2006.

[188] D. Xu, K. F. King, Y. Zhu, G. C. McKinnon, and Z.-P. Liang, "A noniterative method to design large-tip-angle multidimensional spatially-selective radio frequency pulses for parallel transmission," *Magnetic Resonance in Medicine: An Official Journal of the International Society for Magnetic Resonance in Medicine*, vol. 58, no. 2, pp. 326–334, 2007.

[189] B. van den Bergen, C. A. van den Berg, D. W. Klomp, and J. J. Lagendijk, "SAR and power implications of different RF shimming strategies in the pelvis for 7T MRI," *Journal of Magnetic Resonance Imaging: An Official Journal of the International Society for Magnetic Resonance in Medicine*, vol. 30, no. 1, pp. 194–202, 2009.

[190] R. E. Prieto, "A general solution to the maximization of the multidimensional generalized Rayleigh quotient used in linear discriminant analysis for signal classification," in *2003 IEEE International Conference on Acoustics, Speech, and Signal Processing, 2003. Proceedings.(ICASSP'03).*, vol. 6. IEEE, 2003, pp. VI–157.

[191] C.-T. Tai, *Dyadic Green functions in electromagnetic theory*. Institute of Electrical & Electronics Engineers (IEEE), 1994.

[192] J. D. Jackson, "Classical electrodynamics," 1999.

[193] E. Martini, G. Carli, and S. Maci, "An equivalence theorem based on the use of electric currents radiating in free space," *IEEE Antennas and Wireless Propagation Letters*, vol. 7, pp. 421–424, 2008.

[194] C. E. Hayes, W. A. Edelstein, J. F. Schenck, O. M. Mueller, and M. Eash, "An efficient, highly homogeneous radiofrequency coil for whole-body NMR imaging at 1.5 T," *Journal of Magnetic Resonance (1969)*, vol. 63, no. 3, pp. 622–628, 1985.

[195] A. Kumar and P. A. Bottomley, "Optimized quadrature surface coil designs," *Magnetic Resonance Materials in Physics, Biology and Medicine*, vol. 21, no. 1-2, p. 41, 2008.

[196] A. Reykowski and H. Fischer, "V-cage and V-array: Novel coil structures for higher field strengths," in *Proceedings of the 13h Annual Meeting of ISMRM*, 2005, pp. 7–13.

[197] Q. Duan, D. Sodickson, R. Lattanzi, B. Zhang, and G. Wiggins, "Optimizing 7 T spine array design through offsetting of transmit and receive elements and quadrature excitation," in *Proceedings of the 18th Annual Meeting of ISMRM*, 2010, p. 51.

[198] G. Wiggins, Q. Duan, R. Lattanzi, and D. Sodickson, "B1+ and SNR optimization of high field RF coils through offsetting of transmit and receive elements," in *Proceedings of the 17th Annual Meeting of ISMRM*, 2009, p. 2951.

[199] P. Kellman and E. R. McVeigh, "Image reconstruction in SNR units: a general method for SNR measurement," *Magnetic resonance in medicine*, vol. 54, no. 6, pp. 1439–1447, 2005.

[200] P. M. Morse and H. Feshbach, "Methods of theoretical physics," *American Journal of Physics*, vol. 22, no. 6, pp. 410–413, 1954.

[201] J. Kong, *Theory of electromagnetic waves*, ser. A Wiley-Interscience publication. Wiley, 1975. [Online]. Available: https://books.google.ru/books?id=QLnvAAAAMAAJ

[202] A. D. Yaghjian, "Electric dyadic Green's functions in the source region," *Proceedings of the IEEE*, vol. 68, no. 2, pp. 248–263, 1980.

[203] G. Green, *An essay on the application of mathematical analysis to the theories of electricity and magnetism*. Wezäta-Melins Aktiebolag, 1828.

[204] W. C. Chew, M. S. Tong, and B. Hu, "Integral equation methods for electromagnetic and elastic waves," *Synthesis Lectures on Computational Electromagnetics*, vol. 3, no. 1, pp. 1–241, 2008.

[205] A. J. Poggio and E. K. Miller, *Integral equation solutions of three-dimensional scattering problems*. MB Assoc., 1970.

[206] E. K. Miller, L. Medgyesi-Mitschang, and E. H. Newman, *Computational electromagnetics: frequency-domain method of moments*. IEEE Press, 1992.

[207] J. R. Mautz and R. F. Harrington, "Electromagnetic scattering from a homogeneous body of revolution," SYRACUSE UNIV NY DEPT OF ELECTRICAL AND COMPUTER ENGINEERING, Tech. Rep., 1977.

[208] L. Medgyesi-Mitschang, J. Putnam, and M. Gedera, "Generalized method of moments for three-dimensional penetrable scatterers," *JOSA A*, vol. 11, no. 4, pp. 1383–1398, 1994.

[209] J. Zhu, S. Omar, and D. Jiao, "Solution of the electric field integral equation when it breaks down," *IEEE Transactions on Antennas and Propagation*, vol. 62, no. 8, pp. 4122–4134, 2014.

[210] N. Morita, J. R. Mautz, and N. Kumagai, *Integral equation methods for electromagnetics*. Artech house, 1990.

[211] J. M. Rius, E. Ubeda, and J. Parrón, "On the testing of the magnetic field integral equation with RWG basis functions in method of moments," *IEEE Transactions on Antennas and Propagation*, vol. 49, no. 11, pp. 1550–1553, 2001.

[212] E. Ubeda and J. M. Rius, "Monopolar RWG MoM-MFIE formulation outperforming the conventional dipolar RWG MoM-MFIE in the electromagnetic scattering analysis," in *2005 IEEE Antennas and Propagation Society International Symposium*, vol. 4. IEEE, 2005, pp. 276–279.

[213] ——, "MFIE MoM-formulation with curl-conforming basis functions and accurate kernel integration in the analysis of perfectly conducting sharp-edged objects," *Microwave and Optical Technology Letters*, vol. 44, no. 4, pp. 354–358, 2005.

[214] ——, "Novel monopolar MFIE MoM-discretization for the scattering analysis of small objects," *IEEE Transactions on Antennas and Propagation*, vol. 54, no. 1, pp. 50–57, 2006.

[215] L. Zhang, A. Deng, and M. Wang, "Application of a novel formulation to the MFIE using RWG basis functions in method of moments," *Engineering analysis with boundary elements*, vol. 33, no. 6, pp. 880–884, 2009.

[216] L. Zhang, A. Deng, M. Wang, and S. Yang, "Numerical study of a novel MFIE formulation using monopolar RWG basis functions," *Computer Physics Communications*, vol. 181, no. 1, pp. 52–60, 2010.

[217] O. Ergul and L. Gurel, "Improved testing of the magnetic-field integral equation," *IEEE microwave and wireless components letters*, vol. 15, no. 10, pp. 615–617, 2005.

[218] ——, "The use of curl-conforming basis functions for the magnetic-field integral equation," *IEEE Transactions on Antennas and Propagation*, vol. 54, no. 7, pp. 1917–1926, 2006.

[219] D. R. Wilton, "Review of current status and trends in the use of integral equations in computational electromagnetics," *Electromagnetics*, vol. 12, no. 3-4, pp. 287–341, 1992.

[220] A. F. Peterson, "The "interior resonance" problem associated with surface integral equations of electromagnetics: Numerical consequences and a survey of remedies," *Electromagnetics*, vol. 10, no. 3, pp. 293–312, 1990.

[221] S. M. Rao and D. R. Wilton, "E-field, H-field, and combined field solution for arbitrarily shaped three-dimensional dielectric bodies," *Electromagnetics*, vol. 10, no. 4, pp. 407–421, 1990.

[222] J.-S. Zhao and W. C. Chew, "Integral equation solution of Maxwell's equations from zero frequency to microwave frequencies," *IEEE Transactions on Antennas and Propagation*, vol. 48, no. 10, pp. 1635–1645, 2000.

[223] K. T. McDonald, "The Helmholtz decomposition and the Coulomb gauge."

[224] J.-F. Lee, R. Lee, and R. J. Burkholder, "Loop star basis functions and a robust preconditioner for EFIE scattering problems," *IEEE Transactions on Antennas and Propagation*, vol. 51, no. 8, pp. 1855–1863, 2003.

[225] G. Vecchi, "Loop-star decomposition of basis functions in the discretization of the EFIE," *IEEE Transactions on Antennas and Propagation*, vol. 47, no. 2, pp. 339–346, 1999.

[226] S. Uckun, T. K. Sarkar, S. M. Rao, and M. Salazar-Palma, "A novel technique for analysis of electromagnetic scattering from microstrip antennas of arbitrary shape," *IEEE Transactions on microwave theory and techniques*, vol. 45, no. 4, pp. 485–491, 1997.

[227] F. Vipiana, P. Pirinoli, and G. Vecchi, "Spectral properties of the EFIE-MoM matrix for dense meshes with different types of bases," *IEEE Transactions on Antennas and Propagation*, vol. 55, no. 11, pp. 3229–3238, 2007.

[228] F. P. Andriulli, K. Cools, H. Bagci, F. Olyslager, A. Buffa, S. Christiansen, and E. Michielssen, "A multiplicative Calderon preconditioner for the electric field integral equation," *IEEE Transactions on Antennas and Propagation*, vol. 56, no. 8, pp. 2398–2412, 2008.

[229] A. G. Polimerids, J. F. Villena, and J. Seralles, "MARIE - MAgnetic Resonance Integral Equation suite, available online," 2015. [Online]. Available: `https://github.com/thanospol/MARIE`

[230] C.-T. Tsai, H. Massoudi, C. H. Durney, and M. F. Iskander, "A procedure for calculating fields inside arbitrarily shaped, inhomogeneous dielectric bodies using linear basis functions with the moment method," *IEEE transactions on microwave theory and techniques*, vol. 34, no. 11, pp. 1131–1139, 1986.

[231] J. Markkanen and P. Ylä-Oijala, "Discretization of electric current volume integral equation with piecewise linear basis functions," *IEEE Transactions on Antennas and Propagation*, vol. 62, no. 9, pp. 4877–4880, 2014.

[232] M. Francavilla, E. Attardo, F. Vipiana, and G. Vecchi, "A GPU acceleration for FFT-based fast solvers for the integral equation," in *Proceedings of the Fourth European Conference on Antennas and Propagation*. IEEE, 2010, pp. 1–4.

[233] A. Polimeridis, J. F. Villena, L. Daniel, and J. White, "Robust J-EFVIE solvers based on purely surface integrals," in *Electromagnetics in Advanced Applications (ICEAA), 2013 International Conference on*. IEEE, 2013, pp. 379–381.

[234] E. H. Bleszynski, M. K. Bleszynski, and T. Jaroszewicz, "Reduction of volume integrals to nonsingular surface integrals for matrix elements of tensor and vector Green functions of Maxwell equations," *IEEE Transactions on Antennas and Propagation*, vol. 61, no. 7, pp. 3642–3647, 2013.

[235] L. Knockaert, "On the analytic calculation of multiple integrals in electromagnetics," in *Electromagnetics in Advanced Applications (ICEAA), 2011 International Conference on*. IEEE, 2011, pp. 595–598.

[236] J. Rivero, F. Vipiana, D. Wilton, and W. Johnson, "Acceleration of volume-volume (6-D) integrals for numerical evaluation by double application of the divergence theorem," in *2019 International Applied Computational Electromagnetics Society Symposium (ACES)*. IEEE, 2019, pp. 1–2.

[237] A. G. Polimeridis and J. K. White, "On the compression of system tensors arising in FFT-VIE solvers," in *Antennas and Propagation Society International Symposium (APSURSI), 2014 IEEE*. IEEE, 2014, pp. 2144–2145.

[238] I. I. Giannakopoulos, M. S. Litsarev, and A. G. Polimeridis, "3D cross-Tucker approximation in FFT-based volume integral equation methods." in *Antennas and Propagation Society International Symposium (APSURSI), 2018 IEEE*, 2018.

[239] J. P. Webb, "Hierarchal vector basis functions of arbitrary order for triangular and tetrahedral finite elements," *IEEE Transactions on antennas and propagation*, vol. 47, no. 8, pp. 1244–1253, 1999.

[240] G. C. Hsiao and R. E. Kleinman, "Mathematical foundations for error estimation in numerical solutions of integral equations in electromagnetics," *IEEE transactions on Antennas and Propagation*, vol. 45, no. 3, pp. 316–328, 1997.

[241] J. Markkanen and P. Ylä-Oijala, "Numerical comparison of spectral properties of volume-integral-equation formulations," *Journal of Quantitative Spectroscopy and Radiative Transfer*, vol. 178, pp. 269–275, 2016.

[242] A. Tambova, S. P. Groth, J. K. White, and A. G. Polimeridis, "Adiabatic absorbers in photonics simulations with the volume integral equation method," *Journal of Lightwave Technology*, vol. 36, no. 17, pp. 3765–3777, 2018.

[243] S. Jarvenpaa, M. Taskinen, and P. Yla-Oijala, "Singularity subtraction technique for high-order polynomial vector basis functions on planar triangles," *IEEE transactions on antennas and propagation*, vol. 54, no. 1, pp. 42–49, 2006.

[244] P. Yla-Oijala and M. Taskinen, "Calculation of CFIE impedance matrix elements with RWG and $n \times$ RWG functions," *IEEE Transactions on Antennas and Propagation*, vol. 51, no. 8, pp. 1837–1846, 2003.

[245] A. C. Yucel, H. Bagci, I. P. Georgakis, G. Athanasios, and J. K. White, "An FFT-accelerated inductance extractor for voxelized structures," in *2018 International Applied Computational Electromagnetics Society Symposium (ACES)*. IEEE, 2018, pp. 1–2.

[246] A. C. Yucel, I. P. Georgakis, A. G. Polimeridis, H. Bağcı, and J. K. White, "VoxHenry: FFT-accelerated inductance extraction for voxelized geometries," *IEEE Transactions on Microwave Theory and Techniques*, vol. 66, no. 4, pp. 1723–1735, 2018.

[247] L. R. Tucker, "Some mathematical notes on three-mode factor analysis," *Psychometrika*, vol. 31, no. 3, pp. 279–311, 1966.

[248] L. De Lathauwer, B. De Moor, and J. Vandewalle, "A multilinear singular value decomposition," *SIAM journal on Matrix Analysis and Applications*, vol. 21, no. 4, pp. 1253–1278, 2000.

[249] I. V. Oseledets, D. Savostianov, and E. E. Tyrtyshnikov, "Tucker dimensionality reduction of three-dimensional arrays in linear time," *SIAM Journal on Matrix Analysis and Applications*, vol. 30, no. 3, pp. 939–956, 2008.

[250] M. Rakhuba and I. V. Oseledets, "Fast multidimensional convolution in low-rank tensor formats via cross approximation," *SIAM Journal on Scientific Computing*, vol. 37, no. 2, pp. A565–A582, 2015.

[251] Z. Chen, S. Zheng, and V. I. Okhmatovski, "Tensor train accelerated solution of volume integral equation for 2-D scattering problems and magneto-quasi-static characterization of multiconductor transmission lines," *IEEE Transactions on Microwave Theory and Techniques*, vol. 67, no. 6, pp. 2181–2196, 2019.

[252] I. Oseledets and E. Tyrtyshnikov, "TT-cross approximation for multidimensional arrays," *Linear Algebra and its Applications*, vol. 432, no. 1, pp. 70–88, 2010.

[253] C. Temperton, "A generalized prime factor FFT algorithm for any $N = 2^p 3^q 5^r$," *SIAM Journal on Scientific and Statistical Computing*, vol. 13, no. 3, pp. 676–686, 1992.

[254] D. Takahashi and Y. Kanada, "High-performance radix-2, 3 and 5 parallel 1-D complex FFT algorithms for distributed-memory parallel computers," *The Journal of Supercomputing*, vol. 15, no. 2, pp. 207–228, 2000.

[255] G. P. Zouros and N. V. Budko, "Transverse electric scattering on inhomogeneous objects: Spectrum of integral operator and preconditioning," *SIAM Journal on Scientific Computing*, vol. 34, no. 3, pp. B226–B246, 2012.

[256] N. V. Budko and A. B. Samokhin, "Spectrum of the volume integral operator of electromagnetic scattering," *SIAM Journal on Scientific Computing*, vol. 28, no. 2, pp. 682–700, 2006.

[257] A. G. Polimeridis, M. H. Reid, S. G. Johnson, J. K. White, and A. W. Rodriguez, "On the computation of power in volume integral equation formulations," *IEEE Transactions on Antennas and Propagation*, vol. 63, no. 2, pp. 611–620, 2015.

[258] C. Gabriel, "Compilation of the dielectric properties of body tissues at RF and microwave frequencies." KING'S COLL LONDON (UNITED KINGDOM) DEPT OF PHYSICS, Tech. Rep., 1996.

[259] S. Y. Huang, Z.-H. Ma, L. Wan, W. Yu, and J. T. Vaughan, "Fast full-wave calculation of electromagnetic fields based on weak-form volume integral equation for MRI applications," *The Journal of Engineering*, vol. 2018, no. 9, pp. 762–767, 2018.

[260] A. Webb, "Dielectric materials in magnetic resonance," *Concepts in Magnetic Resonance Part A*, vol. 38A, no. 4, pp. 148–184, 2011.

[261] P. de Heer, W. M. Brink, B. Kooij, and A. Webb, "Increasing signal homogeneity and image quality in abdominal imaging at 3 T with very high permittivity materials," *Magnetic resonance in medicine*, vol. 68, no. 4, pp. 1317–1324, 2012.

[262] W. M. Brink and A. G. Webb, "High permittivity pads reduce specific absorption rate, improve B1 homogeneity, and increase contrast-to-noise ratio for functional cardiac MRI at 3T," *Magnetic resonance in medicine*, vol. 71, no. 4, pp. 1632–1640, 2014.

[263] W. M. Brink, J. S. van den Brink, and A. G. Webb, "The effect of high-permittivity pads on specific absorption rate in radiofrequency-shimmed dual-transmit cardiovascular magnetic resonance at 3T," *Journal of Cardiovascular Magnetic Resonance*, vol. 17, no. 1, p. 82, 2015.

[264] R. Schmidt and A. Webb, "Improvements in RF shimming in high field MRI using high permittivity materials with low order pre-fractal geometries," *IEEE transactions on medical imaging*, vol. 35, no. 8, pp. 1837–1844, 2016.

[265] W. M. Brink, R. F. Remis, and A. G. Webb, "A theoretical approach based on electromagnetic scattering for analysing dielectric shimming in high-field MRI," *Magnetic resonance in medicine*, vol. 75, no. 5, pp. 2185–2194, 2016.

[266] K. Koolstra, P. Börnert, W. Brink, and A. Webb, "Improved image quality and reduced power deposition in the spine at 3T using extremely high permittivity materials," *Magnetic resonance in medicine*, 2017.

[267] M. V. Vaidya, C. M. Deniz, C. M. Collins, D. K. Sodickson, and R. Lattanzi, "Manipulating transmit and receive sensitivities of radiofrequency surface coils using shielded and unshielded high-permittivity materials," *Magnetic Resonance Materials in Physics, Biology and Medicine*, pp. 1–12, 2018.

[268] M. V. Vaidya, M. Lazar, C. M. Deniz, G. G. Haemer, G. Chen, M. Bruno, D. K. Sodickson, R. Lattanzi, and C. M. Collins, "Improved detection of fMRI activation in the cerebellum at 7T with dielectric pads extending the imaging region of a commercial head coil," *Journal of Magnetic Resonance Imaging*, 2018.

[269] J. E. C. Serralles, I. P. Georgakis, A. G. Polimeridis, L. Daniel, J. K. White, D. K. Sodickson, and R. Lattanzi, "Volumetric reconstruction of tissue electrical properties from B1+ and MR signals using Global Maxwell Tomography: Theory and simulation results," in *Proceedings of ISMRM 25th Annual Meeting Exhibition, 2017 Apr, Honolulu, HI, USA*, 2017, p. 3647.

[270] J. Bruning and Y. Lo, "Multiple scattering of EM waves by spheres part I–multipole expansion and ray-optical solutions," *IEEE Transactions on Antennas and Propagation*, vol. 19, no. 3, pp. 378–390, 1971.

[271] R. Harrington and J. Mautz, "Theory of characteristic modes for conducting bodies," *IEEE Transactions on Antennas and Propagation*, vol. 19, no. 5, pp. 622–628, 1971.

[272] R. Garbacz and R. Turpin, "A generalized expansion for radiated and scattered fields," *IEEE Transactions on Antennas and Propagation*, vol. 19, no. 3, pp. 348–358, 1971.

[273] B. Fuchs and A. G. Polimeridis, "Reduced-order models for fast antenna characterization," *IEEE Transactions on Antennas and Propagation*, 2019.

[274] N. Kishore Kumar and J. Schneider, "Literature survey on low rank approximation of matrices," *Linear and Multilinear Algebra*, vol. 65, no. 11, pp. 2212–2244, 2017.

[275] T. B. Hansen, "Complex-point dipole formulation of probe-corrected cylindrical and spherical near-field scanning of electromagnetic fields," *IEEE Transactions on Antennas and Propagation*, vol. 57, no. 3, pp. 728–741, 2009.

[276] B. T. Draine and P. J. Flatau, "Discrete-dipole approximation for scattering calculations," *JOSA A*, vol. 11, no. 4, pp. 1491–1499, 1994.

[277] K. Tap, P. H. Pathak, and R. J. Burkholder, "Exact complex source point beam expansions for electromagnetic fields," *IEEE Transactions on Antennas and Propagation*, vol. 59, no. 9, pp. 3379–3390, 2011.

[278] B. Guérin, M. Gebhardt, S. Cauley, E. Adalsteinsson, and L. L. Wald, "Local specific absorption rate (SAR), global SAR, transmitter power, and excitation accuracy tradeoffs in low flip-angle parallel transmit pulse design," *Magnetic resonance in medicine*, vol. 71, no. 4, pp. 1446–1457, 2014.

[279] M. Barrault, Y. Maday, N. C. Nguyen, and A. T. Patera, "An 'empirical interpolation'method: application to efficient reduced-basis discretization of partial differential equations," *Comptes Rendus Mathematique*, vol. 339, no. 9, pp. 667–672, 2004.

[280] S. Chaturantabut and D. C. Sorensen, "Nonlinear model reduction via discrete empirical interpolation," *SIAM Journal on Scientific Computing*, vol. 32, no. 5, pp. 2737–2764, 2010.

[281] A. G. Polimeridis, M. Reid, W. Jin, S. G. Johnson, J. K. White, and A. W. Rodriguez, "Fluctuating volume-current formulation of electromagnetic fluctuations in inhomogeneous media: Incandescence and luminescence in arbitrary geometries," *Physical Review B*, vol. 92, no. 13, p. 134202, 2015.

[282] V. I. Lebedev, "Spherical quadrature formulas exact to orders 25–29," *Siberian Mathematical Journal*, vol. 18, no. 1, pp. 99–107, 1977.

[283] K. Ugurbil. (2019) Still pushing the limits. [Online]. Available: https://med.umn.edu/news-events/medical-bulletin/still-pushing-limits

[284] M. A. Erturk, X. Li, P.-F. Van de Moortele, K. Ugurbil, and G. J. Metzger, "Evolution of UHF body imaging in the human torso at 7T: Technology, applications, and future

directions," *Topics in Magnetic Resonance Imaging*, vol. 28, no. 3, pp. 101–124, 2019.

[285] N. Arango, J. Stockmann, and J. White, "Ultimate B0 shim and the design of optimal shim bases," in *Proceedings of ISMRM 27th Annual Meeting and Exhibition, Montreal, Canada*, 2019, p. 1462.

[286] M. Davids, B. Guérin, L. R. Schad, and L. L. Wald, "Peripheral nerve stimulation (PNS) constrained gradient coil design within a boundary element method stream function (BEM-SF) optimization," in *Proceedings of ISMRM 27th Annual Meeting and Exhibition, Montreal, Canada*, 2019, p. 1039.

[287] J. van Gemert, W. M. Brink, A. Webb, and R. F. Remis, "High-permittivity pad design for dielectric shimming in magnetic resonance imaging using projection-based model reduction and a nonlinear optimization scheme," *IEEE transactions on medical imaging*, vol. 37, no. 4, pp. 1035–1044, 2018.

[288] M. Rahim, S. Ullah, and P. Mueller, "Advances and challenges of biodegradable implant materials with a focus on magnesium-alloys and bacterial infections," *Metals*, vol. 8, no. 7, p. 532, 2018.

[289] Y. E. Lee, O. D. Miller, M. H. Reid, S. G. Johnson, and N. X. Fang, "Computational inverse design of non-intuitive illumination patterns to maximize optical force or torque," *Optics express*, vol. 25, no. 6, pp. 6757–6766, 2017.

[290] L. Jelinek and M. Capek, "Optimal currents on arbitrarily shaped surfaces," *IEEE Transactions on Antennas and Propagation*, vol. 65, no. 1, pp. 329–341, 2016.

[291] K. Bahrami, F. Shi, I. Rekik, and D. Shen, "Convolutional neural network for reconstruction of 7T-like images from 3T MRI using appearance and anatomical features," in *Deep Learning and Data Labeling for Medical Applications*. Springer, 2016, pp. 39–47.